

# Characterising the deglacial history of the East Antarctic Ice Sheet in central Wilkes Land using marine sediment cores

by

**Sian Tooze**

*Bsc (with Hons).* Geology, *Msc.* Applied Marine Geoscience

*Submitted in fulfilment of the requirements*

*for the degree of Doctor of Philosophy*

in

*Natural and Physical Sciences*

*(A UTAS PhD program)*

Institute for Marine and Antarctic Studies (IMAS)

UNIVERSITY OF TASMANIA

February 2022





## Declaration

I acknowledge the following people for their technical expertise and processing of some of the data I attained during my PhD: Patricia Gadd (Australian Nuclear Science and Technology Organisation) (x-ray fluorescence data, Chapter 2), Gabriel Enge (The Australian National University) (neodymium isotope data, Chapter 4) and Bruce Charlier (Victoria University of Wellington) (strontium isotope data, Chapter 4). The diatom abundance data in this thesis (Chapter 2) was provided by Amy Leventer (Colgate University). This thesis contains no material which has been accepted for a degree or diploma by the University or any other institution, except by way of background information and duly acknowledged here and in the thesis, and to the best of my knowledge and belief no material previously published or written by another person except where due acknowledgement is made in the text of the thesis, nor does the thesis contain any material that infringes copyright.

Signed:

Sian Tooze

Date: 22-10-2021

## **Authority of Access**

This thesis may be made available for loan. Copying and communication of any part of this thesis is prohibited for two years from the date this statement was signed; after that time limited copying and communication is permitted in accordance with the Copyright Act 1968.

Signed:

Sian Tooze

Date: 22-10-2021

## **Statement Regarding Published Work Contained in Thesis**

The publishers of the papers comprising Chapter 3 hold the copyright for that content and access to the material should be sought from the respective journals. The remaining nonpublished content of the thesis may be made available for loan and limited copying and communication in accordance with the Copyright Act 1968.

Signed:

Sian Tooze

Date: 22-10-2021

## Statement of Co-authorship

The following people and institutions contributed to the publication of work undertaken as part of this thesis:

**PhD candidate:** Sian Tooze, Institute for Marine and Antarctic Studies (IMAS)

**Author 1:** Dr. Jacqueline A. Halpin, Institute for Marine and Antarctic Studies (IMAS)

**Author 2:** Prof. Zanna Chase, Institute for Marine and Antarctic Studies (IMAS)

**Author 3:** Dr. Taryn Noble, Institute for Marine and Antarctic Studies (IMAS)

**Author 4:** Prof. Philip E. O'Brien, Macquarie University

**Author 5:** Prof. Leanne K. Armand, The Australian National University

### Contribution of work by co-authors for each paper:

**Paper 1: Scratching the surface: A marine sediment provenance record from the continental slope of central Wilkes Land, East Antarctica**

Located in Chapter 3

*Tooze, S., Halpin, J. A., Noble, T. L., Chase, Z., O'Brien, P. E., & Armand, L. (2020). Scratching the surface: A marine sediment provenance record from the continental slope of central Wilkes Land, East Antarctica. *Geochemistry, Geophysics, Geosystems*, 21(11), e2020GC009156*

Conceived Study: PhD candidate, Author 1, Author 2, Author 3

Analysis of data: PhD candidate

Data interpretation: PhD candidate, Author 1, Author 2, and Author 3

Manuscript writing: PhD candidate, Author 1, Author 2, and Author 3

Final edits and feedback on manuscript: Author 4, Author 5

Lead Author: PhD candidate

Corresponding Author: PhD candidate

**We, the undersigned, endorse the above stated contribution of work undertaken for each of the published (or submitted) peer-reviewed manuscripts contributing to this thesis:**

Signed:

Sian Tooze  
PhD Candidate  
O & C, IMAS  
University of Tasmania

Dr. Taryn Noble  
Primary Supervisor  
O & C, IMAS  
University of Tasmania

Prof. Neil Holbrook  
Head of Centre  
O & C, IMAS  
University of Tasmania

Date: 19/10/2021

19/10/2021

22/10/2021

# Foreword

Chapter 3 of this thesis was published in the journal *Geochemistry, Geophysics, Geosystems* in 2020. The age model in Chapter 3 was constructed using the Marine13 calibration curve, whereas the age models in Chapter 2 were constructed using the Marine20 calibration curve. This difference is due to the fact that Chapter 3 was written first and published before the Marine20 calibration curve was developed.

# *Acknowledgements*

My PhD journey has been a long bush hike into the Australian wilderness. The road has been rocky, and sometimes I wandered off path into the unexplored. Many times it rained and I got muddy feet, but the sun always came out shining through the trees. Overall, it has been an incredible and unique experience. I met many people along the way: some who led, some who walked with me and others who cheered me on from the sidelines. To all those who have given me direction, strength, support and encouragement, I would like to thank you here.

Firstly, I would like to thank my amazing supervisory team: Taryn Noble, Jacqueline Halpin and Zanna Chase. Thankyou for your expertise, support, patience and leadership. I am especially thankful for your enthusiasm, for always being available and helpful when I have approached your desk or office, and for presenting me with unique opportunities throughout my PhD. Thankyou Nils Jansen, Axel Durand, Habacuc Perez-Tribouiller, Pam Quayle, Ashley Townsend, Layla Creach, Giarn Carroll, Sandrin Feig, Karsten Goemann, Jay Thompson and Sebastien Meffre for your expertise, technical assistance, and support in the laboratory. Thank you to the Marine National Facility, the scientists and crew of voyage IN2017-V01 and the Sabrina Research Team for data collection and collaboration, and my co-authors: Philip O'Brien and Leanne Armand. To all my friends at IMAS, of which there are too many of you to name, thank you all for the support, laughs, tea breaks, brunches, coffees and walks.

I am enormously grateful to my beautiful family: Susan, Robert and Nicole Tooze. Thank you for your continual love and encouragement, the pep talks, the jokes, the Sunday Skype calls, the care packages, the handwritten letters and the daily updates that made me smile. I feel incredibly lucky to have such a loving and supportive family. To Melissa Oliver, undoubtedly THE best person on the planet. Thank you for always being there for me whether near or far, for your sarcasm and

wicked sense of humour, the phone calls that made my tummy ache with laughter, the road trips around Tassie and the Lake District, and most importantly for encouraging me to believe in myself. You have supported me through thick and thin and I could not have asked for a better best mate - you are stuck with me. To my truly awesome boyfriend, Matt Gmelig, thank you for being so supportive and encouraging during the final months of my PhD. A huge thank you must also go to my friends and coworkers at the Fern Tree Tavern and within the Fern Tree Community. Thank you for being my second, slightly crazy, Aussie family.

Finally, I would like to thank all those organisations and charities who contributed toward the funding of my PhD. My project was funded under Australian Research Council's Special Research Initiative for the Antarctic Gateway Partnership (Project ID SR140300001). Thank you to Jenna Patterson and Richard Coleman from the Antarctic Gateway Partnership for your assistance with finances related to my project. I would also like to express my gratitude to the Antarctic Science Foundation for the Covid-19 PhD Student Support Grant which provided valuable financial support through the final stages of my PhD.

# Contents

Declaration.....	iii
Authority of Access .....	iv
Statement Regarding Published Work Contained In Thesis .....	v
Statement of Co-Authorship .....	vi
Foreword.....	viii
Acknowledgements.....	ix
List of Figures .....	xiv
List of Tables .....	xxiv

<b>Abstract.....</b>	<b>1</b>
----------------------	----------

## Chapter 1

<b>Introduction .....</b>	<b>5</b>
1.1. PREAMBLE .....	5
1.2. THESIS AIMS AND OBJECTIVES.....	8
1.3. BACKGROUND .....	9
1.3.1. Modern Interactions between the Antarctic Ice Sheet and the Southern Ocean ...	9
1.3.2. Reconstructing the history of the EAIS using marine sediment cores .....	17
1.3.2.1. Age model construction using acid-insoluble organic matter.....	18
1.3.2.2. Paleoclimate proxies in marine sediment.....	23
1.3.2.3. Marine sediment provenance techniques.....	28
1.4. STUDY REGION .....	32
1.4.1. Sediment depositional regime .....	33
1.4.2. Subglacial geology .....	34
REFERENCES.....	39

## Chapter 2

<b>The wrath of thaw! Multi-proxy constraints on the nature and timing of the last deglaciation in central Wilkes Land .....</b>	<b>69</b>
ABSTRACT .....	69
2.1. INTRODUCTION .....	70
2.2. METHODS.....	73
2.2.1. Sampling locations .....	73
2.2.2. Biogenic silica and diatom abundance .....	74

Page

2.2.3. Radiocarbon dating and age model construction.....	75
2.2.4. Mass accumulation rates.....	77
2.2.5. Particle size analysis.....	78
2.2.6. X-ray fluorescence and magnetic susceptibility.....	80
2.3. RESULTS.....	81
2.3.1. Core sedimentology.....	81
2.3.2. Age models.....	83
2.3.3. Paleoproductivity across the deglaciation.....	88
2.3.4. IBRD MAR.....	95
2.3.5. Grain size variability.....	95
2.4. DISCUSSION.....	97
2.4.1. The Last Glacial Period.....	98
2.4.2. The last deglaciation.....	104
2.4.3. Holocene climate variability.....	113
2.5. CONCLUSIONS.....	114
2.6. SUPPLEMENTARY INFORMATION.....	116
REFERENCES.....	165

## Chapter 3

### Scratching the surface: a marine sediment provenance record from the continental slope of central Wilkes Land, East Antarctica.....178

ABSTRACT.....	178
3.1. INTRODUCTION.....	179
3.2. BACKGROUND: A BRIEF GLACIOLOGICAL AND GEOLOGICAL HISTORY OF WILKES LAND .	181
3.2.1. <i>Evolution of the East Antarctic Ice Sheet from the Late Pleistocene to present</i>	182
3.2.2. <i>The subglacial geology of central Wilkes Land</i> .....	183
3.3. METHODS.....	187
3.3.1. Sampling locations and descriptions.....	187
3.3.2. Radiocarbon dating.....	187
3.3.3. Quantification of iceberg-rafted debris flux.....	188
3.3.4. Biogenic silica concentrations.....	188
3.3.5. Trace element, U-Pb and Pb-Pb analysis.....	189
3.3.5.1. <i>Sample preparation</i> .....	189
3.3.5.2. <i>Sample Imaging</i> .....	189
3.3.5.3. <i>LA-ICPMS analysis</i> .....	190
3.4. RESULTS.....	192
3.4.1. Bulk organic carbon ages, IBRD flux and biogenic silica concentrations.....	192
3.4.2. Detrital mineralogy and grain morphology/textures.....	195
3.4.3. Detrital zircon, apatite and titanite geochronology.....	197
3.4.4. Detrital zircon, apatite and titanite trace element geochemistry.....	199
3.4.5. Feldspar Pb-isotopic compositions.....	202
3.5. DISCUSSION.....	204
3.5.1. Was the Totten Glacier the main conduit for KC14 detritus?.....	205
3.5.2. A case for a distributed Wilkes Land provenance for KC14.....	209
3.5.2.1. <i>A broad source region during interglacials</i> .....	209

3.5.2.2. <i>Debris flows during the Last Glacial Period</i> .....	210
3.5.2.3. <i>A proximal provenance during deglaciation</i> .....	211
3.5.2.4. <i>Evidence for minor far-field provenance</i> .....	212
3.6. CONCLUSIONS .....	214
3.7. SUPPLEMENTARY INFORMATION .....	216
REFERENCES .....	222

## Chapter 4

### **Exhibit A: Nd-Sr isotopic fingerprint of marine sediments offshore central Wilkes Land, East Antarctica .....234**

ABSTRACT .....	234
4.1. INTRODUCTION .....	235
4.2. BACKGROUND: EXISTING ND-ISOTOPIC SIGNATURES IN SOUTHERN AUSTRALIA AND CENTRAL WILKES LAND.....	239
4.2.1. Whole rock $\epsilon_{Nd}$ signatures .....	240
4.2.2. Detrital $\epsilon_{Nd}$ signatures offshore central Wilkes Land .....	243
4.3. METHODS .....	244
4.3.1. Core locations .....	244
4.3.2. Sediment sampling .....	244
4.3.3. Reductive leaching and sediment digestion.....	245
4.3.4. Extraction chromatography for REE isolation .....	245
4.3.5. Lanthanide extraction for Nd isolation .....	246
4.3.6. Extraction chromatography for Sr isolation .....	246
4.3.7. Instrumental analysis and data processing.....	247
4.4. RESULTS .....	249
4.4.1. Neodymium isotope composition.....	249
4.4.2. Strontium isotope composition .....	251
4.5. DISCUSSION.....	253
4.5.1. Broad versus narrow sediment provenance .....	254
4.5.2. The role of Totten Glacier in supplying detritus to the continental margin .....	258
4.5.3. Temporal variation in sediment provenance .....	259
4.5.4. Current-driven changes to the Sr-isotopic compositions.....	261
4.6. CONCLUSIONS .....	265
4.7. SUPPLEMENTARY INFORMATION.....	267
REFERENCES .....	268

## Chapter 5

### **Main conclusions and future work .....275**

5.1. CONCLUSIONS.....	275
5.2. FUTURE WORK.....	280
REFERENCES .....	282

# List of Figures

**Figure 1.1. Subglacial topography of Antarctica.** Subglacial topography is from BedMachine (version 1.0) (Morlighem et al., 2020). The red box outlines the central Wilkes Land region, the region of East Antarctica that is the focus of this thesis. Dark blue lines illustrate the approximate outlines of subglacial basins in central Wilkes Land. ASB – Aurora Subglacial Basin, SSB – Sabrina Subglacial Basin, WSB – Wilkes Subglacial Basin.

**Figure 1.2. Antarctic ice shelves: melting rates and annual mass loss.** Taken from Rignot et al. (2013). Map of Antarctica, indicating the location, melt rate and mass loss of the circum-Antarctic ice shelves. Black lines represent the ice shelf borders as observed in 2007 and 2008. Pie charts are relative in size to the mass loss (Gt/yr) at each location and are categorised into calving (striped infill) and basal melting (black infill) events.

**Figure 1.3. Southern Ocean systems. (a)** Map of Antarctica showing the combined westward-flowing currents (The Antarctic Coastal Current and the Antarctic Slope Current; mid blue dashed arrows proximal to Antarctic coastline), the southern boundary of the eastward-flowing Antarctic Circumpolar Current (ACC) and the Antarctic Polar Front (light blue) (Orsi et al., 1995). The location and flow direction of the Weddell (Deacon, 1979; Fahrbach et al., 1994), Ross (Jacobs et al., 1970) and Kerguelen (McCartney and Donohue, 2007) gyres (Gordon, 1971) are shown in orange. **(b)** Schematic diagram taken from Carter et al. (2004) showing the approximate depths and movements of water masses in the Southern Ocean. AABW – Antarctic Bottom Water, LCDW – Lower Circumpolar Deepwater, NADW – North Atlantic Deepwater, UCDW – Upper Circumpolar Deepwater, AAIW – Antarctic Intermediate Water, SAMW – Subantarctic Mode Water, ASF – Antarctic Slope Front, SB – Southern Boundary of the ACC, SF – Southern Front, PF – Polar Front, SAF – Subantarctic Front, STF – Subtropical Front.

**Figure 1.4. Map of central Wilkes Land.** Subglacial topography is from BedMachine (version 1.0) (Morlighem et al., 2020). The location of the cores used in this thesis are shown as pink circles (see section 1.4.). TG – Totten Glacier, MUG – Moscow University Glacier. Inset shows a NASA satellite image (taken on 25-05-2018) of the sea-ice conditions in central Wilkes Land. The location of the Dalton Polynya is outlined in blue. The Dalton Iceberg Tongue (hashed area) is also shown.

**Figure 1.5. Core locations.** Map of central Wilkes Land, East Antarctica, with core locations (pink). Offshore bathymetry and 1000 m contours are shown using the International Bathymetric Chart of the Southern Ocean (IBCSO), version 1.0 (Arndt et al., 2013). High resolution bathymetry was acquired from the *RV Investigator* (voyage IN2017\_V01; Armand et al., 2018). The southern boundary of the east-flowing Antarctic Circumpolar Current is shown in light blue (Orsi et al., 1995). The west-flowing Antarctic Coastal Current is represented by blue arrows proximal to the coast. The approximate position of an eddy identified by Wakatsuchi et al. (1994) is shown with black dashed arrows.

**Figure 1.6. Basement rock provinces in southern Australia and East Antarctica.** Full-fit Gondwana (c. 160 Ma) reconstruction, with Antarctica fixed in its present-day reference frame (Matthews et al., 2016). Basement rock provinces are shown using most recent interpretation of Maritati et al. (2019). Fault positions are after Aitken et al. (2014) and Maritati et al. (2019).

**Figure 2.1.** Central Wilkes Land. Map showing location of central Wilkes Land. Subglacial topography is from BedMachine (version 1.0) (Morlighem et al., 2020). Dark blue lines illustrate the approximate outlines of subglacial basins. Dashed blue line represents the southern boundary of the east-flowing Antarctic Circumpolar Current. Top left inset shows the location on a map of Antarctica. Bottom left inset shows a NASA satellite image (taken on 25-05-2018) of the sea-ice conditions in central Wilkes Land, highlighting the Dalton Polynya.

**Figure 2.2.** Timing of the onset of deglaciation around the East Antarctic margin. Compilation of terrestrial and marine sediment core age data from East Antarctica with approximate timings of the regional onset of deglaciation. Yellow box highlights the absence of data from central Wilkes Land. SG - Sørtdal Glacier. Offshore data are from Gingele et al. (1997) (Dronning Maud Land), Igarashi et al. (2001) (Lützhow-Holm Bay), Leventer et al. (2006) and Harris and O'Brien (1998) (Mac.Robertson Land), Domack et al. (1991, 1998), Leventer et al., (2006) and Hemer and Harris, (2003) (Prydz Bay), (Berg et al., 2010a, 2010b) (Rauer Group), Crosta et al. (2007), Harris et al. (2001), Mackintosh et al. (2014) and McMullen et al. (2006) (George V Land) and Prothro et al. (2020) (The Ross Sea). Onshore data are from Miura et al. (1998) (Lützhow-Holm Bay), MacKintosh et al. (2011) (Framnes Mountains), Wagner et al. (2004) (Prince Charles Mountains), Hodgson et al. (2001) (Larsemann Hills), Adamson and Pickard, (1983), Coolen et al. (2004), Gibson et al. (2009), Huang et al. (2009), McMinn (2000), Roberts and McMinn (1999), Zhang (1985) and Zwart

et al. (1998) (Vestfold Hills), Gore et al. (2001) (Bunger Hills), and Goodwin (1993), Kirkup et al. (2002) and Roberts et al. (2006) (Windmill Islands).

**Figure 2.3. Sample locations.** Map of central Wilkes Land, East Antarctica, with core locations (pink). Offshore bathymetry and 1000 m contours are shown using the International Bathymetric Chart of the Southern Ocean (IBCSO), version 1.0 (Arndt et al., 2013). High resolution bathymetry was acquired from the *RV Investigator* (voyage IN2017\_V01; Armand et al., 2018). The southern boundary of the east-flowing Antarctic Circumpolar Current is shown in light blue (Orsi et al., 1995). The west-flowing Antarctic Coastal Current is represented by darker blue arrows proximal to the coast.

**Figure 2.4. Lithological units.** Diagram presenting the lithological units that comprise the four sediment cores. Interpreted lithostratigraphic correlations are shown as dashed lines.

**Figure 2.5.** Sedimentary logs of each of the cores, reconstructed from Armand et al. (2018). Bulk grain size (GS) data from Geoscience Australia were plotted using the grain size parameters of Folk and Ward (1957). Magnetic susceptibility (MS) is shown to the right of each core.

**Figure 2.6. Age models.** Graphs showing the age model for each core. Age distribution curves for each calibrated radiocarbon age are shown in orange, median ages are shown with a black line and the associated  $2\sigma$  model error in grey. Insets show the  $2\sigma$  model age error with depth.

**Figure 2.7. Linear Sedimentation Rates.** Graph showing the LSR and the calibrated radiocarbon ages for each core. Green stars mark where sediment was sampled for AIOM dating.

**Figure 2.8. Proxies for biological productivity.** Graphs showing the BiSi concentration, diatom abundance and Si/Al and Ba/Al XRF ratios in each core as proxies for biological productivity. Each proxy is plotted against age using the age model described in the methods.

**Figure 2.9.** Crossplots showing the correlation between BiSi concentration and the Si/Al XRF ratio in each of the cores.

**Figure 2.10. Permanently Open Ocean Zone.** Graphs showing the temporal variation in absolute diatom abundance at each core site (orange) and the percent proportion (of the total diatom abundance) of diatom species *Fragilariopsis kerguelensis*, (red), an indicator of open surface waters. Grey panels indicate a period of continental shelf sediment reworking (Rw) during ice sheet advance.

**Figure 2.11. Meltwater production.** Graphs showing the temporal variation in absolute diatom abundance at each core site (orange) and the percent proportion (of the total diatom abundance) of diatom species *Chaetoceros* subg. *Hyalochaete* (pink), an indicator of spring blooms associated with deglaciation and meltwater input. Grey panels indicate the period of continental shelf sediment reworking (Rw) during ice sheet advance.

**Figure 2.12. Extinct and robust diatom species.** Graphs showing temporal variation in the percentage of extinct (*Actinocyclus ingens*, *Denticulopsis* spp., *Hemidiscus karstenii*, *Pyxilla reticulata*, *Rouxia* spp. and *Stephanopyxis* spp.) and robust (*Rhizosolenia* spp.) diatoms compared with the IBRD MAR in each core.

**Figure 2.13. Mass accumulation rates.** Graphs showing temporal variation in the IBRD MAR and BiSi MAR at each core site. The coarse sand fraction (CSF) used to quantify the IBRD MAR is also shown.

**Figure 2.14. Proxies for paleocurrent speed.** Graphs showing the mean grain size from bulk and BiSi-leached sediments, Zr/Rb XRF ratio and SS% in each of the cores, as proxies for paleocurrent speed.

**Figure 2.15.** Crossplots showing the correlation between SS% and the Zr/Rb ratio in each of the cores.

**Figure 2.16. Key proxies in KC02.** (a) Zr/Rb as a proxy for paleocurrent speed, (b), (c) Si/Al and absolute diatom abundance, respectively, as proxies for total primary productivity, (d) percent of the total diatom abundance of *Chaetoceros* subg. *Hyalochaete* as a proxy for meltwater input, (e) percent of the total diatom abundance of extinct diatoms, (f) the IBRD MAR. The dark grey bar represents the possible range of time in which the last deglaciation initiated. Light grey bars highlight key climate events observed in the record. HO – Holocene Optimum, ACR – Antarctic Cold Reversal (Blunier et al., 1997; Pedro et al., 2011), LGP – Last Glacial Period. Tabs at the top of the graph indicate the timing of key climate events in

the Northern Hemisphere. HE 1 – Henrich Event I (~18-15 ka), BA - Bølling–Allerød interstadial (14.7-12.9 ka).

**Figure 2.17. Key proxies in KC14.** (a) Zr/Rb as a proxy for paleocurrent speed, (b), (c) Si/Al and absolute diatom abundance, respectively, as proxies for total primary productivity, (d) percent of the total diatom abundance of *Chaetoceros* subg. *Hyalochaete* as a proxy for meltwater input, (e) percent of the total diatom abundance of extinct diatoms, (f) the IBRD MAR. Grey bar represents the possible range of time in which the last deglaciation initiated. Black dashed lines show the minimum and maximum age model errors for the onset of deglaciation. Light grey bars highlight key climate events observed in the record. HO – Holocene Optimum, ACR – Antarctic Cold Reversal (Blunier et al., 1997; Pedro et al., 2011), MWP-1A – Meltwater Pulse 1A (Deschamps et al., 2012), LGP – Last Glacial Period. Tabs at the top of the graph indicate the timing of key climate events in the Northern Hemisphere. HE 1 – Henrich Event I (~18-15 ka).

**Figure 2.18. Key proxies in KC04.** (a) Zr/Rb as a proxy for paleocurrent speed, (b), (c) Si/Al and absolute diatom abundance, respectively, as proxies for total primary productivity, (d) percent of the total diatom abundance of *Chaetoceros* subg. *Hyalochaete* as a proxy for meltwater input, (e) percent of the total diatom abundance of extinct diatoms, (f) the IBRD MAR. Grey bar represents the possible range of time in which the last deglaciation initiated. Light grey bars highlight key climate events observed in the record. HO – Holocene Optimum, LGP – Last Glacial Period. Tabs at the top of the graph indicate the timing of key climate events in the Northern Hemisphere. HE 1 – Henrich Event I (~18-15 ka), BA - Bølling–Allerød interstadial (14.7-12.9 ka).

**Figure 2.19. Key proxies in KC12.** (a) Zr/Rb as a proxy for paleocurrent speed, (b), (c) Si/Al and absolute diatom abundance, respectively, as proxies for total primary productivity, (d) percent of the total diatom abundance of *Chaetoceros* subg. *Hyalochaete* as a proxy for meltwater input, (e) percent of the total diatom abundance of extinct diatoms, (f) the IBRD MAR. Grey bar represents the possible range of time in which the last deglaciation initiated. Black dashed lines show the minimum and maximum age model errors for the onset of deglaciation. Light grey bars highlight key climate events observed in the record. HO – Holocene Optimum, ACR – Antarctic Cold Reversal (Blunier et al., 1997; Pedro et al., 2011), MWP-1A – Meltwater Pulse 1A (Deschamps et al., 2012), LGP – Last Glacial Period. Tabs at the top of the graph indicate the timing of key climate events in the Northern Hemisphere. HE 1 – Henrich Event I (~18-15 ka), BA - Bølling–Allerød interstadial (14.7-12.9 ka).

**Figure 3.1.** Simplified outline of the Sabrina Sedimentary Basin (bold dark blue line) is from Maritati et al. (2019) after (Aitken et al., 2016b). Region A, an area of thin sedimentary rock cover (<1 km thick) and basement rock exposure is interpreted by Aitken et al. (2016b). Grey lines mark the boundaries of ice drainage basins (Mouginot et al., 2017). Black arrows represent the westward-flowing Antarctic Coastal Current. Inset shows the study location (red box) on a map of Antarctica. **(b)** MEaSURES surface ice velocity from InSAR data, highlighting major glacier outflows in central Wilkes Land (Mouginot et al., 2012; Rignot et al., 2011).

**Figure 3.2.** Geological provinces of southern Australia and East Antarctica. **(a)** Full-fit Gondwana tectonic reconstruction at c. 160 Ma with Antarctica fixed in its present-day reference frame (Matthews et al., 2016). Larger-scale geographic location is shown in the inset. Geological provinces in southern Australia and conjugate regions of East Antarctica shown using most recent interpretation of Maritati et al. (2019). Fault positions are after Aitken et al. (2014) and Maritati et al. (2019). **(b)** Time-space diagram with geological provinces of southern Australia and their Antarctic counterparts shown from west to east. Key magmatic and metamorphic events associated with the formation of provinces are interpreted from U-Pb analyses of in-situ zircon from basement rocks. Data from southern Australia is from Wingate et al. (2015a, 2015b) and data from East Antarctica is from Maritati et al. (2019) and Morrissey et al. (2017). AOC – Arubiddy Ophiolite Complex, MM – Malcolm Metamorphics, MRF – Mount Ragged Formation, Ss. - Supersuite. Ages and spatial positions are approximate.

**Figure 3.3.** KC14 downcore calibrated bulk organic radiocarbon ages, LSR, CSF, IBRD flux, BiSi flux and BiSi concentrations. A sedimentary log (Armand et al., 2018) shows downcore variability in sedimentary features and composition. Variation in colour on the sedimentary log represents sediment colour logged onboard *RV Investigator* using the Munsell Color Chart. Four depth intervals, representing distinct changes in BiSi concentrations, are separated by grey lines. The horizontal dashed line corresponds with a marked decrease in the IBRD flux and an increase in BiSi concentrations. These changes are interpreted to represent the beginning of the deglacial transition between the Last Glacial Period and the Holocene.

**Figure 3.4.** Representative CL images of detrital zircon grains from the intermediate fraction of KC14. Circles represent LA-ICPMS analysis sites. Scale bars at 50  $\mu\text{m}$  are shown as

white lines under each grain. Ages are  $^{207}\text{Pb}/^{206}\text{Pb}$  where  $> 1000$  Ma and  $^{207}\text{Pb}$ -corrected  $^{206}\text{Pb}/^{238}\text{U}$  where  $< 1000$  Ma  $\pm 1\sigma$  error. Grains are divided into the following broad age groups, most of which are associated with major periods of magmatism and metamorphism in southern Australia and East Antarctica (Fig. 3.2): **(a)** c. 1250-1100 Ma (Albany-Fraser/Wilkes Province Stage II, including the Moodini Supersuite) **(b)** c. 1345-1260 Ma (Albany-Fraser/Wilkes Province Stage I) **(c)** c. 1480-1390 Ma (Madura/Nuyina Province) **(d)** c. 1610-1490 Ma (Toolgana and Undawidgi supersuites of Coompana/Banzare Province) **(e)**  $> 1610$  Ma.

**Figure 3.5.** Detrital age signatures in KC14. **(a)** Age spectra for detrital zircon, titanite and apatite for the entire KC14 core presented as probability-density plots (black curve, grey fill). Kernel density curve is shown in red. **(b)** Probability-density plots showing downcore age variability in detrital zircon, titanite and apatite. Grey rectangles within the stylised core on left hand side show where sediment samples were taken from within each depth interval of KC14 for U-Pb analysis. Major age peaks and total number of analyses (n) are indicated. Age signatures of geological provinces in East Antarctica/southern Australia (as in Figure 3.2) are highlighted as coloured bars for comparison. Although the Moodini Supersuite intrudes the Banzare/Coompana and Nuyina/Madura provinces, it is here grouped with the Wilkes Province/Albany-Fraser Orogen due to the overlap in age ranges. Pie charts show relative proportion of each mineral size fraction contributing to the age signature for each depth interval. Intervals 1-4 represent changes in BiSi concentration and are the same as those presented in Figure 3.3.

**Figure 3.6.** Detrital zircon trace element geochemistry. **(a)** Chondrite-normalised REE diagrams and Th/U ratios for detrital zircon in KC14 and primary c. 1150 Ma zircon from Chick Island basement rocks (Maritati et al., 2019). Typical REE compositions for magmatic and granulitic (i.e., high temperature metamorphic) zircon from Rubatto (2017) are shown. **(b, c)** KC14 detrital zircon trace element data overlain on source rock discrimination diagrams from Belousova et al. (2002b).

**Figure 3.7.** New detrital and bedrock feldspar Pb-isotopic datasets compared to regional Antarctic feldspar Pb-isotopic compositions. **(a)** Pb-isotopic signatures from detrital feldspar in KC14 (pink symbols) and basement rock feldspar from Balaena Islets (green symbols) and Chick Island (yellow symbols) overlain on Pb-isotopic feldspar domains from various locations in East Antarctica. Error bars ( $2\sigma$ ) are shown for all analyses in this study. Indo-Antarctic basement rock data are from Flowerdew et al. (2013) and Mulder et al. (2019). Australo-Antarctic basement rock data are from Mulder et al. (2019) (Windmill Islands,

Bunger Hills, Charcot) and this study (Chick Island and Balaena Islets). Growth curves for the mantle ( $\mu = 9$ ), average crust ( $\mu = 9.74$ ) and upper crust ( $\mu = 12$ ) are plotted using the Pb isotope evolution model of Stacey and Kramers (1975). **(b)** Inset to **(a)**, highlighting the analyses from this study. Black outline/green fill polygon shows Pb-isotopic compositions of basement rocks from the Wilkes Province (Windmill Islands and Balaena Islets).

**Figure 3.8.** Comparison of predicted detrital source regions from the East Antarctic coast with onshore and offshore marine core records. Shown are locations of cores from Pierce et al. (2014) (orange symbols) and of KC14 (pink circle). Inset: U-Pb detrital zircon age signatures for each sector including KC14. Offshore data from Pierce et al. (2014). Striped boxes highlight dominant age populations of compiled onshore data from Veevers (2012) and Veevers and Saeed (2011). Coloured bars represent main detrital age populations in KC14 and correspond with coloured text on the map, indicating inferred provenance regions of each respective age population. WSB – Wilkes Subglacial Basin, SSB – Sabrina Sedimentary Basin (blue polygons). CG – Cook Glacier, FG – Fox Glacier, HG – Holmes Glacier, MUG – Moscow University Glacier, NG – Ninnis Glacier, NV – Northern Victoria, TG – Totten Glacier, ThG – Thompson Glacier, WG – Williamson Glacier. Blue dashed line with arrows shows the position of the southern boundary of the eastward-flowing Antarctic Circumpolar Current (Orsi et al., 1995). Black arrows represent the westward-flowing Antarctic Coastal Current. Modelled basal velocity contours for an ice sheet slightly advanced relative to the present-day grounding line are from Aitken et al. (2016b) for the region between 90°E and 180°E.

**Figure 3.9.** Basal ice sheet velocity in central Wilkes Land overlain on subglacial geological provinces interpreted from geophysical data and coastal outcrop (Aitken et al., 2014; Maritati et al., 2019). Coastal (yellow) and offshore (pink) sample locations are shown. Grey lines mark the boundaries of ice drainage basins (Mouginot et al., 2017). **(a)** Map showing modelled ice sheet basal velocity contours predicted for an ice sheet slightly advanced relative to the present from Aitken et al. (2016b) and clipped to the modern grounding line (Mouginot et al., 2017). **(b)** Map showing modelled basal erosion potential at 21 ka from Golledge et al. (2013). The modelled maximum extent of the ice sheet is indicated with a blue dashed line (Golledge et al., 2013). The position of a grounding zone wedge (GSW) identified by Post et al. (2020) is shown (white star), as new evidence indicating the former maximum extent of the ice sheet at that location.

**Supplementary Fig. 3.1.** Terra-Wasserburg diagrams for detrital zircon, titanite and apatite in KC14. Error ellipses are plotted at  $2\sigma$ . **(a)** Detrital zircon analyses showing high

concordance. **(b)** Highly discordant detrital titanite analyses. Discordia line fitted through analyses is shown in black with  $2\sigma$  uncertainty (grey). **(c)** Highly discordant detrital apatite analyses. Discordia line fitted through analyses is shown in black with  $2\sigma$  uncertainty (grey).

**Supplementary Fig. 3.2.** Chondrite-normalised REE and trace element compositions for detrital apatite and titanite in KC14. **(a)** Chondrite-normalised REE composition for detrital apatite analyses. **(b)** Chondrite-normalised REE composition for detrital titanite analyses. **(c)** Detrital apatite analyses overlain on source rock composition discrimination diagram of Belousova et al. (2002b). **(d)** Fe concentrations in detrital titanite with approximate ranges for typical metamorphic and igneous source rock types shown from Olierook et al. (2019).

**Figure 4.1. Central Wilkes Land.** Map of central Wilkes Land, East Antarctica with core locations for this study (pink). Basement rock provinces (the Wilkes, Nuyina and Banzare provinces) and igneous plutons (Moodini, Undawidgi and Toolgana supersuites) are interpreted from airborne geophysical data (Aitken et al., 2014; Maritati et al., 2019) and rare rock outcrop sampled at Chick Island (Maritati et al., 2019). Ice drainage divides (Mouginot et al., 2017) are shown as blue lines. Bathymetry and 1000 m contours are shown using the International Bathymetric Chart of the Southern Ocean (IBCSO), version 1.0 (Arndt et al., 2013). High resolution bathymetry of the continental slope was acquired from *RV Investigator* (voyage IN2017\_V01) (Armand et al., 2018). Inset shows study location (black box) on a map of Antarctica.

**Figure 4.2. Whole-rock  $\epsilon_{Nd}$  signatures from southern Australia and East Antarctica.** **(a)** Map showing the margins of southern Australia and central Wilkes Land, East Antarctica in a full-fit Gondwana reconstruction (c. 160 Ma) with Antarctica fixed in its present-day reference frame (Matthews et al., 2016). Geological provinces in southern Australia and conjugate regions of East Antarctica are shown using the most recent interpretation of Maritati et al. (2019). Fault positions are after Aitken et al. (2014) and Maritati et al. (2019). The locations of boreholes in southern Australia and rare rock outcrop from both margins from which whole-rock  $\epsilon_{Nd}$  signatures were obtained (Kirkland et al., 2015, 2017; Spaggiari et al., 2018) are shown as white circles and black stars, respectively. **(b)** Whole-rock  $\epsilon_{Nd}$  signatures plotted against U-Pb primary zircon ages from rocks recovered from boreholes (Kirkland et al., 2015, 2017; Spaggiari et al., 2018) and rare outcrop from the Albany-Fraser Orogen/Wilkes Province (Black et al., 1992a, 1992b; Nelson et al., 1995; Zhang et al., 2012). Although most of the  $\epsilon_{Nd}$  values were obtained from rocks samples from southern Australia, basement rock provinces are referred to in the figure by their Antarctic equivalent names for simplicity.

**Figure 4.3. Whole-rock and detrital  $\epsilon_{Nd}$  signatures from central Wilkes Land.** Map showing sparse detrital  $\epsilon_{Nd}$  signatures from core top sediments offshore central Wilkes Land (Pierce et al., 2011; Roy et al., 2007; van de Fliedert et al., 2007) and whole rock  $\epsilon_{Nd}$  signatures from rare outcrop at Bunger Hills (Black et al., 1992b; Sheraton et al., 1990) and the Windmill Islands (Möller et al., 2002; Zhang et al., 2012). Data sources for basement rock provinces, bathymetry and oceanography are as per Figure 4.1.

**Figure 4.4. Neodymium isotopic compositions.** Graph showing measured  $\epsilon_{Nd}$  values for the bulk and fine (< 63  $\mu\text{m}$ ) sediment fractions in each core with **(a)** depth and **(b)** age (fine fraction only).  $2\sigma$  error bars for  $\epsilon_{Nd}$  values are shown. Age model construction in **(b)** is described in Chapter 2. Data for KC12 is cut off at 25 ka.

**Figure 4.5. Strontium isotopic compositions.** Graph showing measured  $^{87}\text{Sr}/^{86}\text{Sr}$  ratios of the bulk and fine (< 63  $\mu\text{m}$ ) sediment fractions in each core with **(a)** depth at **(b)** age (fine fraction only).  $2\sigma$  error bars for  $^{87}\text{Sr}/^{86}\text{Sr}$  ratios are smaller than the markers. Age model construction in **(b)** is described in Chapter 2. Data for KC12 is cut off at 25 ka.

**Figure 4.6. Nd and Sr isotopic compositions.** Crossplots comparing the  $\epsilon_{Nd}$  and  $^{87}\text{Sr}/^{86}\text{Sr}$  signatures for fine detrital sediment samples at each core site. Error bars for  $^{87}\text{Sr}/^{86}\text{Sr}$  are smaller than the markers.

**Figure 4.7. Whole-rock and detrital  $\epsilon_{Nd}$  signatures.** **(a)** Whole-rock  $\epsilon_{Nd}$  signatures are from the southern Australian (Black et al., 1992a; Kirkland et al., 2015, 2017; Nelson et al., 1995; Spaggiari et al., 2018) and East Antarctic (Zhang et al., 2012) margins and are plotted against the primary zircon  $^{207}\text{Pb}/^{206}\text{Pb}$  crystallisation age. The dominant magmatic composition of the rocks sampled are shown, though many of the rocks from the Wilkes Province have been regionally metamorphosed (Clark et al., 2000). The total range of detrital  $\epsilon_{Nd}$  signatures from glacial-interglacial bulk and fine sediments from this study are shown as a grey bar. **(b)** Composite probability density plots showing detrital zircon  $^{207}\text{Pb}/^{206}\text{Pb}$  ages and detrital apatite and titanite  $^{206}\text{Pb}/^{238}\text{U}$  ages from KC14 (Chapter 3; Tooze et al., 2020). Age scale is cut off at 1700 Ma and 1100 Ma.

**Figure 4.8. Sediment provenance.** Maps showing two scenarios outlining possible sediment provenance pathways to the continental rise in central Wilkes Land. All map features are as given in Figure 4.1. **(a)** detrital sediment is sourced only from rocks of the Moodini Supersuite that intrudes the Nuyina Province in the coastal region of the Totten and

Moscow University glacier catchments. **(b)** Detrital sediment is derived from multiple source rocks in all three basement provinces via multiple outlet glaciers.

**Figure 4.9.** Temporal variation in  $\epsilon_{Nd}$  signatures at each core site compared with Si/Al ratios (black curve) representing changes in primary biological productivity during the last deglaciation.

**Figure 4.10.** Temporal variation in  $^{87}Sr/^{86}Sr$  signatures (coloured curves) at each core site compared with biological productivity (black curve) as an indicator for warming conditions and ice sheet retreat over the Last Glacial Period-Holocene transition. Increase in current-driven sediment redistribution during the deglaciation may have contributed to the decrease to less radiogenic 87/86 values through time.

**Figure 4.11. Comparison between Zr/Rb and Sr-isotopic compositions.** Graphs showing the correlation ( $R^2$ ) between the  $^{87}Sr/^{86}Sr$  ratio and the Zr/Rb ratio (representing both grain size and paleocurrent speed) in each core.

**Figure 4.12. Comparison between mean grain size and Sr-isotopic compositions.** Graphs showing the correlation ( $R^2$ ) between the  $^{87}Sr/^{86}Sr$  ratio and the mean (BiSi-leached) grain size in each core.

**Figure 5.1.** Different phases of ice sheet configuration and the marine sediment depositional regime on the adjacent continental margin. **(a)** the Last Glacial Period, **(b)** deglaciation, **(c)** the modern day ice sheet.

## List of Tables

**Table 1.1.** Locations and water depths at which the Multicores (MC) and Kasten cores (KC) used in this thesis were recovered (voyage INV2017-V01; Armand et al., 2018).

**Table 2.1. Regional marine reservoir ages.** Table showing the regional MRA used for each radiocarbon age interval based on values from the literature. Full compilation of estimated regional MRAs for the Southern Ocean can be found in Skinner et al. (2019). For radiocarbon age ranges where the estimated regional MRA for the Southern Ocean was close to the modern-day MRA estimated for the study region, the latter was used in the

marine reservoir correction. The  $\Delta R$  value for each radiocarbon age was calculated using the difference between the regional MRA and the global mean MRA provided by Heaton et al. (2020).

**Table 2.2.** Degree of sediment sorting in each core based on the classification scheme of Blott and Pye (2001), modified from Folk and Ward (1957). Samples are those leached of BiSi and used to calculate the mean leached grain size and the SS%. Bright green – very well-sorted (< 1.27), mid green – well-sorted (1.27-1.41), dark green – moderately well-sorted (1.41-1.62), orange – moderately-sorted (1.62-2), light blue – poorly-sorted (2-4), dark blue – extremely poorly-sorted (> 16).

**Table 2.3. Radiocarbon age data.** Table showing all primary and calibrated Kasten and Multicore ages. Primary surface ages for KC14 and KC12 are model-predicted (\*) and were extrapolated using the uncalibrated downcore ages and the BChron package and BChronology function in R (Haslett and Parnell, 2008; Parnell et al., 2008). The Local Contamination Offset (LCO) was calculated from the difference between the surface age at each site and a regional MRA of  $925 \pm 30$  yr (Holder et al., 2020). Ages were corrected for the LCO and calibrated in Matlab using the Marine20 calibration curve (Heaton et al., 2020) and the calculated  $\Delta R$  values. Final ages and errors are reported at a 95% confidence limit using the  $2\sigma$  highest posterior density interval.

**Supplementary Table 2.1.** XRF data for KC02.

**Supplementary Table 2.2.** XRF data for KC14.

**Supplementary Table 2.3.** XRF data for KC04.

**Supplementary Table 2.4.** XRF data for KC12.

**Supplementary Table 2.5.** Measured CSF, DBD, IBRD MAR, BiSi and BiSi MAR in KC02.

**Supplementary Table 2.6.** Measured CSF, DBD, IBRD MAR, BiSi and BiSi MAR in KC14.

**Supplementary Table 2.7.** Measured CSF, DBD, IBRD MAR, BiSi and BiSi MAR in KC04.

**Supplementary Table 2.8.** Measured CSF, DBD, IBRD MAR, BiSi and BiSi MAR in KC12.

**Supplementary Table 2.9.** Total diatom abundance and the proportion of *Fragilariopsis kerguelensis*, *Chaetoceros* subg. *Hyalochaete*, extinct species and robust species (as a percentage of the total diatom abundance) measured in KC02.

**Supplementary Table 2.10.** Total diatom abundance and the proportion of *Fragilariopsis kerguelensis*, *Chaetoceros* subg. *Hyalochaete*, extinct species and robust species (as a percentage of the total diatom abundance) measured in KC14.

**Supplementary Table 2.11.** Total diatom abundance and the proportion of *Fragilariopsis kerguelensis*, *Chaetoceros* subg. *Hyalochaete*, extinct species and robust species (as a percentage of the total diatom abundance) measured in KC04.

**Supplementary Table 2.12.** Total diatom abundance and the proportion of *Fragilariopsis kerguelensis*, *Chaetoceros* subg. *Hyalochaete*, extinct species and robust species (as a percentage of the total diatom abundance) measured in KC12.

**Supplementary Table 2.13.** Bulk mean grain size measured in KC02.

**Supplementary Table 2.14.** Bulk mean grain size measured in KC14.

**Supplementary Table 2.15.** Bulk mean grain size measured in KC04.

**Supplementary Table 2.16.** Bulk mean grain size measured in KC12.

**Supplementary Table 2.17.** BiSi-leached mean grain size and sortable silt percent measured in KC02.

**Supplementary Table 2.18.** BiSi-leached mean grain size and sortable silt percent measured in KC14.

**Supplementary Table 2.19.** BiSi-leached mean grain size and sortable silt percent measured in KC04.

**Supplementary Table 2.20.** BiSi-leached mean grain size and sortable silt percent measured in KC12.

**Supplementary Table 3.1.** Sample locations and descriptions.

**Supplementary Table 3.2.** List of parameters and Standard Reference Materials used for detrital zircon, apatite, and titanite U-Pb analysis and detrital feldspar Pb-Pb analysis. REEs – Rare Earth Elements.

**Supplementary Table 3.3.** List of secondary Standard Reference Materials used for U-Pb analysis of detrital zircon, titanite and apatite, and Pb-Pb analysis of detrital feldspar. Weighted average values for each session on the instrument are shown. Published recommended values are given. All errors are  $2\sigma$ .

**Table 4.1. Blank levels for sample preparation and Sr extraction.** Blanks 1-3 represent contamination introduced during sediment digestion and two sets of chromatographic columns for REE and Sr extraction, respectively. Blanks 4-6 represent contamination introduced during Sr extraction chromatography only. The number of ratios measured (n) for the isotopic composition of Blanks 3 and 5 is shown. n.d – not determined.

**Supplementary Table 4.1.** Nd and Sr isotopic compositions of all analysed samples.

# Abstract

The East Antarctic Ice Sheet (EAIS) retains the largest volume of ice on the planet and has the capacity to raise global sea level by a substantial 52 m. Marine-based sectors of the EAIS are particularly susceptible to retreat and collapse and are currently losing mass at an unprecedented rate. Masked by kilometres of ice and shielded by extensive sea-ice proximal to the coast, central Wilkes Land (between 105-128°E) is one of the most poorly investigated regions of the EAIS. The Totten Glacier, situated in a trench at the Sabrina Coast of central Wilkes Land, drains the largest portion of the EAIS and has one of the highest thinning rates in East Antarctica. Complete melting of the ice drained by the Totten Glacier alone is anticipated to contribute 3.5 m to global sea-level rise. With large portions of the ice sheet in central Wilkes Land grounded below sea-level, on a retrograde slope steepening inland from the coast to the interior basins, this part of the EAIS is sensitive to ocean-forced retreat and marine ice sheet instability, rendering it an important region in the context of global climate change.

Understanding the response of the ice sheet to past climate variation is integral for forecasting its future behaviour and for identifying those parts of the ice sheet that are most vulnerable to collapse and retreat in a warming climate. Two high priority objectives in Antarctic paleoclimate research are to determine the principal drivers of ice sheet retreat and to establish the timing of regional deglaciation over the Last Glacial Period-Holocene transition (from c. 25 ka). Thus far, the factors driving ice sheet retreat at the coast of central Wilkes Land over the Last Glacial Period-Holocene transition are not well understood and the timing of the last deglaciation is poorly constrained. The lack of physical samples and the absence of detailed paleoclimate and sediment provenance records from central Wilkes Land provides strong motivation for the research conducted in this thesis. The principal aims of this thesis are: 1. to constrain the timing of the last deglaciation in central Wilkes Land, 2. to characterise the nature of ice sheet retreat, and 3. to uncover more about the age and composition of the concealed subglacial basement rocks. To accomplish these aims, four marine sediment Kasten cores recovered by the *RV Investigator* from the

upper continental slope of the Sabrina Coast, central Wilkes Land, were investigated. A broad range of measurements and analyses were conducted on each of the cores to reconstruct the deglacial history of the ice sheet in central Wilkes Land. This thesis presents the first detailed, multi-proxy paleoclimate and sediment provenance records for offshore central Wilkes Land. The research provides constraints on the timing of the last deglaciation and insights into the paleoenvironmental conditions of this important region over the Last Glacial Period-Holocene transition.

The first research chapter explores the response of the ice sheet to climate change over the Last Glacial Period-Holocene transition and the timing of the onset of the last deglaciation. Multiple proxies were measured from all four of the cores to assess changes in processes on and above the continental rise associated with variation in climate and ice sheet configuration. Age models for each core were determined using bulk acid-insoluble organic matter radiocarbon ages. Primary biological productivity was reconstructed using biogenic silica concentrations, diatom abundances and Si/Al and Ba/Al ratios from x-ray fluorescence (XRF) measurements. Continental slope sedimentation was investigated using linear sedimentation rates, the iceberg-rafted debris flux and particle size. Current speed was qualitatively assessed using the calculated sortable silt percent. The last deglaciation was identified by the rise in biological productivity, an increase in current speed and changes to sedimentation on the continental slope associated with a retreating ice sheet and reducing sea-ice conditions at the coast. The results indicate that deglaciation at the coast of central Wilkes Land was possibly the earliest in East Antarctica, initiating at some time between  $22.0 \pm 3.2$  ka and  $19.2 \pm 0.6$  ka. Prompt retreat in the central Wilkes Land region suggests that this part of the ice sheet is highly sensitive to climate change and may pose a larger threat to future global sea-level rise than other regions of the EAIS.

The second research chapter investigates a source-to-sink history of sediment transport at one of the core sites via detrital zircon, apatite, titanite and feldspar analysis. Multiple single-grain sediment provenance tracers were employed including

U-Pb and Pb-Pb geochronology, rare earth element geochemistry and grain morphology. Results reveal a predominantly proximal source with U-Pb detrital zircon age signatures unique to the interpreted Mesoproterozoic basement rock terranes of central Wilkes Land: the Wilkes, Nuyina and Banzare provinces. A dominant c. 1200-1100 Ma age peak was consistent in the U-Pb age spectra for all minerals analysed. Pb-Pb compositions of detrital feldspar grains match those of feldspars from nearby rare coastal outcrop at Balaena Islets and Chick Island in central Wilkes Land, further supporting a local source. The rare earth element geochemistry indicated primarily felsic granitoid source rock compositions. Grain morphological analysis and the abundance of detrital feldspar in all samples indicated short-distance transport. Subtle temporal changes in sediment provenance are attributed to variation in climate and ice sheet configuration. Exceptionally high sedimentation rates during the glacial suggest the downslope redistribution of continental shelf sediments in gravity flows as the ice sheet advanced. Fluxes of meltwater principally fed by the Totten Glacier are deemed responsible for supplying detritus to the continental slope during the last deglaciation. A broad sediment provenance is interpreted during interglacial periods, with detritus delivered to the slope via multiple glaciers along the coast. The results from this chapter provide the first substantial offshore physical evidence for the age and composition of the concealed subglacial geology of central Wilkes Land and support geophysical interpretations of the basement rock terranes and two models that predict the erosion potential at the base of the ice sheet.

The third research chapter provides Nd-Sr isotopic signatures from all four cores to establish the combined detrital Nd-Sr fingerprint, trace the source rock terranes and investigate spatial variability in sediment provenance along the upper continental slope of central Wilkes Land. Detrital  $\epsilon_{Nd}$  signatures were compared with whole rock  $\epsilon_{Nd}$  signatures from boreholes recovered from the conjugate region of southern Australia, and from rare outcrop at the coast of central Wilkes Land and in southern Australia. The  $\epsilon_{Nd}$  signal revealed that mafic rocks of the Haig Cave Supersuite (c. 1415-1390 Ma) of the Nuyina Province must be contributing to the Nd-isotopic signature. This finding supports geophysical interpretations of the subglacial geology in central Wilkes Land and suggests that the Totten Glacier, underlain by the Nuyina

Province, likely had a major role in the supply of detritus to the continental slope, not only during the initial stages of the last deglaciation, but throughout the Last Glacial Period-Holocene transition. The  $\epsilon_{Nd}$  signature was spatially consistent, suggesting similar sediment provenance across the continental rise of central Wilkes Land. The  $^{87}Sr/^{86}Sr$  ratios had been affected to some extent by the grain size distribution in each of the cores, providing more insight into the recent history of the ice sheet.

The rich physical data and findings in this thesis can be used to inform future paleoclimate and sediment provenance studies of central Wilkes Land, paleoclimate models, plate tectonic reconstructions and ice sheet models that forecast the future response of this important part of the ice sheet to a warming climate.

# Chapter 1

## Introduction

### 1.1. Preamble

The Antarctic Ice Sheet contains the highest volume of ice on Earth, equating to ~58 m of global mean sea level (GMSL) rise (Fretwell et al., 2013; Rignot et al., 2013). At a maintained present-day level of atmospheric CO<sub>2</sub>, Antarctica is predicted to contribute more than 15 m to GMSL rise by the year 2500 (DeConto and Pollard, 2016). The Antarctic Ice Sheet is currently losing mass (Rignot et al., 2019; Shepherd et al., 2018, 2019), with the largest loss of ice occurring within the marine-based sectors (Noble et al., 2020), which are grounded (i.e., where the ice is situated on top of bedrock) below sea level and susceptible to marine ice sheet instability (Schoof, 2007; Weertman, 1974). Since large portions of the Antarctic Ice Sheet are marine-based (Fig. 1.1; Fretwell et al., 2013; Morlighem et al., 2020), and buttressed by the ice shelves and sea ice, the ocean has a strong influence over the loss of mass from the ice sheet (Crosta et al., 2018; Levy et al., 2019).

The West Antarctic Ice Sheet (WAIS) is almost entirely marine-based (Fig. 1.1; Fretwell et al., 2013; Morlighem et al., 2020), with many of its glaciers grounded on retrograde bedding (e.g., Favier et al., 2014; Holt et al., 2006; Vaughan et al., 2006). It is therefore well recognised that the WAIS is a highly dynamic body of ice, strongly influenced by the ocean (e.g., Alley and Bindschadler, 2013; Gardner et al., 2018; Joughin and Alley, 2011; Payne et al., 2004a; Rignot et al., 2019; Shepherd et al., 2004; Smith et al., 2020; Thomas et al., 2004). Rapid mass loss from the WAIS is occurring in the Amundsen and Bellingshausen Sea sectors (Rignot et al., 2013, 2019; Smith et al., 2020), where ice shelves are rapidly thinning and their glaciers accelerating (e.g., Medley et al., 2014; Mougnot et al., 2014; Rignot et al., 2014,

2019; Scott et al., 2009; Selley et al., 2021; Seroussi et al., 2017; Steig et al., 2012; Sutterley et al., 2014; Turner et al., 2017; Yu et al., 2019). Due to its configuration below sea level (Fig. 1.1) and its rapid mass loss, the WAIS has for a long time been at the forefront of investigation in Antarctic studies, whilst less was known about its neighbour, the EAIS. It is only in recent years that the EAIS has been observed to be vulnerable to ocean-forced melting and therefore considered in its potential to contribute to GMSL rise (e.g., Rignot et al., 2019; Smith et al., 2020; Witze, 2018).

The EAIS is poorly investigated due to its size and remoteness, resulting in poorly-constrained ice sheet models and sea-level predictions (Gomez et al., 2015; Jones et al., 2016; King et al., 2012; Nowicki et al., 2014; Pattyn, 2018; Pattyn et al., 2017). Some sea level models estimate that the EAIS has had very little impact on the GMSL (e.g.,  $-1.1 \pm 0.4$  mm, 1992-2017, Shepherd et al. 2018) and near equilibrium between loss and gain from the EAIS has led to the notion that it is relatively stable and not showing significant change (e.g., Gardner et al., 2018; Martín-Español et al., 2016; Smith et al., 2020). However, whilst some regions of the EAIS are experiencing mass gain (e.g., in Dronning Maud Land, where snow accumulation exceeds ice melt; Boening et al., 2012), others are experiencing significant mass loss (e.g., in Wilkes Land; Rignot et al., 2019; Shen et al., 2018). These marine-based portions of the EAIS (Fig. 1.1) are losing mass at an increasing rate and are behaving in a similar manner to the WAIS (Rignot et al., 2019; Shen et al., 2018). Marine-terminating glaciers in these regions, such as the Totten and Denman glaciers, are experiencing high melting rates and grounding line retreat (Brancato et al., 2020; Konrad et al., 2018; Li et al., 2015, 2016; Miles et al., 2016, 2021). Moreover, the recent study of Rignot et al. (2019) estimates an important ( $4.4 \pm 0.4$  mm) contribution from the EAIS to  $13.9 \pm 2.0$  mm of total GMSL rise from the Antarctic Ice Sheet (1979-2017). Continued loss of ice from the marine-based sectors of the EAIS implicates their eventual collapse into the interior basins, and GMSL rise. Due to the potential for marine-based portions of the EAIS to substantially raise the GMSL, it is crucial that investigation is prioritised in these regions (Noble et al., 2020, and references therein).



**Figure 1.1. Subglacial topography of Antarctica.** Subglacial topography is from BedMachine (version 1.0) (Morlighem et al., 2020). The red box outlines the central Wilkes Land region, the region of East Antarctica that is the focus of this thesis. Dark blue lines illustrate the approximate outlines of subglacial basins in central Wilkes Land. ASB – Aurora Subglacial Basin, SSB – Sabrina Subglacial Basin, WSB – Wilkes Subglacial Basin.

Central Wilkes Land (~105-128°E) is the largest marine-based sector of the East Antarctic Ice Sheet (Fig. 1.1). The region is underlain by the Sabrina and Aurora subglacial basins (Fig. 1.1), which are interconnected by deep-seated fjords that formed during primary ice sheet development (Young et al., 2011). The basins deepen inland from the coast (Fretwell et al., 2013; Morlighem et al., 2020), resulting in much of the region being grounded below sea level and at risk of marine ice sheet instability in a warming climate (Fig. 1.1; Harley et al., 2013; Schoof, 2007; Weertman, 1974). Freshwater and ice are drained from the basins by the Totten and Moscow University glaciers at the Sabrina Coast (Wright et al., 2012; Zwally et al., 2012), which together comprise enough freshwater to raise the GMSL by ~ 5 m

(Mohajerani et al., 2018). The Totten Glacier is a highly dynamic glacier and has undergone significant thinning and grounding line retreat in recent years (e.g., Greenbaum et al., 2015; Li et al., 2015, 2016; Rintoul et al., 2016; Roberts et al., 2018; Silvano et al., 2019). The Totten Glacier drains ice from the EAIS at a rate of approximately  $71 \pm 3$  Gt/yr, producing one of the largest outflows of all the glaciers in East Antarctica (Rignot et al., 2013, 2019). It is estimated that all ice from the inland subglacial basins drained by the Totten Glacier could raise GMSL by a significant 3.5 m (Greenbaum et al., 2015), compared to a modelled  $\sim 5$  m rise in GMSL that would be initiated by the complete collapse of the WAIS (DeConto and Pollard, 2016; Tinto et al., 2019). Despite the importance of central Wilkes Land in the context of mass loss from the EAIS and its contribution to sea level rise, the region is poorly investigated and very little is known about the regional history of the ice sheet, providing motivation for this thesis.

## **1.2. Thesis aims and objectives**

In order to facilitate the development of ice sheet models that project the future behaviour of the ice sheet, it is crucial to understand its dynamic history and its past response to climate variation. Marine sediment cores recovered from the continental margin of East Antarctica archive historic changes in the oceanic and sediment depositional regimes associated with the dynamics of the proximal ice sheet and climate variation. Continentally-derived detritus deposited in the ocean can provide important information on the glaciological and sedimentological histories of the EAIS (Hochmuth et al., 2020), its configuration, and the age and composition of the basement rock terranes concealed beneath the ice (Licht and Hemming, 2017). Currently, physical data from central Wilkes Land and the adjacent continental margin is very sparse, resulting in poorly-constrained ice sheet models and large uncertainties about the behaviour of the EAIS in this important region.

In this thesis, I use marine sediment from four Kasten cores and two Multicores from the upper continental rise of central Wilkes Land to address two primary aims:

- 1) To constrain the timing and nature of the last deglaciation in central Wilkes Land using multiple paleoenvironmental proxies and an age model derived from radiocarbon ages (Chapter 2) and,
- 2) To establish variation in basement rock erosion, sediment transport pathways and the glaciers responsible for the delivery of detritus to the margin using a range of single-grain (Chapter 3) and bulk Nd and Sr isotope (Chapter 4) sediment provenance techniques.

In addressing these primary aims, I also contribute to the understanding of the subglacial geology and the ancient (> 1 billion year) relationship between southern Australia and this sector of East Antarctica. Below I provide a background and summary of: 1) modern observations of the Antarctic Ice Sheet and the Southern Ocean, 2) conventional methods for establishing the history of the ice sheet using marine sediment and 3) the study region in central Wilkes Land.

## **1.3. Background**

### **1.3.1. Modern interactions between the Antarctic Ice Sheet and the Southern Ocean**

The greatest mass loss from the Antarctic Ice Sheet is taking place at the ice shelves, where the ice becomes ungrounded and floats over the surface of the ocean (Fig. 1.2; Paolo et al., 2015; Pritchard et al., 2012; Rignot et al., 2013, 2019). Ice shelves play an important role in buttressing grounded upstream ice and glacial ice flow (Dupont and Alley, 2005; Fürst et al., 2016; Gagliardini et al., 2010; Goldberg et al., 2009). Prolonged melting of the ice shelves triggers grounding line retreat (Konrad et al., 2018) as the ice flux to the Southern Ocean increases and upstream grounded ice is progressively removed (Gagliardini et al., 2010; Goldberg et al., 2009; Gudmundsson, 2013; Roberts et al., 2018). Accelerated mass loss at the margins of the Antarctic Ice Sheet is raising the GMSL at an unprecedented rate

(e.g., Golledge et al., 2015; Ivins et al., 2013; King et al., 2012; Rignot et al., 2011, 2019; Smith et al., 2020; Velicogna et al., 2014).

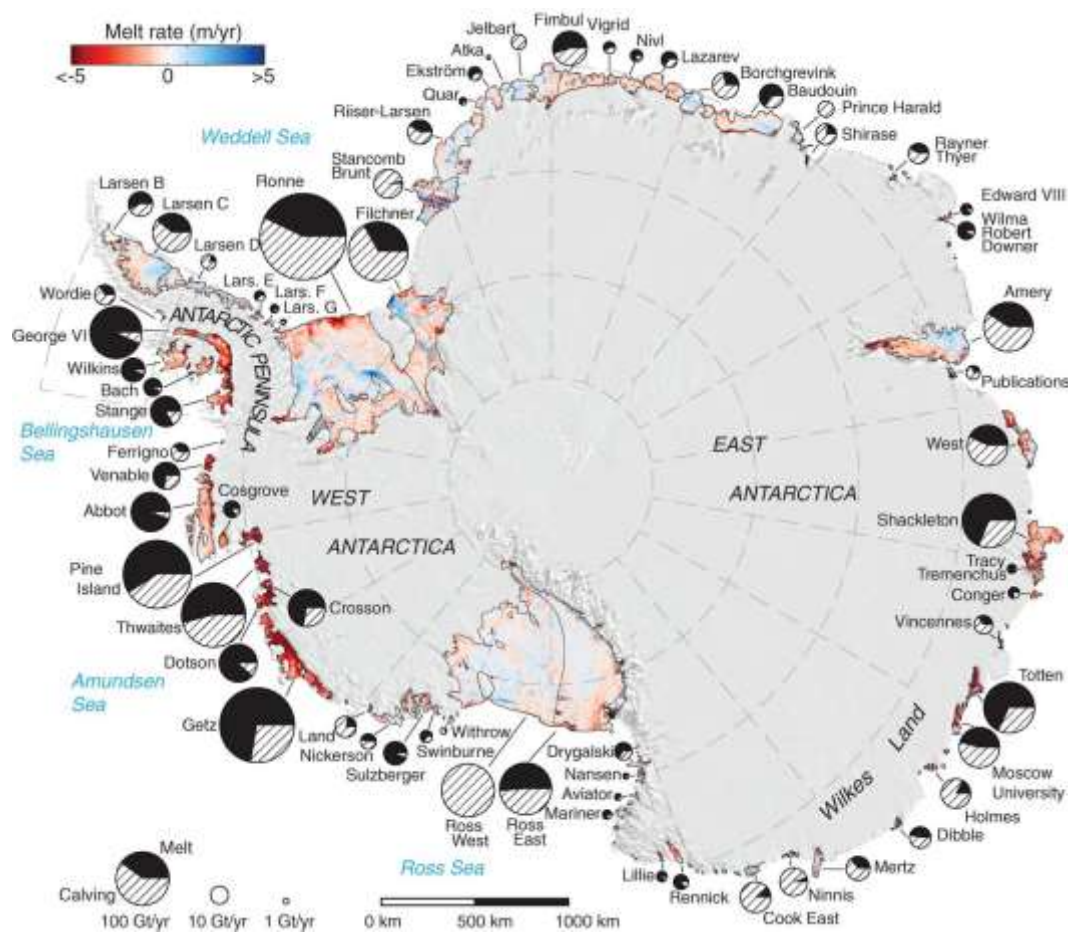


**Figure 1.2. Antarctic ice shelves: melting rates and annual mass loss.** Taken from Rignot et al. (2013). Map of Antarctica, indicating the location, melt rate and mass loss of the circum-Antarctic ice shelves. Black lines represent the ice shelf borders as observed in 2007 and 2008. Pie charts are relative in size to the mass loss (Gt/yr) at each location and are categorised into calving (striped infill) and basal melting (black infill) events.

Basal melting is responsible for the greatest loss of ice from the Antarctic ice shelves of the modern day ice sheet (Holland et al., 2008; Pritchard et al., 2012; Rignot et al., 2013, 2019) (Fig. 1.2) and is driven by influxes of relatively warm, modified Circumpolar Deepwater (mCDW) which drives high melt rates at the ice shelf base (mode 2 of basal melting from Jacobs et al., 1992), inducing dynamic thinning and

an increased ice flux to the Southern Ocean (Rignot et al., 2013). Circumpolar Deepwater (CDW) lies below ~2,000 m depth in the Southern Ocean equatorward of the Antarctic Polar Front (Fig. 1.3) and is characterised by high salinity (~ 34.7 ‰), low oxygen levels (~ 4.5 mL/L) and a higher temperature (~ 1.5-3 °C) relative to the surrounding waters (Orsi et al., 1995). Poleward of the Antarctic Polar Front, CDW loses buoyancy with proximity to ice at the continental margin and mixes with fresher waters, causing a reduction in the temperature and salinity of the water mass to form mCDW (Orsi and Wiederwohl, 2009). Incursions of relatively warm mCDW have been observed in many regions of the circum-Antarctic continental shelf (e.g., Castagno et al., 2017; Dinniman and Klinck, 2004; Dutrieux et al., 2014; Greenbaum et al., 2015; Jenkins and Jacobs, 2008; Moffat et al., 2009; Ribeiro et al., 2021; Rintoul et al., 2016; Silvano et al., 2019; Thoma et al., 2008; Turner et al., 2017; Webber et al., 2017).

Currents and frontal systems of the Southern Ocean (Fig. 1.3) have a major influence over the transfer of mCDW to the base of the Antarctic ice shelves and subsequent loss of mass from the ice sheet. The Antarctic Circumpolar Current (ACC) encircles the Antarctic continent in a clockwise perpetual flow that traverses each of the ocean basins, linking them together (Fig. 1.3; Orsi et al., 1995; Rintoul et al., 2001). Proximal to the Antarctic coastline, the Antarctic Coastal Current and the Antarctic Slope Current flow counter-clockwise over the continental shelf and slope, respectively, and are driven by the easterly winds (e.g., Mathiot et al., 2011; Peña-Molino et al., 2016; Sverdrup, 1954; Thompson et al., 2018, 2020; Fig. 1.3). These west-flowing currents are bounded to the north by the Antarctic Slope Front which forms a barrier between fresher colder water masses proximal to the coast and warm, saline water masses further offshore (Jacobs, 1991; Whitworth et al., 1985). The Antarctic Slope Front therefore has an important influence over the exchange of heat and nutrients across the continental shelf and slope of Antarctica (Jacobs, 1991; Whitworth et al., 1985). Three large gyres: the Ross, Weddell and Kerguelen gyres, exist where current flow circulates clockwise around low pressure focal points in the ocean (Fig. 1.3; Rintoul et al., 2001). These gyres also control the exchange of heat from the ocean to the ice sheet and are maintained by interaction between the ACC and the continental shelf.

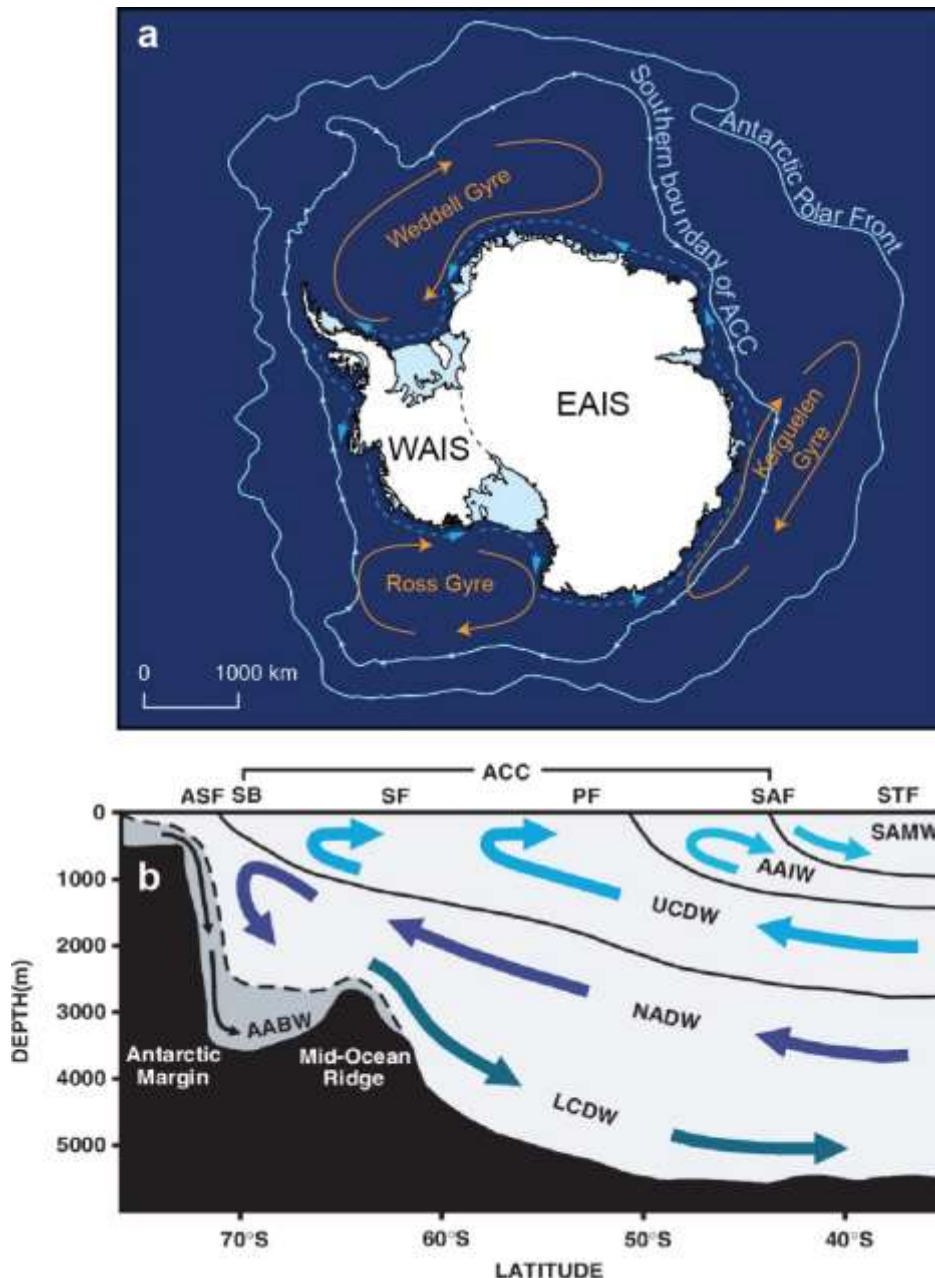


**Figure 1.3. Southern Ocean systems. (a)** Map of Antarctica showing the combined westward-flowing currents (The Antarctic Coastal Current and the Antarctic Slope Current; mid blue dashed arrows proximal to Antarctic coastline), the southern boundary of the eastward-flowing Antarctic Circumpolar Current (ACC) and the Antarctic Polar Front (light blue) (Orsi et al., 1995). The location and flow direction of the Weddell (Deacon, 1979; Fahrbach et al., 1994), Ross (Jacobs et al., 1970) and Kerguelen (McCartney and Donohue, 2007) gyres (Gordon, 1971) are shown in orange. **(b)** Schematic diagram taken from Carter et al. (2004) showing the approximate depths and movements of water masses in the Southern Ocean. AABW – Antarctic Bottom Water, LCDW – Lower Circumpolar Deepwater, NADW – North Atlantic Deepwater, UCDW – Upper Circumpolar Deepwater, AAIW –

Antarctic Intermediate Water, SAMW – Subantarctic Mode Water, ASF – Antarctic Slope Front, SB – Southern Boundary of the ACC, SF – Southern Front, PF – Polar Front, SAF – Subantarctic Front, STF – Subtropical Front.

Eddies play another important role in the Southern Ocean current system, as they transfer heat poleward to compensate for heat loss at higher latitudes (Foppert et al., 2019; Stewart and Thompson, 2015). A cyclonic eddy above the continental rise of central Wilkes Land (at 64°S, 115°E) has been resolved from palaeoceanographic data, causing a diversion in southern boundary of the ACC towards the coastline (Wakatsuchi et al., 1994). The eddy is thought to be maintained by upwelling of mCDW to the upper layers of the ocean, along the isobaths of the large contourite ridge in the western part of the study region (Wakatsuchi et al., 1994) where two of the Kasten cores used in this thesis (IN2017\_V01-A005\_KC02 and IN2017\_V01-A042-KC14 (see section 1.4)) were recovered. Interaction between the Antarctic Coastal Current and bathymetric ridges on the continental shelf can also generate eddies which transport heat across the continental shelf (Gwyther et al., 2014).

Recent studies propose that influxes of mCDW onto the continental shelf adjacent to the Sabrina Coast (Greenbaum et al., 2015; Gwyther et al., 2014; Rintoul et al., 2016; Roberts et al., 2018; Silvano et al., 2019) are primarily responsible for the high basal melt rate of the Totten Glacier Ice Shelf ( $63.2 \pm 4$  Gt/yr (2003-2008); Rignot et al., 2013) compared to other glaciers in East Antarctica. Intrusions of mCDW have also been observed on the continental shelf of the Amundsen Sea Embayment in West Antarctica (e.g., Arneborg et al., 2012; Assmann et al., 2013; Dutrieux et al., 2014; Jacobs et al., 2011; Jenkins, 2010; Nakayama et al., 2013; Steig et al., 2012; Thoma et al., 2008; Wåhlin et al., 2010; Walker et al., 2007; Webber et al., 2017). Changes in the position of the Antarctic Slope Front, and modes of Southern Hemisphere climate variability (e.g., the El Niño-Southern Oscillation and the Southern Annular Mode) are considered to have a significant influence over the transfer of heat via mCDW to the Antarctic margin in areas of high basal melting of the WAIS and the Totten Glacier in East Antarctica (Thompson et al., 2018).

Bathymetry plays an important role in facilitating ocean-driven melting of the ice sheet in central Wilkes Land. A large depression in the continental shelf break between the Totten and Moscow University glaciers has recently been discovered (Nitsche et al., 2017), where the continental shelf is lowered by ~500 m, allowing incursions of mCDW to migrate over the continental shelf (Nitsche et al., 2017; Silvano et al., 2019). Bathymetric channels and valleys function as passageways for the transport of relatively warm mCDW from the continental shelf to the ice shelf cavity. It has also been shown that the seabed bathymetry influences the glacial melt rate, due to incursions of mCDW adhering to bathymetric contours, and in some cases blocking upwelling onto the continental shelf (Greene et al., 2017). A geophysical investigation conducted by Greenbaum et al. (2015) identified a ~4.9 km-wide oceanic trough beneath the Totten Glacier Ice Shelf at a depth of ~1400 metres below sea level (mbsl), enabling infiltration of mCDW from the ocean to the ice shelf cavity. Whilst it was previously suggested that mCDW was accessing the cavity and promoting basal melting (Bindoff et al., 2000; Williams et al., 2011), the study by Greenbaum et al. (2015) was the first to identify a conduit that would allow for this phenomenon to occur. Evidence for mCDW reaching the ice shelf cavity was recovered on a voyage to the Totten Glacier Ice Shelf in 2015 (Rintoul et al., 2016). Several bathymetric channels infilled with mCDW proximal to the Totten Glacier Ice Shelf were identified on this voyage, indicating a network of passageways between the Southern Ocean and the ice shelf cavity (Rintoul et al., 2016). Frequent contact between relatively warm mCDW and the main ice shelf cavity is thought to be the principal cause of increased basal ice sheet temperatures, resulting in dynamic thinning of the Totten Glacier and increased ice flow to the Southern Ocean at the Sabrina Coast (Rintoul et al., 2016).

Upwelling of mCDW over the continental margin of central Wilkes Land is primarily controlled by the regional wind regime (Greene et al., 2017). Surface currents in the ocean are controlled by a combination of the Coriolis Force, the pressure gradient force and wind stress. In the Southern Hemisphere, currents are diverted approximately 45° left of prevailing winds due to the Coriolis Force. Ekman transport further displaces the direction of the surface current flow approximately perpendicular to the wind direction as layers of the water column replace wind-

displaced surface layers and are refracted at different angles with depth. Therefore, where the westerly winds prevail above the Southern Ocean, the fresh surface layer, consisting of Antarctic Surface Water (ASW) (~400-500 m depth), will be displaced to the north. When surface displacement occurs perpendicular to the coastline, mCDW upwells onto the continental slope and shelf (to between ~400-1000 m depth) to replace surface layers. A modelling study of the winds at the Sabrina Coast of central Wilkes Land found a positive relationship between the ice flux at the Totten Glacier Ice Shelf and the strength of the easterly winds (Greene et al., 2017). This relationship was attributed to the easterly winds functioning as the southern constituent of the Ekman spiral, inducing upwelling of mCDW as surface waters are diverted away from the Totten Glacier Ice Shelf (Greene et al., 2017). Greater incursions of mCDW reaching the cavity of the Totten Glacier Ice Shelf enhances basal melting, resulting in higher ice flow velocities. A stronger north-flowing ice flux causes the continued displacement of surface waters, instigating further upwelling at the margin (Greene et al., 2017). The rate at which ice from the Totten Glacier Ice Shelf flows into the Southern Ocean therefore has a greater impact on the displacement of surface waters than the prevailing easterly winds (Greene et al., 2017).

On the continental shelf of the Sabrina Coast, mCDW occupies waters at the base of water column because Dense Shelf Water (DSW) is not produced in sufficient volumes, despite the presence of the Dalton Polynya (Rintoul et al., 2016; Silvano et al., 2017). The Dalton Polynya is a latent heat polynya, situated proximal to the Moscow University Glacier (Fig. 1.4; Massom et al., 1998). Along the eastern boundary of the Dalton Polynya, a tail of fast ice and grounded icebergs protrudes seaward from the coastline, forming The Dalton Ice Tongue (Fig. 1.4; Gwyther et al., 2014). The polynya is primarily maintained by the Dalton Ice Tongue and strong katabatic winds that drive fresh sea ice further offshore (Gwyther et al., 2014; Massom et al., 1998). The subsequent exposure of the ocean results in heat loss from the surface layers, promoting continued sea-ice formation. A modelling study by Gwyther et al. (2014) showed that when activity in the Dalton Polynya was high, the ice flux from the Totten Glacier Ice Shelf slowed down. It was interpreted from this that a strong Antarctic Coastal Current, powered by the easterly winds, drives DSW

from the Dalton Polynya towards the main ice shelf cavity of the Totten Glacier Ice Shelf (Gwyther et al., 2014). From here, the DSW reduces basal melting by protecting the ice shelf cavity from warm mCDW intrusions (Gwyther et al., 2014; Khazendar et al., 2013). Conversely, some studies have proposed that surges of DSW down submarine canyons may actually induce upwelling of mCDW onto the continental shelf (Kämpf, 2005, 2007; Morrison et al., 2020). However, despite strong sea ice production in the Dalton Polynya (Tamura et al., 2016), no DSW was found on the 2015 voyage to the continental shelf of the Sabrina Coast (Rintoul et al., 2016; Roberts et al., 2018).

It was recently proposed that basal melt rates and ice flow velocity at the Sabrina Coast are controlled predominantly by 1) the availability of mCDW on the continental shelf (Roberts et al., 2018; Silvano et al., 2019) and 2) the rate of fresh meltwater input (Silvano et al., 2018). Meltwater from the Moscow University Glacier is carried to the Dalton Polynya by the west-flowing Antarctic Coastal Current (Silvano et al., 2018). The addition of fresh water to the polynya balances salinification by brine rejection as new sea ice is formed, prohibiting the formation of DSW (Silvano et al., 2018). The absence of DSW at the continental shelf of the Sabrina Coast explains the persistence of mCDW in the deepest layers of the water column and enhanced basal melting of the Totten and Moscow University ice shelves via incursions of mCDW into the ice shelf cavities (Silvano et al., 2018). The Totten and Moscow University glaciers are therefore described as having warm water cavities that are not protected by cold DSW (e.g., Holland et al., 2020).

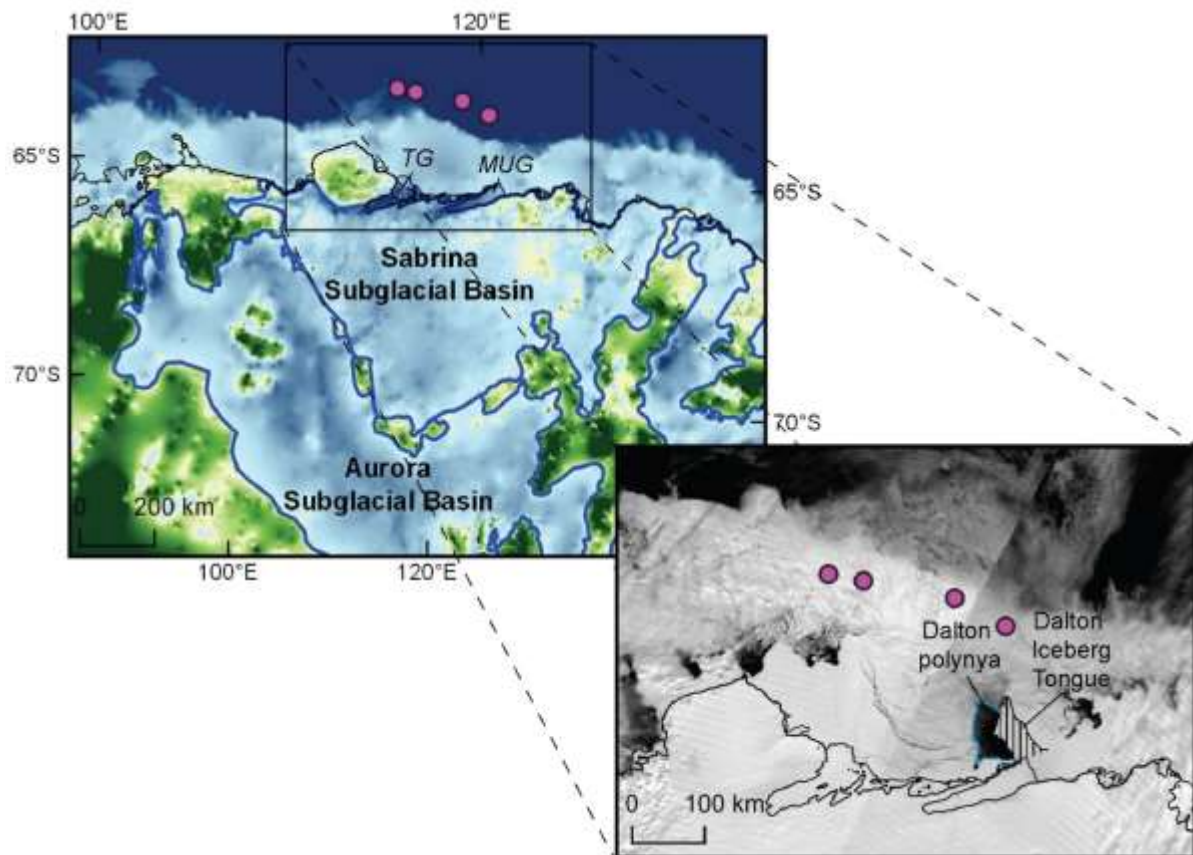


**Figure 1.4. Map of central Wilkes Land.** Subglacial topography is from BedMachine (version 1.0) (Morlighem et al., 2020). The location of the cores used in this thesis are shown as pink circles (see section 1.4.). TG – Totten Glacier, MUG – Moscow University Glacier. Inset shows a NASA satellite image (taken on 25-05-2018) of the sea-ice conditions in central Wilkes Land. The location of the Dalton Polynya is outlined in blue. The Dalton Iceberg Tongue (hashed area) is also shown.

### 1.3.2. Reconstructing the history of the EAIS using marine sediment cores

Marine sediment from the continental margin adjacent to the East Antarctic Ice Sheet comprises biogenic matter, authigenic sediments and detritus eroded from the continent. The physical, geochemical and biological composition of marine sediment cores therefore captures an intricate, multi-layered record of processes associated with variation in the climate and the behaviour of the proximal ice sheet. These

processes include: ice sheet, ocean and sea ice dynamics; biological productivity, basement rock erosion, sediment transport, glaciology and the wind strength, to name a few. Below I provide a summary of 1) the processes and caveats associated with Antarctic age model construction using acid insoluble organic matter from marine sediments, 2) common proxies used to reconstruct the history of the ice sheet, and 3) single-grain U-Pb dating and bulk Nd and Sr isotopes as marine sediment provenance tools. Each of the methods and applications described here were employed in the research conducted for this thesis.

### **1.3.2.1. Age model construction using acid-insoluble organic matter**

Determining the age of marine sediment is important for constructing an age model, which coupled with proxy data provides constraints on the temporal response of the Antarctic Ice Sheet to climate change. Radiocarbon dating of Antarctic marine sediment is typically performed on either biogenic carbonates (e.g., foraminifera tests, fish teeth or bivalve shells), or the bulk acid-insoluble organic matter (AIOM) fraction of the sediment. However, acquiring an accurate age model for Antarctic marine sediment cores is challenging for four reasons: 1) the uncertainty of circum-Antarctic marine reservoir ages (see below), 2) the lack of abundant biogenic carbonate for radiocarbon dating, 3) the low total carbon percent for dating in some regions of the Southern Ocean and 4) carbon contamination of the AIOM fraction. Here I discuss the main caveats and processes involved in constructing an age model using radiocarbon dates from the AIOM fraction of marine sediment.

#### *Radiocarbon formation*

Radiocarbon ( $^{14}\text{C}$ ) is a fundamental component of the global carbon cycle and is present in minute concentrations in the atmosphere, oceans, and in all living organisms. The radioactive carbon isotope is a cosmogenic nuclide and is a product of multiple spallation and nuclear reactions between cosmogenic rays and  $^{14}\text{N}$  atoms in the Earth's upper atmosphere (Anderson et al., 1947a, 1947b; Grosse and Libby, 1947; Libby, 1946). Once formed, the  $^{14}\text{C}$  reacts with oxygen to produce 'heavy'

carbon dioxide molecules ( $^{14}\text{CO}_2$ ) that enter the oceans and are taken up by phytoplankton during photosynthesis. When a marine organism dies, it sinks through the water column and is buried as part of a process known as the 'biological pump' (Volk and Hoffert, 1985). From this point, no further absorption of  $^{14}\text{C}$  from the atmosphere takes place and the amount of  $^{14}\text{C}$  within the organism is solely controlled by radioactive (beta) decay. The total time passed between the death of the organism and the present day (termed 'before present' (BP) and defined as the time prior to 1950, when radiocarbon dating was widely implemented; (Godwin, 1962)) is known as the calendar age and provides the foundations for radiocarbon dating (Libby et al., 1949).

### *The Marine Reservoir Effect*

Once  $^{14}\text{CO}_2$  is sequestered by the oceans, it is distributed throughout the water column during the ocean mixing process. As ocean mixing takes considerably longer than the uptake of newly formed  $^{14}\text{CO}_2$  at the ocean-atmosphere interface, the deepest layers of the ocean contain less  $^{14}\text{C}$  than the surface layers due to radioactive decay (Alves et al., 2018, and references therein). In regions of enhanced upwelling, water masses with an older radiocarbon age (i.e., with less  $^{14}\text{C}$  due to radioactive decay) mix with surface waters with a younger radiocarbon age signal. Therefore, the radiocarbon age of a marine organism not only reflects the radioactive decay of  $^{14}\text{C}$  after death, but also the uptake of older carbon due to oceanographic processes such as oceanic upwelling when the organism was alive. Consequently, the conventional radiocarbon age is typically several hundreds of years older in marine organisms than terrestrial organisms at any point in calendar time (Stuiver and Polach, 1977). This phenomenon is known as the Marine Reservoir Effect (Alves et al., 2018; Stuiver and Polach, 1977). The offset in the conventional radiocarbon age between the marine and atmospheric carbon reservoirs within a specific region at zero calendar years (cal yr) is termed the regional Marine Reservoir Age (MRA). Any conventional radiocarbon ages must be corrected for the Marine Reservoir Effect by calculating and deducting the regional MRA (Alves et al., 2019; Butzin et al., 2017; Heaton et al., 2020; Skinner et al., 2019).

Regional, and even local differences in the MRA are largely caused by spatial variation in bathymetry and wind strength, which control the degree of oceanic upwelling (Gordon and Harkness, 1992). Whilst the spatial heterogeneity in the MRA is usually accounted for in Antarctic paleoclimate studies, temporal variation in the MRA at any one location is difficult to determine and apply to radiocarbon age corrections (Skinner et al., 2019). At polar latitudes, temporal variation in the MRA is particularly important, as coastal sea-ice cover during glacial periods inhibits sequestering of newly-formed  $^{14}\text{CO}_2$  from the atmosphere at the surface of the ocean, causing the marine carbon reservoir to have considerably less radiocarbon than the atmosphere, resulting in a MRA possibly exceeding 2 kyr during glaciation (Adkins, 2013; Adkins and Boyle, 1997; Heaton et al., 2020; Kohfeld and Chase, 2017; Skinner et al., 2010, 2019).

A common correction for the Marine Reservoir Effect is to assume that the surface sediment was deposited recently and should therefore be approximately 0 cal yr BP in age (where 0 cal yr BP corresponds to the year 1950, when radiocarbon dating was first widely implemented). The difference between the conventional radiocarbon age and zero is therefore deemed an appropriate estimate of the MRA and can be subtracted from all downcore radiocarbon ages in a marine sediment core (Andrews et al., 1999). This method is hereafter referred to as the Surface Subtraction Method and is widely applied in Antarctic paleoclimate research. The Surface Subtraction Method assumes that: a) the surface sediment was deposited recently (i.e., there has been no hiatus in modern sedimentation or removal of modern sediments by erosional processes) and b) the MRA is constant over time. Alternatively, the MRA can be approximated from marine carbonates (e.g., coral, planktonic foraminifera) within sediment of a known age (e.g., in surface sediment assumed to be recently deposited, within an event horizon or within a section of the core that has been stratigraphically dated by comparing proxies to terrestrial records such as ice cores and tree rings). The difference between the dated carbonate and the known calendar age will give the approximate MRA.

A time-varying global average MRA for the mixed (surface) layer of the Southern Ocean is incorporated in the Marine20 calibration curve for radiocarbon age calibration of marine sediment (Heaton et al., 2020). If the regional MRA is known, the difference between the regional MRA and the global mean MRA ( $\Delta R$ ) can be used to correct for regional variability in the marine carbon reservoir over time (Stuiver et al., 1986). The regional MRA at polar latitudes differs substantially more from the global mean MRA during glacials than during the present interglacial due to variation in gas exchange ( $^{14}\text{CO}_2$ ) at the surface ocean caused by widespread sea ice (Alves et al., 2018, 2019; Butzin et al., 2017; Heaton et al., 2020). The  $\Delta R$  during glacial periods should therefore be higher than the predicted modern  $\Delta R$ . As a first order solution, the  $\Delta R$  at any point in time can be calculated using the difference between the closest regional MRA for the Southern Ocean provided by Skinner et al. (2019) and the global mean average MRA given by Heaton et al. (2020).

### *Carbon contamination*

The use of AIOM for radiocarbon dating of marine sediment is common practice in Antarctic paleoclimate research (Andrews et al., 1999; DeMaster et al., 1996; Domack et al., 1999; Prothro et al., 2020), due to the typically poor preservation of marine carbonates at polar latitudes of the Southern Ocean. However, a major limitation of the use of AIOM for radiocarbon-dating is contamination of the sediment by allochthonous carbon (carbon from a different source). Mixing of allochthonous and autochthonous carbon (carbon deposited in situ) causes the conventional radiocarbon age to deviate even further from the calendar age. The three different types of allochthonous carbon are: dead carbon, old carbon and modern carbon.

Due to the short half-life of  $^{14}\text{C}$  ( $5720 \pm 47$  yrs, Engelkemeir et al., 1949), only sediment with an age of up to  $\sim 50$  kyr can be dated. Beyond this age, the  $^{14}\text{C}$  has decayed through multiple half-lives and the amount of  $^{14}\text{C}$  left within the sediment is undetectable and referred to as 'radiocarbon-dead'. Dead carbon and old carbon from ancient terrestrial plant matter eroded from the continent (e.g., the 'Sabrina Flora' of the continental shelf of central Wilkes Land (Smith et al., 2019)) may be reworked from sediments at greater depths below the seabed and mixed with

younger sediment through bioturbation and other sediment processes, contaminating the radiocarbon age signature (Andrews et al., 1999; Harris et al., 1996; Licht et al., 1996). Old and dead carbon (hereafter collectively referred to as recycled carbon) will therefore give an apparent age for the sediment that is thousands of years older than the true age.

An additional source of radiocarbon contamination comes from inputs of modern carbon that can be introduced to samples during preparation and AMS analysis in the laboratory (Paul et al., 2016). Modern carbon is defined as any  $^{14}\text{C}$  post-dating 1950 and is commonly expressed as the percent modern carbon (pMC) within a sample (Stuiver and Polach, 1977). In younger samples with a naturally higher pMC (and a  $^{14}\text{C}$  concentration closer to modern atmospheric concentrations), the effect of modern carbon contamination is dampened. However, older sediment at depth contains approximately three times less  $^{14}\text{C}$  than the modern atmosphere, and only a small amount of modern carbon contamination in the laboratory (e.g., from  $\text{CO}_2$  in the atmosphere) can cause the conventional radiocarbon age of the sample to be thousands of years younger than the true age (Paul et al., 2016). Furthermore, modern carbon contamination has a much greater impact on samples with smaller quantities of total organic carbon (TOC). Old glaciogenic sediment samples from Antarctica therefore contain a low pMC and minute TOC, making them highly sensitive to modern carbon contamination (Paul et al., 2016; Zheng et al., 2002).

Two methods have been developed to unmix the radiocarbon age signature of carbon from different sources in bulk AIOM: compound specific  $^{14}\text{C}$  dating and ramped pyrolysis. Compound specific  $^{14}\text{C}$  dating involves isolating individual organic carbon compounds in AIOM using gas chromatographic techniques (Eglinton et al., 1996), whereas ramped pyrolysis is an incremental, temperature-controlled technique used to separate autochthonous carbon from allochthonous carbon in AIOM by exploiting their distinct thermochemical stabilities (Rosenheim et al., 2008). As an alternative to these methods, a rudimentary correction can be applied to account for the input of recycled carbon, that assumes the same degree of contamination over time. The difference between the uncalibrated conventional

radiocarbon age of surface sediment (assumed to have been deposited at 0 cal yr BP) and the present day MRA at the same location represents the age disparity caused by recycled carbon contamination and is termed the 'Local Contamination Offset' (Hillenbrand et al., 2010). Before calibration and correction for the Marine Reservoir Effect, the LCO can be subtracted from each of the conventional radiocarbon ages in a core. Alternatively, if the modern MRA is not known, the Surface Subtraction Method can be applied, assuming that the surface age is a result of recycled carbon contamination and the Marine Reservoir Effect combined (Andrews et al., 1999). Despite the widespread application of each of these methods, there is no accurate method, at present, for correcting the conventional radiocarbon age of AIOM samples for contamination by allochthonous carbon in Antarctic marine sediments.

### **1.3.2.2. Paleoclimate proxies in marine sediment**

#### *Biological productivity*

In the surface waters above the Antarctic continental margin, primary biological productivity is influenced by multiple environment conditions such as: surface water temperature and salinity, light availability, and nutrient supply (e.g., Si, Fe) (Arrigo et al., 2008; Ragueneau et al., 2000). These in turn are controlled by broad-scale changes in the Earth's climate and the regional oceanography, wind regime and sea-ice conditions. The release of iron and silica into the water by melting of iron-rich sea-ice, sediment scouring or upwelling of nutrient-rich mCDW has another important control over the rate of primary production (Alderkamp et al., 2012; Arrigo et al., 2000; Gerringa et al., 2012; Lannuzel et al., 2007, 2010; Martin et al., 1990; Moreau et al., 2019; Pollard et al., 2009; Sweeney et al., 2000; Vancoppenolle et al., 2013). Polynyas above the continental shelf are often rich in primary productivity as they provide localised open waters, replenished with nutrients from upwelling mCDW (Arrigo et al., 2015; Arrigo and van Dijken, 2003; Maddison et al., 2006; Mezgec et al., 2017; Moreau et al., 2019).

Productivity over the continental margin of Antarctica also varies on different timescales, in response to annual sea-ice fluctuations, polynya activity and millennial

to orbital-scale climate change. In general, biological productivity over the Antarctic margin is elevated during warm climate periods when sea-surface temperatures are high and sea-ice concentration is low and is limited during cold climate periods when sea-ice is widespread and glacier ice shelves extend further offshore. This relationship makes the temporal variation in primary productivity effective for tracking larger scale changes in climate, with peaks and lows commonly used to identify warm interglacials and cold glacial periods, respectively, in Antarctic marine sediment cores (e.g., Bertram et al., 2018; Ghadi et al., 2020; Holder et al., 2020; Wilson et al., 2018; Wu et al., 2017). Four common proxies for biological productivity in marine sediment cores are: 1) Diatom frustule abundance, 2) Biogenic silica (BiSi) concentration, 3) The x-ray fluorescence (XRF) Si/Al ratio and 4) The XRF Ba/Al ratio.

Diatoms are photosynthetic primary producers that predominantly dwell in the ice-free surface waters of the photic zone. These organisms dominate the biological productivity in the Southern Ocean (Arrigo et al., 2008) and account for most of the BiSi in the ocean (Ragueneau et al., 2000, and references therein). Diatom frustule abundance, BiSi concentration and Si/Al variability in marine cores have frequently been used as relative measures of diatom productivity around the East Antarctic margin, such as Prydz Bay (Wu et al., 2017), George V Land (Bertram et al., 2018; Wilson et al., 2018), Wilkes Land (Holder et al., 2020), the Scotia Sea (Weber et al., 2014), Adélie Land (Jimenez-Espejo et al., 2020), and the Ross Sea (Cunningham et al., 1999; McKay et al., 2016). Peaks in productivity are associated with a warmer climate, and often correspond with peaks in the iceberg-rafted debris (IBRD) flux (due to enhanced calving and basal melting of icebergs) (e.g., Bertram et al., 2018; Weber et al., 2014; Wilson et al., 2018) and the sortable silt percent (representative of increased bottom current speed in response to strengthening of the regional wind stress as the climate warms) (e.g., Passchier et al., 2019).

The amount of BiSi in marine sediment is rarely a complete reflection of the total primary biological production, export (sinking to the seafloor after death), and burial at the seabed (Anderson and Winckler, 2005). Some diatom species readily dissolve in the water column before they are buried, whilst others comprise of thicker frustules and more robust parts, allowing them to withstand higher energy conditions

(DeMaster et al., 1996). The degree of preservation can therefore affect the extent of biological productivity perceived from the measured BiSi concentration or absolute diatom abundance (DeMaster et al., 1996). In addition to different levels of preservation between species, the diatom assemblages in the sediment may also comprise of reworked species that do not reflect the surface water productivity contemporaneous with sediment deposition at the seabed (e.g., Holder et al., 2020; Kellogg and Kellogg, 1987; Leventer et al., 1996). However, general trends in the proxies used to gauge diatom productivity have proven to be effective as relative measures.

Barium in the form of barite ( $\text{BaSO}_4$ ) in marine sediment is another useful indicator of paleoproductivity (Bonn et al., 1998; Dymond et al., 1992a; Dymond and Collier, 1996; McManus et al., 1998). Barite is formed when decaying organic matter from siliceous and carbonate primary producers sinks through the water column, releasing barium and sulphur, which binds with oxygen in the water (Bertram and Cowen, 1997; Dymond and Collier, 1996; Paytan and Griffith, 2007). The close proximity to terrestrial lithogenic inputs at the Antarctic margin requires this potentially larger Ba contribution to be separated from the authigenic contribution. The barium exclusively associated with barite, known as excess barium ( $\text{Ba}_{\text{xs}}$ ) has been used to account for the contribution of Ba from the terrigenous source in some recent studies (e.g., Wu et al., 2017).

Despite the caveats and challenges associated with quantifying paleoproductivity (e.g., Anderson and Winckler, 2005), relative temporal changes in each of the diatom abundance, Si/Al, BiSi concentration and Ba/Al typically show clear peaks during interglacial periods and lows during glacial periods, and as such have been applied in many marine sediment studies around the East Antarctic margin (e.g., Bertram et al., 2018; Cook et al., 2013; Holder et al., 2020; Wilson et al., 2018; Wu et al., 2017). The measurement of multiple proxies for primary productivity will undoubtedly provide a clearer picture of the absolute productivity in a particular region as opposed to the perceived productivity influenced by other factors and processes occurring within the marine environment.

### *Iceberg-rafted debris*

The IBRD in marine sediment is detritus originally eroded from the continent and mechanically entrained in the ice. In Antarctic marine sediments, the IBRD flux has been used as a proxy for iceberg calving and melting during warm climate periods (e.g., Bertram et al., 2018; Cook et al., 2014; Kanfoush et al., 2000; Patterson et al., 2014; Smith et al., 2019; Weber et al., 2014; Williams et al., 2010; Wilson et al., 2018). During deglaciation and warm interglacials, the release of englacial IBRD is instigated by calving of icebergs off marine-terminating glaciers and melting at the base of the icebergs, sea ice and ice shelves. The IBRD flux to the seabed therefore reflects changes in the stability of the proximal ice sheet, with peaks in marine sediment cores representing past melting events (Jonkers et al., 2010; Liu et al., 2015; Patterson et al., 2014; Weber et al., 2014). The first IBRD records were established from North Atlantic sediments, which indicated the duration of Heinrich Events. Heinrich Events were past periods of cold climate in the Northern Hemisphere when instabilities in the Laurentide Ice Sheet (and possibly other ice sheets of the Northern Hemisphere) led to iceberg calving and the subsequent release of IBRD to the seabed, forming 'Heinrich layers' (Álvarez-Solas et al., 2011; Bond et al., 1992; Heinrich, 1988; Hemming, 2004; MacAyeal, 1993; Marshall and Koutnik, 2006). During millennial-scale periods of warmer climate in the Northern Hemisphere, known as Dansgaard-Oeschger Events, the IBRD is interpreted to be sourced from icebergs calved from the glaciers as the ice sheet retreated (Marshall and Koutnik, 2006). In Antarctica, the IBRD flux from marine sediment cores has been used to mark melting events associated with deglaciation of the ice sheet during Pliocene (Bertram et al., 2018; Patterson et al., 2014) and Pleistocene (Wilson et al., 2018) interglacials, and over the Last Glacial Period-Holocene transition (e.g., Kanfoush et al., 2000; Weber et al., 2014).

The IBRD in marine sediment is typically defined as poorly-sorted, coarse (either 150  $\mu\text{m}$  – 2 mm or 250 $\mu\text{m}$  – 2 mm), angular material (e.g., Patterson et al., 2014), though fine IBRD does also exist (e.g., McCave and Andrews, 2019) and may not be represented in core records. Icebergs can transport IBRD long distances around the Antarctic continent, driven by the west-flowing Antarctic Coastal Current, resulting in the release of IBRD at a distance from its source (e.g., Budge and Long, 2018;

Gladstone et al., 2001; Williams et al., 2010). The distance that an iceberg travels is controlled predominantly by sea surface temperatures, with colder temperatures resulting in longer distances and warmer temperatures resulting in basal melting closer to the source of the IBRD (Cook et al., 2014). However, a recent study of grounding zone proximal sediments from the Ross Sea interpreted that the rainout of basal debris occurs at a distance no greater than ~1.2 km, resulting in most of the IBRD being deposited proximal to its source, giving a melting event signature representative of the location (Prothro et al., 2018).

### *Paleocurrent speed*

The grain size distribution in marine sediment contains evidence for temporal changes in current speed. Since currents primarily control the transport of fine sediment (< 63  $\mu\text{m}$ ), size variability within the fine fraction can be attributed to variation in current speed, where larger grains within the fine fraction represent faster current speeds with the strength to transport heavier loads, and smaller grains represent slower current speeds (McCave and Hall, 2006). Due to the tendency of very fine clays (< 10  $\mu\text{m}$ ) to aggregate and form flocs unrepresentative of size sorting influenced by current transport, this portion of the fine fraction is disregarded when interpreting grain size in relation to current speed (McCave et al., 1995). The remainder of the fine fraction, referred to as sortable silt (10-63  $\mu\text{m}$ ) has long been established as an effective indicator of sediment size sorting and selective deposition relative to paleocurrent speed (McCave, 2008; McCave and Hall, 2006; McCave et al., 1995, 2017).

Processes other than paleocurrent speed affecting the measurable sortable silt percent at any given site are: 1) The deposition of abundant fine-grained ice-rafted debris, 2) Multiple sediment sources, 3) The removal of fines by the process of winnowing and 4) the type of grain size analyser employed (McCave and Hall, 2006). The quantification of ice-rafted debris ordinarily employs any angular detrital grains within the 150  $\mu\text{m}$  – 2 mm or 250  $\mu\text{m}$  – 2 mm size fractions (e.g., Bertram et al., 2018; Cook et al., 2014; Patterson et al., 2014; Tooze et al., 2020; Williams et al., 2010; Wilson et al., 2018). While detrital grains of this description can be defined

exclusively as ice-rafted debris, fine-grained ice-rafted debris does exist, and may affect interpretations of the sorting of fines in relation to paleocurrent speed (Jonkers et al., 2015; Wu et al., 2018). However, McCave and Andrews (2019) dispute that, provided that the sediment has been current-sorted after deposition, it does not matter the initial process by which it was deposited, including via glacial meltwater plumes, debris flows, icebergs or sea-ice. Regions where the ice-rafted debris flux is high, therefore, should not significantly affect interpretations of paleocurrent speed from the sortable silt fraction, except in the rare instance that fine ice-rafted debris is deposited into a very gentle current of insufficient speed to resuspend and sort the sediment (McCave and Andrews, 2019).

A recent study by (Wu et al., 2020) found that the XRF Zr/Rb ratio in sediment from the Southern Ocean positively correlates with absolute elemental abundances of zirconium (Zr) and rubidium (Rb), particle size and the average sortable silt grain size, deeming it an effective proxy for paleocurrent speed. Zirconium is typically concentrated in coarser, magmatic and metamorphic zircon grains which are heavy and have a high resistance to weathering and erosion (Dypvik and Harris, 2001). In contrast, rubidium is found primarily in potassium-rich fine-grained clay minerals such as illite and mica (Dypvik and Harris, 2001). The Zr/Rb ratio therefore gives an indication of changes in grain size, which in turn can be related to bottom current strength (with stronger currents transporting coarser, Zr-rich grains, and slower currents transporting finer Rb-rich grains). The Zr/Rb ratio was found to have no correlation with the ice-rafted debris content (Wu et al., 2020), supporting the interpretation that fine ice-rafted debris does not limit interpretations of the paleocurrent speed from the sortable silt fraction (McCave and Andrews, 2019).

### **1.3.2.3. Marine sediment provenance techniques**

Crystalline basement rock in Antarctica is eroded by the overlying ice sheet, causing detrital grains to become entrained in the ice and transported to the Southern Ocean via glaciers, icebergs, and meltwater streams. Since ice covers approximately 99.8% of Antarctica (Burton-Johnson et al., 2016), and coastal rock outcrop is rare, the

study of detritus originally eroded from the continent is valuable and can provide evidence for the regional geological and tectonic history; sediment transport pathways, glaciological processes, and variation in ice sheet dynamics and the marine sediment depositional regime in response to climate variation (Licht and Hemming, 2017). Here I summarise two effective sediment provenance techniques: U-Pb dating of detrital grains and the measurement of the bulk Nd and Sr isotope signature in marine sediment.

### *Single-grain U-Pb dating*

One of the most powerful sediment provenance tools is the U-Pb dating of detrital grains from marine sediment, which has been applied in Antarctic research (e.g., Licht and Palmer, 2013; Pierce et al., 2014; Veevers et al., 2008; Williams et al., 2017). The radioactive decay of  $^{235}\text{U}$  to  $^{207}\text{Pb}$  and  $^{238}\text{U}$  to  $^{206}\text{Pb}$  provides an age for single detrital grains originally eroded from crystalline basement rock beneath the Antarctic Ice Sheet. Provided that the age of proximal basement geology is known, the source and provenance of detrital grains can be traced using this technique. Temporal changes in the erosion of subglacial bedrock are therefore recorded in proximal marine sediments of the Antarctic continental margin. Variation in the detrital U-Pb provenance signal can be used to reconstruct ice sheet advance and retreat, sediment transport pathways, basement rock erosion and the regional geological and tectonic histories (Licht and Hemming, 2017).

### *Bulk Nd and Sr isotopes*

The radioactive isotopes  $^{143}\text{Nd}$  and  $^{87}\text{Sr}$  are decay products of the respective Sm-Nd and Rb-Sr radioactive systems and are present in all rock types (Goldstein and Hemming, 2003). The Nd and Sr isotopic composition of a sample is measured as  $^{143}\text{Nd}/^{144}\text{Nd}$  and  $^{87}\text{Sr}/^{86}\text{Sr}$ , respectively, where the radiogenic isotope (i.e.,  $^{143}\text{Nd}$  and  $^{87}\text{Sr}$ ) is measured relative to a stable isotope ( $^{144}\text{Nd}$  and  $^{86}\text{Sr}$ ). The Nd-isotopic composition is typically expressed as  $\epsilon_{\text{Nd}}$ , which is the deviation of the measured  $^{143}\text{Nd}/^{144}\text{Nd}$  in a sample from the  $^{143}\text{Nd}/^{144}\text{Nd}$  of the Earth's Chondritic Uniform Reservoir (Jacobsen and Wasserburg, 1980). The Nd and Sr isotopic composition of

a rock is a function of: 1) the geochemical properties of the rock (controlled by magmatic processes) and 2) the age of the rock (and thus the amount of radioactive decay of the parent to the daughter isotope).

The oceanic crust contains higher Sm/Nd ratios than the continental crust due to the preferential incorporation of the parent isotope ( $^{147}\text{Sm}$ ) into the mantle melt, leaving higher concentrations of the daughter isotope ( $^{143}\text{Nd}$ ) in the residue that forms continental rocks (Licht and Hemming, 2017, and references therein). In the Rb-Sr system, which behaves differently, the daughter isotope ( $^{87}\text{Sr}$ ) is more compatible in the mantle melt than the parent isotope ( $^{87}\text{Rb}$ ), leading to lower Rb/Sr ratios in the oceanic crust than the continental crust. Mafic rocks (and in particular Mid-Ocean Ridge Basalt (MORB) that dominates the Earth's oceanic crust) therefore have a primitive, mantle-like isotopic character with higher  $\epsilon_{\text{Nd}}$  values and lower  $^{87}\text{Sr}/^{86}\text{Sr}$  ratios compared to felsic rocks of the continental crust. Since  $^{87}\text{Rb}$  has a shorter half-life ( $49.61 \pm 0.16$  Ga; Villa et al., 2015) than  $^{143}\text{Sm}$  ( $107.9 \pm 2.6$  Ga; Tavares and Terranova, 2018), the Sr-isotopic composition of a rock is more greatly affected by the passage of time than the Nd-isotopic composition. Moreover, continental (felsic) rocks contain a higher Rb/Sr than oceanic (mafic) rocks, meaning that the temporal change in the Sr-isotopic composition is more pronounced in felsic rocks.

The unique Nd and Sr isotopic compositions of different rock types and ages allow detrital Antarctic marine sediments to be traced back to their continental source (Cook et al., 2013, 2017; Goldstein and Hemming, 2003; Hemming et al., 2000; Licht and Hemming, 2017; Pierce et al., 2011, 2017; Roy et al., 2007; van de Flierdt et al., 2007), provided that there is an understanding of source basement rock Nd-Sr isotopic compositions. Contributions of detritus from multiple different source rocks terranes eroded in the same glacial catchment result in an integrated offshore Nd-Sr isotopic signal, that is influenced by contribution from different rocks beneath the ice sheet at the coast (Cook et al., 2017; Licht and Hemming, 2017). Since the bulk Nd-Sr isotopic signal is related to the erosion of rocks at the base of the ice sheet, temporal changes in the signature (as commonly seen in marine sediment cores) often reflect 1) variation in the contribution of detritus from different basement rock

sources to the combined Nd-Sr isotopic signal, and/or 2) the erosion of different substrates related to variation in the configuration of the ice sheet in response to changes in the climate (typically on orbital scales). Bulk Nd-Sr isotopic signatures are therefore useful for tracking dynamic changes to the ice sheet in response to climate change (e.g., Bertram et al., 2018; Cook et al., 2013, 2017; Pierce et al., 2017; Wilson et al., 2018).

The detrital Nd and Sr isotopic signal of marine sediments from the continental margin may be affected by other factors in addition to the source rock composition and ice sheet configuration. The amount of detritus from each basement rock terrane represented in the bulk Nd-Sr isotopic signal may, for example, be affected by erosion rates at the base of the ice sheet, sedimentation rates, mineral composition and transport processes (Cook et al., 2017; Goldstein and Hemming, 2003; Licht and Hemming, 2017). High basal erosion/sedimentation rates at one part of the coast may result in one basement rock terrane being overly represented in the signal. Additionally, mafic minerals are typically less resistant to weathering than felsic minerals, potentially resulting in a sediment provenance signal biased in favour of felsic sources, depending on the distance of the core site from the basement rock source (Licht and Hemming, 2017). Finally, the grain size effect, explained by a naturally higher concentration of  $^{87}\text{Rb}$  (and therefore higher  $^{87}\text{Sr}/^{86}\text{Sr}$  ratios) in fine clays and lower  $^{87}\text{Rb}$  (lower  $^{87}\text{Sr}/^{86}\text{Sr}$  ratios) in sands and silts can have a major influence over the Sr-isotopic signal (Biscaye and Dasch, 1971; Diekmann and Kuhn, 1999; Goldstein and Hemming, 2003). Though grain size-affected Sr-isotopic signatures do not fully represent the sediment provenance signal, they can provide useful information on the marine sediment depositional regime associated with the response of the ice sheet to climate variation, by indicating periods of glacial (clay) and interglacial (coarser silty clay) sedimentation.

## 1.4. Study region

Multiple glacier catchments are situated along the Budd (Vanderford, Fox and Williamson glaciers), Sabrina (Totten and Moscow University glaciers) and Banzare (Thompson and Holmes glaciers) coasts of central Wilkes Land (Fig. 1.5), draining ice and sediment-laden meltwater from the ice sheet and interior basins to the Southern Ocean (Mouginot et al., 2017; Wright et al., 2012; Zwally et al., 2012). In 2017, multiple Multicores (MC), Kasten cores (KC) and Piston cores were recovered from the upper continental rise adjacent to the Sabrina Coast by the *RV Investigator* (Fig. 1.5; Armand et al., 2018). In this study, the following cores were used: IN2017\_V01-A005\_MC01, IN2017\_V01-A005\_KC02, IN2017\_V01-A042-KC14, IN2017\_V01-C012\_MC03, IN2017\_V01-C012\_KC04, IN2017\_V01-C025\_KC12, and (hereafter referred to as MC01, KC02, KC14, MC03, KC04 and KC12, respectively). The locations and water depths at which the cores were recovered are provided in Table 1.1.

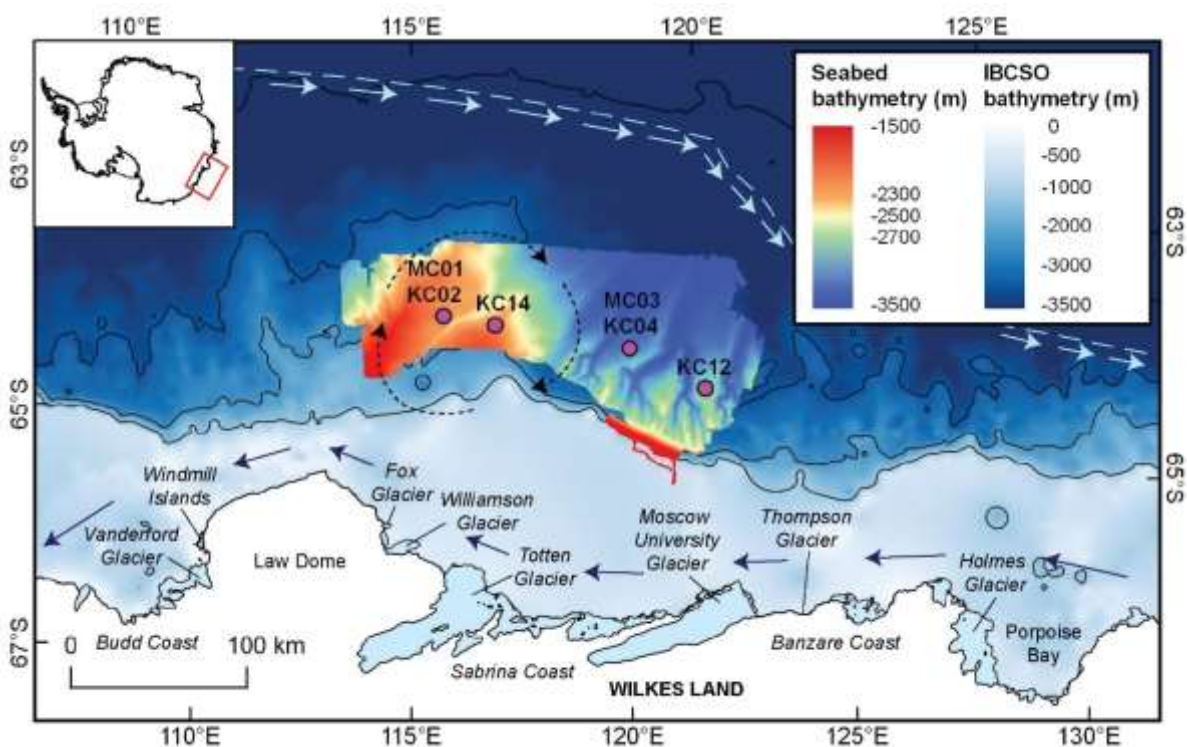


**Figure 1.5. Core locations.** Map of central Wilkes Land, East Antarctica, with core locations (pink). Offshore bathymetry and 1000 m contours are shown using the International Bathymetric Chart of the Southern Ocean (IBCSO), version 1.0 (Arndt et al., 2013). High

resolution bathymetry was acquired from the *RV Investigator* (voyage IN2017\_V01; Armand et al., 2018). The southern boundary of the east-flowing Antarctic Circumpolar Current is shown in light blue (Orsi et al., 1995). The west-flowing Antarctic Coastal Current is represented by blue arrows proximal to the coast. The approximate position of an eddy identified by Wakatsuchi et al. (1994) is shown with black dashed arrows.

Station	Core	Latitude	Longitude	Depth (mbsl)
A-005	KC02	64°28'15.6"S	115°37'22.8"E	2161
A-005	MC01	64°28'15.6"S	115°37'22.8"E	2161
A-042	KC14	64°32'20.4"S	116°38'24"E	2100
C-012	KC04	64°40'30"S	119°18'3.6"E	3104
C-012	MC03	64°40'30"S	119°18'3.6"E	3104
C-025	KC12	64°57'14.4"S	120°51'50.4"E	2779

**Table 1.1.** Locations and water depths at which the Multicores (MC) and Kasten cores (KC) used in this thesis were recovered (voyage INV2017-V01; Armand et al., 2018).

### 1.4.1. Sediment depositional regime

In the western part of the study region, on the continental rise (between approximately 114°-118° E), two large sediment contourite ridges, from which KC02, KC14 and MC01 were recovered, extend northward over the upper continental rise (Fig. 1.5). These ridges are maintained by sediment-laden meltwater fluxes from the proximal Totten Glacier and by the resuspension and westward transport of finer material from the channel levee deposits in the east of the study region via west-flowing bottom-intensified currents (O'Brien et al., 2020). In the eastern part of the study region (between approximately 118°-122° E), numerous gullies characterise the upper continental slope, which develop into a dendritic network of submarine canyons across the continental rise (Fig. 1.5). Asymmetric ridges between the submarine canyons were formed by the resuspension and westward current advection of fine hemipelagic sediments (Post et al., 2020). These sediments originated from sediment-laden meltwater migrating rapidly down the canyons in

turbidite flows during glacial maxima and emanating from the ice sheet during deglaciation (Donda et al., 2020; Gales et al., 2013; O'Brien et al., 2020). It is interpreted that much of this sediment originated from the Totten Glacier catchment throughout the Late Cenozoic era (Phases 2 - 4 of Donda et al. (2007)) (Donda et al., 2020). Cores KC04, KC12 and MC03 were recovered from the leeward slope of these 'giant levee deposits' (Fig. 1.5; Armand et al., 2018; Post et al., 2020).

The continental shelf of central Wilkes Land is incised by deep tunnel valleys (Gulick et al., 2017; Kehew et al., 2012) and is imprinted with grounding zone wedges and scour marks that record former positions of the ice sheet grounding line (Fernandez et al., 2018; Post et al., 2020). Sediments on the continental shelf of central Wilkes Land record multiple cycles of advance and retreat of the ice sheet over former glacial-interglacials (Donda et al., 2007; Fernandez et al., 2018; Gulick et al., 2017).

## **1.4.2. Subglacial geology**

An understanding of the subglacial geology of Antarctica is important not only for establishing the geological and tectonic evolution of the continent, but also the dynamic response of the overlying ice sheet to a changing climate. Some knowledge of the geology is needed for determining the source of detritus in marine sediment cores, which can subsequently provide insight into past glaciological processes, basement rock erosion and sediment pathways related to ice sheet advance and retreat over multiple glacial-interglacial cycles. An overview of the current knowledge of the subglacial geology in central Wilkes Land is provided below.

During multiple collisional events associated with the formation of past supercontinents throughout Earth's tectonic history, the East Antarctic and southern Australian margins were adjoined, forming a strong geological relationship between the two now separate margins (e.g., Aitken et al., 2016; Boger, 2011; Fitzsimons, 2000; Fig. 1.6). Airborne geophysical data (Aitken et al., 2014), boreholes (e.g., Kirkland et al., 2011, 2015, 2017; Spaggiari et al., 2015, 2018), rare rock outcrop

(Black et al., 1992; Black et al., 1992; Maritati et al., 2019; Möller et al., 2002; Morrissey et al., 2017; Sheraton et al., 1990, 1992, 1995; Tucker et al., 2017; Zhang et al., 2012) and marine sediment provenance analysis (Pierce et al., 2011, 2014; Tooze et al., 2020) has been used to probe the basement rock types and structural features that are hidden beneath regolith in southern Australia and thick ice in East Antarctica. Based on this data, three Mesoproterozoic provinces have been interpreted across the two margins. From west to east in southern Australia, these provinces are: the Albany-Fraser Orogen, the Madura Province and the Coompana Province (Fig. 1.6). The corresponding terranes in Antarctica are known as the Wilkes, Nuyina and Banzare provinces, respectively (Fig. 1.6). Below I introduce the geological history of rocks from the Albany-Fraser Orogen, the Madura Province and the Coompana Province and, where possible, link this geology to the corresponding Wilkes, Nuyina and Banzare provinces in central Wilkes Land.

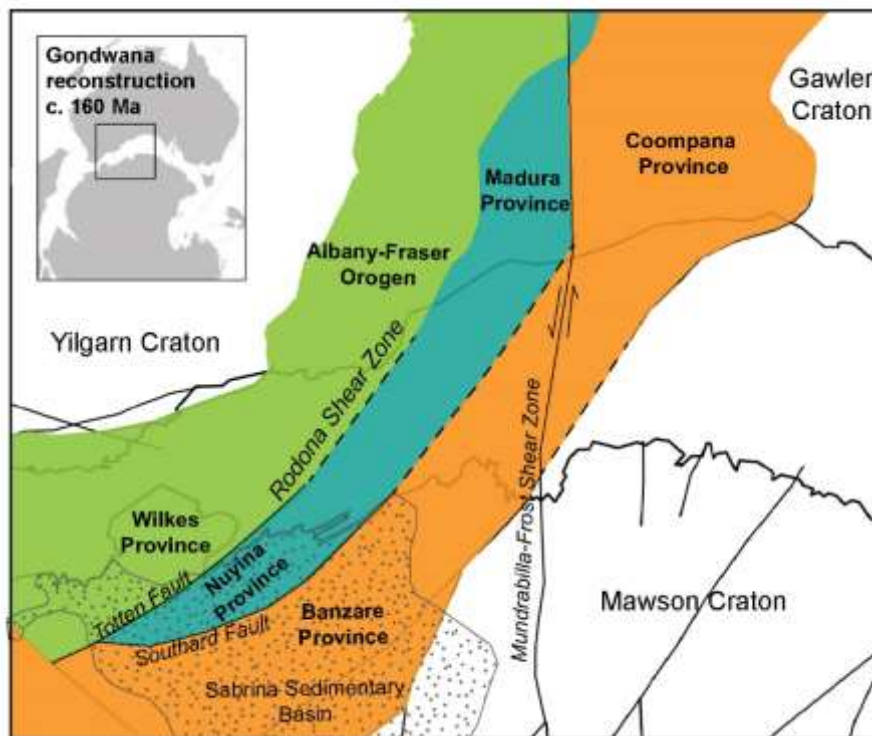


**Figure 1.6. Basement rock provinces in southern Australia and East Antarctica.** Full-fit Gondwana (c. 160 Ma) reconstruction, with Antarctica fixed in its present-day reference frame (Matthews et al., 2016). Basement rock provinces are shown using most recent interpretation of Maritati et al. (2019). Fault positions are after Aitken et al. (2014) and Maritati et al. (2019).

In southern Australia, the Albany-Fraser Orogen is situated on the southern and south-eastern margins of the Archean Yilgarn Craton (Fig. 1.6) and is characterised by Archean and Proterozoic crust that was reworked between c. 1815-1140 Ma (Beeson et al., 1988; Black et al., 1992; Clark et al., 2000; Kirkland et al., 2011; Nelson et al., 1995; Spaggiari et al., 2015; Waddell et al., 2015). Reworking of the Yilgarn craton margin began at c. 1815 Ma with the formation of the Barren Basin and a continued extensional regime led to the development of the oceanic Arid Basin at c. 1600 Ma (Spaggiari et al., 2015). Widespread regional metamorphism of the rocks within the Albany-Fraser Orogen took place in two stages: at c. 1340-1260 Ma (Stage I) and at c. 1200-1100 Ma (Stage II) (Clark et al., 2000). The crust becomes progressively more juvenile with distance from the craton margin, with remnants of Archean crust present in the geology in the western parts of the Albany-Fraser Orogen and younger, Mesoproterozoic magmatic intrusions dominating the eastern parts.

The geology of the Albany-Fraser Orogen is divided into three geophysically-distinct complexes: the Biranup Complex, the Fraser Complex and the Nornalup Complex (Myers, 1993; Nelson et al., 1995). The Biranup Complex is situated adjacent to the Yilgarn Craton and largely consists of Paleoproterozoic orthogneisses and remnants of Archean cratonic crust (Myers, 1993; Nelson et al., 1995). In the Bungee Hills region, west of central Wilkes Land in East Antarctica, the U-Pb ages of primary zircon from rare coastal outcrop are dominantly Archean and Paleoproterozoic in age (Tucker et al., 2017). This region therefore comprises rocks equivalent to those of the Biranup Complex and marks the westernmost part of the Wilkes Province. The Fraser Complex is geographically constrained to a relatively small region of the Albany-Fraser Orogen in southern Australia and largely consists of metagabbros and metagranites (Clark et al., 2014; Clark et al., 1999; de Waele and Pisarevsky, 2008; Myers, 1993; Nelson et al., 1995). Sedimentary protoliths of the rocks were deposited between c. 1330-1290 Ma and underwent high-grade metamorphism at c. 1290 Ma (Clark et al., 2014). Emplacement of mafic magmatism was coeval with peak metamorphism at c. 1290 Ma, indicating that metamorphism was likely driven

by high temperatures associated with mafic magmatism (Clark et al., 2014; Clark et al., 1999; de Waele and Pisarevsky, 2008). These events led to the formation of granulite facies metagabbros (Clark et al., 2014).

The easternmost complex of the Albany Fraser Orogen, the Nornalup Complex, consists predominantly of the Recherche Granite which was emplaced between c. 1330-1290 Ma (Myers, 1993; Nelson et al., 1995), intruding into the metamorphic basement rock (the Malcolm Gneiss) of the Arid Basin (Clark et al., 2000). This magmatism marked the beginning of Stage I of the Albany-Fraser Orogeny and was initiated by the accretion of Loogana Arc onto the craton margin (Spaggiari et al., 2015). The Mount Ragged sedimentary rocks were then deposited at c. 1310 Ma and metamorphosed during Stage II of the Albany-Fraser Orogeny (Waddell et al., 2015). Based on shared detrital zircon peaks, this metasedimentary unit is equivalent to metasedimentary rocks of the Wilkes Province dated in the Windmill Islands in central Wilkes Land (Fitzsimons, 2000; Morrissey et al., 2017).

Emplacement of the Esperance Granite took place between c. 1200-1140 Ma during most of Stage II of the Albany-Fraser Orogeny (Nelson et al., 1995). Most, if not all of the Wilkes Province that underlies the study region in central Wilkes Land is likely to comprise rocks equivalent to the Nornalup Complex.

The Madura Province lies to the east of the Rodona Shear Zone adjacent to Albany-Fraser Orogen (Fig. 1.6) and is dominated by mafic magmatic rocks that were emplaced predominantly during oceanic crust subduction between c. 1480-1390 Ma (Spaggiari et al., 2018). The recent discovery of the Arubiddy Ophiolite Complex preserved in the Madura Province has led to the most complete interpretation of the formation and tectonic evolution of this region (Spaggiari et al., 2018). The opening of the oceanic Arid Basin during rifting at the margin of Yilgarn Craton initiated mafic magmatism described as the Pinto Basalt between c. 1900-1600 Ma (Spaggiari et al., 2018). Subsequent closure of the Arid Basin commenced at c. 1480 Ma in a convergent setting and subducted oceanic crust promoted magmatism associated with the Sleeper Camp Formation (Kirkland et al., 2015, 2017). Continued subduction of oceanic crust gave rise to the formation of Loogana Arc and

associated ocean-arc mafic magmatism of Haig Cave Supersuite at c. 1415 Ma (Spaggiari et al., 2018). Haig Cave Supersuite dominantly consists of tholeiitic gabbros and periodotite intruded by plagiogranite (Spaggiari et al., 2018). Detrital zircons from the Arid basin have a dominant age signature between c. 1425-1375 Ma, suggesting that rocks of the Haig Cave Supersuite are the source of this detritus (Wingate et al., 2015). Accretion of Loongana arc onto the edge of the continental margin occurred at c. 1390 Ma, triggering Stage I of the Albany-Fraser Orogeny (Spaggiari et al., 2015, 2018). During Stage II, the Moodini Supersuite intruded into both Madura Province (c. 1180-1125 Ma; Kirkland et al., 2017) and the adjacent Coompana Province (c. 1190-1140 Ma; Kirkland et al., 2017).

The Coompana Province is situated to the east of Madura Province and Mundrabilla-Frost Shear Zone (Fig. 1.6) and consists of three magmatic supersuites: the Toolgana Supersuite (c. 1600 Ma), the Undawidgi Supersuite (c. 1490 Ma) and the Moodini Supersuite (c. 1190-1140 Ma) (Kirkland et al., 2017). The Toolgana Supersuite is interpreted to represent primitive magmatic arc setting that was active between c. 1720-1610Ma and formed during oceanic crust subduction in the Madura Province region (Kirkland et al., 2017). The Undawidgi Supersuite represents magmatism during the extension of the Arid Basin and oceanic crust gneiss (Kirkland et al., 2017). The Madura and Coompana provinces in southern Australia correlate with the East Antarctic Nuyina and Banzare provinces, respectively, based on matching geophysical signatures and limited geological evidence (Aitken et al., 2014; Maritati et al., 2019). Granodioritic plutons at Chick Island have an age (primary zircon U-Pb age: c. 1150 Ma) and geochemical composition similar to rocks of the Moodini Supersuite in southern Australia (Maritati et al., 2019). Xenocrysts from the same region exhibit primary zircon U-Pb ages that correspond to those of magmatic rocks within both the Madura and Coompana provinces in southern Australia, suggesting that Chick Island is proximal to the boundary between the Nuyina and Banzare provinces in central Wilkes Land (Maritati et al., 2019).

## References

- Adkins, J. F. (2013). The role of deep ocean circulation in setting glacial climates. *Paleoceanography*, 28(3), 539–561. <https://doi.org/10.1002/palo.20046>
- Adkins, J. F., & Boyle, E. A. (1997). Changing atmospheric  $\Delta^{14}\text{C}$  and the record of deep water paleoventilation ages. *Paleoceanography*, 12(3), 337–344. <https://doi.org/10.1029/97PA00379>
- Aitken, A. R. A., Betts, P. G., Young, D. A., Blankenship, D. D., Roberts, J. L., & Siegert, M. J. (2016). The Australo-Antarctic Columbia to Gondwana transition. *Gondwana Research*, 29(1), 136–152. <https://doi.org/10.1016/j.gr.2014.10.019>
- Aitken, A. R. A., Young, D. A., Ferraccioli, F., Betts, P. G., Greenbaum, J. S., Richter, T. G., Roberts, J. L., Blankenship, D. D., & Siegert, M. J. (2014). The subglacial geology of Wilkes Land, East Antarctica. *Geophysical Research Letters*, 41(7), 2390–2400. <https://doi.org/10.1002/2014GL059405>
- Alderkamp, A. C., Mills, M. M., van Dijken, G. L., Laan, P., Thuróczy, C. E., Gerringa, L. J. A., de Baar, H. J. W., Payne, C. D., Visser, R. J. W., Buma, A. G. J., & Arrigo, K. R. (2012). Iron from melting glaciers fuels phytoplankton blooms in the Amundsen Sea (Southern Ocean): Phytoplankton characteristics and productivity. *Deep-Sea Research Part II: Topical Studies in Oceanography*, 71–76, 32–48. <https://doi.org/10.1016/j.dsr2.2012.03.005>
- Alley, R. B., & Bindschadler, R. A. (2013). *The West Antarctic Ice Sheet and Sea-Level Change*. 1–11. <https://doi.org/10.1029/ar077p0001>
- Álvarez-Solas, J., Montoya, M., Ritz, C., Ramstein, G., Charbit, S., Dumas, C., Nisancioglu, K., Dokken, T., & Ganopolski, A. (2011). Heinrich event 1: An example of dynamical ice-sheet reaction to oceanic changes. *Climate of the Past*, 7(4), 1297–1306. <https://doi.org/10.5194/cp-7-1297-2011>
- Alves, E. Q., Macario, K., Ascough, P., & Bronk Ramsey, C. (2018). The Worldwide Marine Radiocarbon Reservoir Effect: Definitions, Mechanisms, and Prospects. *Reviews of Geophysics*, 56(1), 278–305. <https://doi.org/10.1002/2017RG000588>
- Alves, E. Q., Macario, K. D., Urrutia, F. P., Cardoso, R. P., & Bronk Ramsey, C. (2019). Accounting for the marine reservoir effect in radiocarbon calibration. *Quaternary Science Reviews*, 209, 129–138. <https://doi.org/10.1016/j.quascirev.2019.02.013>

- Anderson, E. C., Libby, W. F., Weinhouse, S., Reid, A. F., Kirshenbaum, A. D., & Grosse, A. V. (1947a). Natural radiocarbon from cosmic radiation. *Physical Review*, *72*(10), 931–936. <https://doi.org/10.1103/PhysRev.72.931>
- Anderson, E. C., Libby, W. F., Weinhouse, S., Reid, A. F., Kirshenbaum, A. D., & Grosse, A. V. (1947b). Radiocarbon from cosmic radiation. *Science*, *105*(2735), 576. <https://doi.org/10.1126/science.105.2735.576>
- Anderson, R. F., & Winckler, G. (2005). Problems with paleoproductivity proxies. *Paleoceanography*, *20*(3), 1–7. <https://doi.org/10.1029/2004PA001107>
- Andrews, J. T., Domack, E. W., Cunningham, W. L., Leventer, A., Licht, K. J., Jull, A. J. T., DeMaster, D. J., & Jennings, A. E. (1999). Problems and possible solutions concerning radiocarbon dating of surface marine sediments, Ross Sea, Antarctica. *Quaternary Research*, *52*(2), 206–216. <https://doi.org/10.1006/qres.1999.2047>
- Armand, L., O'Brien, P., Armbrecht, L., Barker, H., Caburlotto, A., Connell, T., Cotterle, D., Duffy, M., Edwards, S., Evangelinos, D., Fazey, J., Flint, A., Focardi, A., Gifford, S., Holder, L., Hughes, P., Lawler, K.-A., Lieser, J., Leventer, A., ... Young, A. (2018). *Interactions of the Totten Glacier with the Southern Ocean through multiple glacial cycles (IN2017-V01): Post-survey report. March*. <https://doi.org/10.4225/13/5ACEA64C48693>
- Arndt, J. E., Schenke, H. W., Jakobsson, M., Nitsche, F. O., Buys, G., Goleby, B., Rebesco, M., Bohoyo, F., Hong, J., Black, J., Greku, R., Udintsev, G., Barrios, F., Reynoso-Peralta, W., Taisei, M., & Wigley, R. (2013). The international bathymetric chart of the Southern Ocean (IBCSO) version 1.0-A new bathymetric compilation covering circum-Antarctic waters. *Geophysical Research Letters*, *40*(12), 3111–3117. <https://doi.org/10.1002/grl.50413>
- Arneborg, L., Wahlin, A. K., Björk, G., Liljebladh, B., & Orsi, A. H. (2012). Persistent inflow of warm water onto the central Amundsen shelf. *Nature Geoscience*, *5*(12), 876–880. <https://doi.org/10.1038/ngeo1644>
- Arrigo, K. R., DiTullio, G. R., Dunbar, R. B., Robinson, D. H., VanWoert, M., Worthen, D. L., & Lizotte, M. P. (2000). Phytoplankton taxonomic variability in nutrient utilization and primary production in the Ross Sea. *Journal of Geophysical Research: Oceans*, *105*(C4), 8827–8846. <https://doi.org/10.1029/1998jc000289>
- Arrigo, K. R., & van Dijken, G. L. (2003). Phytoplankton dynamics within 37 Antarctic coastal polynya systems. *Journal of Geophysical Research: Oceans*, *108*(8). <https://doi.org/10.1029/2002jc001739>

- Arrigo, K. R., van Dijken, G. L., & Bushinsky, S. (2008). Primary production in the Southern Ocean, 1997-2006. *Journal of Geophysical Research: Oceans*, 113(8).  
<https://doi.org/10.1029/2007JC004551>
- Arrigo, K. R., van Dijken, G. L., & Strong, A. L. (2015). Environmental controls of marine productivity hot spots around Antarctica. *Journal of Geophysical Research: Oceans*, 120(8), 5545–5565. <https://doi.org/10.1002/2015JC010888>
- Assmann, K. M., Jenkins, A., Shoosmith, D. R., Walker, D. P., Jacobs, S. S., & Nicholls, K. W. (2013). Variability of circumpolar deep water transport onto the Amundsen Sea Continental shelf through a shelf break trough. *Journal of Geophysical Research: Oceans*, 118(12), 6603–6620. <https://doi.org/10.1002/2013JC008871>
- Beeson, J., Delor, C. P., & Harris, L. B. (1988). A structural and metamorphic traverse across the Albany Mobile Belt, Western Australia. *Precambrian Research*, 40–41(C), 117–136.  
[https://doi.org/10.1016/0301-9268\(88\)90064-2](https://doi.org/10.1016/0301-9268(88)90064-2)
- Bertram, M. A., & Cowen, J. P. (1997). Morphological and compositional evidence for biotic precipitation of marine barite. *Journal of Marine Research*, 55(3), 577–593.  
<https://doi.org/10.1357/0022240973224292>
- Bertram, R. A., Wilson, D. J., van de Flierdt, T., McKay, R. M., Patterson, M. O., Jimenez-Espejo, F. J., Escutia, C., Duke, G. C., Taylor-Silva, B. I., & Riesselman, C. R. (2018). Pliocene deglacial event timelines and the biogeochemical response offshore Wilkes Subglacial Basin, East Antarctica. *Earth and Planetary Science Letters*, 494, 109–116.  
<https://doi.org/10.1016/j.epsl.2018.04.054>
- Bindoff, N. L., Rosenberg, M. A., & Warner, M. J. (2000). On the circulation and water masses over the Antarctic continental slope and rise between 80 and 150°E. *Deep-Sea Research Part II: Topical Studies in Oceanography*, 47(12–13), 2299–2326.  
[https://doi.org/10.1016/S0967-0645\(00\)00038-2](https://doi.org/10.1016/S0967-0645(00)00038-2)
- Biscaye, P. E., & Dasch, E. J. (1971). The rubidium, strontium, strontium-isotope system in deep-sea sediments: Argentine Basin. *Journal of Geophysical Research*, 76(21), 5087–5096.  
<https://doi.org/10.1029/JC076i021p05087>
- Black, L. P., Harris, L. B., & Delor, C. P. (1992). Reworking of Archaean and Early Proterozoic components during a progressive, Middle Proterozoic tectonothermal event in the Albany Mobile Belt, Western Australia. *Precambrian Research*, 59(1–2), 95–123.  
[https://doi.org/10.1016/0301-9268\(92\)90053-Q](https://doi.org/10.1016/0301-9268(92)90053-Q)

- Black, L. P., Sheraton, J. W., Tingey, R. J., & McCulloch, M. T. (1992). New U-Pb zircon ages from the Denman Glacier area, East Antarctica, and their significance for Gondwana reconstruction. *Antarctic Science*, 4(4), 447–460.  
<https://doi.org/10.1017/S095410209200066X>
- Boening, C., Lebrock, M., Landerer, F., & Stephens, G. (2012). Snowfall-driven mass change on the East Antarctic ice sheet. *Geophysical Research Letters*, 39(21).  
<https://doi.org/10.1029/2012GL053316>
- Boger, S. D. (2011). Antarctica - Before and after Gondwana. In *Gondwana Research* (Vol. 19, Issue 2, pp. 335–371). <https://doi.org/10.1016/j.gr.2010.09.003>
- Bond, G., Heinrich, H., Broecker, W., Labeyrie, L., McManus, J., Andrews, J., Huon, S., Jantschik, R., Clasen, S., Simet, C., Tedesco, K., Klas, M., Bonani, G., & Ivy, S. (1992). Evidence for massive discharges of icebergs into the North Atlantic ocean during the last glacial period. *Nature*, 360(6401), 245–249. <https://doi.org/10.1038/360245a0>
- Bonn, W. J., Gingele, F. X., Grobe, H., Mackensen, A., & Fütterer, D. K. (1998). Palaeoproductivity at the Antarctic continental margin: Opal and barium records for the last 400 ka. *Palaeogeography, Palaeoclimatology, Palaeoecology*, 139(3–4), 195–211.  
[https://doi.org/10.1016/S0031-0182\(97\)00144-2](https://doi.org/10.1016/S0031-0182(97)00144-2)
- Brancato, V., Rignot, E., Milillo, P., Morlighem, M., Mouginot, J., An, L., Scheuchl, B., Jeong, S., Rizzoli, P., Bueso Bello, J. L., & Prats-Iraola, P. (2020). Grounding Line Retreat of Denman Glacier, East Antarctica, Measured With COSMO-SkyMed Radar Interferometry Data. *Geophysical Research Letters*, 47(7), e2019GL086291.  
<https://doi.org/10.1029/2019GL086291>
- Budge, J. S., & Long, D. G. (2018). A Comprehensive Database for Antarctic Iceberg Tracking Using Scatterometer Data. *IEEE Journal of Selected Topics in Applied Earth Observations and Remote Sensing*, 11(2), 434–442. <https://doi.org/10.1109/JSTARS.2017.2784186>
- Burton-Johnson, A., Black, M., Peter, T. F., & Kaluza-Gilbert, J. (2016). An automated methodology for differentiating rock from snow, clouds and sea in Antarctica from Landsat 8 imagery: A new rock outcrop map and area estimation for the entire Antarctic continent. *Cryosphere*, 10(4), 1665–1677. <https://doi.org/10.5194/tc-10-1665-2016>
- Butzin, M., Köhler, P., & Lohmann, G. (2017). Marine radiocarbon reservoir age simulations for the past 50,000 years. *Geophysical Research Letters*, 44(16), 8473–8480.  
<https://doi.org/10.1002/2017GL074688>

- Carter, L., McCave, I. N., & Williams, M. J. M. (2008). Chapter 4 Circulation and Water Masses of the Southern Ocean: A Review. *Developments in Earth and Environmental Sciences*, 8, 85–114. [https://doi.org/10.1016/S1571-9197\(08\)00004-9](https://doi.org/10.1016/S1571-9197(08)00004-9)
- Castagno, P., Falco, P., Dinniman, M. S., Spezie, G., & Budillon, G. (2017). Temporal variability of the Circumpolar Deep Water inflow onto the Ross Sea continental shelf. *Journal of Marine Systems*, 166, 37–49. <https://doi.org/10.1016/j.jmarsys.2016.05.006>
- Clark, C., Kirkland, C. L., Spaggiari, C. v., Oorschot, C., Wingate, M. T. D., & Taylor, R. J. (2014). Proterozoic granulite formation driven by mafic magmatism: An example from the Fraser Range Metamorphics, Western Australia. *Precambrian Research*, 240, 1–21. <https://doi.org/10.1016/j.precamres.2013.07.024>
- Clark, D. J., Hensen, B. J., & Kinny, P. D. (2000). Geochronological constraints for a two-stage history of the Albany-Fraser Orogen, Western Australia. *Precambrian Research*, 102(3–4), 155–183. [https://doi.org/10.1016/S0301-9268\(00\)00063-2](https://doi.org/10.1016/S0301-9268(00)00063-2)
- Clark, D. J., Kinny, P. D., Post, N. J., & Hensen, B. J. (1999). Relationships between magmatism, metamorphism and deformation in the Fraser Complex, Western Australia: Constraints from new SHRIMP U-Pb zircon geochronology. *Australian Journal of Earth Sciences*, 46(6), 923–932. <https://doi.org/10.1046/j.1440-0952.1999.00753.x>
- Cook, C. P., Hemming, S. R., van de Flierdt, T., Pierce Davis, E. L., Williams, T., Galindo, A. L., Jiménez-Espejo, F. J., & Escutia, C. (2017). Glacial erosion of East Antarctica in the Pliocene: A comparative study of multiple marine sediment provenance tracers. *Chemical Geology*, 466, 199–218. <https://doi.org/10.1016/j.chemgeo.2017.06.011>
- Cook, C. P., Hill, D. J., van de Flierdt, T., Williams, T., Hemming, S. R., Dolan, A. M., Pierce, E. L., Escutia, C., Harwood, D., Cortese, G., & Gonzales, J. J. (2014). Sea surface temperature control on the distribution of far-traveled Southern Ocean ice-rafted detritus during the Pliocene. *Paleoceanography*, 29(6), 533–548. <https://doi.org/10.1002/2014PA002625>
- Cook, C. P., van de Flierdt, T., Williams, T., Hemming, S. R., Iwai, M., Kobayashi, M., Jimenez-Espejo, F. J., Escutia, C., González, J. J., Khim, B. K., McKay, R. M., Passchier, S., Bohaty, S. M., Riesselman, C. R., Tauxe, L., Sugisaki, S., Galindo, A. L., Patterson, M. O., Sangiorgi, F., ... Yamane, M. (2013). Dynamic behaviour of the East Antarctic ice sheet during Pliocene warmth. *Nature Geoscience*, 6(9), 765–769. <https://doi.org/10.1038/ngeo1889>
- Crosta, X., Crespin, J., Swingedouw, D., Marti, O., Masson-Delmotte, V., Etourneau, J., Goosse, H., Braconnot, P., Yam, R., Brailovski, I., & Shemesh, A. (2018). Ocean as the main driver of

Antarctic ice sheet retreat during the Holocene. *Global and Planetary Change*, 166, 62–74. <https://doi.org/10.1016/j.gloplacha.2018.04.007>

Cunningham, W. L., Leventer, A., Andrews, J. T., Jennings, A. E., & Licht, K. J. (1999). Late Pleistocene-Holocene marine conditions in the Ross Sea, Antarctica: Evidence from the diatom record. *Holocene*, 9(2), 129–139. <https://doi.org/10.1191/095968399675624796>

de Waele, B., & Pisarevsky, S. A. (2008). Geochronology, paleomagnetism and magnetic fabric of metamorphic rocks in the northeast Fraser Belt, Western Australia. *Australian Journal of Earth Sciences*, 55(5), 605–621. <https://doi.org/10.1080/08120090801979112>

Deacon, G. E. R. (1979). The Weddell gyre. *Deep Sea Research Part A, Oceanographic Research Papers*, 26(9), 981–995. [https://doi.org/10.1016/0198-0149\(79\)90044-X](https://doi.org/10.1016/0198-0149(79)90044-X)

DeConto, R. M., & Pollard, D. (2016). Contribution of Antarctica to past and future sea-level rise. *Nature*, 531(7596), 591–597. <https://doi.org/10.1038/nature17145>

DeMaster, D. J., Ragueneau, O., & Nittrouer, C. A. (1996). Preservation efficiencies and accumulation rates for biogenic silica and organic C, N, and P in high-latitude sediments: The Ross Sea. In *Journal of Geophysical Research C: Oceans* (Vol. 101, Issue C8). American Geophysical Union. <https://doi.org/10.1029/96JC01634>

Diekmann, B., & Kuhn, G. (1999). Provenance and dispersal of glacial-marine surface sediments in the Weddell Sea and adjoining areas, Antarctica: Ice-rafting versus current transport. *Marine Geology*, 158(1–4), 209–231. [https://doi.org/10.1016/S0025-3227\(98\)00165-0](https://doi.org/10.1016/S0025-3227(98)00165-0)

Dinniman, M. S., & Klinck, J. M. (2004). A model study of circulation and cross-shelf exchange on the west Antarctic Peninsula continental shelf. *Deep-Sea Research Part II: Topical Studies in Oceanography*, 51(17–19), 2003–2022. <https://doi.org/10.1016/j.dsr2.2004.07.030>

Domack, E. W., Jacobson, E. A., Shipp, S., & Anderson, J. B. (1999). Late Pleistocene-Holocene retreat of the West Antarctic Ice-Sheet system in the Ross Sea: Part 2 - Sedimentologic and stratigraphic signature. *Bulletin of the Geological Society of America*, 111(10), 1517–1536. [https://doi.org/10.1130/0016-7606\(1999\)111<1517:lphrot>2.3.co;2](https://doi.org/10.1130/0016-7606(1999)111<1517:lphrot>2.3.co;2)

Donda, F., Brancolini, G., O'Brien, P. E., De Santis, L., & Escutia, C. (2007). Sedimentary processes in the Wilkes Land margin: A record of the Cenozoic East Antarctic Ice Sheet evolution. *Journal of the Geological Society*, 164(1), 243–256. <https://doi.org/10.1144/0016-76492004-159>

Donda, F., Leitchenkov, G., Brancolini, G., Romeo, R., de Santis, L., Escutia, C., O'brien, P., Armand, L., Caburlotto, A., & Cotterle, D. (2020). The influence of Totten Glacier on the Late

Cenozoic sedimentary record. *Antarctic Science*, 1–13.

<https://doi.org/10.1017/S0954102020000188>

Dupont, T. K., & Alley, R. B. (2005). Assessment of the importance of ice-shelf buttressing to ice-sheet flow. *Geophysical Research Letters*, 32(4), 1–4.

<https://doi.org/10.1029/2004GL022024>

Dutrieux, P., de Rydt, J., Jenkins, A., Holland, P. R., Ha, H. K., Lee, S. H., Steig, E. J., Ding, Q., Abrahamsen, E. P., & Schröder, M. (2014). Strong sensitivity of pine Island ice-shelf melting to climatic variability. *Science*, 343(6167), 174–178. <https://doi.org/10.1126/science.1244341>

Dymond, J., & Collier, R. (1996). Particulate barium fluxes and their relationships to biological productivity. *Deep-Sea Research Part II: Topical Studies in Oceanography*, 43(4–6), 1283–1308. [https://doi.org/10.1016/0967-0645\(96\)00011-2](https://doi.org/10.1016/0967-0645(96)00011-2)

Dymond, J., Suess, E., & Lyle, M. (1992). Barium in Deep-Sea Sediment: A Geochemical Proxy for Paleoproductivity. *Paleoceanography*, 7(2), 163–181. <https://doi.org/10.1029/92PA00181>

Dypvik, H., & Harris, N. B. (2001). Geochemical facies analysis of fine-grained siliciclastics using Th/U, Zr/Rb and (Zr + Rb)/Sr ratios. *Chemical Geology*, 181(1–4), 131–146.

[https://doi.org/10.1016/S0009-2541\(01\)00278-9](https://doi.org/10.1016/S0009-2541(01)00278-9)

Eglinton, T. I., Aluwihare, L. I., Bauer, J. E., Druffel, E. R. M., & McNichol, A. P. (1996). Gas Chromatographic Isolation of Individual Compounds from Complex Matrices for Radiocarbon Dating. *Analytical Chemistry*, 68(5), 904–912. <https://doi.org/10.1021/AC9508513>

Engelkemeir, A. G., Hamill, W. H., Inghram, M. G., & Libby, W. F. (1949). The half-life of radiocarbon (C<sup>14</sup>). *Physical Review*, 75(12), 1825–1833.

<https://doi.org/10.1103/PhysRev.75.1825>

Fahrbach, E., Rohardt, G., Schröder, M., & Strass, V. (1994). Transport and structure of the weddell gyre. *Annales Geophysicae*, 12(9), 840–855. <https://doi.org/10.1007/s00585-994-0840-7>

Favier, L., Durand, G., Cornford, S. L., Gudmundsson, G. H., Gagliardini, O., Gillet-Chaulet, F., Zwinger, T., Payne, A. J., & le Brocq, A. M. (2014). Retreat of Pine Island Glacier controlled by marine ice-sheet instability. *Nature Climate Change*, 4(2), 117–121.

<https://doi.org/10.1038/nclimate2094>

Fernandez, R., Gulick, S., Domack, E., Montelli, A., Leventer, A., Shevenell, A., & Frederick, B. (2018). Past ice stream and ice sheet changes on the continental shelf off the Sabrina

Coast, East Antarctica. *Geomorphology*, 317, 10–22.

<https://doi.org/10.1016/j.geomorph.2018.05.020>

Fitzsimons, I. C. W. (2000). Grenville-age basement provinces in East Antarctica: Evidence for three separate collisional orogens. *Geology*, 28(10), 879–882. [https://doi.org/10.1130/0091-7613\(2000\)28<879:GBPIEA>2.0.CO;2](https://doi.org/10.1130/0091-7613(2000)28<879:GBPIEA>2.0.CO;2)

Foppert, A., Rintoul, S. R., & England, M. H. (2019). Along-Slope Variability of Cross-Slope Eddy Transport in East Antarctica. *Geophysical Research Letters*, 46(14), 8224–8233. <https://doi.org/10.1029/2019GL082999>

Fretwell, P., Pritchard, H. D., Vaughan, D. G., Bamber, J. L., Barrand, N. E., Bell, R., Bianchi, C., Bingham, R. G., Blankenship, D. D., Casassa, G., Catania, G., Callens, D., Conway, H., Cook, A. J., Corr, H. F. J., Damaske, D., Damm, V., Ferraccioli, F., Forsberg, R., ... Zirizzotti, A. (2013). Bedmap2: Improved ice bed, surface and thickness datasets for Antarctica. *Cryosphere*, 7(1), 375–393. <https://doi.org/10.5194/tc-7-375-2013>

Fürst, J. J., Durand, G., Gillet-Chaulet, F., Tavard, L., Rankl, M., Braun, M., & Gagliardini, O. (2016). The safety band of Antarctic ice shelves. *Nature Climate Change*, 6(5), 479–482. <https://doi.org/10.1038/nclimate2912>

Gagliardini, O., Durand, G., Zwinger, T., Hindmarsh, R. C. A., & le Meur, E. (2010). Coupling of ice-shelf melting and buttressing is a key process in ice-sheets dynamics. *Geophysical Research Letters*, 37(14). <https://doi.org/10.1029/2010GL043334>

Gales, J. A., Larter, R. D., Mitchell, N. C., & Dowdeswell, J. A. (2013). Geomorphic signature of Antarctic submarine gullies: Implications for continental slope processes. *Marine Geology*, 337, 112–124. <https://doi.org/10.1016/j.margeo.2013.02.003>

Gardner, A. S., Moholdt, G., Scambos, T., Fahnestock, M., Ligtenberg, S., van den Broeke, M., & Nilsson, J. (2018). Increased West Antarctic and unchanged East Antarctic ice discharge over the last 7 years. *Cryosphere*, 12(2), 521–547. <https://doi.org/10.5194/tc-12-521-2018>

Gerringa, L. J. A., Alderkamp, A. C., Laan, P., Thuróczy, C. E., de Baar, H. J. W., Mills, M. M., van Dijken, G. L., Haren, H. van, & Arrigo, K. R. (2012). Iron from melting glaciers fuels the phytoplankton blooms in Amundsen Sea (Southern Ocean): Iron biogeochemistry. *Deep-Sea Research Part II: Topical Studies in Oceanography*, 71–76, 16–31. <https://doi.org/10.1016/j.dsr2.2012.03.007>

Ghadi, P., Nair, A., Crosta, X., Mohan, R., Manoj, M. C., & Meloth, T. (2020). Antarctic sea-ice and palaeoproductivity variation over the last 156,000 years in the Indian sector of Southern Ocean. *Marine Micropaleontology*, 160. <https://doi.org/10.1016/j.marmicro.2020.101894>

- Gladstone, R. M., Bigg, G. R., & Nicholls, K. W. (2001). Iceberg trajectory modeling and meltwater injection in the Southern Ocean. *Journal of Geophysical Research: Oceans*, 106(C9), 19903–19915. <https://doi.org/10.1029/2000jc000347>
- Godwin, H. (1962). Radiocarbon dating: Fifth International Conference. *Nature*, 195(4845), 943–945. <https://doi.org/10.1038/195943a0>
- Goldberg, D., Holland, D. M., & Schoof, C. (2009). Grounding line movement and ice shelf buttressing in marine ice sheets. *Journal of Geophysical Research: Earth Surface*, 114(4), F04026. <https://doi.org/10.1029/2008JF001227>
- Goldstein, S. L., & Hemming, S. R. (2003). Long-lived Isotopic Tracers in Oceanography, Paleooceanography, and Ice-sheet Dynamics. *Treatise on Geochemistry*, 6–9, 1–37. <https://doi.org/10.1016/B0-08-043751-6/06179-X>
- Golledge, N. R., Kowalewski, D. E., Naish, T. R., Levy, R. H., Fogwill, C. J., & Gasson, E. G. W. (2015). The multi-millennial Antarctic commitment to future sea-level rise. *Nature*, 526(7573), 421–425. <https://doi.org/10.1038/nature15706>
- Gomez, N., Pollard, D., & Holland, D. (2015). Sea-level feedback lowers projections of future Antarctic Ice-Sheet mass loss. *Nature Communications*, 6. <https://doi.org/10.1038/ncomms9798>
- Gordon, A. L. (1971). Oceanography of Antarctic waters. *Amer Geophys Union, Antarctic Res Ser*, 15, 169–203. <https://doi.org/10.1029/ar015p0169>
- Gordon, J. E., & Harkness, D. D. (1992). Magnitude and geographic variation of the radiocarbon content in Antarctic marine life: Implications for reservoir corrections in radiocarbon dating. *Quaternary Science Reviews*, 11(7–8), 697–708. [https://doi.org/10.1016/0277-3791\(92\)90078-M](https://doi.org/10.1016/0277-3791(92)90078-M)
- Greenbaum, J. S., Blankenship, D. D., Young, D. A., Richter, T. G., Roberts, J. L., Aitken, A. R. A., Legresy, B., Schroeder, D. M., Warner, R. C., van Ommen, T. D., & Siegert, M. J. (2015). Ocean access to a cavity beneath Totten Glacier in East Antarctica. *Nature Geoscience*, 8(4), 294–298. <https://doi.org/10.1038/ngeo2388>
- Greene, C. A., Blankenship, D. D., Gwyther, D. E., Silvano, A., & van Wijk, E. (2017). Wind causes Totten Ice Shelf melt and acceleration. *Science Advances*, 3(11). <https://doi.org/10.1126/sciadv.1701681>
- Grosse, A. V., & Libby, W. F. (1947). Cosmic radiocarbon and natural radioactivity of living matter. *Science*, 106(2743), 88–89. <https://doi.org/10.1126/science.106.2743.88>

- Gudmundsson, G. H. (2013). Ice-shelf buttressing and the stability of marine ice sheets. *Cryosphere*, 7(2), 647–655. <https://doi.org/10.5194/tc-7-647-2013>
- Gulick, S. P. S., Shevenell, A. E., Montelli, A., Fernandez, R., Smith, C., Warny, S., Bohaty, S. M., Sjunneskog, C., Leventer, A., Frederick, B., & Blankenship, D. D. (2017). Initiation and long-term instability of the East Antarctic Ice Sheet. *Nature*, 552(7684), 225–229. <https://doi.org/10.1038/nature25026>
- Gwyther, D. E., Galton-Fenzi, B. K., Hunter, J. R., & Roberts, J. L. (2014). Simulated melt rates for the Totten and Dalton ice shelves. *Ocean Science*, 10(3), 267–279. <https://doi.org/10.5194/os-10-267-2014>
- Harley, S. L., Fitzsimons, I. C. W., & Zhao, Y. (2013). Antarctica and supercontinent evolution: Historical perspectives, recent advances and unresolved issues. *Geological Society Special Publication*, 383(1), 1–34. <https://doi.org/10.1144/SP383.9>
- Harris, P. T., O'Brien, P. E., Sedwick, P., & Truswell, E. M. (1996). Late Quaternary history of sedimentation on the Mac. Robertson Shelf, East Antarctica: problems with 14C-dating of marine sediment cores. *Papers and Proceedings - Royal Society of Tasmania*, 130(2), 47–53. <https://doi.org/10.26749/rstpp.130.2.47>
- Heaton, T. J., Köhler, P., Butzin, M., Bard, E., Reimer, R. W., Austin, W. E. N., Bronk Ramsey, C., Grootes, P. M., Hughen, K. A., Kromer, B., Reimer, P. J., Adkins, J., Burke, A., Cook, M. S., Olsen, J., & Skinner, L. C. (2020). Marine20 - The Marine Radiocarbon Age Calibration Curve (0-55,000 cal BP). *Radiocarbon*, 62(4), 779–820. <https://doi.org/10.1017/RDC.2020.68>
- Heinrich, H. (1988). Origin and consequences of cyclic ice rafting in the Northeast Atlantic Ocean during the past 130,000 years. *Quaternary Research*, 29(2), 142–152. [https://doi.org/10.1016/0033-5894\(88\)90057-9](https://doi.org/10.1016/0033-5894(88)90057-9)
- Hemming, S. R. (2004). Heinrich events: Massive late Pleistocene detritus layers of the North Atlantic and their global climate imprint. *Reviews of Geophysics*, 42(1). <https://doi.org/10.1029/2003RG000128>
- Hemming, S. R., Bond, G. C., Broecker, W. S., Sharp, W. D., & Klas-Mendelson, M. (2000). Evidence from 40Ar/39Ar ages of individual hornblende grains for varying Laurentide sources of iceberg discharges 22, 000 to 10, 500 yr B.P. *Quaternary Research*, 54(3), 372–383. <https://doi.org/10.1006/qres.2000.2181>
- Hillenbrand, C. D., Smith, J. A., Kuhn, G., Esper, O., Gersonde, R., Larter, R. D., Maher, B., Moreton, S. G., Shimmiel, T. M., & Korte, M. (2010). Age assignment of a diatomaceous

ooze deposited in the Western Amundsen Sea embayment after the last glacial maximum. *Journal of Quaternary Science*, 25(3), 280–295. <https://doi.org/10.1002/jqs.1308>

Hochmuth, K., Gohl, K., Leitchenkov, G., Sauermilch, I., Whittaker, J. M., Uenzelmann-Neben, G., Davy, B., & de Santis, L. (2020). The Evolving Paleobathymetry of the Circum-Antarctic Southern Ocean Since 34 Ma: A Key to Understanding Past Cryosphere-Ocean Developments. *Geochemistry, Geophysics, Geosystems*, 21(8), e2020GC009122. <https://doi.org/10.1029/2020GC009122>

Holder, L., Duffy, M., Opdyke, B., Leventer, A., Post, A., O'Brien, P., & Armand, L. K. (2020). Controls Since the mid-Pleistocene Transition on Sedimentation and Primary Productivity Downslope of Totten Glacier, East Antarctica. *Paleoceanography and Paleoclimatology*, 35(12). <https://doi.org/10.1029/2020PA003981>

Holland, D. M., Nicholls, K. W., & Basinski, A. (2020). The Southern Ocean and its interaction with the Antarctic Ice Sheet. In *Science* (Vol. 367, Issue 6484, pp. 1326–1330). American Association for the Advancement of Science. <https://doi.org/10.1126/science.aaz5491>

Holland, P. R., Jenkins, A., & Holland, D. M. (2008). The response of Ice shelf basal melting to variations in ocean temperature. *Journal of Climate*, 21(11), 2558–2572. <https://doi.org/10.1175/2007JCLI1909.1>

Holt, J. W., Blankenship, D. D., Morse, D. L., Young, D. A., Peters, M. E., Kempf, S. D., Richter, T. G., Vaughan, D. G., & Corr, H. F. J. (2006). New boundary conditions for the West Antarctic Ice Sheet: Subglacial topography of the Thwaites and Smith glacier catchments. *Geophysical Research Letters*, 33(9). <https://doi.org/10.1029/2005GL025561>

Ivins, E. R., James, T. S., Wahr, J., Ernst, E. J., Landerer, F. W., & Simon, K. M. (2013). Antarctic contribution to sea level rise observed by GRACE with improved GIA correction. *Journal of Geophysical Research: Solid Earth*, 118(6), 3126–3141. <https://doi.org/10.1002/jgrb.50208>

Jacobs, S. S. (1991). On the nature and significance of the Antarctic Slope Front. *Marine Chemistry*, 35(1–4), 9–24. [https://doi.org/10.1016/S0304-4203\(09\)90005-6](https://doi.org/10.1016/S0304-4203(09)90005-6)

Jacobs, S. S., Amos, A. F., & Bruchhausen, P. M. (1970). Ross sea oceanography and antarctic bottom water formation. *Deep-Sea Research and Oceanographic Abstracts*, 17(6), 935–962. [https://doi.org/10.1016/0011-7471\(70\)90046-X](https://doi.org/10.1016/0011-7471(70)90046-X)

Jacobs, S. S., Helmer, H. H., Doake, C. S. M., Jenkins, A., & Frolich, R. M. (1992). Melting of ice shelves and the mass balance of Antarctica. *Journal of Glaciology*, 38(130), 375–387. <https://doi.org/10.3189/s0022143000002252>

- Jacobs, S. S., Jenkins, A., Giulivi, C. F., & Dutrieux, P. (2011). Stronger ocean circulation and increased melting under Pine Island Glacier ice shelf. *Nature Geoscience*, 4(8), 519–523. <https://doi.org/10.1038/ngeo1188>
- Jacobsen, S. B., & Wasserburg, G. J. (1980). Sm-Nd isotopic evolution of chondrites. *Earth and Planetary Science Letters*, 50(1), 139–155. [https://doi.org/10.1016/0012-821X\(80\)90125-9](https://doi.org/10.1016/0012-821X(80)90125-9)
- Jenkins, A. (2010). Observations beneath Pine Island Glacier in West Antarctica and implications for its retreat. *Nat. Geosci.*, 3(7), 468–472. <https://doi.org/10.1038/ngeo890>
- Jenkins, A., & Jacobs, S. (2008). Circulation and melting beneath George VI ice shelf, Antarctica. *Journal of Geophysical Research: Oceans*, 113(4). <https://doi.org/10.1029/2007JC004449>
- Jimenez-Espejo, F. J., Presti, M., Kuhn, G., McKay, R., Crosta, X., Escutia, C., Lucchi, R. G., Tolotti, R., Yoshimura, T., Ortega Huertas, M., Macrì, P., Caburlotto, A., & de Santis, L. (2020). Late Pleistocene oceanographic and depositional variations along the Wilkes Land margin (East Antarctica) reconstructed with geochemical proxies in deep-sea sediments. *Global and Planetary Change*, 184, 103045. <https://doi.org/10.1016/j.gloplacha.2019.103045>
- Jones, J. M., Gille, S. T., Goosse, H., Abram, N. J., Canziani, P. O., Charman, D. J., Clem, K. R., Crosta, X., de Lavergne, C., Eisenman, I., England, M. H., Fogt, R. L., Frankcombe, L. M., Marshall, G. J., Masson-Delmotte, V., Morrison, A. K., Orsi, A. J., Raphael, M. N., Renwick, J. A., ... Vance, T. R. (2016). Assessing recent trends in high-latitude Southern Hemisphere surface climate. In *Nature Climate Change* (Vol. 6, Issue 10, pp. 917–926). Nature Publishing Group. <https://doi.org/10.1038/nclimate3103>
- Jonkers, L., Barker, S., Hall, I. R., & Prins, M. A. (2015). Correcting for the influence of ice-rafted detritus on grain size-based paleocurrent speed estimates. *Paleoceanography*, 30(10), 1347–1357. <https://doi.org/10.1002/2015PA002830>
- Jonkers, L., Moros, M., Prins, M. A., Dokken, T., Dahl, C. A., Dijkstra, N., Perner, K., & Brummer, G. J. A. (2010). A reconstruction of sea surface warming in the northern North Atlantic during MIS 3 ice-rafting events. *Quaternary Science Reviews*, 29(15–16), 1791–1800. <https://doi.org/10.1016/j.quascirev.2010.03.014>
- Joughin, I., & Alley, R. B. (2011). Stability of the West Antarctic ice sheet in a warming world. In *Nature Geoscience* (Vol. 4, Issue 8, pp. 506–513). <https://doi.org/10.1038/ngeo1194>
- Kämpf, J. (2005). Cascading-driven upwelling in submarine canyons at high latitudes. *Journal of Geophysical Research C: Oceans*, 110(2), 1–10. <https://doi.org/10.1029/2004JC002554>

- Kämpf, J. (2007). On the magnitude of upwelling fluxes in shelf-break canyons. *Continental Shelf Research*, 27(17), 2211–2223. <https://doi.org/10.1016/j.csr.2007.05.010>
- Kanfoush, S. L., Hodell, D. A., Charles, C. D., Guilderson, T. P., Graham Mortyn, P., & Ninnemann, U. S. (2000). Millennial-scale instability of the Antarctic Ice Sheet during the last glaciation. *Science*, 288(5472), 1815–1818. <https://doi.org/10.1126/science.288.5472.1815>
- Kehew, A. E., Piotrowski, J. A., & Jørgensen, F. (2012). Tunnel valleys: Concepts and controversies - A review. *Earth-Science Reviews*, 113(1–2), 33–58. <https://doi.org/10.1016/j.earscirev.2012.02.002>
- Kellogg, D. E., & Kellogg, T. B. (1987). Diatoms of the McMurdo ice shelf, Antarctica: Implications for sediment and biotic reworking. *Palaeogeography, Palaeoclimatology, Palaeoecology*, 60(C), 77–96. [https://doi.org/10.1016/0031-0182\(87\)90025-3](https://doi.org/10.1016/0031-0182(87)90025-3)
- Khazendar, A., Schodlok, M. P., Fenty, I., Ligtenberg, S. R. M., Rignot, E., & van den Broeke, M. R. (2013). Observed thinning of Totten Glacier is linked to coastal polynya variability. *Nature Communications*, 4(1), 1–9. <https://doi.org/10.1038/ncomms3857>
- King, M. A., Bingham, R. J., Moore, P., Whitehouse, P. L., Bentley, M. J., & Milne, G. A. (2012). Lower satellite-gravimetry estimates of Antarctic sea-level contribution. *Nature*, 491(7425), 586–589. <https://doi.org/10.1038/nature11621>
- Kirkland, C. L., Smithies, R. H., & Spaggiari, C. v. (2015). Foreign contemporaries - Unravelling disparate isotopic signatures from Mesoproterozoic Central and Western Australia. *Precambrian Research*, 265, 218–231. <https://doi.org/10.1016/j.precamres.2014.12.001>
- Kirkland, C. L., Smithies, R. H., Spaggiari, C. V., Wingate, M. T. D., Quentin de Gromard, R., Clark, C., Gardiner, N. J., & Belousova, E. A. (2017). Proterozoic crustal evolution of the Eucla basement, Australia: Implications for destruction of oceanic crust during emergence of Nuna. *Lithos*, 278–281, 427–444. <https://doi.org/10.1016/j.lithos.2017.01.029>
- Kirkland, C. L., Spaggiari, C. v., Pawley, M. J., Wingate, M. T. D., Smithies, R. H., Howard, H. M., Tyler, I. M., Belousova, E. A., & Poujol, M. (2011). On the edge: U-Pb, Lu-Hf, and Sm-Nd data suggests reworking of the Yilgarn craton margin during formation of the Albany-Fraser Orogen. *Precambrian Research*, 187(3–4), 223–247. <https://doi.org/10.1016/j.precamres.2011.03.002>
- Kohfeld, K. E., & Chase, Z. (2017). Temporal evolution of mechanisms controlling ocean carbon uptake during the last glacial cycle. *Earth and Planetary Science Letters*, 472, 206–215. <https://doi.org/10.1016/j.epsl.2017.05.015>

- Konrad, H., Shepherd, A., Gilbert, L., Hogg, A. E., McMillan, M., Muir, A., & Slater, T. (2018). Net retreat of Antarctic glacier grounding lines. *Nature Geoscience*, *11*(4), 258–262.  
<https://doi.org/10.1038/s41561-018-0082-z>
- Lannuzel, D., Schoemann, V., de Jong, J., Pasquer, B., van der Merwe, P., Masson, F., Tison, J. L., & Bowie, A. (2010). Distribution of dissolved iron in Antarctic sea ice: Spatial, seasonal, and inter-annual variability. *Journal of Geophysical Research: Biogeosciences*, *115*(3).  
<https://doi.org/10.1029/2009JG001031>
- Lannuzel, D., Schoemann, V., de Jong, J., Tison, J. L., & Chou, L. (2007). Distribution and biogeochemical behaviour of iron in the East Antarctic sea ice. *Marine Chemistry*, *106*(1-2 SPEC. ISS.), 18–32. <https://doi.org/10.1016/j.marchem.2006.06.010>
- Leventer, A., Domack, E. W., Ishman, S. E., Brachfeld, S., McClennen, C. E., & Manley, P. (1996). Productivity cycles of 200-300 years in the Antarctic Peninsula region: Understanding linkages among the sun, atmosphere, oceans, sea ice, and biota. *Bulletin of the Geological Society of America*, *108*(12), 1626–1644. [https://doi.org/10.1130/0016-7606\(1996\)108<1626:PCOYIT>2.3.CO;2](https://doi.org/10.1130/0016-7606(1996)108<1626:PCOYIT>2.3.CO;2)
- Levy, R. H., Meyers, S. R., Naish, T. R., Golledge, N. R., McKay, R. M., Crampton, J. S., DeConto, R. M., de Santis, L., Florindo, F., Gasson, E. G. W., Harwood, D. M., Luyendyk, B. P., Powell, R. D., Clowes, C., & Kulhanek, D. K. (2019). Antarctic ice-sheet sensitivity to obliquity forcing enhanced through ocean connections. *Nature Geoscience*, *12*(2), 132–137.  
<https://doi.org/10.1038/s41561-018-0284-4>
- Li, X., Rignot, E., Morlighem, M., Mouginot, J., & Scheuchl, B. (2015). Grounding line retreat of Totten Glacier, East Antarctica, 1996 to 2013. In *Geophysical Research Letters* (Vol. 42, Issue 19, pp. 8049–8056). Blackwell Publishing Ltd. <https://doi.org/10.1002/2015GL065701>
- Li, X., Rignot, E., Mouginot, J., & Scheuchl, B. (2016). Ice flow dynamics and mass loss of Totten Glacier, East Antarctica, from 1989 to 2015. *Geophysical Research Letters*, *43*(12), 6366–6373. <https://doi.org/10.1002/2016GL069173>
- Libby, W. F. (1946). Atmospheric helium three and radiocarbon from cosmic radiation [8]. In *Physical Review* (Vol. 69, Issues 11–12, pp. 671–672). American Physical Society.  
<https://doi.org/10.1103/PhysRev.69.671.2>
- Libby, W. F., Anderson, E. C., & Arnold, J. R. (1949). Age determination by radiocarbon content: World-wide assay of natural radiocarbon. *Science*, *109*(2827), 227–228.  
<https://doi.org/10.1126/science.109.2827.227>

- Licht, K. J., & Hemming, S. R. (2017). Analysis of Antarctic glacial sediment provenance through geochemical and petrologic applications. In *Quaternary Science Reviews* (Vol. 164, pp. 1–24). Elsevier Ltd. <https://doi.org/10.1016/j.quascirev.2017.03.009>
- Licht, K. J., Jennings, A. E., Andrews, J. T., & Williams, K. M. (1996). Chronology of late Wisconsin ice retreat from the western Ross Sea, Antarctica. *Geology*, *24*(3), 223–226. [https://doi.org/10.1130/0091-7613\(1996\)024<0223:COLWIR>2.3.CO;2](https://doi.org/10.1130/0091-7613(1996)024<0223:COLWIR>2.3.CO;2)
- Licht, K. J., & Palmer, E. F. (2013). Erosion and transport by Byrd Glacier, Antarctica during the Last Glacial Maximum. *Quaternary Science Reviews*, *62*, 32–48. <https://doi.org/10.1016/j.quascirev.2012.11.017>
- Liu, Y., Moore, J. C., Cheng, X., Gladstone, R. M., Bassis, J. N., Liu, H., Wen, J., & Hui, F. (2015). Ocean-driven thinning enhances iceberg calving and retreat of Antarctic ice shelves. *Proceedings of the National Academy of Sciences of the United States of America*, *112*(11), 3263–3268. <https://doi.org/10.1073/pnas.1415137112>
- MacAyeal, D. R. (1993). Binge/purge oscillations of the Laurentide Ice Sheet as a cause of the North Atlantic's Heinrich events. *Paleoceanography*, *8*(6), 775–784. <https://doi.org/10.1029/93PA02200>
- Maddison, E. J., Pike, J., Leventer, A., Dunbar, R., Brachfeld, S., Domack, E. W., Manley, P., & McClennen, C. (2006). Post-glacial seasonal diatom record of the Mertz Glacier Polynya, East Antarctica. *Marine Micropaleontology*, *60*(1), 66–88. <https://doi.org/10.1016/j.marmicro.2006.03.001>
- Maritati, A., Halpin, J. A., Whittaker, J. M., & Daczko, N. R. (2019). Fingerprinting Proterozoic Bedrock in Interior Wilkes Land, East Antarctica. *Scientific Reports*, *9*(1), 1–12. <https://doi.org/10.1038/s41598-019-46612-y>
- Marshall, S. J., & Koutnik, M. R. (2006). Ice sheet action versus reaction: Distinguishing between Heinrich events and Dansgaard-Oeschger cycles in the North Atlantic. *Paleoceanography*, *21*(2), 2021. <https://doi.org/10.1029/2005PA001247>
- Martin, J. H., Gordon, R. M., & Fitzwater, S. E. (1990). Iron in Antarctic waters. *Nature*, *345*(6271), 156–158. <https://doi.org/10.1038/345156a0>
- Martín-Español, A., Zammit-Mangion, A., Clarke, P. J., Flament, T., Helm, V., King, M. A., Luthcke, S. B., Petrie, E., Rémy, F., Schön, N., Wouters, B., & Bamber, J. L. (2016). Spatial and temporal Antarctic Ice Sheet mass trends, glacio-isostatic adjustment, and surface processes from a joint inversion of satellite altimeter, gravity, and GPS data. *Journal of*

*Geophysical Research: Earth Surface*, 121(2), 182–200.

<https://doi.org/10.1002/2015JF003550>

Massom, R. A., Harris, P. T., Michael, K. J., & Potter, M. J. (1998). The distribution and formative processes of latent-heat polynyas in East Antarctica. *Annals of Glaciology*, 27, 420–426.

<https://doi.org/10.3189/1998aog27-1-420-426>

Mathiot, P., Goosse, H., Fichet, T., Barnier, B., & Gallée, H. (2011). Modelling the seasonal variability of the Antarctic Slope Current. *Ocean Science*, 7(4), 455–470.

<https://doi.org/10.5194/os-7-455-2011>

Matthews, K. J., Maloney, K. T., Zahirovic, S., Williams, S. E., Seton, M., & Müller, R. D. (2016).

Global plate boundary evolution and kinematics since the late Paleozoic. *Global and Planetary Change*, 146, 226–250. <https://doi.org/10.1016/j.gloplacha.2016.10.002>

McCartney, M. S., & Donohue, K. A. (2007). A deep cyclonic gyre in the Australian-Antarctic Basin. *Progress in Oceanography*, 75(4), 675–750.

<https://doi.org/10.1016/j.pocean.2007.02.008>

McCave, I. N. (2008). Chapter 8 Size Sorting During Transport and Deposition of Fine Sediments. Sortable Silt and Flow Speed. In *Developments in Sedimentology* (Vol. 60, pp. 121–142).

Elsevier. [https://doi.org/10.1016/S0070-4571\(08\)10008-5](https://doi.org/10.1016/S0070-4571(08)10008-5)

McCave, I. N., & Andrews, J. T. (2019). Distinguishing current effects in sediments delivered to the ocean by ice. I. Principles, methods and examples. In *Quaternary Science Reviews* (Vol. 212, pp. 92–107). Elsevier Ltd. <https://doi.org/10.1016/j.quascirev.2019.03.031>

McCave, I. N., & Hall, I. R. (2006). Size sorting in marine muds: Processes, pitfalls, and prospects for paleoflow-speed proxies. *Geochemistry, Geophysics, Geosystems*, 7(10), n/a-n/a.

<https://doi.org/10.1029/2006GC001284>

McCave, I. N., Manighetti, B., & Robinson, S. G. (1995). Sortable silt and fine sediment size/composition slicing: Parameters for palaeocurrent speed and palaeoceanography.

*Paleoceanography*, 10(3), 593–610. <https://doi.org/10.1029/94PA03039>

McCave, I. N., Thornalley, D. J. R., & Hall, I. R. (2017). Relation of sortable silt grain-size to deep-sea current speeds: Calibration of the ‘Mud Current Meter.’ *Deep-Sea Research Part I: Oceanographic Research Papers*, 127, 1–12. <https://doi.org/10.1016/j.dsr.2017.07.003>

McKay, R., Golledge, N. R., Maas, S., Naish, T., Levy, R., Dunbar, G., & Kuhn, G. (2016).

Antarctic marine ice-sheet retreat in the Ross Sea during the early Holocene. *Geology*, 44(1), 7–10. <https://doi.org/10.1130/G37315.1>

- McManus, J., Berelson, W. M., Klinkhammer, G. P., Johnson, K. S., Coale, K. H., Anderson, R. F., Kumar, N., Burdige, D. J., Hammond, D. E., Brumsack, H. J., McCorkle, D. C., & Rushdi, A. (1998). Geochemistry of barium in marine sediments: Implications for its use as a paleoproxy. *Geochimica et Cosmochimica Acta*, *62*(21–22), 3453–3473. [https://doi.org/10.1016/s0016-7037\(98\)00248-8](https://doi.org/10.1016/s0016-7037(98)00248-8)
- Medley, B., Joughin, I., Smith, B. E., Das, S. B., Steig, E. J., Conway, H., Gogineni, S., Lewis, C., Criscitiello, A. S., McConnell, J. R., van den Broeke, M. R., Lenaerts, J. T. M., Bromwich, D. H., Nicolas, J. P., & Leuschen, C. (2014). Constraining the recent mass balance of pine island and thwaites glaciers, west antarctica, with airborne observations of snow accumulation. *Cryosphere*, *8*(4), 1375–1392. <https://doi.org/10.5194/TC-8-1375-2014>
- Mezgec, K., Stenni, B., Crosta, X., Masson-Delmotte, V., Baroni, C., Braida, M., Ciardini, V., Colizza, E., Melis, R., Salvatore, M. C., Severi, M., Scarchilli, C., Traversi, R., Udisti, R., & Frezzotti, M. (2017). Holocene sea ice variability driven by wind and polynya efficiency in the Ross Sea. *Nature Communications*, *8*(1), 1–12. <https://doi.org/10.1038/s41467-017-01455-x>
- Miles, B. W. J., Jordan, J. R., Stokes, C. R., Jamieson, S. S. R., Hilmar Gudmundsson, G., & Jenkins, A. (2021). Recent acceleration of Denman Glacier (1972–2017), East Antarctica, driven by grounding line retreat and changes in ice tongue configuration. *Cryosphere*, *15*(2), 663–676. <https://doi.org/10.5194/tc-15-663-2021>
- Miles, B. W. J., Stokes, C. R., & Jamieson, S. S. R. (2016). Pan-ice-sheet glacier terminus change in East Antarctica reveals sensitivity of Wilkes Land to sea-ice changes. *Science Advances*, *2*(5), e1501350. <https://doi.org/10.1126/sciadv.1501350>
- Moffat, C., Owens, B., & Beardsley, R. C. (2009). On the characteristics of Circumpolar Deep Water intrusions to the west Antarctic Peninsula Continental Shelf. *Journal of Geophysical Research: Oceans*, *114*(5). <https://doi.org/10.1029/2008JC004955>
- Mohajerani, Y., Velicogna, I., & Rignot, E. (2018). Mass Loss of Totten and Moscow University Glaciers, East Antarctica, Using Regionally Optimized GRACE Mascons. *Geophysical Research Letters*, *45*(14), 7010–7018. <https://doi.org/10.1029/2018GL078173>
- Möller, A., Post, N. J., & Hensen, B. J. (2002). Crustal residence history and garnet Sm-Nd ages of high-grade metamorphic rocks from the Windmill Islands area, East Antarctica. *International Journal of Earth Sciences*, *91*(6), 993–1004. <https://doi.org/10.1007/s00531-002-0291-x>
- Moreau, S., Lannuzel, D., Janssens, J., Arroyo, M. C., Corkill, M., Cougnon, E., Genovese, C., Legresy, B., Lenton, A., Puigcorbé, V., Ratnarajah, L., Rintoul, S., Roca-Martí, M.,

- Rosenberg, M., Shadwick, E. H., Silvano, A., Strutton, P. G., & Tilbrook, B. (2019). Sea Ice Meltwater and Circumpolar Deep Water Drive Contrasting Productivity in Three Antarctic Polynyas. *Journal of Geophysical Research: Oceans*, 124(5), 2943–2968. <https://doi.org/10.1029/2019JC015071>
- Morlighem, M., Rignot, E., Binder, T., Blankenship, D., Drews, R., Eagles, G., Eisen, O., Ferraccioli, F., Forsberg, R., Fretwell, P., Goel, V., Greenbaum, J. S., Gudmundsson, H., Guo, J., Helm, V., Hofstede, C., Howat, I., Humbert, A., Jokat, W., ... Young, D. A. (2020). Deep glacial troughs and stabilizing ridges unveiled beneath the margins of the Antarctic ice sheet. *Nature Geoscience*, 13(2), 132–137. <https://doi.org/10.1038/s41561-019-0510-8>
- Morrison, A. K., McC. Hogg, A., England, M. H., & Spence, P. (2020). Warm Circumpolar Deep Water transport toward Antarctica driven by local dense water export in canyons. *Science Advances*, 6(18), eaav2516. <https://doi.org/10.1126/sciadv.aav2516>
- Morrissey, L. J., Payne, J. L., Hand, M., Clark, C., Taylor, R., Kirkland, C. L., & Kylander-Clark, A. (2017). Linking the Windmill Islands, east Antarctica and the Albany–Fraser Orogen: Insights from U–Pb zircon geochronology and Hf isotopes. *Precambrian Research*, 293, 131–149. <https://doi.org/10.1016/j.precamres.2017.03.005>
- Mouginot, J., Rignot, E., & Scheuchl, B. (2014). Sustained increase in ice discharge from the Amundsen Sea Embayment, West Antarctica, from 1973 to 2013. *Geophysical Research Letters*, 41(5), 1576–1584. <https://doi.org/10.1002/2013GL059069>
- Mouginot, J., Scheuchl, B., & Rignot, E. (2017). MEaSUREs Antarctic Boundaries for IPY 2007–2009 from Satellite Radar, Version 2. *NASA National Snow and Ice Data Center Distributed Active Archive Center*. <https://doi.org/https://doi.org/10.5067/AXE4121732AD>
- Myers, J. S. (1993). Precambrian history of the West Australian Craton and adjacent orogens. *Annual Review of Earth & Planetary Sciences*, 21, 453–485. <https://doi.org/10.1146/annurev.ea.21.050193.002321>
- Nakayama, Y., Schröder, M., & Hellmer, H. H. (2013). From circumpolar deep water to the glacial meltwater plume on the eastern Amundsen Shelf. *Deep-Sea Research Part I: Oceanographic Research Papers*, 77, 50–62. <https://doi.org/10.1016/j.dsr.2013.04.001>
- Nelson, D. R., Myers, J. S., & Nutman, A. P. (1995). Chronology and evolution of the middle proterozoic albania-fraser orogen, western australia. *Australian Journal of Earth Sciences*, 42(5), 481–495. <https://doi.org/10.1080/08120099508728218>

- Nitsche, F. O., Porter, D., Williams, G., Cougnon, E. A., Fraser, A. D., Correia, R., & Guerrero, R. (2017). Bathymetric control of warm ocean water access along the East Antarctic Margin. *Geophysical Research Letters*, *44*(17), 8936–8944. <https://doi.org/10.1002/2017GL074433>
- Noble, T. L., Rohling, E. J., Aitken, A. R. A., Bostock, H. C., Chase, Z., Gomez, N., Jong, L. M., King, M. A., Mackintosh, A. N., McCormack, F. S., McKay, R. M., Menviel, L., Phipps, S. J., Weber, M. E., Fogwill, C. J., Gayen, B., Golledge, N. R., Gwyther, D. E., Hogg, A. M. C., ... Williams, T. (2020). The Sensitivity of the Antarctic Ice Sheet to a Changing Climate: Past, Present, and Future. *Reviews of Geophysics*, *58*(4), e2019RG000663. <https://doi.org/10.1029/2019RG000663>
- Nowicki, S., Oceanography, H. S.-, & 2018, undefined. (2014). Projections of future sea level contributions from the Greenland and Antarctic Ice Sheets: Challenges beyond dynamical ice sheet modeling. *JSTOR*, *31*(2), 109–117. <https://doi.org/10.5670/oceanog.2018.216>
- O'Brien, P. E., Post, A. L., Edwards, S., Martin, T., Caburlotto, A., Donda, F., Leitchenkov, G., Romeo, R., Duffy, M., Evangelinos, D., Holder, L., Leventer, A., López-Quirós, A., Opdyke, B. N., & Armand, L. K. (2020). Continental slope and rise geomorphology seaward of the Totten Glacier, East Antarctica (112°E–122°E). *Marine Geology*, *427*, 106221. <https://doi.org/10.1016/j.margeo.2020.106221>
- Orsi, A. H., Whitworth III, T., & Nowlin, W., D. (1995). On the extent and frontal structure of the Antarctic Circumpolar Current. *Deep Sea Res. Pt. I*, *2*(43), 96–97.
- Orsi, A. H., & Wiederwohl, C. L. (2009). A recount of Ross Sea waters. *Deep-Sea Research Part II: Topical Studies in Oceanography*, *56*(13–14), 778–795. <https://doi.org/10.1016/j.dsr2.2008.10.033>
- Paolo, F. S., Fricker, H. A., & Padman, L. (2015). Volume loss from Antarctic ice shelves is accelerating. *Science*, *348*(6232), 327–331. <https://doi.org/10.1126/science.aaa0940>
- Passchier, S., Ciarletta, D. J., Henao, V., & Sekkas, V. (2019). Sedimentary processes and facies on a high-latitude passive continental margin, Wilkes Land, East Antarctica. *Geological Society Special Publication*, *475*(1), 181–201. <https://doi.org/10.1144/SP475.3>
- Patterson, M. O., McKay, R., Naish, T., Escutia, C., Jimenez-Espejo, F. J., Raymo, M. E., Meyers, S. R., Tauxe, L., Brinkhuis, H., Klaus, A., Fehr, A., Bendle, J. A. P., Bijl, P. K., Bohaty, S. M., Carr, S. A., Dunbar, R. B., Flores, J. A., Gonzalez, J. J., Hayden, T. G., ... Yamane, M. (2014). Orbital forcing of the East Antarctic ice sheet during the Pliocene and Early Pleistocene. *Nature Geoscience*, *7*(11), 841–847. <https://doi.org/10.1038/ngeo2273>

- Pattyn, F. (2018). The paradigm shift in Antarctic ice sheet modelling. *Nature Communications* 2018 9:1, 9(1), 1–3. <https://doi.org/10.1038/s41467-018-05003-z>
- Pattyn, F., Favier, L., Sun, S., & Durand, G. (2017). Progress in Numerical Modeling of Antarctic Ice-Sheet Dynamics. *Current Climate Change Reports* 2017 3:3, 3(3), 174–184. <https://doi.org/10.1007/S40641-017-0069-7>
- Paul, D., Been, H. A., Aerts-Bijma, A. T., & Meijer, H. A. J. (2016). Contamination on AMS sample targets by modern carbon is inevitable. *Radiocarbon*, 58(2), 407–418. <https://doi.org/10.1017/RDC.2016.9>
- Payne, A. J., Vieli, A., Shepherd, A. P., Wingham, D. J., & Rignot, E. (2004). Recent dramatic thinning of largest West Antarctic ice stream triggered by oceans. *Geophysical Research Letters*, 31(23), 1–4. <https://doi.org/10.1029/2004GL021284>
- Paytan, A., & Griffith, E. M. (2007). Marine barite: Recorder of variations in ocean export productivity. *Deep-Sea Research Part II: Topical Studies in Oceanography*, 54(5–7), 687–705. <https://doi.org/10.1016/j.dsr2.2007.01.007>
- Peña-Molino, B., McCartney, M. S., & Rintoul, S. R. (2016). Direct observations of the Antarctic Slope Current transport at 113°E. *Journal of Geophysical Research: Oceans*, 121(10), 7390–7407. <https://doi.org/10.1002/2015JC011594>
- Pierce, E. L., Hemming, S. R., Williams, T., van de Flierdt, T., Thomson, S. N., Reiners, P. W., Gehrels, G. E., Brachfeld, S. A., & Goldstein, S. L. (2014). A comparison of detrital U-Pb zircon, <sup>40</sup>Ar/<sup>39</sup>Ar hornblende, <sup>40</sup>Ar/<sup>39</sup>Ar biotite ages in marine sediments off East Antarctica: Implications for the geology of subglacial terrains and provenance studies. In *Earth-Science Reviews* (Vol. 138, pp. 156–178). Elsevier. <https://doi.org/10.1016/j.earscirev.2014.08.010>
- Pierce, E. L., van de Flierdt, T., Williams, T., Hemming, S. R., Cook, C. P., & Passchier, S. (2017). Evidence for a dynamic East Antarctic ice sheet during the mid-Miocene climate transition. *Earth and Planetary Science Letters*, 478, 1–13. <https://doi.org/10.1016/j.epsl.2017.08.011>
- Pierce, E. L., Williams, T., van de Flierdt, T., Hemming, S. R., Goldstein, S. L., & Brachfeld, S. A. (2011). Characterizing the sediment provenance of East Antarctica's weak underbelly: The Aurora and Wilkes sub-glacial basins. *Paleoceanography*, 26(4). <https://doi.org/10.1029/2011PA002127>
- Pollard, R. T., Salter, I., Sanders, R. J., Lucas, M. I., Moore, C. M., Mills, R. A., Statham, P. J., Allen, J. T., Baker, A. R., Bakker, D. C. E., Charette, M. A., Fielding, S., Fones, G. R.,

- French, M., Hickman, A. E., Holland, R. J., Hughes, J. A., Jickells, T. D., Lampitt, R. S., ... Zubkov, M. v. (2009). Southern Ocean deep-water carbon export enhanced by natural iron fertilization. *Nature*, *457*(7229), 577–580. <https://doi.org/10.1038/nature07716>
- Post, A. L., O'Brien, P. E., Edwards, S., Carroll, A. G., Malakoff, K., & Armand, L. K. (2020). Upper slope processes and seafloor ecosystems on the Sabrina continental slope, East Antarctica. *Marine Geology*, *422*, 106091. <https://doi.org/10.1016/j.margeo.2019.106091>
- Pritchard, H. D., Ligtenberg, S. R. M., Fricker, H. A., Vaughan, D. G., van den Broeke, M. R., & Padman, L. (2012). Antarctic ice-sheet loss driven by basal melting of ice shelves. *Nature*, *484*(7395), 502–505. <https://doi.org/10.1038/nature10968>
- Prothro, L. O., Majewski, W., Yokoyama, Y., Simkins, L. M., Anderson, J. B., Yamane, M., Miyairi, Y., & Ohkouchi, N. (2020). Timing and pathways of East Antarctic Ice Sheet retreat. *Quaternary Science Reviews*, *230*. <https://doi.org/10.1016/j.quascirev.2020.106166>
- Prothro, L. O., Simkins, L. M., Majewski, W., & Anderson, J. B. (2018). Glacial retreat patterns and processes determined from integrated sedimentology and geomorphology records. *Marine Geology*, *395*, 104–119. <https://doi.org/10.1016/j.margeo.2017.09.012>
- Ragueneau, O., Tréguer, P., Leynaert, A., Anderson, R. F., Brzezinski, M. A., DeMaster, D. J., Dugdale, R. C., Dymond, J., Fischer, G., François, R., Heinze, C., Maier-Reimer, E., Martin-Jézéquel, V., Nelson, D. M., & Quéguiner, B. (2000). A review of the Si cycle in the modern ocean: Recent progress and missing gaps in the application of biogenic opal as a paleoproductivity proxy. *Global and Planetary Change*, *26*(4), 317–365. [https://doi.org/10.1016/S0921-8181\(00\)00052-7](https://doi.org/10.1016/S0921-8181(00)00052-7)
- Ribeiro, N., Herraiz-Borreguero, L., Rintoul, S. R., McMahon, C. R., Hindell, M., Harcourt, R., & Williams, G. (2021). Warm Modified Circumpolar Deep Water Intrusions Drive Ice Shelf Melt and Inhibit Dense Shelf Water Formation in Vincennes Bay, East Antarctica. *Journal of Geophysical Research: Oceans*, *126*(8), e2020JC016998. <https://doi.org/10.1029/2020jc016998>
- Rignot, E., Jacobs, S., Mouginot, J., & Scheuchl, B. (2013). Ice-shelf melting around antarctica. *Science*, *341*(6143), 266–270. <https://doi.org/10.1126/science.1235798>
- Rignot, E., Mouginot, J., Morlighem, M., Seroussi, H., & Scheuchl, B. (2014). Widespread, rapid grounding line retreat of Pine Island, Thwaites, Smith, and Kohler glaciers, West Antarctica, from 1992 to 2011. *Geophysical Research Letters*, *41*(10), 3502–3509. <https://doi.org/10.1002/2014GL060140>

- Rignot, E., Mouginot, J., Scheuchl, B., van den Broeke, M., van Wessem, M. J., & Morlighem, M. (2019). Four decades of Antarctic ice sheet mass balance from 1979–2017. In *Proceedings of the National Academy of Sciences of the United States of America* (Vol. 116, Issue 4, pp. 1095–1103). National Academy of Sciences. <https://doi.org/10.1073/pnas.1812883116>
- Rignot, E., Velicogna, I., van den Broeke, M. R., Monaghan, A., & Lenaerts, J. (2011). Acceleration of the contribution of the Greenland and Antarctic ice sheets to sea level rise. *Geophysical Research Letters*, 38(5). <https://doi.org/10.1029/2011GL046583>
- R. Rintoul, S., W. Hughes, C., & Olbers, D. (2001). Chapter 4.6 The antarctic circumpolar current system. *International Geophysics*, 77(C), 271–XXXVI. [https://doi.org/10.1016/S0074-6142\(01\)80124-8](https://doi.org/10.1016/S0074-6142(01)80124-8)
- Rintoul, S. R., Silvano, A., Pena-Molino, B., van Wijk, E., Rosenberg, M., Greenbaum, J. S., & Blankenship, D. D. (2016). Ocean heat drives rapid basal melt of the totten ice shelf. *Science Advances*, 2(12). <https://doi.org/10.1126/sciadv.1601610>
- Roberts, J., Galton-Fenzi, B. K., Paolo, F. S., Donnelly, C., Gwyther, D. E., Padman, L., Young, D., Warner, R., Greenbaum, J., Fricker, H. A., Payne, A. J., Cornford, S., Brocq, A. le, van Ommen, T., Blankenship, D., & Siegert, M. J. (2018). Ocean forced variability of Totten Glacier mass loss. In *Geological Society Special Publication* (Vol. 461, Issue 1, pp. 175–186). Geological Society of London. <https://doi.org/10.1144/SP461.6>
- Rosenheim, B. E., Day, M. B., Domack, E., Schrum, H., Benthien, A., & Hayes, J. M. (2008). Antarctic sediment chronology by programmed-temperature pyrolysis: Methodology and data treatment. *Geochemistry, Geophysics, Geosystems*, 9(4). <https://doi.org/10.1029/2007GC001816>
- Roy, M., van de Flierdt, T., Hemming, S. R., & Goldstein, S. L. (2007).  $^{40}\text{Ar}/^{39}\text{Ar}$  ages of hornblende grains and bulk Sm/Nd isotopes of circum-Antarctic glacio-marine sediments: Implications for sediment provenance in the southern ocean. *Chemical Geology*, 244(3–4), 507–519. <https://doi.org/10.1016/j.chemgeo.2007.07.017>
- Scambos, T. A., Bell, R. E., Alley, R. B., Anandakrishnan, S., Bromwich, D. H., Brunt, K., Christianson, K., Creyts, T., Das, S. B., DeConto, R., Dutrieux, P., Fricker, H. A., Holland, D., MacGregor, J., Medley, B., Nicolas, J. P., Pollard, D., Siegfried, M. R., Smith, A. M., ... Yager, P. L. (2017). How much, how fast?: A science review and outlook for research on the instability of Antarctica's Thwaites Glacier in the 21st century. *Global and Planetary Change*, 153, 16–34. <https://doi.org/10.1016/j.gloplacha.2017.04.008>

- Schoof, C. (2007). Ice sheet grounding line dynamics: Steady states, stability, and hysteresis. *Journal of Geophysical Research: Earth Surface*, 112(3), F03S28. <https://doi.org/10.1029/2006JF000664>
- Scott, J. B. T., Gudmundsson, G. H., Smith, A. M., Bingham, R. G., Pritchard, H. D., & Vaughan, D. G. (2009). Increased rate of acceleration on Pine Island Glacier strongly coupled to changes in gravitational driving stress. *Cryosphere*, 3(1), 125–131. <https://doi.org/10.5194/tc-3-125-2009>
- Selley, H. L., Hogg, A. E., Cornford, S., Dutrieux, P., Shepherd, A., Wuite, J., Floricioiu, D., Kusk, A., Nagler, T., Gilbert, L., Slater, T., & Kim, T. W. (2021). Widespread increase in dynamic imbalance in the Getz region of Antarctica from 1994 to 2018. *Nature Communications*, 12(1). <https://doi.org/10.1038/S41467-021-21321-1>
- Seroussi, H., Nakayama, Y., Larour, E., Menemenlis, D., Morlighem, M., Rignot, E., & Khazendar, A. (2017). Continued retreat of Thwaites Glacier, West Antarctica, controlled by bed topography and ocean circulation. *Geophysical Research Letters*, 44(12), 6191–6199. <https://doi.org/10.1002/2017GL072910>
- Shen, Q., Wang, H., Shum, C. K., Jiang, L., Hsu, H. T., & Dong, J. (2018). Recent high-resolution Antarctic ice velocity maps reveal increased mass loss in Wilkes Land, East Antarctica. *Scientific Reports*, 8(1), 1–8. <https://doi.org/10.1038/s41598-018-22765-0>
- Shepherd, A., Gilbert, L., Muir, A. S., Konrad, H., McMillan, M., Slater, T., Briggs, K. H., Sundal, A. v., Hogg, A. E., & Engdahl, M. E. (2019). Trends in Antarctic Ice Sheet Elevation and Mass. *Geophysical Research Letters*, 46(14), 8174–8183. <https://doi.org/10.1029/2019GL082182>
- Shepherd, A., Ivins, E., Rignot, E., Smith, B., van den Broeke, M., Velicogna, I., Whitehouse, P., Briggs, K., Joughin, I., Krinner, G., Nowicki, S., Payne, T., Scambos, T., Schlegel, N., Geruo, A., Agosta, C., Ahlstrøm, A., Babonis, G., Barletta, V., ... Wouters, B. (2018). Mass balance of the Antarctic Ice Sheet from 1992 to 2017. *Nature*, 558(7709), 219–222. <https://doi.org/10.1038/s41586-018-0179-y>
- Shepherd, A., Wingham, D., & Rignot, E. (2004). Warm ocean is eroding West Antarctic Ice Sheet. *Geophysical Research Letters*, 31(23), 1–4. <https://doi.org/10.1029/2004GL021106>
- Sheraton, J. W., Black, L. P., McCulloch, M. T., & Oliver, R. L. (1990). Age and origin of a compositionally varied mafic dyke swarm in the Bunger Hills, East Antarctica. *Chemical Geology*, 85(3–4), 215–246. [https://doi.org/10.1016/0009-2541\(90\)90002-O](https://doi.org/10.1016/0009-2541(90)90002-O)

- Sheraton, J. W., Black, L. P., & Tindle, A. G. (1992). Petrogenesis of plutonic rocks in a Proterozoic granulite-facies terrane - the Bunger Hills, East Antarctica. *Chemical Geology*, 97(3–4), 163–198. [https://doi.org/10.1016/0009-2541\(92\)90075-G](https://doi.org/10.1016/0009-2541(92)90075-G)
- Sheraton, J. W., Tingey, R. J., Oliver, R. L., & Black, L. P. (1995). *Geology of the Bunger Hills-Denman Glacier region, East Antarctica*. Bulletin - Australian Geological Survey Organisation.  
[https://scholar.google.com.au/scholar?hl=en&as\\_sdt=0%2C5&q=Geology+o+f+the+Bunger+Hills-Denma+n+++Glacier+region%2C+Eas+t+Antarctic&btnG=](https://scholar.google.com.au/scholar?hl=en&as_sdt=0%2C5&q=Geology+o+f+the+Bunger+Hills-Denma+n+++Glacier+region%2C+Eas+t+Antarctic&btnG=)
- Silvano, A., Rintoul, S. R., Kushara, K., Peña-Molino, B., van Wijk, E., Gwyther, D. E., & Williams, G. D. (2019). Seasonality of Warm Water Intrusions Onto the Continental Shelf Near the Totten Glacier. *Journal of Geophysical Research: Oceans*, 124(6), 4272–4289. <https://doi.org/10.1029/2018JC014634>
- Silvano, A., Rintoul, S. R., Peña-Molino, B., Hobbs, W. R., van Wijk, E., Aoki, S., Tamura, T., & Williams, G. D. (2018). Freshening by glacial meltwater enhances melting of ice shelves and reduces formation of Antarctic Bottom Water. *Science Advances*, 4(4), eaap9467. <https://doi.org/10.1126/sciadv.aap9467>
- Silvano, A., Rintoul, S. R., Peña-Molino, B., & Williams, G. D. (2017). Distribution of water masses and meltwater on the continental shelf near the Totten and Moscow University ice shelves. *Journal of Geophysical Research: Oceans*, 122(3), 2050–2068. <https://doi.org/10.1002/2016JC012115>
- Skinner, L. C., Fallon, S., Waelbroeck, C., Michel, E., & Barker, S. (2010). Ventilation of the deep southern ocean and deglacial CO<sub>2</sub> rise. *Science*, 328(5982), 1147–1151. <https://doi.org/10.1126/science.1183627>
- Skinner, L. C., Muschitiello, F., & Scrivner, A. E. (2019). Marine Reservoir Age Variability Over the Last Deglaciation: Implications for Marine Carbon Cycling and Prospects for Regional Radiocarbon Calibrations. *Paleoceanography and Paleoclimatology*, 34(11), 1807–1815. <https://doi.org/10.1029/2019PA003667>
- Smith, B., Fricker, H. A., Gardner, A. S., Medley, B., Nilsson, J., Paolo Nicholas Holschuh, F. S., Adusumilli, S., Brunt, K., Csatho, B., Harbeck, K., Markus, T., Neumann, T., Siegfried, M. R., & Jay Zwally, H. (2020). Pervasive ice sheet mass loss reflects competing ocean and atmosphere processes. *Science*, 368(6496), 1239–1242. <https://doi.org/10.1126/science.aaz5845>

- Smith, C., Warny, S., Shevenell, A. E., Gulick, S. P. S., & Leventer, A. (2019). New species from the Sabrina Flora: an early Paleogene pollen and spore assemblage from the Sabrina Coast, East Antarctica. *Palynology*, 43(4), 650–659.  
<https://doi.org/10.1080/01916122.2018.1471422>
- Smith, J. A., Graham, A. G. C., Post, A. L., Hillenbrand, C. D., Bart, P. J., & Powell, R. D. (2019b). The marine geological imprint of Antarctic ice shelves. In *Nature Communications* (Vol. 10, Issue 1, pp. 1–16). Nature Research. <https://doi.org/10.1038/s41467-019-13496-5>
- Spaggiari, C. V., Kirkland, C. L., Smithies, R. H., Wingate, M. T. D., & Belousova, E. A. (2015). Transformation of an Archean craton margin during Proterozoic basin formation and magmatism: The Albany-Fraser Orogen, Western Australia. *Precambrian Research*, 266, 440–466. <https://doi.org/10.1016/j.precamres.2015.05.036>
- Spaggiari, C. v., Smithies, R. H., Kirkland, C. L., Wingate, M. T. D., England, R. N., & Lu, Y. J. (2018). Buried but preserved: The Proterozoic Arubiddy Ophiolite, Madura Province, Western Australia. *Precambrian Research*, 317, 137–158.  
<https://doi.org/10.1016/j.precamres.2018.08.025>
- Steig, E. J., Ding, Q., Battisti, D. S., & Jenkins, A. (2012). Tropical forcing of circumpolar deep water inflow and outlet glacier thinning in the amundsen sea embayment, west antarctica. *Annals of Glaciology*, 53(60), 19–28. <https://doi.org/10.3189/2012AoG60A110>
- Stewart, A. L., & Thompson, A. F. (2015). Eddy-mediated transport of warm Circumpolar Deep Water across the Antarctic Shelf Break. *Geophysical Research Letters*, 42(2), 432–440.  
<https://doi.org/10.1002/2014GL062281>
- Stuiver, M., Pearson, G. W., & Braziunas, T. (1986). Radiocarbon Age Calibration of Marine Samples Back to 9000 Cal Yr BP. *Radiocarbon*, 28(2B), 980–1021.  
<https://doi.org/10.1017/s0033822200060264>
- Stuiver, M., & Polach, H. A. (1977). Reporting of <sup>14</sup>C data. *Radiocarbon*, 19(3), 355–363.  
<https://www.cambridge.org/core/journals/radiocarbon/article/discussion-reporting-of-14c-data/D686D7894B8BAC3212589AFE418E147E>
- Sutterley, T. C., Velicogna, I., Rignot, E., Mouginot, J., Flament, T., van den Broeke, M. R., van Wessem, J. M., & Reijmer, C. H. (2014). Mass loss of the Amundsen Sea Embayment of West Antarctica from four independent techniques. *Geophysical Research Letters*, 41(23), 8421–8428. <https://doi.org/10.1002/2014GL061940>

- Sverdrup, H. U. (1954). The currents off the coast of queen maud land. *Norsk Geografisk Tidsskrift - Norwegian Journal of Geography*, 14(1–4), 239–249.  
<https://doi.org/10.1080/00291955308542731>
- Sweeney, C., Smith, W. O., Hales, B., Bidigare, R. R., Carlson, C. A., Codispoti, L. A., Gordon, L. I., Hansell, D. A., Millero, F. J., Park, M. O., & Takahashi, T. (2000). Nutrient and carbon removal ratios and fluxes in the Ross Sea, Antarctica. *Deep-Sea Research Part II: Topical Studies in Oceanography*, 47(15–16), 3395–3421. [https://doi.org/10.1016/S0967-0645\(00\)00073-4](https://doi.org/10.1016/S0967-0645(00)00073-4)
- Tamura, T., Ohshima, K. I., Fraser, A. D., & Williams, G. D. (2016). Sea ice production variability in Antarctic coastal polynyas. *Journal of Geophysical Research: Oceans*, 121(5), 2967–2979. <https://doi.org/10.1002/2015JC011537>
- Tavares, O. A. P., & Terranova, M. L. (2018). Toward an accurate determination of half-life of 147Sm isotope. *Applied Radiation and Isotopes*, 139, 26–33.  
<https://doi.org/10.1016/j.apradiso.2018.04.001>
- Thoma, M., Jenkins, A., Holland, D., & Jacobs, S. (2008). Modelling Circumpolar Deep Water intrusions on the Amundsen Sea continental shelf, Antarctica. *Geophysical Research Letters*, 35(18), L18602. <https://doi.org/10.1029/2008GL034939>
- Thomas, R., Rignot, E., Casassa, G., Kanagaratnam, P., Acuña, C., Akins, T., Brecher, H., Frederick, E., Gogineni, P., Krabill, W., Manizade, S., Ramamoorthy, H., Rivera, A., Russell, R., Sonntag, J., Swift, R., Yungel, J., & Zwally, J. (2004). Accelerated sea-level rise from west Antarctica. *Science*, 306(5694), 255–258. <https://doi.org/10.1126/science.1099650>
- Thompson, A. F., Speer, K. G., & Schulze Chretien, L. M. (2020). Genesis of the Antarctic Slope Current in West Antarctica. *Geophysical Research Letters*, 47(16).  
<https://doi.org/10.1029/2020GL087802>
- Thompson, A. F., Stewart, A. L., Spence, P., & Heywood, K. J. (2018). The Antarctic Slope Current in a Changing Climate. *Reviews of Geophysics*, 56(4), 741–770.  
<https://doi.org/10.1029/2018RG000624>
- Tinto, K. J., Padman, L., Siddoway, C. S., Springer, S. R., Fricker, H. A., Das, I., Caratori Tontini, F., Porter, D. F., Frearson, N. P., Howard, S. L., Siegfried, M. R., Mosbeux, C., Becker, M. K., Bertinato, C., Boghosian, A., Brady, N., Burton, B. L., Chu, W., Cordero, S. I., ... Bell, R. E. (2019). Ross Ice Shelf response to climate driven by the tectonic imprint on seafloor bathymetry. *Nature Geoscience*, 12(6), 441–449. <https://doi.org/10.1038/s41561-019-0370-2>

- Tooze, S., Halpin, J. A., Noble, T. L., Chase, Z., O'Brien, P. E., & Armand, L. (2020). Scratching the Surface: A Marine Sediment Provenance Record From the Continental Slope of Central Wilkes Land, East Antarctica. *Geochemistry, Geophysics, Geosystems*, 21(11).  
<https://doi.org/10.1029/2020GC009156>
- Tucker, N. M., Payne, J. L., Clark, C., Hand, M., Taylor, R. J. M., Kylander-Clark, A. R. C., & Martin, L. (2017). Proterozoic reworking of Archean (Yilgarn) basement in the Bunger Hills, East Antarctica. *Precambrian Research*, 298, 16–38.  
<https://doi.org/10.1016/j.precamres.2017.05.013>
- Turner, J., Orr, A., Gudmundsson, G. H., Jenkins, A., Bingham, R. G., Hillenbrand, C. D., & Bracegirdle, T. J. (2017). Atmosphere-ocean-ice interactions in the Amundsen Sea Embayment, West Antarctica. In *Reviews of Geophysics* (Vol. 55, Issue 1, pp. 235–276). Blackwell Publishing Ltd. <https://doi.org/10.1002/2016RG000532>
- van de Fliertdt, T., Goldstein, S. L., Hemming, S. R., Roy, M., Frank, M., & Halliday, A. N. (2007). Global neodymium-hafnium isotope systematics - revisited. *Earth and Planetary Science Letters*, 259(3–4), 432–441. <https://doi.org/10.1016/j.epsl.2007.05.003>
- Vancoppenolle, M., Meiners, K. M., Michel, C., Bopp, L., Brabant, F., Carnat, G., Delille, B., Lannuzel, D., Madec, G., Moreau, S., Tison, J. L., & van der Merwe, P. (2013). Role of sea ice in global biogeochemical cycles: Emerging views and challenges. *Quaternary Science Reviews*, 79, 207–230. <https://doi.org/10.1016/j.quascirev.2013.04.011>
- Vaughan, D. G., Corr, H. F. J., Ferraccioli, F., Frearson, N., O'Hare, A., Mach, D., Holt, J. W., Blankenship, D. D., Morse, D. L., & Young, D. A. (2006). New boundary conditions for the West Antarctic ice sheet: Subglacial topography beneath Pine Island Glacier. *Geophysical Research Letters*, 33(9). <https://doi.org/10.1029/2005GL025588>
- Veevers, J. J., Saeed, A., & O'Brien, P. E. (2008). Provenance of the Gamburtsev Subglacial Mountains from U–Pb and Hf analysis of detrital zircons in Cretaceous to Quaternary sediments in Prydz Bay and beneath the Amery Ice Shelf. *Sedimentary Geology*, 211(1–2), 12–32. <https://doi.org/10.1016/J.SEDGEO.2008.08.003>
- Velicogna, I., Sutterley, T. C., & van den Broeke, M. R. (2014). Regional acceleration in ice mass loss from Greenland and Antarctica using GRACE time-variable gravity data. *Geophysical Research Letters*, 41(22), 8130–8137. <https://doi.org/10.1002/2014GL061052>
- Villa, I. M., de Bièvre, P., Holden, N. E., & Renne, P. R. (2015). IUPAC-IUGS recommendation on the half life of <sup>87</sup>Rb. *Geochimica et Cosmochimica Acta*, 164, 382–385.  
<https://doi.org/10.1016/j.gca.2015.05.025>

- Volk, T., & Hoffert, M. I. (1985). Ocean carbon pumps: analysis of relative strengths and efficiencies in ocean-driven atmospheric CO<sub>2</sub> changes. In *The carbon cycle and atmospheric CO* (pp. 99–110). American Geophysical Union; Geophysical Monograph 32. <https://doi.org/10.1029/gm032p0099>
- Waddell, P. J. A., Timms, N. E., Spaggiari, C. v., Kirkland, C. L., & Wingate, M. T. D. (2015). Analysis of the Ragged Basin, Western Australia: Insights into syn-orogenic basin evolution within the Albany-Fraser Orogen. *Precambrian Research*, 261, 166–187. <https://doi.org/10.1016/j.precamres.2015.02.010>
- Wåhlin, A. K., Yuan, X., Björk, G., & Nohr, C. (2010). Inflow of warm Circumpolar Deep Water in the central Amundsen shelf. *Journal of Physical Oceanography*, 40(6), 1427–1434. <https://doi.org/10.1175/2010JPO4431.1>
- Wakatsuchi, M., Ohshima, K. I., Hishida, M., & Naganobu, M. (1994). Observations of a street of cyclonic eddies in the Indian Ocean sector of the Antarctic Divergence. In *Journal of Geophysical Research* (Vol. 99, Issue C10). <https://doi.org/10.1029/94jc01478>
- Walker, D. P., Brandon, M. A., Jenkins, A., Allen, J. T., Dowdeswell, J. A., & Evans, J. (2007). Oceanic heat transport onto the Amundsen Sea shelf through a submarine glacial trough. *Geophysical Research Letters*, 34(2). <https://doi.org/10.1029/2006GL028154>
- Webber, B. G. M., Heywood, K. J., Stevens, D. P., Dutrieux, P., Abrahamson, E. P., Jenkins, A., Jacobs, S. S., Ha, H. K., Lee, S. H., & Kim, T. W. (2017). Mechanisms driving variability in the ocean forcing of Pine Island Glacier. *Nature Communications*, 8(1), 1–8. <https://doi.org/10.1038/ncomms14507>
- Weber, M. E., Clark, P. U., Kuhn, G., Timmermann, A., Spreng, D., Gladstone, R., Zhang, X., Lohmann, G., Menviel, L., Chikamoto, M. O., Friedrich, T., & Ohlwein, C. (2014). Millennial-scale variability in Antarctic ice-sheet discharge during the last deglaciation. *Nature*, 510(7503), 134–138. <https://doi.org/10.1038/nature13397>
- Weertman, J. (1974). Stability of the Junction of an Ice Sheet and an Ice Shelf. *Journal of Glaciology*, 13(67), 3–11. <https://doi.org/10.1017/s0022143000023327>
- Whitworth, T., Orsi, A. H., Kim, S.-J., Nowlin, W. D., & Locarnini, R. A. (1985). Water Masses and Mixing Near the Antarctic Slope Front. *Wiley Online Library*, 1–27. <https://doi.org/10.1029/ar075p0001>
- Williams, G. D., Meijers, A. J. S., Poole, A., Mathiot, P., Tamura, T., & Klocker, A. (2011). Late winter oceanography off the Sabrina and BANZARE coast (117–128°E), East Antarctica.

*Deep-Sea Research Part II: Topical Studies in Oceanography*, 58(9–10), 1194–1210.

<https://doi.org/10.1016/j.dsr2.2010.10.035>

Williams, T., Hemming, S. R., Licht, K., Agrios, L., Brachfeld, S. A., van de Flierdt, T., Hillenbrand, C. D., Ehrmann, W. U., Zhai, X., Cai, Y., Corley, A. D., Kuhn, G., Williams, T., Hemming, S. R., Licht, K., Agrios, L., Brachfeld, S. A., van de Flierdt, T., Hillenbrand, C. D., ... Kuhn, G. (2017). Insights into the Geographic Sequence of Deglaciation in the Weddell Sea Embayment by Provenance of Ice-Rafted Debris. *AGUFM*, 2017, C21E-1168.

<https://ui.adsabs.harvard.edu/abs/2017AGUFM.C21E1168W/abstract>

Williams, T., van de Flierdt, T., Hemming, S. R., Chung, E., Roy, M., & Goldstein, S. L. (2010). Evidence for iceberg armadas from East Antarctica in the Southern Ocean during the late Miocene and early Pliocene. *Earth and Planetary Science Letters*, 290(3–4), 351–361.

<https://doi.org/10.1016/j.epsl.2009.12.031>

Wilson, D. J., Bertram, R. A., Needham, E. F., van de Flierdt, T., Welsh, K. J., McKay, R. M., Mazumder, A., Riesselman, C. R., Jimenez-Espejo, F. J., & Escutia, C. (2018). Ice loss from the East Antarctic Ice Sheet during late Pleistocene interglacials. In *Nature* (Vol. 561, Issue 7723, pp. 383–386). Nature Publishing Group. <https://doi.org/10.1038/s41586-018-0501-8>

Wingate, M. T. D., Kirkland, C. L., Spaggiari, C. V., Smithies, R. H. (2015). U-Pb geochronology of the Madura Province. *Eucla Basement Stratigraphic Drilling Results Release Workshop: Extended Abstracts Compiled by C. V. Spaggiari and R. H. Smithies: Geological Survey of Western Australia Record 2015/10*, 14–16.

Witze, A. (2018). East Antarctica is losing ice faster than anyone thought. *Nature*.

<https://doi.org/10.1038/d41586-018-07714-1>

Wright, A. P., Young, D. A., Roberts, J. L., Schroeder, D. M., Bamber, J. L., Dowdeswell, J. A., Young, N. W., le Brocq, A. M., Warner, R. C., Payne, A. J., Blankenship, D. D., van Ommen, T. D., & Siegert, M. J. (2012). Evidence of a hydrological connection between the ice divide and ice sheet margin in the Aurora Subglacial Basin, East Antarctica. *Journal of Geophysical Research: Earth Surface*, 117(1). <https://doi.org/10.1029/2011JF002066>

Wu, L., Wang, R., Xiao, W., Ge, S., Chen, Z., & Krijgsman, W. (2017). Productivity-climate coupling recorded in Pleistocene sediments off Prydz Bay (East Antarctica).

*Palaeogeography, Palaeoclimatology, Palaeoecology*, 485, 260–270.

<https://doi.org/10.1016/j.palaeo.2017.06.018>

Wu, L., Wang, R., Xiao, W., Krijgsman, W., Li, Q., Ge, S., & Ma, T. (2018). Late Quaternary Deep Stratification-Climate Coupling in the Southern Ocean: Implications for Changes in Abyssal

Carbon Storage. *Geochemistry, Geophysics, Geosystems*, 19(2), 379–395.

<https://doi.org/10.1002/2017GC007250>

Wu, L., Wilson, D. J., Wang, R., Yin, X., Chen, Z., Xiao, W., & Huang, M. (2020). Evaluating Zr/Rb ratio from XRF scanning as an indicator of grain-size variations of glaciomarine sediments in the Southern Ocean. *Geochemistry, Geophysics, Geosystems*.

<https://doi.org/10.1029/2020gc009350>

Young, D. A., Wright, A. P., Roberts, J. L., Warner, R. C., Young, N. W., Greenbaum, J. S., Schroeder, D. M., Holt, J. W., Sugden, D. E., Blankenship, D. D., van Ommen, T. D., & Siegert, M. J. (2011). A dynamic early East Antarctic Ice Sheet suggested by ice-covered fjord landscapes. *Nature*, 474(7349), 72–75. <https://doi.org/10.1038/nature10114>

Yu, H., Rignot, E., Seroussi, H., Morlighem, M., & Choi, Y. (2019). Impact of Iceberg Calving on the Retreat of Thwaites Glacier, West Antarctica Over the Next Century With Different Calving Laws and Ocean Thermal Forcing. *Geophysical Research Letters*, 46(24), 14539–14547. <https://doi.org/10.1029/2019GL084066>

Zhang, S. H., Zhao, Y., Liu, X. C., Liu, Y. S., Hou, K. J., Li, C. F., & Ye, H. (2012). U-Pb geochronology and geochemistry of the bedrocks and moraine sediments from the Windmill Islands: Implications for Proterozoic evolution of East Antarctica. *Precambrian Research*, 206–207, 52–71. <https://doi.org/10.1016/j.precamres.2012.02.019>

Zheng, Y., Anderson, R. F., Froelich, P. N., Beck, W., McNichol, A. P., & Guilderson, T. (2002). Challenges in radiocarbon dating organic carbon in opal-rich marine sediments. *Radiocarbon*, 44(1), 123–136. <https://doi.org/10.1017/S0033822200064729>

Zwally, J. H., Giovinetto, M. B., Beckley, M. A., & Saba, J. L. (2012). Antarctic and Greenland Drainage System. *GSFC Cryospheric Sciences Laboratory*, 1, 2–7. [http://icesat4.gsfc.nasa.gov/cryo\\_data/ant\\_grn\\_drainage\\_systems.php](http://icesat4.gsfc.nasa.gov/cryo_data/ant_grn_drainage_systems.php)

## Chapter 2

# The wrath of thaw! Multi-proxy constraints on the nature and timing of the last deglaciation in central Wilkes Land, East Antarctica

### Abstract

Central Wilkes Land is a largely marine-based sector of the EAIS that is sensitive to ocean-forced retreat in a warming climate and currently losing mass. Despite the potential for central Wilkes Land to contribute significantly to sea level rise, the region is poorly investigated and our understanding of the dynamism of this part of the EAIS is largely informed by geophysical investigations and poorly constrained ice sheet models. In this study, I present four multi-proxy marine sediment core records from the continental rise of the Sabrina Coast. Using new radiocarbon ages, an age model is constructed for each core and coupled with multi-proxy measurements to infer the timing and nature of the last deglaciation in central Wilkes Land. Rapid sedimentation rates (30-300 cm/kyr), abundant coarse debris and peak abundances of extinct diatoms indicate sediment redistributed from the continental shelf in gravity flows during ice sheet advance. Deglaciation initiated sometime between  $22.0 \pm 3.2$  ka and  $19.2 \pm 0.6$  ka and is indicated by a rise in primary productivity (Si/Al and diatom abundance), meltwater production (*Chaetoceros* subg. *Hyalochaete*) and paleocurrent speed (Zr/Rb) in each core. The onset of deglaciation in central Wilkes Land is the earliest constrained in East Antarctica. A peak in IBRD at ~14.7 ka in one of the cores suggests an Antarctic contribution to Meltwater Pulse 1A (~14.6 ka) and the major rise in global mean sea level at ~14 ka. Continued deglaciation is interrupted by the Antarctic Cold Reversal which is represented by a temporary decline in primary productivity in three of the cores between ~15-13 ka. Neoglacial cooling from the mid-Holocene to present is indicated by a decline in primary productivity in all cores from ~6 - 4 ka. This study provides the first physical evidence for the response of this important part of

the ice sheet to major climate reorganisation over the Last Glacial Period-Holocene transition.

## 2.1. Introduction

Marine-based sectors of the Antarctic Ice Sheet are sensitive to ocean-forced retreat in a warming climate and have the potential to raise the GMSL by an estimated ~25 m (Fretwell et al., 2013). A large portion of the EAIS is grounded below sea level and has been losing mass over the last decade (Shen et al., 2018). Central Wilkes Land, East Antarctica, encompasses a large portion of the marine-based sector of the EAIS (Fig. 2.1). Meltwater and ice from the Sabrina and Aurora subglacial basins are largely drained at the Sabrina Coast via the Totten Glacier, which is currently thinning at a rate unrivalled by any other glacier in East Antarctica (Li et al., 2016; Rignot et al., 2019). Extensive sea ice in front of the ice sheet at the Sabrina Coast make marine sediment cores difficult to retrieve, resulting in poor physical investigation of the continental margin of central Wilkes Land.

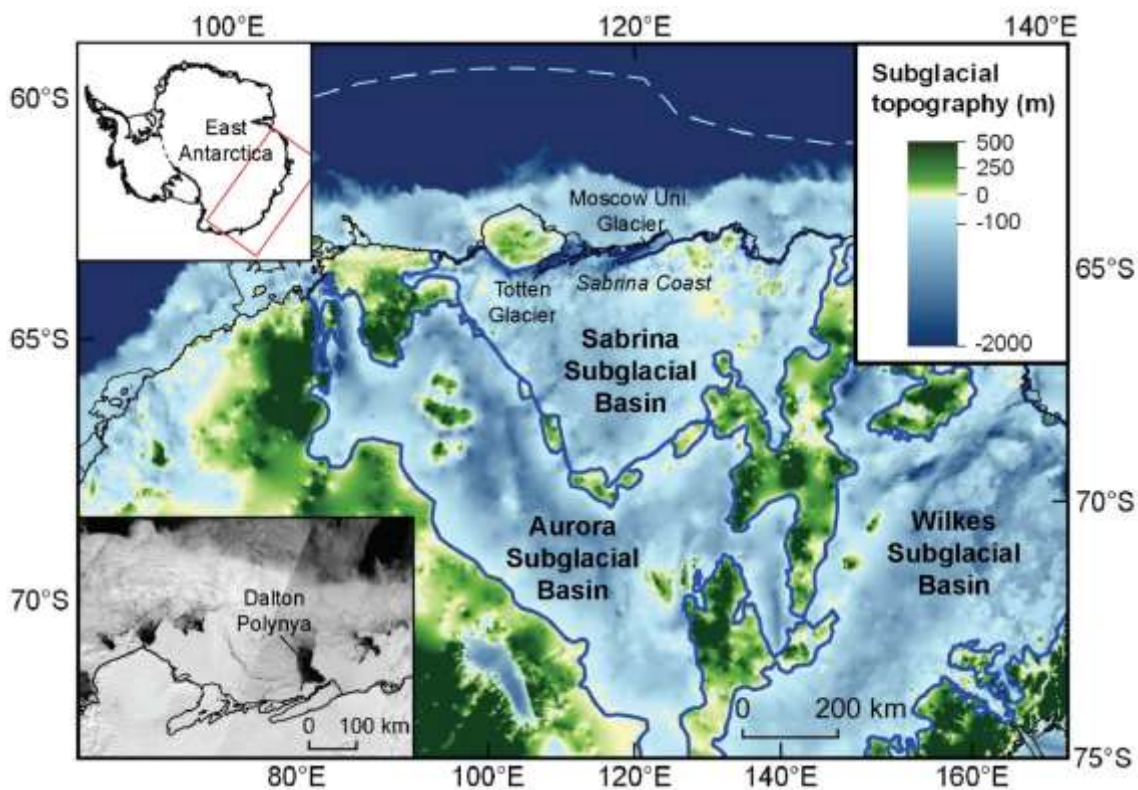


**Figure 2.1.** Central Wilkes Land. Map showing location of central Wilkes Land. Subglacial topography is from BedMachine (version 1.0) (Morlighem et al., 2020). Dark blue lines illustrate the approximate outlines of subglacial basins. Dashed blue line represents the

southern boundary of the east-flowing Antarctic Circumpolar Current. Top left inset shows the location on a map of Antarctica. Bottom left inset shows a NASA satellite image (taken on 25-05-2018) of the sea-ice conditions in central Wilkes Land, highlighting the Dalton Polynya.

Unravelling the response of this dynamic part of the EAIS to past climate change over the Last Glacial Period-Holocene transition (~25 ka - present) is essential for: 1) calculations of glacio-isostatic adjustment and associated sea-level contribution, 2) determining regions susceptible to retreat and/or collapse, and 3) identifying the mechanisms responsible for driving retreat. A better understanding of the ice sheet history in central Wilkes Land will ultimately assist paleoclimate reconstructions and ice sheet models that predict future ice sheet loss from this important region and its potential impact on GMSL rise.

Numerous offshore and terrestrial paleoclimate studies have provided evidence for variation in the timing of the Last Glacial Maximum (Clark et al., 2009) and the onset of deglaciation in East Antarctica (Fig. 2.2; MacKintosh et al., 2011; Mackintosh et al., 2014). The EAIS is therefore thought to have deglaciated asynchronously from the termination of the Last Glacial Period (Fig. 2.2; Bentley et al., 2014; MacKintosh et al., 2011; Mackintosh et al., 2014). An early onset to retreat is interpreted at 21 ka in Dronning Maud Land, whilst other regions, such as George V Land, The Windmill Islands and Lützhof-Holm Bay (Enderby Land) are interpreted to have deglaciated much later, between 11-10 ka (Fig. 2.2). Various timings in between have been constrained for the onset of deglaciation at Mac.Robertson Land, Prydz Bay, the Bunge Hills (Wilkes Land) and in the Ross Sea Embayment (Fig. 2.2; Bentley et al., 2014; Mackintosh et al., 2014; Noble et al., 2020; Prothro et al., 2020, and references therein). Regional variation in the timing of the last deglaciation in East Antarctica is likely associated with regional and temporal differences in the wind regime, oceanography, subglacial geology/topography and proximal seabed bathymetry. To date, there have been no detailed studies focused on the timing and nature of the last deglaciation in central Wilkes Land (yellow box, Fig. 2.2).

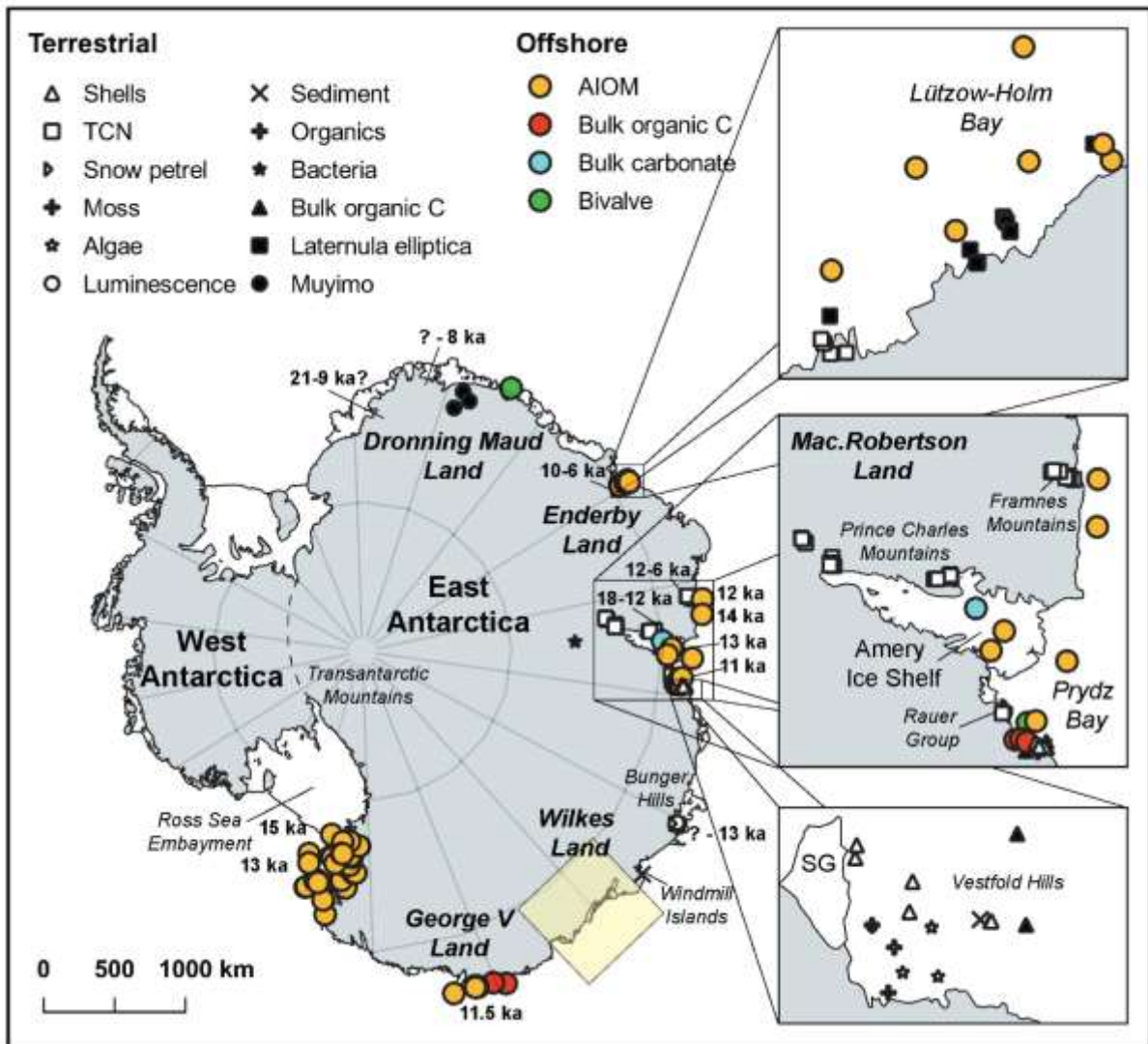


**Figure 2.2. Timing of the onset of deglaciation around the East Antarctic margin.**

Compilation of terrestrial and marine sediment core age data from East Antarctica with approximate timings of the regional onset of deglaciation. Types of material dated are shown as different symbols and colours. TCN – terrestrial cosmogenic nuclides. Yellow box highlights the absence of data from central Wilkes Land. SG - Sørdsdal Glacier. Offshore data are from Gingele et al. (1997) (Dronning Maud Land), Igarashi et al. (2001) (Lützow-Holm Bay), Leventer et al. (2006) and Harris and O'Brien (1998) (Mac.Robertson Land), Domack et al. (1991, 1998), Leventer et al., (2006) and Hemer and Harris, (2003) (Prydz Bay), (Berg et al., 2010a, 2010b) (Rauer Group), Crosta et al. (2007), Harris et al. (2001), Mackintosh et al. (2014) and McMullen et al. (2006) (George V Land) and Prothro et al. (2020) (The Ross Sea). Onshore data are from Miura et al. (1998) (Lützow-Holm Bay), MacKintosh et al. (2011) (Framnes Mountains), Wagner et al. (2004) (Prince Charles Mountains), Hodgson et al. (2001) (Larsemann Hills), Adamson and Pickard, (1983), Coolen et al. (2004), Gibson et al. (2009), Huang et al. (2009), McMinn (2000), Roberts and McMinn (1999), Zhang (1985)

and Zwartz et al. (1998) (Vestfold Hills), Gore et al. (2001) (Bunger Hills), and Goodwin (1993), Kirkup et al. (2002) and Roberts et al. (2006) (Windmill Islands).

Marine sediment from the continental rise archives a continuous record of sedimentation associated with the response of the ocean and ice sheet to a changing climate. These sediments typically comprise a biogenic component, terrigenous detritus and authigenic grains deposited via different processes as the ice sheet expanded and retreated in response to climate fluctuations. In this study, the physical, chemical, and biological composition of four marine sediment cores recovered from across the continental rise of the Sabrina Coast of central Wilkes Land are investigated. Using new radiocarbon ages and multi-proxy data, spatial and temporal changes to the sediment depositional regime on the continental rise over the Last Glacial Period-Holocene transition in response to variation in the climate and ice sheet configuration are characterised.

## **2.2. Methods**

### **2.2.1. Sampling locations**

Kasten cores KC02, KC14, KC04 and KC12 were used for multi-proxy analysis in this study. Multicores MC01 and MC03 were used to obtain core surface ages for the construction of age models (Fig. 2.3).

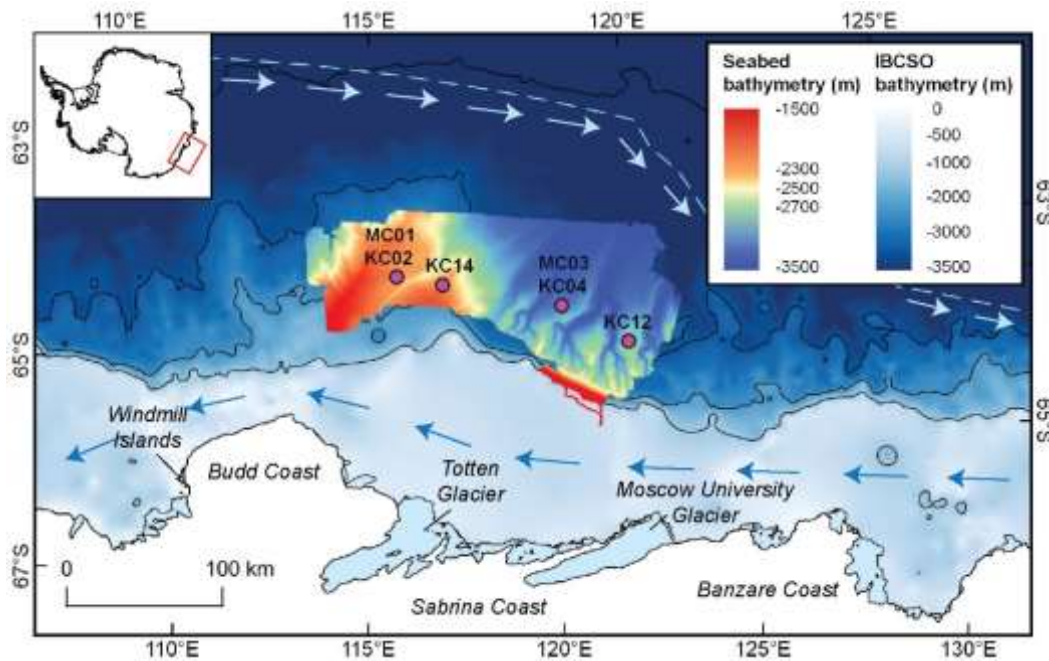


**Figure 2.3. Sample locations.** Map of central Wilkes Land, East Antarctica, with core locations (pink). Offshore bathymetry and 1000 m contours are shown using the International Bathymetric Chart of the Southern Ocean (IBCSO), version 1.0 (Arndt et al., 2013). High resolution bathymetry was acquired from the *RV Investigator* (voyage IN2017\_V01; Armand et al., 2018). The southern boundary of the east-flowing Antarctic Circumpolar Current is shown in light blue (Orsi et al., 1995). The west-flowing Antarctic Coastal Current is represented by darker blue arrows proximal to the coast.

## 2.2.2. Biogenic silica and diatom abundance

The BiSi concentration was measured at 10 cm intervals (minimum) along each core, using a method modified from DeMaster (1981) and Mortlock and Froelich (1989). Ground sediment samples (30 +/- 3 mg) were leached in 30 mL NaCaO<sub>3</sub> solution on a hotblock at 85°C. Every hour, for a total of five hours, a 1 mL aliquot of each sample was taken and centrifuged at 10,000 rpm for 45 seconds to isolate the leached BiSi from the sediment. An aliquot of 200 µL of the leached BiSi from each centrifuged sample was then diluted in 9.8 ml of Milli-Q water and shaken in preparation for immediate analysis on a Quickchem 8500 Series 2 FIA (Method 31-114-27-1-A, Diamond, 2002). Two in-house sediment standards of predetermined BiSi concentration from the Chilean margin (Chile) and the East Antarctic margin

(CMARC) were measured over several months to evaluate long-term reproducibility. The average BiSi concentration was 5.3% for the Chile standard (n = 10) and 12.6% for the CMARC standard (n = 7). The percent standard deviation of ten analyses of Chile over a period of 23 months was 32%. The percent standard deviation of seven analyses of CMARC over a period of six months was 15%. Both in-house standards were measured during the analytical sessions for the KC14 samples. Over the two-day period of sample analysis for KC14, two duplicate analyses of each of the CMARC and Chile standards agreed within 0.1% and 1.4%, respectively (Tooze et al., 2020).

Absolute diatom abundances (per 1 g of sediment) were quantified at the Department of Geology, Colgate University, employing a settling technique described by Warnock and Scherer (2015). In the upper, biosiliceous section of each core, the diatom abundance was calculated from samples at 5-10 cm intervals and in the glacial section at 10 cm intervals. Diatom slides were observed under Olympus CX31, BX60 and Zeiss Primo Star Light microscopes at a total magnification of 1000x. Valves were counted following the protocol of Crosta and Koç (2007) and Warnock and Scherer (2015). Where diatoms were abundant, a minimum of 400 valves were counted. In diatom-poor sediments, a maximum of ten cross-slide transects were counted, as has been done in previous studies (Rebesco et al., 2014a). Counted diatoms were classified to species level.

### **2.2.3. Radiocarbon dating and age model construction**

The AIOM fraction was targeted for radiocarbon dating due to the lack of observable carbonate microfossils. Depth intervals for dating were selected based on peaks and lows in the BiSi concentration. Prior to analysis, all equipment was sterilised in a kiln at 450°C for twelve hours to prevent contamination. The sediment samples (~2-3 g) were oven-dried at 60°C, ground, and leached in 2M HCl on a hotblock at 80°C for several hours to remove any carbonate. The sediment was then rinsed in Milli-Q water to remove residual acid and oven-dried again at 60°C. Radiocarbon analysis

by Accelerator Mass Spectrometry was performed by DirectAMS. All results were corrected for isotopic fractionation.

<sup>14</sup> C age range (kyr)	Regional MRA (yr)	± 1σ error	ΔR (yr)	± 1σ error	Sample ID	Location	Ref.
0 - 12	925	30	518	67	MC03	64.7° S 119.3° E	(Holder et al., 2020)
13 - 14	1278	193	762	204	Drake P Coral	57.75° S 64° W	(Burke and Robinson, 2012)
>14 - 16	925	30	518	67	MC03	64.7° S 119.3° E	(Holder et al., 2020)
18 - 19	2378	236	1631	253	MD7-3076	44.1° S 14.2° W	(Skinner et al., 2010)
>19 - 20	2029	246	1246	263	MD7-3076	44.1° S 14.2° W	(Skinner et al., 2010)
>20 - 21	2093	374	1331	385	MD7-3076	44.1° S 14.2° W	(Skinner et al., 2010)
>21 - 23	1410	363	678	375	TN057-21	41.1° S 7.8° E	(Barker and Diz, 2014)
33 - 34	925	30	518	67	MC03	64.7° S 119.3° E	(Holder et al., 2020)

**Table 2.1. Regional marine reservoir ages.** Table showing the regional MRA used for each radiocarbon age interval based on values from the literature. Full compilation of estimated regional MRAs for the Southern Ocean can be found in Skinner et al. (2019). For radiocarbon age ranges where the estimated regional MRA for the Southern Ocean was close to the modern-day MRA estimated for the study region, the latter was used in the marine reservoir correction. The ΔR value for each radiocarbon age was calculated using the difference between the regional MRA and the global mean MRA provided by Heaton et al. (2020).

The primary radiocarbon ages were first corrected for the LCO using the method outlined by Hillenbrand et al. (2010). The LCO was calculated from the difference between the uncalibrated surface radiocarbon age at each core site and the modern regional MRA. The surface sediment AIOM ages of multicores MC01 and MC03, retrieved from the same core sites as KC02 and KC04, respectively, were used to

represent the surface ages of their respective Kasten cores. The surface ages of KC14 and KC12 were predicted by extrapolating the uppermost uncalibrated radiocarbon ages to depth zero using the BChron package and BChronology function in R (Haslett and Parnell, 2008; Parnell et al., 2008). At MC03, a modern MRA of  $925 \pm 30$  yr was recently estimated from the current atmospheric radiocarbon age of the Southern Hemisphere ( $155 \pm 11$  yr; Hogg et al., 2020, 2019) and the marine radiocarbon age of foraminiferal calcite at the sediment-water interface ( $1080 \pm 28$  yr; Holder et al., 2020). The regional modern MRA estimated by Holder et al. (2020) agrees with former values obtained for the Indian Sector of the Southern Ocean (Paterne et al., 2019) and is similar to the Holocene MRA of the Ross Sea region (Hall et al., 2010).

Once corrected for the LCO, each radiocarbon age was calibrated using the Marine20 calibration curve (Heaton et al., 2020) in MatCal 2.41 (Lougheed and Obrochta, 2016). A  $\Delta R$  of  $518 \pm 67$  yr was applied for Holocene ages, calculated from the difference between the modern regional MRA ( $925 \pm 30$  yr) and the global mean MRA at 0 cal yr BP (Heaton et al., 2020). To account for the temporal variability of  $\Delta R$  values at high latitudes of the Southern Ocean, the  $\Delta R$  estimates provided by Skinner et al. (2019), and references therein, were applied to radiocarbon ages in the corresponding age range (Table 2.1). The modern-day estimated regional MRA for the study region ( $925 \pm 30$  yr) was used when the estimated MRA for the Southern Ocean was similar. Age models were constructed for each of the cores using the default settings of the BChron package and BChronology function in R (Haslett and Parnell, 2008; Parnell et al., 2008) and proxies were plotted against the median ages from the age model for each core.

## **2.2.4. Mass accumulation rates**

The mass accumulation rate (MAR) of IBRD and BiSi was calculated at ~10 cm intervals along each core. To quantify the IBRD MAR, the following protocol was used, as outlined by Kriisek (1995) and Patterson et al. (2014):

$$\mathbf{IBRD\ MAR = CSF \times DBD \times LSR}$$

The coarse sand fraction (CSF) (250  $\mu\text{m}$  – 2 mm) was acquired from each sample by wet-sieving a known weight of bulk sediment. After the removal of authigenic grains and microfossils under a microscope, the remaining material was weighed and calculated as a fraction of the dry bulk sample. Cuvettes with a precise volume of 5.49  $\text{cm}^3$  were used to calculate the dry bulk density (DBD). The linear sedimentation rate (LSR) was calculated between the calibrated radiocarbon ages. The BiSi MAR was calculated in the same way as the IBRD MAR, substituting the CSF with the BiSi mass fraction in each sample:

$$\mathbf{BiSi\ MAR = BiSi \times DBD \times LSR}$$

## **2.2.5. Particle size analysis**

Particle size analysis was conducted on bulk and BiSi-leached sediment samples in each core. Bulk samples were analysed every ~ 5 cm and leached samples every 10 cm. Most of the samples with a BiSi concentration of less than 4% (in the bottom section of each core) were not leached as they were deemed unlikely to significantly impact the mean grain size. Preparation of the leached samples involved first removing the BiSi content by leaching the sediment (weighing 3-5 g) in 1M NaOH solution for twelve hours on a hotblock at 60°C. The samples were then centrifuged at 4,500 rpm for five minutes and the leached BiSi was poured off. The samples were rinsed in Milli-Q water three times to remove any residual solution. The samples were further treated with a 10%  $\text{H}_2\text{O}_2$  solution to remove any organic matter. Particle size analysis was performed by a Malvern Mastersizer 2000 laser particle sizer (Geoscience Australia) using aliquots of the bulk and leached wet sediment samples from the 0-2 mm grain size fraction. Repeat samples were run at 1 m intervals for quality assurance. The mean, median and standard deviation of the grain size distributions were calculated based on the grain size parameters of Folk and Ward (1957). The sortable silt percent (SS%) was calculated from the BiSi-free

grain size fractions as a proxy for paleocurrent speed (McCave et al., 1995, 2017) and is defined as the percent sortable silt (10-63  $\mu\text{m}$ ) within the fine (< 63  $\mu\text{m}$ ) fraction (McCave and Hall, 2006). To eliminate the potential influence of fine IBRD on the SS%, any poorly-sorted samples (i.e., with a sorting factor > 2 based on the classification scheme of Blott and Pye (2001); Table 2.2) were excluded from data interpretation and graphic representation of the SS%.

Core	Depth interval (cm)	Sorting	Depth	
			interval (cm)	Sorting
KC02	0-2	1.56	80-82	2.33
	10-12	1.70	90-92	3.83
	20-22	1.32	100-102	2.18
	30-32	1.42	110-112	1.76
	40-42	1.29	120-122	2.28
	50-52	2.98	130-132	1.54
	60-62	1.16	140-142	43.90
	70-72	1.63	150-152	40.85
	4-5	1.55	83-85	1.51
KC04	13-15	2.31	93-95	15.80
	33-35	1.79	103-105	2.15
	43-45	1.61	114-116	1.48
	53-55	1.67	125-127	27.35
	63-65	1.64	138-140	31.72
	73-75	1.56	148-150	1.49
	0-2	2.09	82-84	1.64
KC12	12-14	1.44	92-94	1.75
	22-24	1.65	102-104	1.57
	32-34	1.37	112-114	1.55
	42-44	1.42	122-124	1.80
	52-54	1.55	132-134	1.64
	62-64	1.41	142-144	1.87
	72-74	1.48	152-154	1.79
	12-14	1.40	120-122	1.25
KC14	24-26	1.56	132-134	1.83
	36-38	1.42	144-146	1.65
	48-50	1.30	156-158	1.31

60-62	1.24	168-170	2.71
72-74	1.29	180-182	1.88
84-86	1.47	192-194	1.65
96-98	1.30	204-206	2.02
108-110	1.34		

**Table 2.2.** Degree of sediment sorting in each core based on the classification scheme of Blott and Pye (2001), modified from Folk and Ward (1957). Samples are those leached of BiSi and used to calculate the mean leached grain size and the SS%. Bright green – very well-sorted (< 1.27), mid green – well-sorted (1.27-1.41), dark green – moderately well-sorted (1.41-1.62), orange – moderately-sorted (1.62-2), light blue – poorly-sorted (2-4), dark blue – extremely poorly-sorted (> 16).

## 2.2.6. X-ray fluorescence and magnetic susceptibility

Scanning x-ray fluorescence (XRF) and magnetic susceptibility measurements were performed simultaneously on 1m u-channel sections of core using a Cox Analytical System ITRAX Core Scanner at the Australian Nuclear Sciences and Technology Organisation, Sydney. XRF measurements were made at 0.5 cm intervals with a Cr-He tube at 30 kV and 55 mA for the semi-quantification of elemental abundances. The magnetic susceptibility was measured at 0.1 cm resolution for use as a preliminary indicator of changes in sediment composition. The primary XRF data was processed by removing any signals with an intensity lower than a threshold of 35,000 kcps. All XRF and magnetic susceptibility data were smoothed in Microsoft Excel using the exponential smoothing function and a damping factor of 0.9. Elemental ratios were used as geochemical proxies for depositional processes and environmental change, for example: Zr/Rb for grain size (Dypvik and Harris, 2001; Fralick and Kronberg, 1997) and paleocurrent speed (Wu et al., 2020) and Si/Al and Ba/Al for primary biological productivity (Bishop, 1988; Chow and Goldberg, 1960; Dehairs et al., 1991; Dymond and Collier, 1996).

## 2.3. Results

### 2.3.1. Core sedimentology

Several distinct lithological units were identified in each core (Fig. 2.4) using shipboard observations (Armand et al., 2018). The downcore sedimentology is relatively similar between all four cores except KC02 which has a less complex composition. In KC14, KC04 and KC12, the uppermost lithology comprises of diatomaceous silty clay (Unit I, Fig. 2.4). Beneath Unit I, a layer of clay-rich diatomaceous ooze (Unit II, Fig. 2.4) is observed, which varies in thickness at each core site. In KC02, the upper 105 cm section of the core consists entirely of Unit II. In KC04 and KC12, Unit II is underlain by a second package of Unit I, and in KC14, first by finer, diatomaceous clay (Unit III, Fig. 2.4), followed by Unit I. Below the diatom-rich units (Units I-III), the sediment becomes gradually more terrigenous in each core with depth.

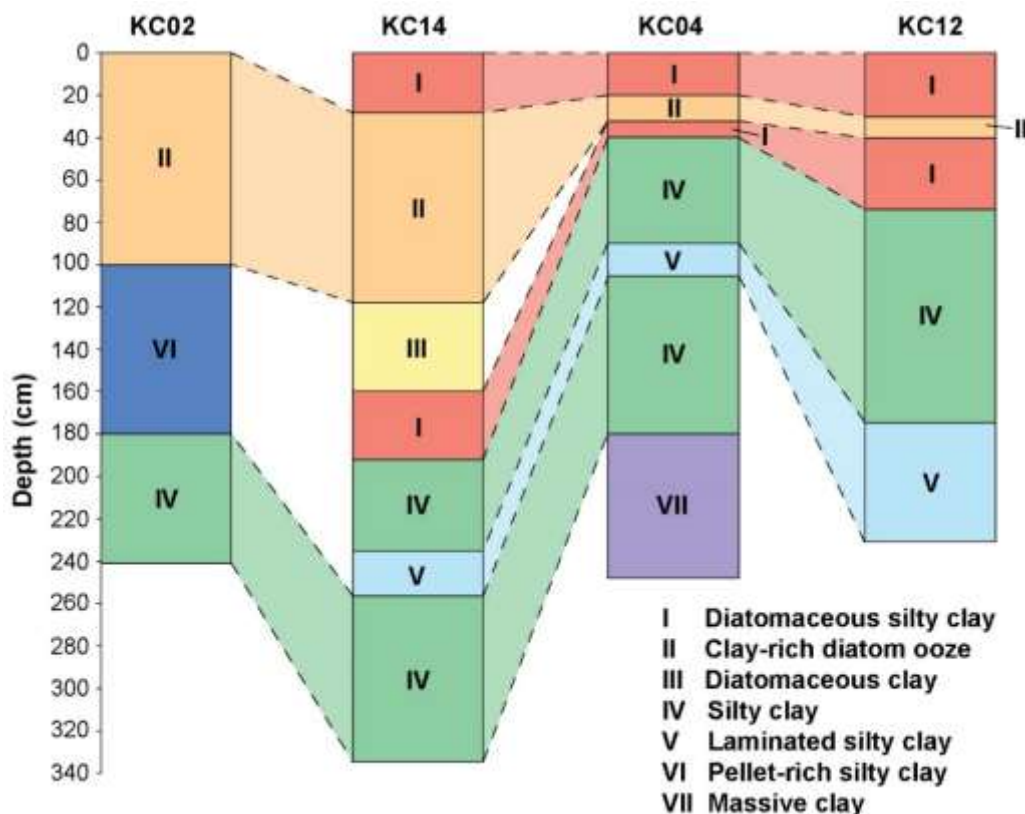


**Figure 2.4. Lithological units.** Diagram presenting the lithological units that comprise the four sediment cores. Interpreted lithostratigraphic correlations are shown as dashed lines.

In KC14, KC04 and KC12, the uppermost terrigenous lithologies comprise of silty clay (Unit IV, Fig. 2.4) underlain by laminated silty clay (Unit V, Fig. 2.4). The alternating light and dark laminae of Unit V are approximately 2 mm thick, and in KC04 are sandwiched between two coarser-grained sandy laminations of the same thickness. In KC12, Unit V comprises a thick ~50 cm section that extends to the bottom of the core. The uppermost terrigenous lithology of KC02 is pellet-rich silty clay (Unit VI, Fig. 2.4). Unit VI has a clotted texture with lumps of aggregated clay and abundant till-like pellets. Beneath Unit VI in KC02, and Unit V in KC14 and KC04, another package of Unit IV is observed which includes dropstones and IBRD. In KC02 and KC14, this unit lies at the bottom of the core, whilst a final package of massive clay with dropstones (Unit VII, Fig. 2.4) characterises the bottommost section of KC04.

The magnetic susceptibility is sensitive to changes in the sediment composition, driven by changes in the relative proportion of clay to BiSi and IBRD. Within the lower glaciogenic section of each of the cores, where there is an abundance of finer clay and silty clay, the average magnetic susceptibility is highest (Fig. 2.5). In this section, the signal is interrupted by IBRD and coarse detrital grains contained within the clay, causing it to vary radically. In the upper section of each core where coarser, silty clay dominates, and there is a higher presence of fine sand, the signal is reduced. Peaks in the magnetic susceptibility in the Holocene are coincident with the presence of diatomaceous sediment (Fig. 2.5).

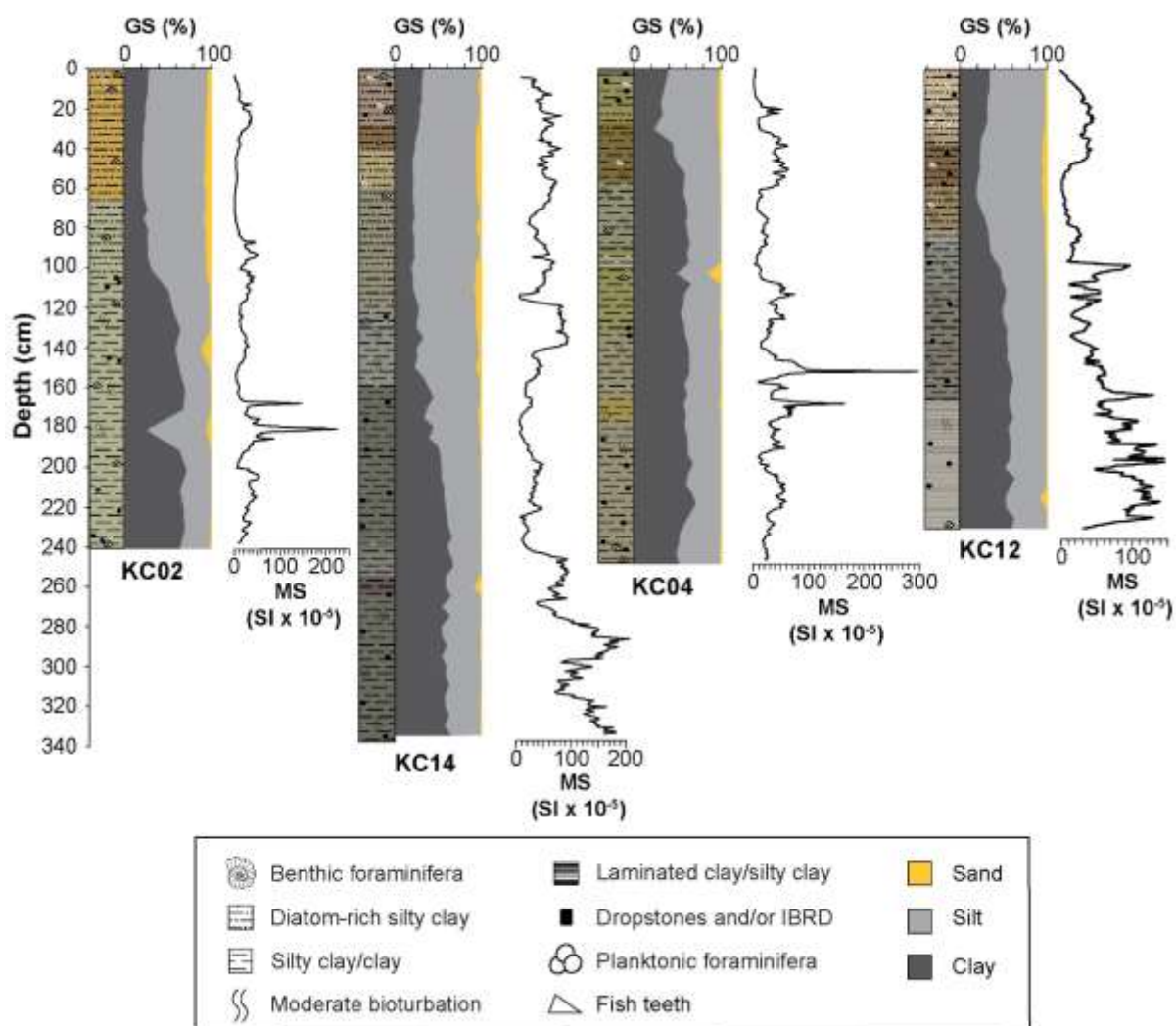


**Figure 2.5.** Sedimentary logs of each of the cores, reconstructed from Armand et al. (2018). Bulk grain size (GS) data from Geoscience Australia were plotted using the grain size parameters of Folk and Ward (1957). Magnetic susceptibility (MS) is shown to the right of each core.

### 2.3.2. Age models

The Kasten cores each capture a record spanning the end of the Last Glacial Period to the Late Holocene. Each record has a continual age progression with depth and no age reversals (Table 2.3; Fig. 2.6). The oldest estimated age is between ~24-22 ka for KC02, KC14 and KC04, and ~44 ka for KC12. Although a much older age is modelled at the bottom of KC12 than in the other cores, there is no evidence in the sedimentology (such as a sharp contact between two lithofacies) to suggest a hiatus

in sediment deposition (Armand et al., 2018; Fig. 2.5). Rather, it seems that either sedimentation rates were much lower at this core site or there was much more relict carbon at the site during the glacial period, causing the apparent age to be considerably older than the true age.

The model-predicted surface age is younger than 500 yr for KC02, KC14, and KC12. An older model-predicted surface AIOM age ( $2203 \pm 310$  cal yr BP) is calculated at KC04, which may be a product of either low Holocene sedimentation at the core site, erosion of the surface sediment, or imperfect retrieval of the surface sediment during core acquisition. Since the associated multicore core, MC03, from the same location, yielded a much younger carbonate-dated surface age ( $52 \pm 11$  cal yr BP; Holder et al., 2020), it is apparent that the older age at the surface of KC04 is not a result of sediment erosion at the core site during the Late Holocene, which would have affected both the Multicore and the Kasten core equally. The physical composition of the core indicates that the surface sediment was not captured during Kasten coring of KC04. For instance, a coarsening upward trend in particle size marks the transition between glacial muds and diatomaceous Holocene sediments, which is much closer to the top of KC04 than in the other cores, leaving a much thinner package of Holocene sediments that cannot be explained by the calculated sedimentation rates.

Core	Depth (cm)	<sup>14</sup> C age (yr BP)	± 1σ error	LCO (yr)	± 1σ error	LCO-corrected <sup>14</sup> C age (yr BP)	± 1σ error	ΔR	± 1σ error	Final age (cal yr BP)	± 2σ error
MC01	0-1	3335	32	2410	44	NA	NA	NA	NA	NA	NA
KC02	2-4	4142	38	2410	44	1732	58	518	67	635	191
KC02	50-52	11117	54	2410	44	8707	69	518	67	8537	395
KC02	112-114	21431	76	2410	44	19021	88	1631	253	20108	676
KC02	236-237	22032	122	2410	44	19622	130	1246	263	21323	747
KC14	0	3947*	15	2647	15	NA	NA	NA	NA	NA	NA
KC14	2-4	4230	33	2647	15	1208	47	518	67	167	167
KC14	96-98	11494	50	2647	15	8472	60	518	67	8426	250
KC14	120-122	13568	57	2647	15	10546	66	518	67	12282	312
KC14	156-158	15250	59	2647	15	12228	68	762	204	14659	670
KC14	204-206	20548	92	2647	15	17526	98	1246	263	21607	698
KC14	336-338	20864	87	2647	15	17842	93	1331	385	22006	949
MC03	0-1	5161	32	4236	44	NA	NA	NA	NA	NA	NA
KC04	4-5	7703	34	4236	44	3467	55	518	67	2535	231
KC04	28-30	10708	52	4236	44	6472	68	518	67	6163	244
KC04	58-60	19054	84	4236	44	14818	95	518	67	16487	373
KC04	238-240	24582	110	4236	44	20346	118	1331	385	22020	965
KC12	0	3224*	27	2300	40	NA	NA	NA	NA	NA	NA
KC12	4-6	4053	36	2300	40	1753	54	518	67	656	189
KC12	68-70	11848	67	2300	40	9548	78	518	67	9589	303
KC12	100-102	21192	88	2300	40	18892	97	1631	253	19943	685
KC12	198-200	36257	249	2300	40	33957	252	518	67	37287	802

**Table 2.3. Radiocarbon age data.** Table showing all primary and calibrated Kasten and Multicore ages. Primary surface ages for KC14 and KC12 are model-predicted (\*) and were extrapolated using the uncalibrated downcore ages and the BChron package and BChronology function in R (Haslett and Parnell, 2008; Parnell et al., 2008). The Local Contamination Offset (LCO) was calculated from the difference between the surface age at each site and a regional MRA of  $925 \pm 30$  yr (Holder et al., 2020). Ages were corrected for the LCO and calibrated in Matlab using the Marine20 calibration curve (Heaton et al., 2020) and the calculated  $\Delta R$  values. Final ages and errors are reported at a 95% confidence limit using the  $2\sigma$  highest posterior density interval.

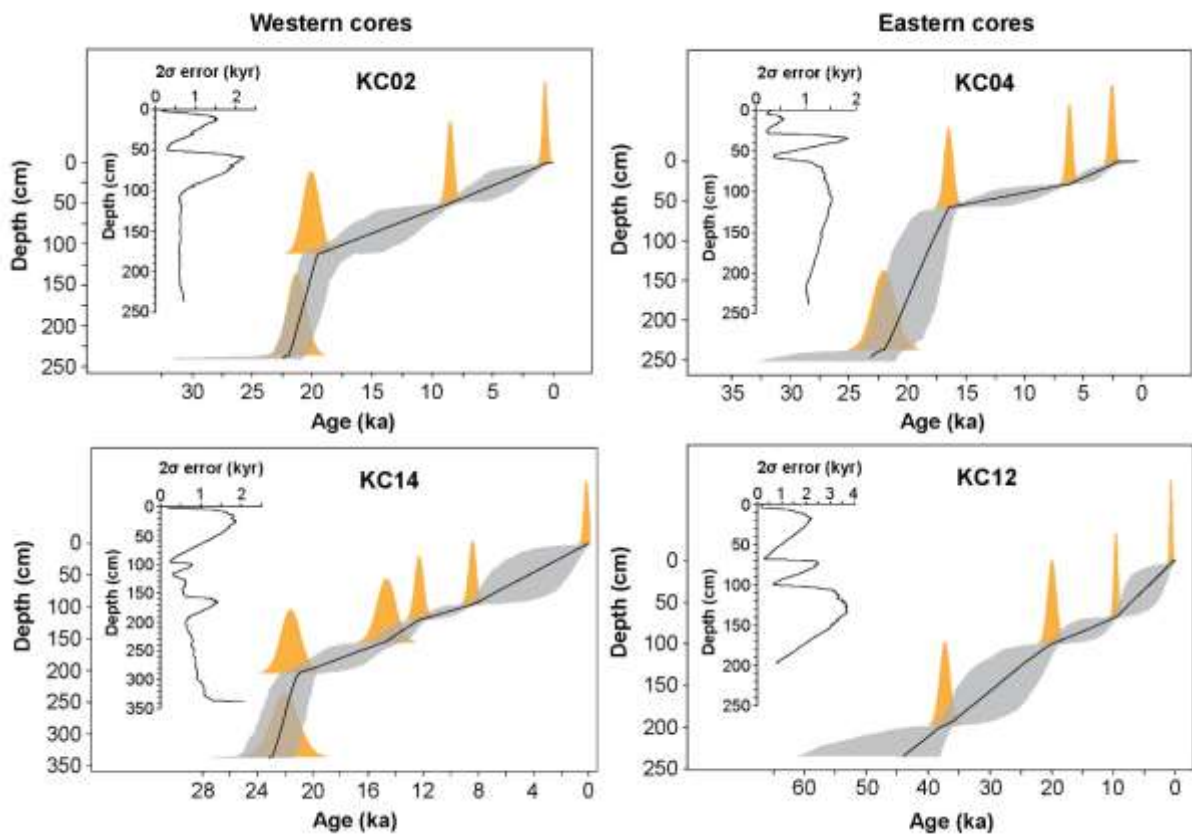


**Figure 2.6. Age models.** Graphs showing the age model for each core. Age distribution curves for each calibrated radiocarbon age are shown in orange, median ages are shown with a black line and the associated  $2\sigma$  model error in grey. Insets show the  $2\sigma$  model age error with depth.

The  $2\sigma$  analytical age error for the final LCO-corrected and calibrated radiocarbon-dated samples increases with depth in each core, with Holocene-aged sediment (~11.7-0 kyr) producing  $2\sigma$  age errors of less than 0.5 kyr, and glacial sediment between 0.5-1 kyr (Table 2.3.; Fig. 2.6). The  $2\sigma$  model age uncertainty increases with distance from each radiocarbon-dated depth interval (Fig. 2.6). For cores KC02, KC04 and KC12, the  $2\sigma$  model age error reaches up to ~2.5 kyr where there is a greater distance (> 1 m) between radiocarbon-dated intervals. In KC12, the greatest  $2\sigma$  model age error between radiocarbon-dated intervals is ~3.7 kyr (between ~123-135 cm depth). The analytical and model age errors are considered when interpreting the timing of important climate events in the discussion.

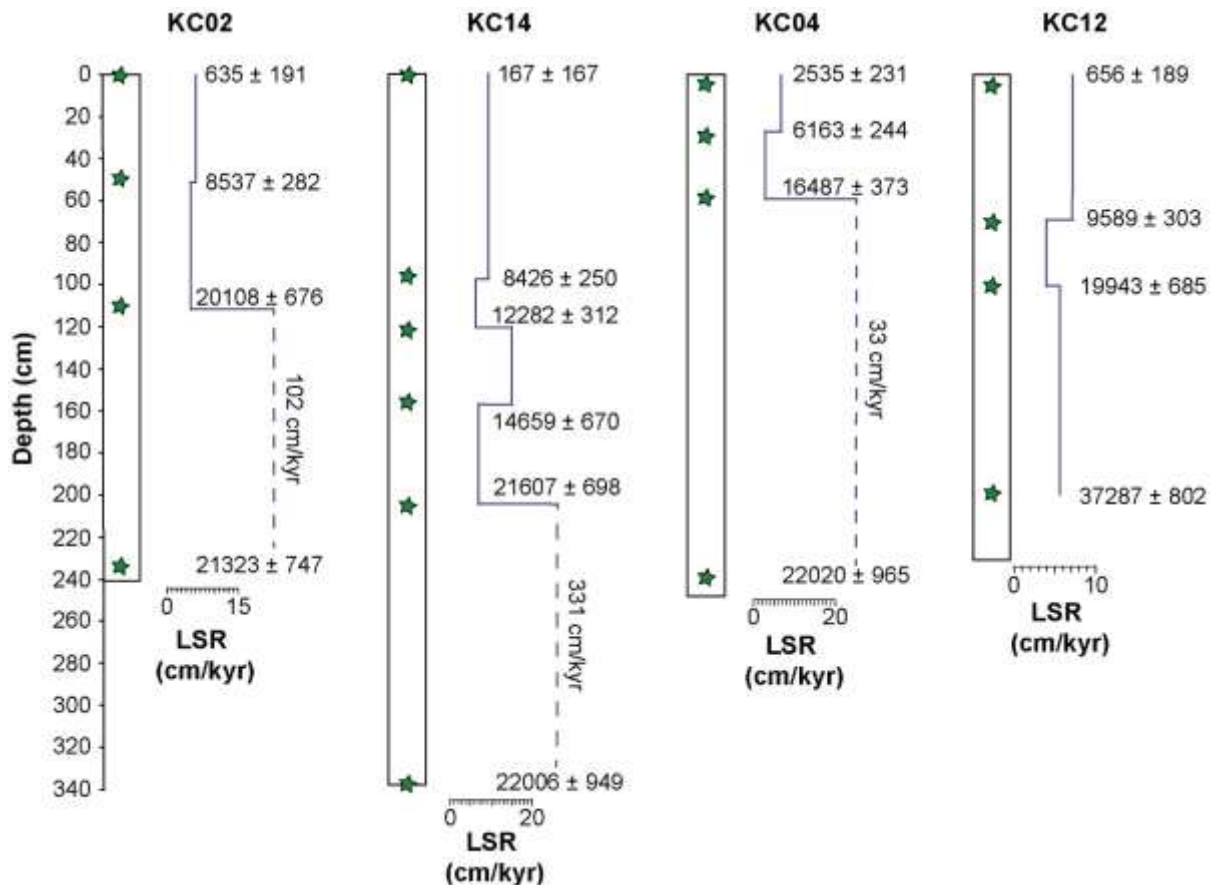


**Figure 2.7. Linear Sedimentation Rates.** Graph showing the LSR and the calibrated radiocarbon ages for each core. Green stars mark where sediment was sampled for AIOM dating.

The LSR was considerably higher in the glacial than in the Holocene at KC02, KC14 and KC04 (Fig. 2.7). The highest glacial LSRs are observed for the cores from the western contourite ridges, where they reached 102 cm/kyr and 331 cm/kyr, at KC02 and KC14, respectively. Lower glacial LSRs are observed in the eastern region, at KC04 (33 cm/kyr) and KC12 (4-7 cm/kyr). At all core sites, the lowest LSR is recorded at the transition between the Last Glacial Period and the Holocene (Fig. 2.7).

### 2.3.3. Paleoproductivity across the deglaciation

Temporal variation in the BiSi concentration, diatom abundance, BiSi MAR, and the Si/Al and Ba/Al ratios was used to assess changes in biological productivity over the continental rise of central Wilkes Land over the Last Glacial Period-Holocene transition. The BiSi concentration in each core increases across the deglaciation with low (< 5%) concentrations in the glacial clays and higher concentrations in the silty Holocene sediments (Fig. 2.8; Supplementary Figs 4.1-4.12). The BiSi first increased between ~21-19 ka at KC02, KC14 and KC12, but later, at ~17 ka at KC04 (Fig. 2.8). A small initial peak is observed between ~17-15 ka at KC02, KC14 and KC12, prior to the main peak during the early Holocene (between 10-7 ka), where the BiSi concentration reaches between 43-53% (Fig. 2.8). In KC04, the peak in BiSi concentration occurs in the Late Holocene (~ 4.1 ka) and is considerably lower (15%) than peak concentrations at the other core sites (Fig. 2.8). During the Late Holocene (from ~4 ka), the BiSi concentrations decrease by 26-37% in KC02, KC14 and KC12, but only by 5% in KC04 (Fig. 2.8).

In all the cores except KC04, there is a strong positive correlation ( $R^2 = 0.67-0.85$ ) between Si/Al and BiSi concentration (Fig. 2.9), demonstrating the value of this ratio as a preliminary measure of biological productivity. In KC02, KC14 and KC12, lower Si/Al ratios (< 20) are associated with reduced BiSi concentrations (< 5%), and the highest Si/Al ratios (between 33-44) coincide with the main peaks in BiSi concentration (Fig. 2.8). In KC04, the correlation between the Si/Al ratio and BiSi concentration is moderate ( $R^2 = 0.39$ , Fig. 2.9), but this may be due to lower overall BiSi concentrations and/or a lower sampling resolution (Fig. 2.8). The Ba/Al ratios also correlate with BiSi concentration and diatom abundance in each core with higher ratios (5 - 10.8) correlating with peak measurements in BiSi and diatom abundance and lower ratios (1.9 – 4.8) where BiSi is scarce (Fig. 2.8).

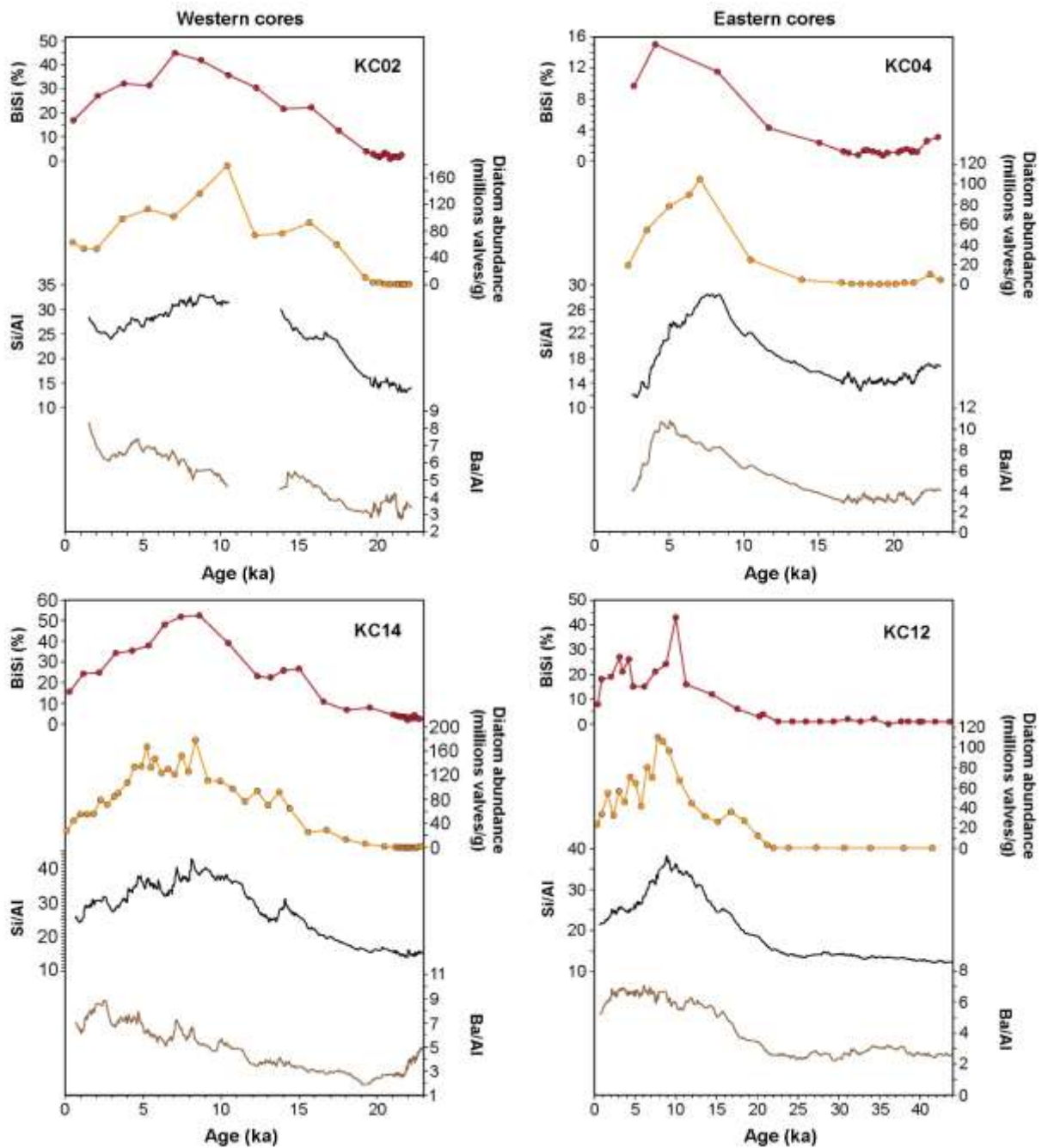


**Figure 2.8. Proxies for biological productivity.** Graphs showing the BiSi concentration, diatom abundance and Si/Al and Ba/Al XRF ratios in each core as proxies for biological productivity. Each proxy is plotted against age using the age model described in the methods.

Temporal variation in the absolute diatom abundance closely correlates with the BiSi concentration in each core during the Last Glacial Period, with low diatom

abundances ( $< 5 \times 10^6$  valves/g of sediment) concurrent with low BiSi concentrations ( $< 5\%$ ) (Fig. 2.8). During the Holocene, the positive correlation between diatom abundance and BiSi concentration continues in KC02, KC14 and KC12. Here, the diatom abundances were highest between 11-7 ka, which is similar to the peak in BiSi concentration in these cores. At KC04, the main peak in BiSi occurs later (at  $\sim 3$  ka) than the peak in diatom abundance ( $\sim 105 \times 10^6$  valves/g of sediment;  $\sim 7$  ka, Fig. 2.8), which is likely due to a lower Holocene sampling resolution for the BiSi concentration compared to the diatom analyses. The cores in the western region of the continental rise (KC02 and KC14) have higher average diatom abundances ( $\sim 180 \times 10^6$  valves/g of sediment) in the Holocene than the cores to the east (KC04 and KC12;  $\sim 110 \times 10^6$  valves/g of sediment) (Fig. 2.8).

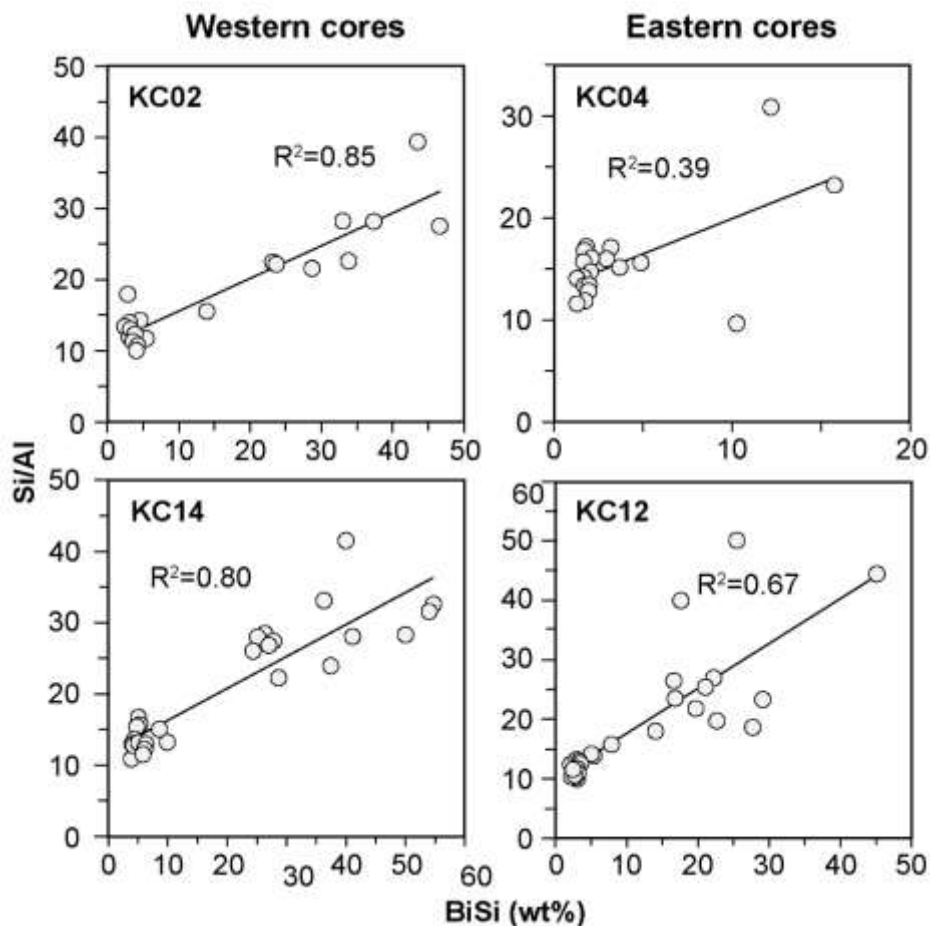


**Figure 2.9.** Crossplots showing the correlation between BiSi concentration and the Si/Al XRF ratio in each of the cores.

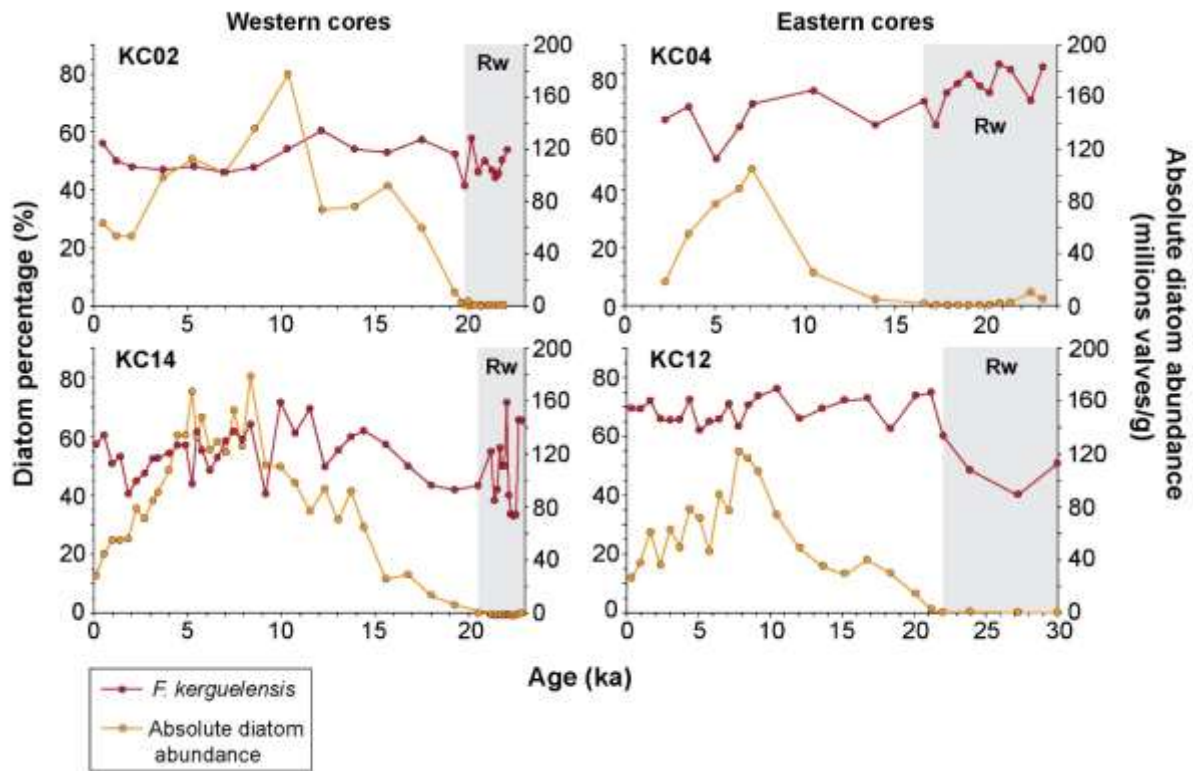


**Figure 2.10. Permanently Open Ocean Zone.** Graphs showing the temporal variation in absolute diatom abundance at each core site (orange) and the percent proportion (of the total diatom abundance) of diatom species *Fragilariopsis kerguelensis*, (red), an indicator of open surface waters. Grey panels indicate a period of continental shelf sediment reworking (Rw) during ice sheet advance.

The Permanently Open Ocean Zone (POOZ) species *Fragilariopsis kerguelensis* is the most common diatom species in each core, making up between 33-83% of the total diatom abundance at any given depth (Supplementary Figs 4.9-4.12). This species is more prevalent in the silty Holocene sediments than the glacial clay sediments, except in KC04 where it is more abundant in the glacial sediments (Fig. 2.10). The transition from lower to higher abundances of *Fragilariopsis kerguelensis* occurs between ~ 22-19 ka at KC02, KC14 and KC12. The diatom species *Chaetoceros* subg. *Hyalochaete* are associated with spring blooms and are most prevalent where the water column is stratified due to enhanced meltwater input (Crosta et al., 1997). In all the cores except KC12, there is a sharp increase in the percent proportion of *Chaetoceros* subg. *Hyalochaete* in sediments immediately

overlying the glacial clays. In the western cores, KC02 and KC14, the percent proportion of *Chaetoceros* subg. *Hyalochaete* increases sharply between ~21-20 ka and peaks at ~19 ka (13 %) and ~18 ka (29 %), respectively (Fig. 2.11). In KC04, the *Chaetoceros* subg. *Hyalochaete* percent increases at ~17 ka (Fig. 2.11). In KC12, the *Chaetoceros* subg. *Hyalochaete* constitutes less than 5% of the total diatom abundance throughout the core and does not vary significantly on temporal scales (Fig. 2.11).

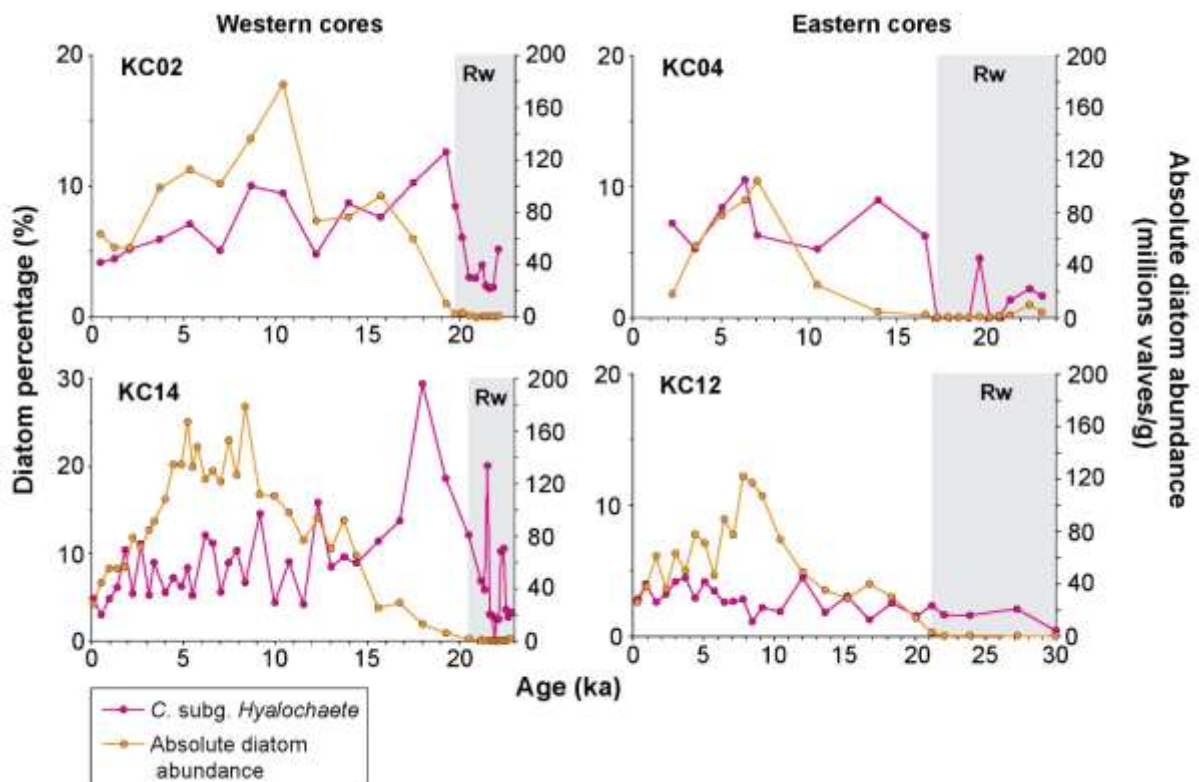


**Figure 2.11. Meltwater production.** Graphs showing the temporal variation in absolute diatom abundance at each core site (orange) and the percent proportion (of the total diatom abundance) of diatom species *Chaetoceros* subg. *Hyalochaete* (pink), an indicator of spring blooms associated with deglaciation and meltwater input. Grey panels indicate the period of continental shelf sediment reworking (Rw) during ice sheet advance.

The glacial clay in each core contains much higher percentages of extinct (*Actinocyclus ingens*, *Denticulopsis* spp., *Hemidiscus karstenii*, *Pyxilla reticulata*, *Rouxia* spp. and *Stephanopyxis* spp.) and robust (*Rhizosolenia* spp.) diatoms (i.e., with strong siliceous frustules) than the siltier Holocene sediments (Fig. 2.12;

Supplementary Figs 4.9-4.12). In the glacial sediments, the total diatom abundance at KC02, KC14 and KC12 comprises between 3-35% extinct diatoms (average: 11 - 17%) and between 2-22% robust diatoms (average: 11 - 12%) (Fig. 2.12). At KC04, the glacial sediment contains between 1-16% extinct diatoms (average: 5%) and between 1 - 13% robust diatoms (average: 4%) (Fig. 2.12). In the deglacial-Holocene sediments of each core (from between ~22 - 19 ka in KC02, KC14 and KC14 and from ~ 17 ka at KC04), the total diatom abundance contains  $\leq 4\%$  of both extinct and robust diatoms (Fig. 2.12). In KC02, KC14 and KC04, there is a positive correlation between the extinct and robust diatom percentages and the IBRD MAR (Fig. 2.12).

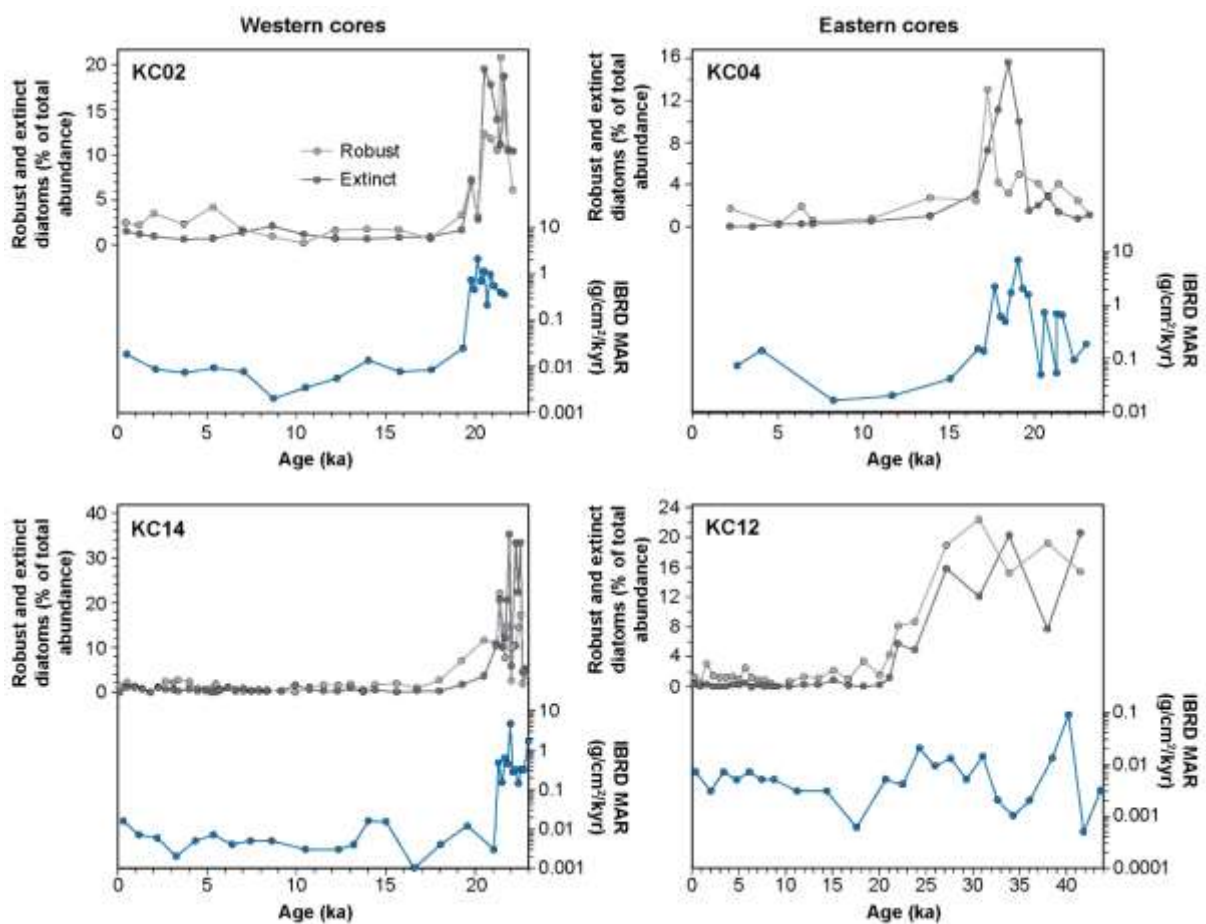


**Figure 2.12. Extinct and robust diatom species.** Graphs showing temporal variation in the percentage of extinct (*Actinocyclus ingens*, *Denticulopsis* spp., *Hemidiscus karstenii*, *Pyxilla reticulata*, *Rouxia* spp. and *Stephanopyxis* spp.) and robust (*Rhizosolenia* spp.) diatoms compared with the IBRD MAR in each core.

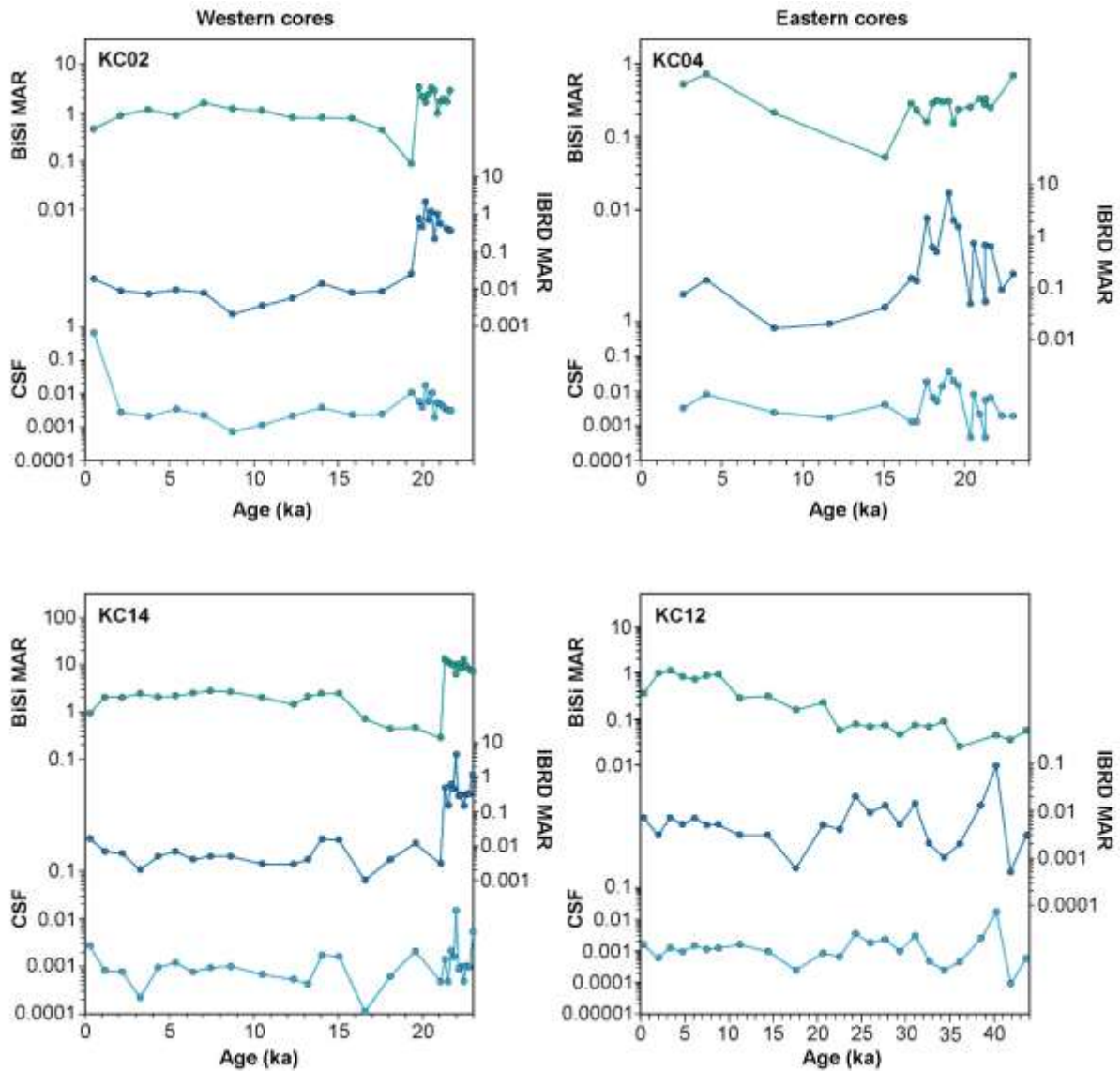


**Figure 2.13. Mass accumulation rates.** Graphs showing temporal variation in the IBRD MAR and BiSi MAR at each core site. The coarse sand fraction (CSF) used to quantify the IBRD MAR is also shown.

The average BiSi MAR at KC02, KC14 and KC04 was much higher during the glacial (1.15 - 9.6 g/cm<sup>2</sup>/kyr) than the Holocene (0.07 - 1.8 g/cm<sup>2</sup>/kyr) (Fig. 2.13). The BiSi MAR during the glacial period at these three core sites coincides with a higher proportion of extinct and robust diatoms and an elevated IBRD MAR, but is anticorrelated with BiSi concentration and diatom abundance (Figs 2.8. and 2.13). Between 21-19 ka, the BiSi MAR began to positively correlate with BiSi

concentration and diatom abundance (Figs 2.8 and 2.13). The average BiSi MAR at KC02, KC14 and KC02 is up to three orders of magnitude higher than at KC12 (Fig. 2.13). In KC12, after ~22 ka, the average BiSi MAR increases tenfold from 0.06 g/cm<sup>2</sup>/kyr during the glacial to 0.6 g/cm<sup>2</sup>/kyr during the Holocene (Fig. 2.13). At this core site, the BiSi MAR negatively correlates with the IBRD MAR and positively correlates with all proxies for biological productivity and mean particle size throughout the record (Figs 2.8 and 2.13).

### **2.3.4. IBRD MAR**

The average IBRD MAR was much higher in the glacial (0.3-1.3 g/cm<sup>2</sup>/kyr) than in the Holocene (0.01-0.07 g/cm<sup>2</sup>/kyr) at KC02, KC14 and KC04 (Fig. 2.13). There was a sharp decrease in the IBRD MAR between ~21-18 ka at these core sites, after which the IBRD MAR remained below 0.15 g/cm<sup>2</sup>/kyr throughout the remainder of the deglacial-Holocene period (Fig. 2.13). At KC12, a similar temporal trend is observed with a slightly higher average IBRD MAR during the glacial (0.014 g/cm<sup>2</sup>/kyr) compared to the Holocene (0.005 g/cm<sup>2</sup>/kyr), but with much lower absolute values than at the other core sites (Fig. 2.13). At this core site, the lowest IBRD MAR is recorded at ~18 ka (Fig. 2.13).

### **2.3.5. Grain size variability**

The leached mean grain size in each core ranges between 2-14 µm, with the smallest grain sizes present in the glacial section and larger grain sizes dominating the silty Holocene sediments (Fig. 2.14; Supplementary Figs 4.17-4.20). The bulk mean particle size positively correlates with BiSi concentration and is generally higher than the leached mean grain size for each record, emphasising the effect of diatom frustules on particle size (Figs 2.8 and 2.14). A temporal transition from smaller to larger grain sizes is seen more prominently in the bulk particle size (Supplementary Figs 4.13-4.16) and occurs between 21-19 ka at KC02, KC14 and KC12, and at ~17 ka at KC04 (Fig. 2.14). In KC02, a single peak in the bulk grain size (12 µm) at 21 ka is likely due to the presence of fine IBRD (Fig. 2.14). The SS%

shows small-scale fluctuations and a general average increase over time in each of the cores, reaching a maximum in the Holocene of 48-53% in KC02, KC14 and KC12, and 28% in KC04 (Fig. 2.14).

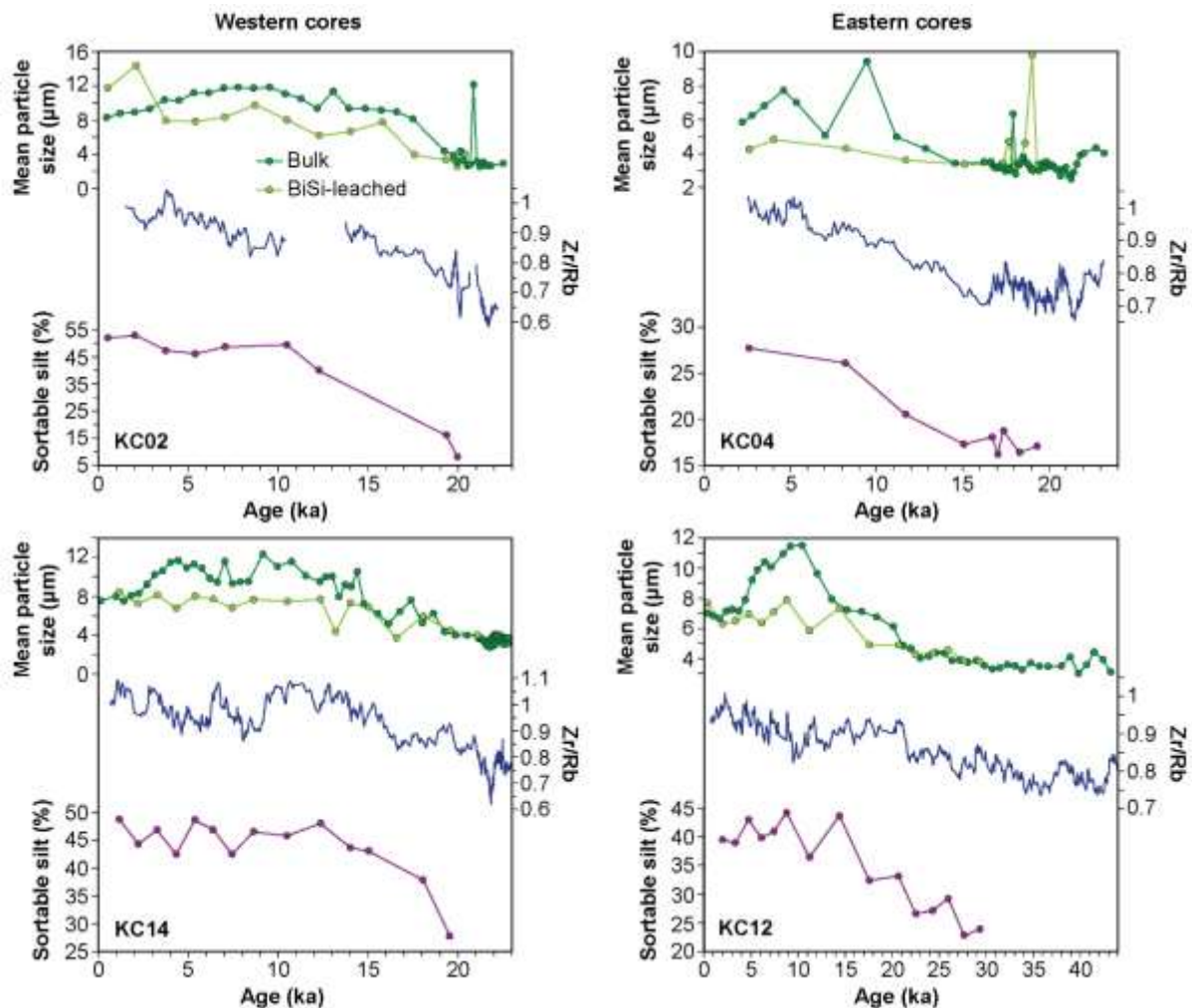


**Figure 2.14. Proxies for paleocurrent speed.** Graphs showing the mean grain size from bulk and BiSi-leached sediments, Zr/Rb XRF ratio and SS% in each of the cores, as proxies for paleocurrent speed.

The Zr/Rb ratios and the SS% exhibit a moderate to strong correlation coefficient ( $R^2 = 0.55-0.75$ ; Fig. 2.15). Despite the complex correlation observed between the Zr/Rb ratio and the mean particle size (bulk and leached), the main temporal change from predominantly lower glacial values to higher values in the Holocene is simultaneous between these two proxies at all core sites (Fig. 2.14). Where the Zr is richer in the

sediment, indicating coarser material, the mean particle size is higher. Lower Zr/Rb ratios (0.6-0.9) occur in the glacial section of each core and increase to higher ratios (0.7-1.1) between 21-19 ka at KC02, KC14, and KC12, and at ~ 17 ka at KC04 (Fig. 2.14). The increase in the Zr/Rb ratio is also synchronous with the main increase in BiSi concentration, diatom abundance and SS% at each core site (Figs 2.8 and 2.14).

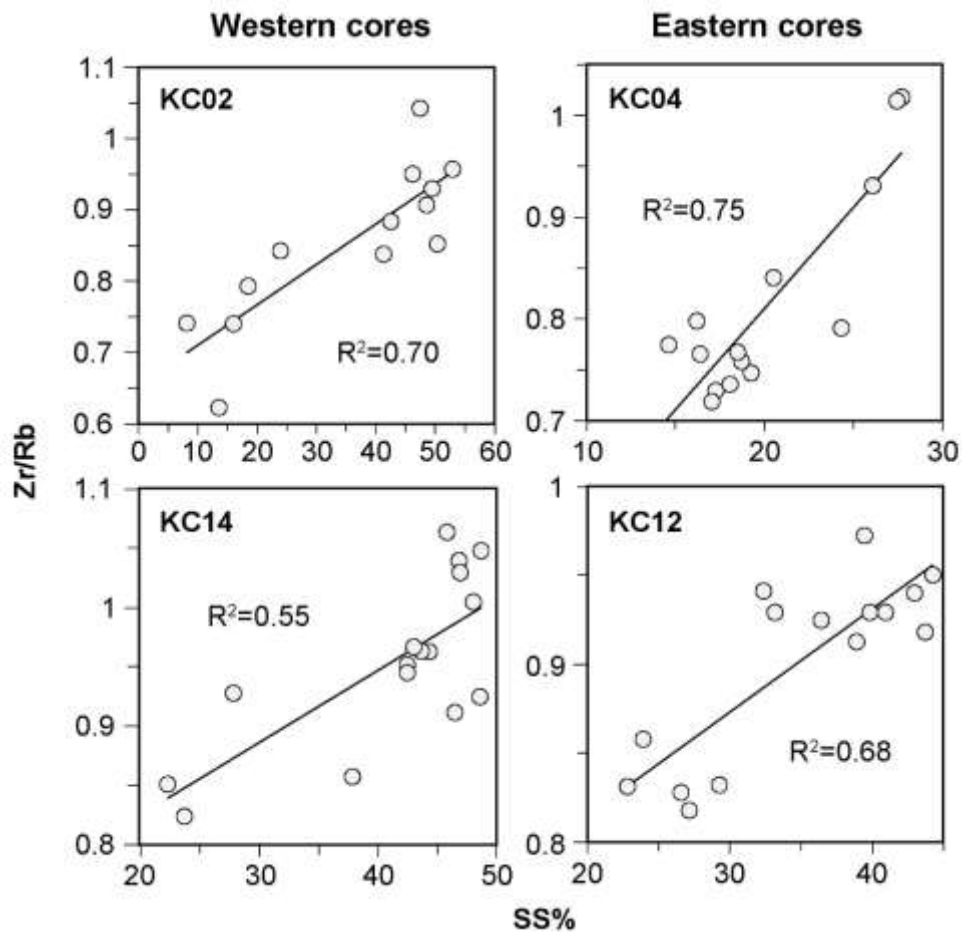


**Figure 2.15.** Crossplots showing the correlation between SS% and the Zr/Rb ratio in each of the cores.

## 2.4. Discussion

The processes that define glacial and interglacial periods leave a fingerprint over time and are reflected in the biological, physical, and geochemical composition of

marine sediment. Temporal changes in primary biological productivity, sedimentation rates, current speed and ice rafting can therefore be used to unravel the response of the ice sheet to climate change over time. Here the spatial and temporal proxy trends at each core site are assessed in order to 1) characterise the paleoenvironmental conditions and sediment depositional regime at the continental rise over the last glacial-interglacial cycle and 2) establish the timing of important climate events at the coast of central Wilkes Land, with particular focus on the last deglaciation.

## 2.4.1. The Last Glacial Period

### *Ice sheet dynamics*

The exceptionally high average glacial sedimentation rates at KC02 (102 cm/kyr; Fig. 2.7) and KC14 (331 cm/kyr; Fig. 2.7) on the contourite drifts and the relatively high glacial sedimentation rate also recorded at KC04 (33 cm/kyr; Fig. 2.7) cannot be explained by current-driven sediment transport alone, as the highest current speeds (> 25 cm/s) are able to deposit sediment at a maximum rate of ~25 cm/kyr (McCave et al., 1995). Instead, it is suggested here that as the ice sheet advanced during the Last Glacial Period, sediments from the continental shelf were scoured by the ice and redeposited downslope in a series of gravity flows (O'Brien et al., 2020; Post et al., 2020). Evidence for gravity flows during ice sheet advance has previously been found in the study region, based on the detailed assessment of bathymetric features of the continental margin (O'Brien et al., 2020; Post et al., 2020) and the remarkably high glacial LSR (> 300 cm/kyr) at KC14 (Tooze et al., 2020). Plumes of fine sediment emanating from these gravity flows are interpreted to have dominated sedimentation during the Last Glacial Period and maintained the contourite ridges in the west of the study region and the giant levees of the submarine canyon network in the east of the study region. Grain size analysis indeed indicated that most of the sediment within each core is fine-grained, with the mean grain size ranging between 2-12  $\mu\text{m}$  (Fig. 2.14). The high IBRD MAR at the core sites during the Last Glacial Period (relative to the Holocene) (Fig. 2.13) indicates secondary sedimentation via an enhanced input of coarse (250 $\mu\text{m}$ -2 mm), detrital angular grains that fit the criteria

of IBRD, that were transported rapidly downslope as the ice sheet advanced (Tooze et al., 2020).

The prevalence of extinct species in glacial sediments and high BiSi MAR further supports the interpretation of shelf sediment redistribution during the glacial and has been so-interpreted in other regions of Antarctica (e.g., in the Ross Sea; Cunningham et al., 1999). The lower, glacial section of each core contained between 30-70% extinct diatom species (e.g., *Actinocyclus ingens*, *Denticulopsis* spp., *Hemidiscus karstenii*, *Pyxilla reticulata*, *Rouxia* spp. and *Stephanopyxis* spp.) (Fig. 2.12). Peak abundances of extinct and robust species have been observed in the glacial intervals of piston cores from the study region (Holder et al., 2020) supporting the results from this study. Where extinct diatom species are most prevalent in each core, the total BiSi concentration and diatom abundance measures less than 4% and 10 million valves/g, respectively (Figs 2.8 and 2.12). Therefore, any sediment containing less than 4% BiSi or less than 10 million diatom valves/g likely comprises mostly, if not entirely, of diatoms reworked with continental shelf sediment as the ice sheet advanced during the Last Glacial Period. Extended ice shelves and widespread sea ice restrict sunlight to the photic zone and inhibit surface biological productivity (Mortlock et al., 1991). The rapid deposition of extinct and reworked diatom species explains the high BiSi MAR during the Last Glacial Period (Fig. 2.13) when primary productivity would have been low.

The robust frustules of *Rhizosolenia* spp. are typically more resistant to dissolution in the water column and as such have high preservation rates (Armand and Zielinski, 2001). The total diatom abundance has been found to comprise a higher percentage of *Rhizosolenia* spp. in glacial sediments than modern sediments from other regions of the Southern Ocean and the genus has been deemed effective for indicating changes in paleoenvironmental conditions associated with glacial-interglacial transitions (Armand and Zielinski, 2001). A northward expansion of sea-ice over the continental margin would have inhibited primary productivity during glacial periods. The higher percentage of *Rhizosolenia* spp. in the glacial sediments at each core site (Fig. 2.12) is therefore likely due to the durability of their frustules and the low

overall productivity, meaning *Rhizosolenia* spp. comprise the bulk of the diatoms preserved.

The sedimentation rate during the glacial varies regionally, with much higher values at the western core sites than the eastern core sites (Fig. 2.7). The gullies and canyons that characterise the bathymetry of the continental rise in the eastern part of the study region may possibly be more efficient at concentrating debris further offshore from the core sites, resulting in lower sedimentation rates at KC04 and KC12. At KC12, the LSR during the Last Glacial Period was considerably lower than at the other core sites (Fig. 2.7) suggesting a lack of sediment supply by gravity flows to this core site. However, like the other core sites, high abundances of extinct diatom species are measured during the glacial period at KC12 (Fig. 2.12), suggesting reworking of continental shelf sediments. The measured LSR at KC12 during the glacial is interpreted here to be affected by the age ( $37287 \pm 802$  cal yr BP) measured in the glaciogenic section of the core (Table 2.3; Fig. 2.7). The calibrated age obtained at 240 cm depth (approximately 10 cm from the bottom of the core) is considerably older (~10 kyr) than the ages measured from the glacial section of the other three cores (Fig. 2.7). The glacial sediments at KC12 are likely affected by more reworked carbon than has been corrected for by the LCO. The true age is possibly much younger, which would result in a higher calculated LSR for the glacial period at KC12 and would support the existence of gravity flows to this site at the end of the Last Glacial Period.

### *Sea-ice dynamics*

The extension of sea-ice over the continental rise during the Last Glacial Period is evidenced by low or absent primary productivity at each core site and lower abundances of the diatom species *Fragilariopsis kerguelensis* in the glacial compared to the modern day (Figs 2.8 and 2.10). *Fragilariopsis kerguelensis* is an indicator of a permanently open ocean zone (POOZ) associated with a warmer climate (Crosta et al., 2005). At each core site, this is the most prevalent diatom species, comprising between 30-60% of the total diatom abundance in the glacial

sediments and 70-85% in the Holocene sediments (Fig. 2.10). Across the region, except at KC04, the average abundance of *Fragilariopsis kerguelensis* is lower in glacial sediments than in modern sediments, indicating widespread sea ice during the Last Glacial Period and the opening of the POOZ above the continental rise from the onset of deglaciation to present (Fig. 2.10).

### *Paleocurrent speed*

At the contourite drifts where KC02 and KC14 were recovered, glacial sedimentation is dominated by the release of fine particles in the water column from plumes of debris to form a nepheloid layer, and subsequent westward transport to the ridges via bottom-intensified geostrophic currents (O'Brien et al., 2020; Post et al., 2020). Resuspension of finer particles in the east of the region at the levees of submarine canyons also contributes to the maintenance of the contourites and has been interpreted in other regions of the Antarctic margin (e.g., Amblas and Canals, 2016; Hillenbrand et al., 2021; Larter et al., 2016; Rebesco et al., 2014b, 2002). Temporal variation in the speed of west-flowing bottom-intensified currents is represented by the SS% which is approximately 50% lower in the glacial section of each core than in the modern sediments (Fig. 2.14), suggesting lower current speeds during the Last Glacial Period. The Zr/Rb ratio at each core site positively correlates with the SS% (Fig. 2.15), reinforcing the use of Zr/Rb as a relative measure of paleocurrent speed (Wu et al., 2020). These changes in bottom current speed are also reflected in the upcore grain size distribution. The dominance of finer, glaciogenic clay during the glacial period (Units IV – VII, Fig. 2.4; Fig. 2.5) represents low speed currents and the deposition of fine grains. During glacial periods when the ice sheet expanded, it is hypothesised that the easterly wind regime weakened and shifted northward away from the coastline (Stewart and Thompson, 2012). Weaker winds are speculated to have caused the slowing of the currents adjacent to the Antarctic margin (e.g., the Antarctic Coastal Current, the Antarctic Slope Current and the ACC) (Stewart and Thompson, 2012).

The deposition of fine ( $< 63 \mu\text{m}$ ) IBRD can, in some cases, affect interpretations of paleocurrent speed. However, provided that the fine IBRD was subsequently transported by a current of sufficient speed to sort the sediment, the input of fine IBRD should not affect the measured SS% (McCave and Andrews, 2019). At each core site, there is a clear transition from less well-sorted sediments to more sorted sediments through time (Table 2.2). At KC02 and KC04, some of the glacial sediment samples are poorly and extremely poorly sorted (blue-shaded values, Table 2.2), and may therefore be affected by the input of fine-grained IBRD. However, most samples in all cores are moderately to well-sorted (orange and green-shaded values, Table 2.2) and the same primary temporal patterns were observed when plotting the SS% against the age model (Fig. 2.14) with or without values from the poorly-sorted samples (i.e., those samples with a sorting value of  $> 2$ ). It is therefore unlikely that the presence of fine ice-rafted debris would significantly affect interpretations of the SS% in relation to paleocurrent speed in this study region.

Multiple sediment sources can also bias a grain size record toward a particular size range representative of source rock type or varying transport processes from source to sink, as opposed to current strength. However, changes in the source supply of terrigenous detritus typically have a negligible impact on the size variability in the fine fraction in comparison to coarse, sandy sediments whose size are significantly influenced by source rock type and mineralogy (McCave and Hall, 2006). Additionally, the high frequency of gravity flows and rapid sedimentation during the glacial at KC02, KC14 and KC04 (and suspected also at KC12) would likely eradicate any source-influenced particle size variability on the timescales represented by each of the cores (McCave and Hall, 2006).

### *The Local Last Glacial Maximum*

The Last Glacial Maximum represents the time at which the Earth's ice sheets had reached their maximum extent during the Last Glacial Period and has been constrained between  $\sim 27$ - $19$  ka, based on evidence for a lowstand in global sea-level (Clark et al., 2009). Antarctica is estimated to have expanded later than the

Northern Hemisphere ice sheets (Clark et al., 2009), and there are thought to be differences in the timing of the Local Last Glacial Maximum (LLGM). In this study, the point at which the sedimentation rates drop at each core site (Fig. 2.7) is interpreted to signify the ceasing of gravity flows associated with maximum expansion of the ice sheet in central Wilkes Land. At KC02, KC14 and KC12, this occurs between 22-20 ka, and at KC04 at 18 ka (Fig. 2.7). Based on the timing of the ceasing of gravity flows recorded in the majority of the cores, it is inferred that the LLGM occurred somewhere between 22-20 ka along the margin of central Wilkes Land.

A well-laminated section (Unit V, Fig. 2.4) is observed in KC14, KC04 and KC12 that can be likened to the sub-ice shelf laminated mud lithofacies of Smith et al. (2019). The laminations comprise of alternating finer and coarser sediment likely formed by intermittent plumes of fine material from gravity flows settling through the water column beneath an ice canopy during the Last Glacial Period. The presence of this lithofacies at KC14, KC04 and KC12 suggests some coverage over the core sites by an ice canopy extending from within the vicinity of the Totten and Moscow University glaciers (at a distance from the grounding line) for a period (c. 0.45 kyr, 0.25 kyr and 9.7 kyr, respectively) during the LLGM. The discovery of a grounding zone wedge close to the modern-day continental shelf break not far from KC12 indicates the position of the maximum extent of the ice sheet at that location (Post et al., 2020). Unit V is thickest (~50 cm-thick) in KC12 (Fig. 2.4), possibly indicating that this core site may have been closest to the grounding line and covered for some time by an ice canopy proximal to Moscow University Glacier during the LLGM. However, the prolonged period (9.7 kyr) of ice cover at KC12 measured from the age model is likely too long an estimate for the duration of the LLGM. Furthermore, the top and bottom ages of Unit V in KC12, at 33.5 ka and 43.2 ka, respectively, are older than the estimated window for the LGM of the global ice sheets (26.5 ka – 19.0 ka; Clark et al., 2009). These two observations provide further support for the interpretation that the oldest radiocarbon age in KC12 is affected by more old, recycled carbon than has been accounted for by the LCO correction.

At KC02, an 80 cm-thick package of pellet-rich silty clay (Unit VI) occupies the middle section of the core (Fig. 2.4), which can be equated to dropstone mud (unit 8 of Smith et al. (2019)) deposited in the ice-calving zone close to the sea ice margin. The till-like pellets of this lithology suggest a high concentration of iceberg calving and the release of dropstones and IBRD within this high energy zone. The glacial sediment in KC02 contains more coarse detritus than any of the other cores (Fig. 2.13), suggesting input from the calving front of the sea ice margin near the proximal Totten Glacier in addition to gravity flows. Due to the position of KC02 within a canyon (Fig. 2.3), more debris from gravity flows may be concentrated in this region, contributing to the till abundance and granulitic texture of the glacial sediment (Smith et al., 2019). The age model indicates that this mode of sedimentation at KC02 occurred for approximately 3.5 kyr during the Last Glacial Period.

## 2.4.2. The last deglaciation

The last deglaciation is defined as the period of time over which the grounding line of the Antarctic Ice Sheet retreated from its maximum to its present day position, due to accelerated melting of the ice in response to climatic warming and Northern Hemisphere-driven sea-level rise. Processes in the Southern Ocean above the continental rise reflect changes to the ice sheet and ocean as the climate warmed. Six proxies were chosen based on their representation of processes associated with the last deglaciation in central Wilkes Land (Figs 2.16 - 2.19). These proxies were used to: 1) constrain the timing of the onset of the last deglaciation and other important deglacial events, and 2) characterise the nature of deglaciation as represented by the marine environment and sediment depositional regime on the upper continental rise. Changes in bottom current speed were inferred using the Zr/Rb ratio, due to the high resolution and strong correlation with SS% in each of the cores (Figs 2.14 and 2.15). Variation in primary productivity was interpreted using the Si/Al ratio and diatom abundance, as diatoms dominate primary productivity in the Southern Ocean (Arrigo et al., 2008). The relative input of meltwater was indicated by the proportion of diatom species *Chaetoceros* subg. *Hyalochaete* (as a percentage of the total diatom abundance). Changes in physical processes on the

continental rise were gauged by the IBRD MAR and the relative abundance of extinct diatom species.

A gradual increase in the Zr/Rb ratio at each core site indicates strengthening of west-flowing bottom currents over the continental rise (Figs 2.16 - 2.19). Siltier sediments with a higher sand content (Units I – III, Fig. 2.4; Fig. 2.5) represent the selective deposition of coarser grains by stronger currents during the deglacial-Holocene period (McCave and Hall, 2006). A poleward shift and strengthening of the easterly winds at the termination of the Last Glacial Period is interpreted to have caused the westward currents to accelerate (Stewart and Thompson, 2012). However, more advanced models are needed to establish key changes in the wind regime from the Last Glacial Period to present and its control over the regional paleoceanography (Kohfeld et al., 2013).

Warming of the climate and subsequent retreat of sea ice at the coast is indicated by a rise in absolute diatom abundance and Si/Al values at each core site, which represent an increase in phytoplankton blooms above the continental rise (Figs 2.16 - 2.19). Retreat of the ice sheet and melting of sea ice in a warmer climate provides an open photic zone, allowing sunlight to penetrate through the surface waters and stimulate primary productivity. Enhanced meltwater input is evidenced by a prominent peak in the proportion of *Chaetoceros* subg. *Hyalochaete* diatoms at KC02, KC14 and KC04, immediately after the period of shelf sediment distribution and gravity flows (Figs 2.16 - 2.18). This peak is interpreted to represent enhanced melting of the ice sheet, when sea surface temperatures and meltwater production increased, and the ocean became more stratified. Resting spores of *Chaetoceros* subg. *Hyalochaete* are more prevalent where the water column is stable, and meltwater from glaciers and sea-ice provides essential nutrients (Fe, Si) for the organisms to maintain their exoskeletons (Crosta et al., 1997). *Chaetoceros* subg. *Hyalochaete* are therefore associated with spring blooms, deglaciation, and higher total productivity (Crosta et al., 1997).

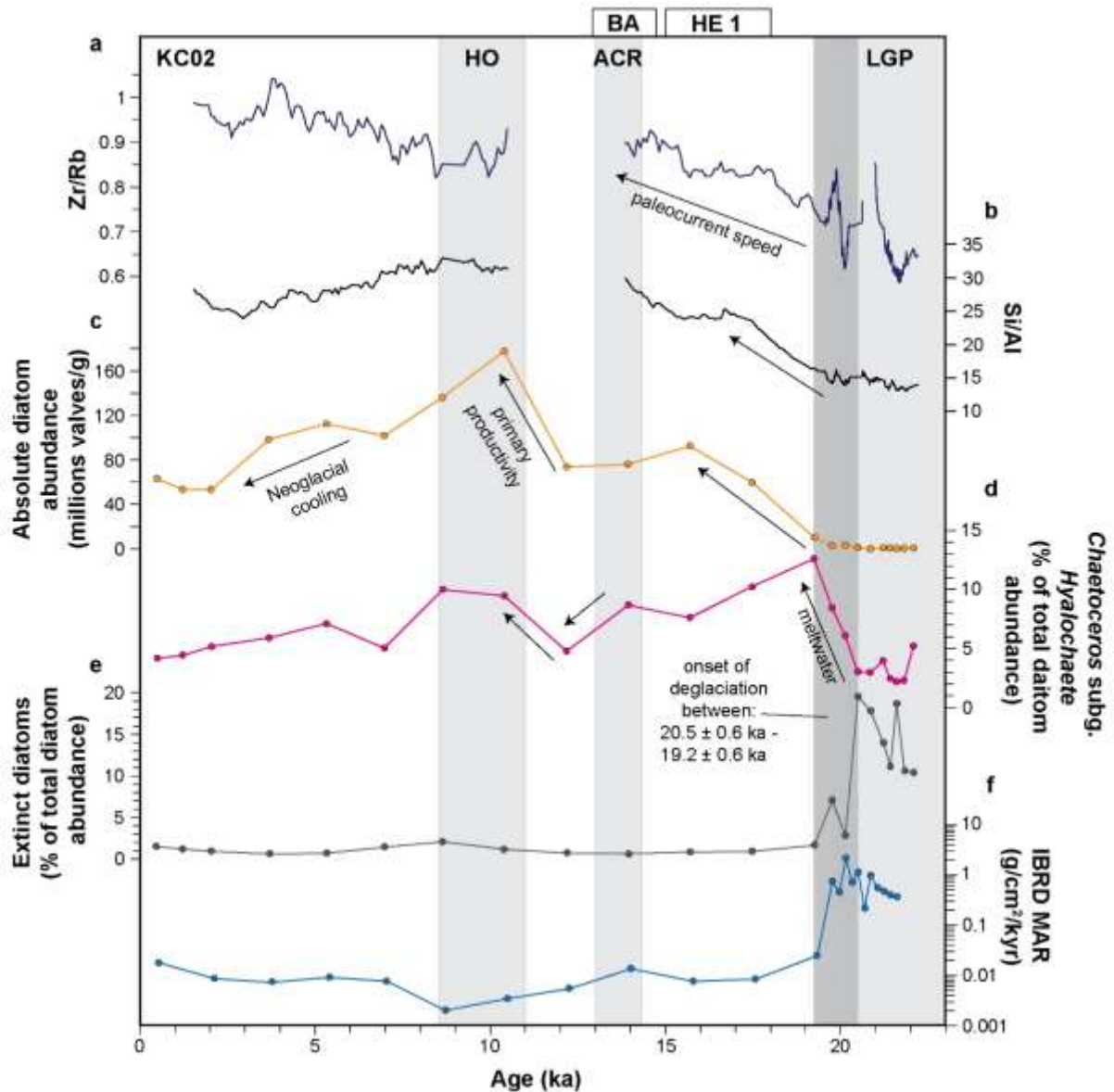


**Figure 2.16. Key proxies in KC02.** (a) Zr/Rb as a proxy for paleocurrent speed, (b), (c) Si/Al and absolute diatom abundance, respectively, as proxies for total primary productivity, (d) percent of the total diatom abundance of *Chaetoceros* subg. *Hyalochaete* as a proxy for meltwater input, (e) percent of the total diatom abundance of extinct diatoms, (f) the IBRD MAR. The dark grey bar represents the possible range of time in which the last deglaciation initiated. Light grey bars highlight key climate events observed in the record. HO – Holocene Optimum, ACR – Antarctic Cold Reversal (Blunier et al., 1997; Pedro et al., 2011), LGP – Last Glacial Period. Tabs at the top of the graph indicate the timing of key climate events in the Northern Hemisphere. HE 1 – Heinrich Event I (~18-15 ka), BA - Bølling–Allerød interstadial (14.7-12.9 ka).

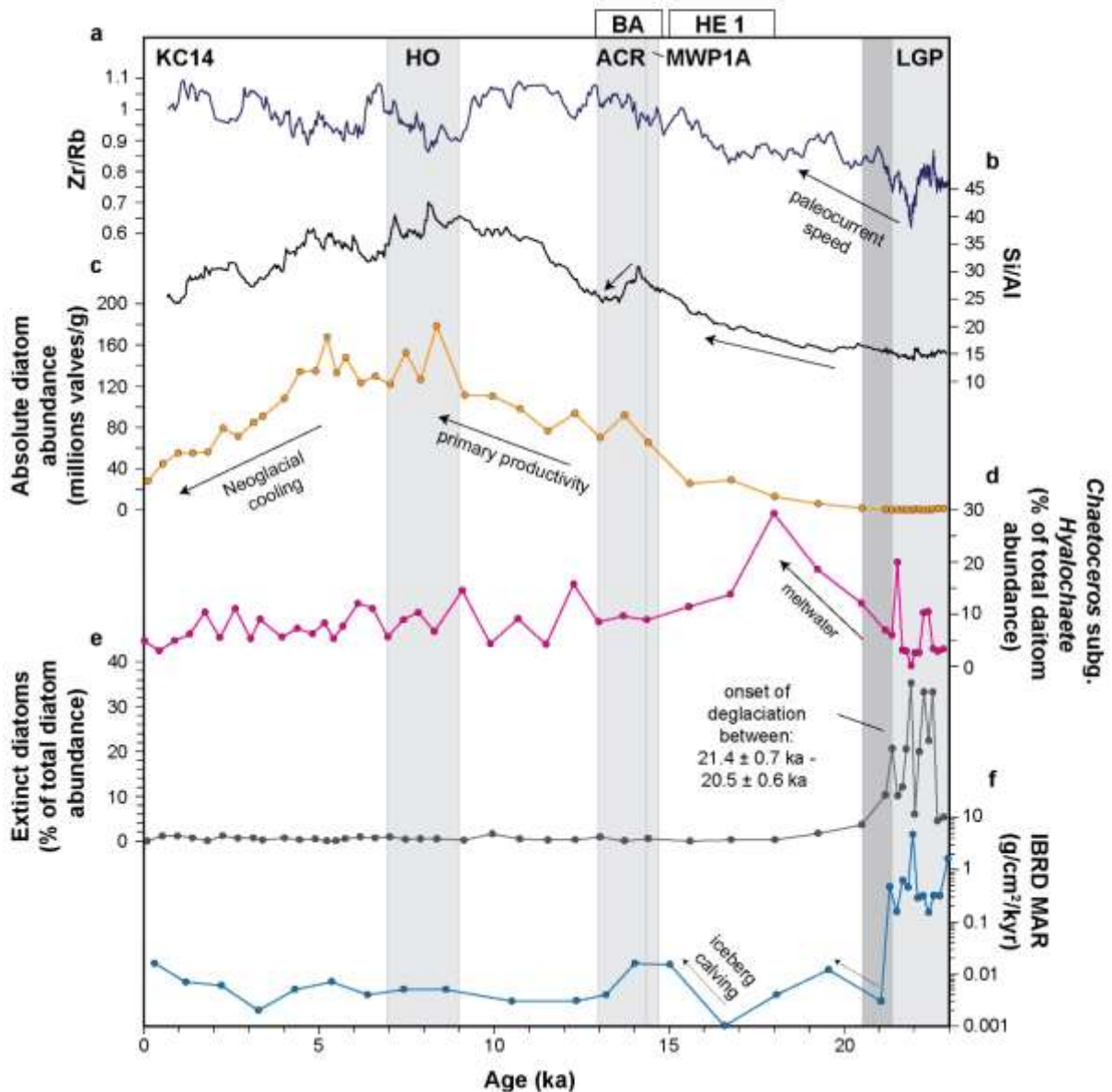


**Figure 2.17. Key proxies in KC14.** (a) Zr/Rb as a proxy for paleocurrent speed, (b), (c) Si/Al and absolute diatom abundance, respectively, as proxies for total primary productivity, (d) percent of the total diatom abundance of *Chaetoceros* subg. *Hyalochaete* as a proxy for meltwater input, (e) percent of the total diatom abundance of extinct diatoms, (f) the IBRD MAR. Grey bar represents the possible range of time in which the last deglaciation initiated. Black dashed lines show the minimum and maximum age model errors for the onset of deglaciation. Light grey bars highlight key climate events observed in the record. HO – Holocene Optimum, ACR – Antarctic Cold Reversal (Blunier et al., 1997; Pedro et al., 2011), MWP-1A – Meltwater Pulse 1A (Deschamps et al., 2012), LGP – Last Glacial Period. Tabs at the top of the graph indicate the timing of key climate events in the Northern Hemisphere. HE 1 – Heinrich Event I (~18-15 ka).

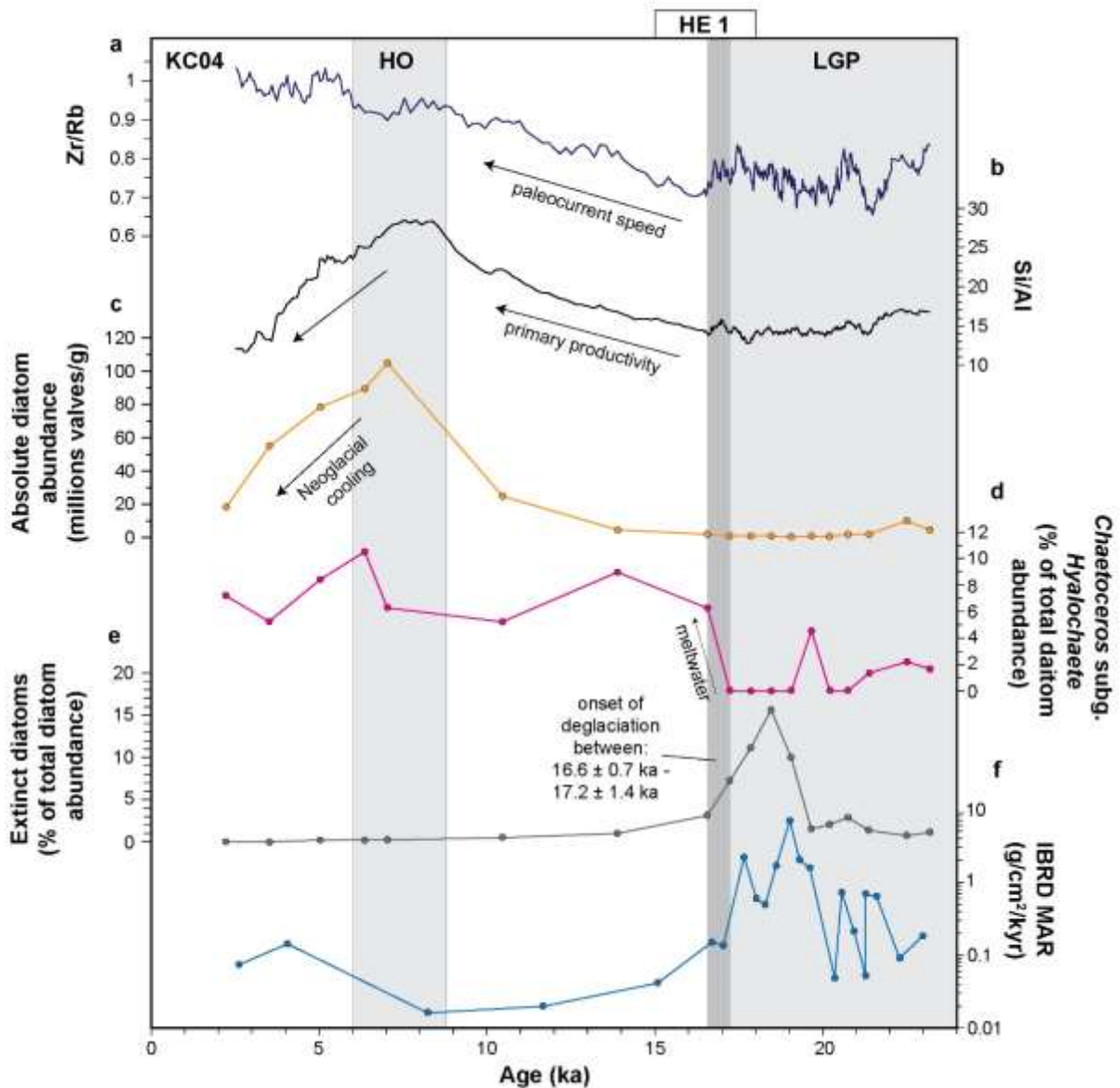


**Figure 2.18. Key proxies in KC04.** (a) Zr/Rb as a proxy for paleocurrent speed, (b), (c) Si/Al and absolute diatom abundance, respectively, as proxies for total primary productivity, (d) percent of the total diatom abundance of *Chaetoceros* subg. *Hyalochaete* as a proxy for meltwater input, (e) percent of the total diatom abundance of extinct diatoms, (f) the IBRD MAR. Grey bar represents the possible range of time in which the last deglaciation initiated. Light grey bars highlight key climate events observed in the record. HO – Holocene Optimum, LGP – Last Glacial Period. Tabs at the top of the graph indicate the timing of key climate events in the Northern Hemisphere. HE 1 – Henrich Event I (~18-15 ka), BA - Bølling–Allerød interstadial (14.7-12.9 ka).

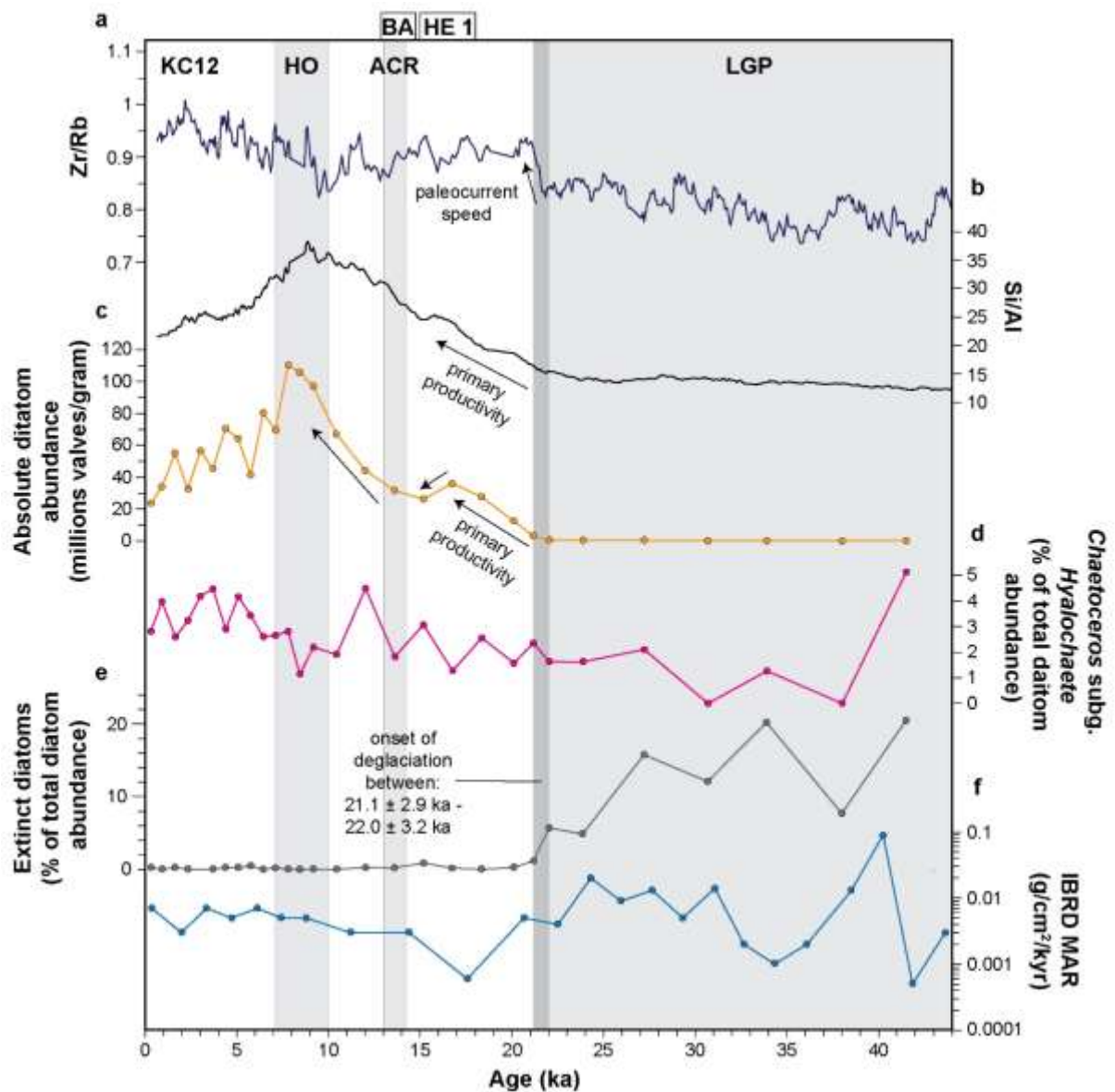


**Figure 2.19. Key proxies in KC12.** (a) Zr/Rb as a proxy for paleocurrent speed, (b), (c) Si/Al and absolute diatom abundance, respectively, as proxies for total primary productivity, (d) percent of the total diatom abundance of *Chaetoceros* subg. *Hyalochaete* as a proxy for meltwater input, (e) percent of the total diatom abundance of extinct diatoms, (f) the IBRD MAR. Grey bar represents the possible range of time in which the last deglaciation initiated. Black dashed lines show the minimum and maximum age model errors for the onset of deglaciation. Light grey bars highlight key climate events observed in the record. HO – Holocene Optimum, ACR – Antarctic Cold Reversal (Blunier et al., 1997; Pedro et al., 2011), MWP-1A – Meltwater Pulse 1A (Deschamps et al., 2012), LGP – Last Glacial Period. Tabs at the top of the graph indicate the timing of key climate events in the Northern Hemisphere. HE 1 – Heinrich Event I (~18-15 ka), BA - Bølling–Allerød interstadial (14.7-12.9 ka).

At the LLGM, the IBRD MAR decreases by up to two orders of magnitude at KC02, KC14 and KC04, and to some degree at KC12, as the delivery of the sediment to the continental rise via gravity flows ceased (Figs 2.16 - 2.19). The IBRD MAR after this point likely reflects the deposition of coarse terrigenous grains released from icebergs in meltwater plumes during deglaciation and a transition into the Holocene. The dearth of extinct diatom species (Figs 2.16 - 2.19) after initially higher percentages further indicates that the sediment depositional regime on the continental rise changed and was no longer dominated by processes associated with ice sheet erosion and reworking, but instead by primary productivity, iceberg calving and bottom currents.

The onset of deglaciation at the Sabrina Coast is marked by a pronounced increase in paleocurrent speed (Zr/Rb), primary productivity (Si/Al and absolute diatom abundance) and meltwater production (*Chaetoceros* subg. *Hyalochaete*) (Figs. 2.16 - 2.19). At approximately the same time, gravity flows to the continental rise had ceased, resulting in a decrease in sedimentation rates (to below 20 cm/kyr), coarse debris (represented by the IBRD MAR) and the proportion of extinct diatom species at each core site, as the ice sheet grounding line and sea ice margin began to migrate poleward. Some uncertainty in identifying the onset of deglaciation comes from 1) the offset in timing in which each of the changes to these processes occur and 2) error associated with the age model. To incorporate this uncertainty, a range for each core is identified that covers the first and last proxies to show a change associated with deglaciation. The model error associated with the age at which the first and last changes occur was also added to give a total window of time within which the onset of deglaciation occurred. Three of the core records, KC02, KC14 and KC12, suggest that deglaciation began immediately following the LLGM (between  $22.0 \pm 3.2$  ka and  $19.2 \pm 0.6$  ka; Figs 2.16, 2.17 and 2.19) while KC04 indicates a later onset to deglaciation (between  $17.2 \pm 1.4$  ka and  $16.6 \pm 0.7$  ka; Fig. 2.18). The contrast in timing appears to be unrelated to core locality and the associated sedimentary environment (i.e., the contourite drifts in the west and the network of gullies in the east). Whilst it cannot be ruled out entirely, it is improbable that retreat of the ice sheet during the last deglaciation would have ensued asynchronously across the slope of central Wilkes Land to the degree portrayed by

the proxies at each core site. Two possible explanations for the relatively significant difference in timing (2 - 4 kyr) are 1) the deglacial ages in KC02, KC14 and KC12 reflect a higher input of old recycled carbon, or 2) more modern carbon was introduced to KC04 in the laboratory during sample preparation and AMS analysis. Since most of the cores indicate that the onset of deglaciation occurred somewhere between  $22.0 \pm 3.2$  ka and  $19.2 \pm 0.6$  ka, this is what is interpreted here as the timing of the beginning of deglaciation in central Wilkes Land.

The interpreted onset of deglaciation over the continental rise adjacent to the Sabrina Coast is one of the earliest indications of deglaciation currently constrained in East Antarctica (Mackintosh et al., 2014). However, previous offshore studies constraining the timing of the onset of deglaciation around the Antarctic margin used continental shelf sediments, and the time taken for the ice sheet to retreat from the continental rise to the continental shelf remains uncertain. During the early deglacial period following glacial maxima, initial increases in productivity and iceberg-rafting are gradual, suggesting slow initial retreat of the ice sheet at the Sabrina Coast. An initial increase is seen in productivity (Si/Al and diatom abundance), current speed (Zr/Rb) and the IBRD MAR between 18-15 ka at KC02 and KC12 (Figs 2.16 and 2.19, respectively) and between 17-13 ka at KC14 (Fig. 2.17). These peaks suggest a period of accelerated ice sheet retreat and are approximately concurrent with the Heinrich Event I (~18-15 ka) in the Northern Hemisphere (Broecker et al., 1992; Broecker, 1994; Heinrich, 1988). Peaks in the IBRD MAR and productivity at the Sabrina Coast during Heinrich Event I of the Northern Hemisphere support enhanced deglaciation in the Southern Hemisphere in response to a weakening of the Atlantic Meridional Overturning Circulation (AMOC). During Heinrich Event I, the AMOC had completely shut down and a cold climate prevailed in the Northern Hemisphere (McManus et al., 2004). Shutdown of the AMOC during this time has commonly been attributed to instabilities in the Laurentide Ice Sheet causing significant calving of icebergs and the release of meltwater into the North Atlantic (Bond et al., 1992; Calov et al., 2002; Heinrich, 1988; Hulbe et al., 2004; MacAyeal, 1993). Some evidence suggests that weakening of the AMOC preceded ice sheet collapse (Hall et al., 2006), and it has been hypothesised that this led to subsurface warming in the ocean, causing the Laurentide Ice Sheet to be unstable (Álvarez-

Solas et al., 2011; Flückiger et al., 2006). Weakening of the AMOC and a reduction in the southern migration of NADW causes a higher distribution of heat to the polar latitudes of the Southern Hemisphere, leading to a net increase in ocean temperatures around Antarctica (Crowley, 1992).

Meltwater Pulse 1A describes a major climate event at ~14.6 ka, where voluminous freshwater input into the ocean during the Bølling–Allerød warm interval in the Northern Hemisphere led to a dramatic ~20 m rise in global sea level in just 500 years (Hanebuth et al., 2000; Weaver et al., 2003). The ice sheets responsible for Meltwater Pulse 1A remains under debate, with some studies interpreting calving of the Laurentide Ice Sheet in the Northern Hemisphere as the primary source (e.g., Bentley et al., 2014; Clark et al., 1996; Gregoire et al., 2016; Mackintosh et al., 2014), whilst others interpret a contribution from Antarctica during the initial period of enhanced deglaciation between ~18-15 ka (e.g., Clark et al., 2002; Golledge et al., 2014; Ivins et al., 2013; Weaver et al., 2003; Weber et al., 2014). The main predicament in this debate is the timing of variation in major processes such as biological productivity and the iceberg calving associated with deglaciation. Many Antarctic records reveal that deglaciation occurred after Meltwater Pulse 1A (~14 ka), and therefore could not have contributed to it (Bentley et al., 2014; Mackintosh et al., 2014). However, other records, suggest earlier deglaciation and the potential for Antarctica to have contributed to Meltwater Pulse 1A. In particular, Weber et al. (2014), hypothesised varying degrees of Antarctic deglaciation from as early as 20 ka. They find prominent peaks in a high resolution IBRD record from the Scotia Sea during deglaciation, with the largest of these observed at ~14.6 ka (Antarctic Ice Discharge 6; Weber et al., 2014), implicating an Antarctic contribution to Meltwater Pulse 1A. A strong peak in the IBRD MAR is observed at ~14.7 ka in KC14 (Fig. 2.17) that is approximately concurrent with the largest peak in IBRD in the Scotia Sea (Weber et al., 2014), supporting an Antarctic contribution to Meltwater Pulse 1A and subsequent GMSL rise at ~14 ka.

Reinvigoration of the AMOC occurred following enhanced deglaciation and Southern Ocean warming between 18-15 ka, due to an increased mass transport of warmer

water from the Southern Hemisphere to the Northern Hemisphere (Knorr and Lohmann, 2003; McManus et al., 2004). The net northward distribution of oceanic heat resulted in an intense warming interval in the Northern Hemisphere known as the Bølling–Allerød interstadial (14.7-13 ka) and a simultaneous period of cold climate in the Southern Hemisphere known as the Antarctic Cold Reversal (Blunier et al., 1997; Pedro et al., 2016, 2011). The Antarctic Cold Reversal can be observed in KC02, KC14 and KC12 (Figs 2.16, 2.17 and 2.19, respectively), with a decrease in productivity at all three sites between ~15-13 ka and a concurrent decrease in IBRD MAR at KC02 and KC14 (Figs 2.16 and 2.17, respectively).

### **2.4.3. Holocene climate variability**

The response of the Antarctic Ice Sheet to millennial-scale climate variability during the Holocene is poorly investigated but is important in understanding the more intricate drivers of climate change in a warming climate. At each core site, between ~9-6 ka, higher amplitude peaks in productivity (Si/Al, Ba/Al, BiSi, diatom abundance) and paleocurrent speed (Zr/Rb, SS%, particle size) mark the timing of the Early Holocene Optimum in central Wilkes Land (Figs 2.16 - 2.19). The Early Holocene Optimum was an episode of higher SSTs, enhanced melting of the ice shelves, and open surface waters enriched with primary productivity. In other regions of East Antarctica, the timing of the Holocene Optimum has been constrained at various periods between the Early to Mid-Holocene (~11.5-6 ka) (Masson et al., 2000; Verleyen et al., 2011) which compares well with the results from this study. Peak ocean temperatures during the Antarctic Holocene Optimum are thought to be associated with a weakening of the AMOC due to the input of fresh glacial meltwater during the early Holocene (~11-8.2 ka) deglaciation of the Northern Hemisphere ice sheets in response to intensified solar insolation (Masson et al., 2000; McManus et al., 2004).

Post-optimum Holocene variability is regionally unique and is largely controlled by interactions between the ice, ocean and atmosphere. Between 6-4 ka in each of the cores, the Si/Al and absolute diatom abundance begin to decrease, marking a period

of climate cooling (Figs 2.16 - 2.19). Isotope measurements from ice cores record a revival of the AMOC following the end of Northern Hemisphere deglaciation, triggering a cooling trend in Antarctica (Masson et al., 2000; McManus et al., 2004). Cooling during the Late Holocene and/or glacioisostatic adjustment may have triggered a modest readvance of the ice sheet in central Wilkes Land, as has been interpreted in other regions of Antarctica, such as the Ross Sea (Greenwood et al., 2018; Kingslake et al., 2018; Prothro et al., 2020; Venturelli et al., 2020), the Weddell Sea (Bradley et al., 2015; Siegert et al., 2019) and at the margins of Adélie Land and George V Land in East Antarctica (Crespin et al., 2014). A readvance of the ice sheet would cause the sea-ice margin to expand northward, resulting in lower primary productivity above the continental rise. A multidisciplinary study of ice and sediment characteristics, glacial moraines, ice margin morphology and structural geology interpreted a readvance of the ice sheet at the nearby Budd Coast (the Windmill Islands; Fig. 2.3) at ~ 4 ka (Goodwin, 1996), but more evidence is needed to interpret ice sheet readvance at the Sabrina Coast during the Late Holocene.

## 2.5. Conclusions

This study presents the first multi-proxy paleoclimate records from four marine sediment cores transecting the continental rise of the Sabrina Coast in central Wilkes Land, East Antarctica. Detailed analysis of the physical, geochemical and biological composition of the sediment in each core and construction of age models from new radiocarbon dates has allowed major climatic events that occurred over the Last Glacial Period-Holocene transition to be constrained, including: the LLGM, the last deglaciation and the Holocene Optimum. From the results of this study, the following conclusions are drawn:

1. High sedimentation rates, abundant coarse, angular detritus and more prevalent extinct, reworked and robust diatom species in the glacial section of each core indicates that rapid sedimentation occurred during the Last Glacial Period and was dominated by the supply of reworked continental shelf sediments in a series of gravity flows as the ice sheet advanced.

2. The ceasing of gravity flows is indicated by a drop in the high sediment accumulation rates at each core site and suggests that the LLGM occurred at some time between ~22-20 ka at the Sabrina Coast.
3. A sudden increase in primary productivity (BiSi, absolute diatom abundance, Si/Al and Ba/Al), paleocurrent speed (mean grain size leached of BiSi, SS% and Zr/Rb), and ice melting (percent proportion of *Chaeteceros* subg. *Hyalochaete*) indicates that deglaciation in central Wilkes Land initiated somewhere between  $22.0 \pm 3.2$  ka and  $19.2 \pm 0.6$  ka, immediately following the LLGM. This is the earliest constrained timing of the onset of deglaciation in East Antarctica.
4. The records from this study provide evidence of temporal coupling of abrupt climate change between the Northern and Southern Hemispheres. A period of enhanced deglaciation (between ~18-15 ka) at three of the core sites is concurrent with Heinrich Event I. Evidence of The Antarctic Cold Reversal (~15-13 ka) is seen by a decrease in primary productivity at three of the core sites during deglaciation. The presence and timing of these events suggests that central Wilkes Land is sensitive to the bipolar seesaw and associated changes in the strength of the AMOC.
5. The deglacial onset (between  $22.0 \pm 3.2$  ka and  $19.2 \pm 0.6$  ka) precedes Meltwater Pulse 1A (~14.6 ka) at the Sabrina Coast, supporting a possible Antarctic contribution to the subsequent period of enhanced global sea level rise (at ~14 ka).

These results provide a more detailed picture of the recent history of the ice sheet in central Wilkes Land and the complex interactions between ice, ocean and atmosphere in response to climate variability over the Last Glacial Period-Holocene transition. From a region of Antarctica with the potential to significantly contribute to future global sea-level rise in a warming climate, these findings will aid paleoclimate models that hindcast events of the Last Glacial Period-Holocene transition and ice sheet models that predict the future ice sheet behaviour and sea-level contribution from central Wilkes Land.

## 2.6. Supplementary Information

KC02				
Depth (cm)	Si/Al (smoothed)	Ba/Al (smoothed)	Zr/Rb (smoothed)	Age (yrs)
7.5	28.30	8.31	0.99	1537
8	27.63	8.02	0.99	1620
8.5	27.52	7.75	0.98	1703
9	26.99	7.49	0.98	1783
9.5	26.82	7.38	0.98	1865
10	26.26	7.14	0.98	1948
10.5	25.62	6.88	0.96	2030
11	25.37	6.79	0.96	2112
11.5	25.45	6.73	0.95	2194
12	25.14	6.58	0.94	2276
12.5	25.14	6.43	0.94	2360
13	25.26	6.34	0.94	2441
13.5	25.34	6.24	0.94	2525
14	25.06	6.19	0.91	2606
14.5	24.93	6.15	0.93	2689
15	24.61	6.19	0.93	2771
15.5	24.27	6.10	0.95	2855
16	23.96	6.31	0.94	2937
16.5	24.28	6.42	0.95	3019
17	24.64	6.45	0.95	3103
17.5	25.08	6.50	0.95	3187
18	25.14	6.32	0.97	3268
18.5	25.47	6.33	0.98	3353
19	26.44	6.63	0.98	3434
19.5	26.41	6.54	0.96	3515
20	26.04	6.60	0.98	3597
20.5	25.65	6.44	1.00	3681
21	25.50	6.50	1.04	3761
21.5	25.70	6.43	1.04	3843
22	26.61	6.64	1.02	3926
22.5	26.83	6.63	1.03	4008
23	27.10	6.95	1.03	4090
23.5	26.97	6.92	1.01	4171
24	28.19	7.14	0.98	4254
24.5	28.16	7.09	0.95	4337
25	27.93	7.28	0.98	4418
25.5	27.62	7.20	0.98	4502
26	27.98	7.34	0.98	4585
26.5	27.63	7.41	0.96	4667
27	27.46	7.12	0.94	4748
27.5	26.77	6.93	0.92	4831
28	26.46	6.80	0.94	4914

<b>28.5</b>	26.41	6.63	0.96	4994
<b>29</b>	26.74	6.72	0.97	5077
<b>29.5</b>	27.63	6.86	0.96	5159
<b>30</b>	28.19	6.94	0.97	5240
<b>30.5</b>	28.00	6.94	0.95	5321
<b>31</b>	28.17	6.96	0.95	5401
<b>31.5</b>	27.66	6.83	0.94	5486
<b>32</b>	28.38	6.86	0.93	5569
<b>32.5</b>	27.58	6.77	0.97	5653
<b>33</b>	28.61	6.90	0.97	5735
<b>33.5</b>	28.27	6.74	0.94	5817
<b>34</b>	28.46	6.49	0.94	5899
<b>34.5</b>	28.72	6.58	0.91	5981
<b>35</b>	28.99	6.47	0.92	6062
<b>35.5</b>	28.87	6.50	0.93	6146
<b>36</b>	28.92	6.33	0.95	6227
<b>36.5</b>	28.49	6.38	0.94	6309
<b>37</b>	29.16	6.43	0.93	6390
<b>37.5</b>	29.39	6.48	0.95	6474
<b>38</b>	28.63	6.36	0.94	6559
<b>38.5</b>	28.48	6.14	0.93	6642
<b>39</b>	29.31	6.34	0.92	6724
<b>39.5</b>	29.72	6.48	0.90	6806
<b>40</b>	31.02	6.74	0.94	6888
<b>40.5</b>	30.75	6.54	0.93	6970
<b>41</b>	30.57	6.46	0.91	7051
<b>41.5</b>	30.94	6.27	0.89	7133
<b>42</b>	30.87	6.10	0.86	7214
<b>42.5</b>	30.58	5.83	0.87	7295
<b>43</b>	31.90	6.09	0.85	7376
<b>43.5</b>	31.83	6.20	0.89	7457
<b>44</b>	31.34	6.17	0.89	7538
<b>44.5</b>	31.79	6.22	0.87	7619
<b>45</b>	31.02	6.07	0.89	7700
<b>45.5</b>	30.63	5.86	0.91	7783
<b>46</b>	31.80	5.77	0.89	7867
<b>46.5</b>	31.42	5.48	0.90	7949
<b>47</b>	32.54	5.69	0.90	8028
<b>47.5</b>	31.79	5.35	0.92	8108
<b>48</b>	30.51	5.01	0.92	8190
<b>48.5</b>	31.34	5.22	0.90	8272
<b>49</b>	30.89	5.42	0.87	8353
<b>49.5</b>	31.13	5.61	0.82	8435
<b>50</b>	32.08	5.53	0.83	8530
<b>50.5</b>	32.96	5.53	0.85	8632
<b>54</b>	32.34	5.60	0.85	9243
<b>54.5</b>	32.39	5.63	0.86	9336
<b>55</b>	32.52	5.50	0.88	9421

<b>55.5</b>	32.79	5.46	0.89	9509
<b>56</b>	31.83	5.30	0.90	9597
<b>56.5</b>	31.54	5.39	0.89	9687
<b>57</b>	30.96	5.23	0.86	9774
<b>57.5</b>	31.33	5.35	0.86	9861
<b>58</b>	31.45	5.27	0.82	9950
<b>58.5</b>	30.75	4.93	0.84	10038
<b>59</b>	31.71	5.03	0.85	10126
<b>59.5</b>	31.46	4.78	0.89	10216
<b>60</b>	31.22	4.80	0.87	10305
<b>60.5</b>	31.51	4.61	0.88	10394
<b>61</b>	31.32	4.44	0.93	10486
<b>79.5</b>	30.60	4.48	0.94	13763
<b>80</b>	29.94	4.52	0.90	13849
<b>80.5</b>	29.40	4.51	0.90	13935
<b>81</b>	28.67	4.61	0.88	14023
<b>81.5</b>	28.18	4.61	0.87	14113
<b>82</b>	27.87	4.59	0.91	14203
<b>82.5</b>	27.93	5.45	0.89	14294
<b>83</b>	27.22	5.36	0.91	14387
<b>83.5</b>	27.03	5.15	0.90	14475
<b>84</b>	26.13	5.14	0.93	14563
<b>84.5</b>	25.59	5.28	0.92	14649
<b>85</b>	26.18	5.49	0.91	14735
<b>85.5</b>	26.24	5.35	0.88	14823
<b>86</b>	25.78	5.28	0.90	14912
<b>87</b>	25.06	5.13	0.89	15087
<b>87.5</b>	24.90	5.19	0.89	15174
<b>88</b>	24.39	5.21	0.89	15261
<b>88.5</b>	24.10	5.08	0.89	15350
<b>89</b>	24.11	5.01	0.87	15437
<b>89.5</b>	23.80	4.88	0.84	15525
<b>90</b>	23.98	4.99	0.83	15614
<b>90.5</b>	24.17	4.96	0.82	15703
<b>91</b>	24.13	4.85	0.84	15792
<b>91.5</b>	24.02	4.67	0.84	15878
<b>92</b>	23.90	4.59	0.84	15967
<b>92.5</b>	24.51	4.72	0.84	16056
<b>93</b>	24.44	4.63	0.82	16145
<b>93.5</b>	24.04	4.67	0.82	16234
<b>94</b>	23.97	4.59	0.83	16326
<b>94.5</b>	23.80	4.51	0.84	16415
<b>95</b>	23.89	4.32	0.84	16505
<b>95.5</b>	23.96	4.18	0.86	16592
<b>96</b>	25.32	4.27	0.83	16682
<b>96.5</b>	25.00	4.14	0.84	16771
<b>97</b>	24.51	4.03	0.84	16860
<b>97.5</b>	24.62	3.84	0.84	16952

<b>98</b>	24.32	3.91	0.83	17037
<b>98.5</b>	24.17	3.82	0.82	17124
<b>100.5</b>	23.57	3.84	0.83	17478
<b>101</b>	22.92	3.95	0.84	17566
<b>101.5</b>	22.36	3.82	0.85	17655
<b>102</b>	22.11	3.80	0.84	17740
<b>102.5</b>	21.64	3.70	0.83	17825
<b>103</b>	21.14	3.61	0.84	17912
<b>103.5</b>	20.72	3.46	0.84	17999
<b>104</b>	20.39	3.34	0.83	18091
<b>104.5</b>	19.95	3.36	0.80	18180
<b>105</b>	19.52	3.27	0.80	18268
<b>105.5</b>	19.33	3.30	0.79	18364
<b>106</b>	18.91	3.26	0.78	18441
<b>106.5</b>	18.57	3.25	0.78	18529
<b>107</b>	18.05	3.19	0.77	18619
<b>107.5</b>	17.80	3.20	0.76	18706
<b>108</b>	17.60	3.26	0.76	18792
<b>108.5</b>	17.32	3.23	0.78	18876
<b>109</b>	17.03	3.20	0.78	18969
<b>109.5</b>	16.74	3.15	0.78	19064
<b>110</b>	16.39	3.12	0.78	19150
<b>110.5</b>	16.48	3.22	0.75	19248
<b>111</b>	16.15	3.24	0.74	19335
<b>111.5</b>	16.05	3.09	0.73	19427
<b>112</b>	15.99	3.13	0.72	19534
<b>112.5</b>	16.05	3.01	0.72	19554
<b>113</b>	15.82	2.95	0.71	19573
<b>113.5</b>	15.56	2.92	0.73	19588
<b>114</b>	15.29	2.81	0.73	19601
<b>114.5</b>	15.10	2.90	0.72	19610
<b>115</b>	14.99	2.95	0.72	19619
<b>115.5</b>	14.78	2.90	0.73	19635
<b>116</b>	14.68	2.87	0.73	19645
<b>116.5</b>	14.70	2.90	0.72	19657
<b>117</b>	14.65	2.86	0.75	19676
<b>117.5</b>	14.61	2.96	0.77	19688
<b>118</b>	14.54	2.87	0.77	19698
<b>118.5</b>	14.52	2.97	0.76	19716
<b>119</b>	14.44	3.10	0.76	19725
<b>119.5</b>	14.38	3.13	0.75	19736
<b>120</b>	14.30	3.22	0.77	19747
<b>120.5</b>	14.52	3.39	0.80	19762
<b>121</b>	14.28	3.21	0.79	19767
<b>121.5</b>	14.22	3.22	0.79	19781
<b>122</b>	14.28	3.17	0.79	19790
<b>122.5</b>	14.49	3.20	0.81	19798
<b>123</b>	14.59	3.31	0.81	19810

<b>123.5</b>	15.23	3.69	0.80	19819
<b>124</b>	15.32	3.64	0.80	19827
<b>124.5</b>	14.99	3.46	0.80	19838
<b>125</b>	15.23	3.47	0.79	19843
<b>125.5</b>	15.49	3.50	0.81	19854
<b>126</b>	15.91	3.52	0.81	19864
<b>126.5</b>	16.13	3.56	0.83	19875
<b>127</b>	16.21	3.64	0.84	19887
<b>127.5</b>	15.76	3.53	0.84	19898
<b>128</b>	15.64	3.51	0.81	19907
<b>128.5</b>	15.43	3.48	0.79	19917
<b>129</b>	15.39	3.55	0.77	19928
<b>129.5</b>	15.35	3.58	0.75	19941
<b>130</b>	15.44	3.52	0.75	19953
<b>130.5</b>	15.24	3.48	0.75	19960
<b>131</b>	15.18	3.48	0.74	19969
<b>131.5</b>	15.17	3.32	0.75	19977
<b>132</b>	15.01	3.23	0.77	19989
<b>132.5</b>	14.81	3.22	0.75	19998
<b>133</b>	14.70	3.22	0.73	20008
<b>133.5</b>	14.67	3.29	0.72	20019
<b>134</b>	14.46	3.27	0.69	20029
<b>134.5</b>	14.33	3.20	0.67	20039
<b>135</b>	14.31	3.29	0.66	20045
<b>135.5</b>	14.43	3.28	0.65	20055
<b>136</b>	14.58	3.22	0.65	20063
<b>136.5</b>	14.58	3.20	0.65	20072
<b>137</b>	14.21	3.06	0.66	20080
<b>137.5</b>	14.17	3.05	0.65	20086
<b>138</b>	14.09	3.04	0.63	20096
<b>138.5</b>	13.96	2.94	0.62	20107
<b>139</b>	13.92	2.90	0.62	20118
<b>139.5</b>	13.91	2.91	0.63	20127
<b>140</b>	14.14	3.11	0.63	20133
<b>140.5</b>	14.26	3.16	0.62	20141
<b>141</b>	14.79	3.35	0.62	20152
<b>141.5</b>	14.77	3.23	0.63	20159
<b>142</b>	14.55	3.15	0.64	20170
<b>142.5</b>	14.47	3.12	0.65	20182
<b>143</b>	14.45	3.20	0.67	20191
<b>143.5</b>	14.36	3.25	0.68	20199
<b>144</b>	14.20	3.25	0.68	20206
<b>144.5</b>	14.54	3.36	0.67	20216
<b>145</b>	14.68	3.25	0.68	20223
<b>145.5</b>	14.65	3.25	0.71	20233
<b>146</b>	14.66	3.23	0.71	20241
<b>146.5</b>	14.52	3.27	0.72	20248
<b>147</b>	14.87	3.48	0.72	20255

147.5	15.14	3.67	0.71	20264
166.5	15.21	3.83	0.72	20609
167	15.28	3.99	0.72	20617
167.5	15.33	3.95	0.77	20624
168	16.08	4.13	1.83	20634
169	15.85	4.11	1.71	20653
169.5	15.57	4.00	1.62	20660
170	15.78	4.08	1.55	20667
170.5	15.72	4.13	1.48	20674
171	15.31	3.97	1.40	20683
171.5	15.66	3.94	1.33	20693
172	15.38	3.86	1.26	20703
172.5	15.36	3.88	1.19	20715
173	15.13	3.78	1.16	20722
173.5	15.05	3.74	1.12	20732
174	15.01	3.73	1.10	20741
174.5	15.00	3.79	1.06	20748
175	15.03	3.85	1.02	20757
175.5	14.74	3.81	0.98	20768
176	14.82	3.82	1.00	20776
176.5	14.89	3.80	1.00	20786
177	14.64	3.79	0.99	20794
177.5	14.69	3.86	0.94	20803
178	14.71	3.77	0.93	20811
178.5	14.66	3.85	0.91	20820
179	14.34	3.74	0.90	20831
179.5	14.04	3.72	0.89	20838
180	14.61	3.68	1.02	20845
181	14.65	3.69	1.05	20862
182	14.69	3.74	1.06	20882
182.5	14.64	3.67	1.03	20892
183	14.56	3.78	0.99	20902
183.5	14.60	3.83	0.94	20911
184	14.52	3.79	0.91	20921
184.5	14.90	4.03	0.88	20929
185	14.70	4.05	0.86	20939
185.5	14.48	3.90	0.89	20947
186	14.84	3.96	0.93	20956
186.5	14.89	4.03	0.92	20964
187	15.01	4.10	0.90	20974
187.5	14.80	3.97	0.87	20982
188	14.55	3.89	0.85	20992
188.5	14.76	3.90	0.85	21002
189	15.00	4.05	0.82	21013
189.5	14.86	4.10	0.79	21024
190	15.12	3.98	0.77	21034
190.5	15.08	3.92	0.78	21044
191	15.12	3.99	0.76	21054

191.5	15.00	4.02	0.75	21064
192	14.68	3.87	0.75	21075
192.5	14.57	3.88	0.74	21083
193	14.76	4.02	0.73	21090
194	14.88	4.24	0.72	21110
200.5	14.68	4.15	0.71	21226
201	14.60	4.00	0.71	21236
201.5	14.50	3.87	0.70	21246
202	14.34	3.65	0.69	21260
202.5	14.13	3.59	0.67	21271
203	13.98	3.50	0.67	21282
203.5	13.78	3.35	0.66	21292
204	13.68	3.37	0.65	21302
204.5	13.72	3.32	0.65	21312
205	13.62	3.18	0.67	21323
205.5	13.73	3.21	0.67	21332
206	13.57	3.12	0.66	21344
206.5	13.82	3.19	0.65	21354
207	13.64	3.16	0.68	21361
207.5	13.43	3.04	0.68	21368
208	13.30	2.97	0.67	21376
208.5	13.22	2.89	0.65	21385
209	13.58	2.90	0.64	21393
209.5	13.56	2.84	0.65	21401
210	13.62	2.82	0.64	21409
210.5	13.79	2.90	0.63	21417
211	13.76	2.85	0.64	21426
211.5	13.85	2.86	0.64	21436
212	14.00	2.98	0.66	21444
212.5	14.14	3.03	0.64	21451
213	14.47	3.10	0.64	21460
213.5	14.65	3.07	0.65	21470
214	14.48	3.00	0.63	21481
214.5	14.52	3.06	0.64	21492
215	14.35	3.00	0.61	21504
215.5	14.13	2.90	0.61	21514
216	14.09	2.79	0.61	21520
216.5	14.13	2.87	0.63	21527
217	14.06	2.90	0.62	21536
217.5	13.88	2.88	0.62	21550
218	13.76	2.79	0.61	21558
218.5	13.66	2.73	0.62	21567
219	13.42	2.74	0.62	21574
219.5	13.38	2.77	0.61	21581
220	13.27	2.77	0.60	21593
220.5	13.20	2.86	0.60	21604
221	13.27	2.84	0.61	21614
221.5	13.41	2.95	0.62	21625

<b>222</b>	13.23	2.89	0.62	21635
<b>222.5</b>	13.28	2.83	0.60	21648
<b>223</b>	13.28	2.83	0.59	21659
<b>223.5</b>	13.34	2.82	0.61	21666
<b>224</b>	13.24	2.89	0.62	21672
<b>224.5</b>	13.30	3.04	0.61	21685
<b>225</b>	13.37	3.10	0.59	21697
<b>225.5</b>	13.62	3.30	0.60	21706
<b>226</b>	13.56	3.26	0.59	21719
<b>226.5</b>	13.52	3.23	0.60	21733
<b>227</b>	13.52	3.29	0.61	21743
<b>227.5</b>	13.61	3.43	0.61	21751
<b>228</b>	13.75	3.46	0.61	21761
<b>228.5</b>	13.56	3.42	0.60	21771
<b>229</b>	13.62	3.49	0.61	21783
<b>229.5</b>	13.51	3.42	0.62	21796
<b>230</b>	13.46	3.37	0.63	21809
<b>230.5</b>	13.35	3.36	0.63	21820
<b>231</b>	13.15	3.32	0.63	21829
<b>231.5</b>	13.19	3.47	0.62	21841
<b>232</b>	13.27	3.52	0.63	21858
<b>232.5</b>	13.20	3.49	0.64	21873
<b>233</b>	13.26	3.44	0.66	21886
<b>233.5</b>	13.08	3.36	0.65	21894
<b>234</b>	13.32	3.70	0.63	21908
<b>234.5</b>	13.36	3.74	0.63	21924
<b>235</b>	13.54	3.68	0.63	21934
<b>235.5</b>	13.42	3.58	0.64	21947
<b>236</b>	13.59	3.59	0.64	21973
<b>236.5</b>	13.86	3.54	0.66	22088
<b>237</b>	13.90	3.44	0.64	22156
<b>237.5</b>	14.05	3.38	0.65	22215

**Supplementary Table 2.1.** XRF data for KC02.

**KC14**

<b>Depth (cm)</b>	<b>Si/Al (smoothed)</b>	<b>Ba/Al (smoothed)</b>	<b>Zr/Rb (smoothed)</b>	<b>Age (yrs)</b>
7	25.34	7.00	1.00	668
7.5	25.88	6.97	1.01	711
8	25.29	6.75	1.01	752
8.5	24.91	6.78	1.02	796
9	24.60	6.61	1.00	838
9.5	24.35	6.47	1.01	883
10	24.17	6.53	1.02	927
10.5	24.47	6.22	1.04	969
11	24.22	6.11	1.08	1013
11.5	24.92	6.43	1.09	1055
12	25.29	6.38	1.09	1098
12.5	25.32	6.32	1.06	1144
13	25.79	6.48	1.05	1189
13.5	28.19	7.02	1.03	1228
14	28.48	7.28	1.07	1273
14.5	29.19	7.55	1.08	1314
15	28.40	7.29	1.07	1357
15.5	28.64	7.32	1.07	1401
16	28.58	7.41	1.03	1446
16.5	29.05	7.78	1.03	1488
17	28.66	7.89	1.05	1529
17.5	28.77	7.87	1.06	1574
18	29.54	7.96	1.06	1616
18.5	28.99	7.74	1.06	1659
19	28.73	7.64	1.05	1703
19.5	30.90	8.09	1.06	1746
20	30.44	8.04	1.05	1791
20.5	29.94	7.92	1.05	1831
21	29.34	7.85	1.02	1873
21.5	30.43	8.32	1.01	1917
22	30.49	8.49	0.99	1958
22.5	30.38	8.58	0.97	2000
24.5	30.59	8.55	0.96	2171
27	30.16	8.39	0.96	2385
27.5	31.64	8.80	0.97	2428
29.5	31.49	8.80	0.96	2603
30	31.00	8.48	0.98	2647
30.5	30.03	8.11	0.98	2691
31	29.65	7.96	0.99	2735
31.5	29.18	7.67	1.01	2778
32	28.84	7.37	1.07	2826
32.5	28.79	7.26	1.04	2868
33	28.15	7.11	1.04	2908
33.5	27.87	6.96	1.05	2952
34	27.79	6.83	1.06	2998

<b>34.5</b>	27.30	6.74	1.05	3041
<b>35</b>	27.32	6.78	1.06	3086
<b>35.5</b>	27.25	6.72	1.05	3132
<b>36</b>	27.97	6.83	1.05	3178
<b>36.5</b>	27.84	6.63	1.04	3224
<b>37</b>	28.53	6.81	1.04	3267
<b>37.5</b>	28.93	7.01	1.04	3308
<b>38</b>	28.83	7.12	1.01	3350
<b>38.5</b>	28.58	7.16	1.00	3397
<b>39</b>	28.69	6.98	1.04	3442
<b>39.5</b>	29.19	7.27	1.02	3486
<b>40</b>	29.14	7.45	1.01	3527
<b>40.5</b>	29.74	7.38	0.97	3573
<b>41</b>	30.35	7.37	0.97	3616
<b>41.5</b>	30.46	7.33	0.98	3660
<b>42</b>	30.87	7.09	0.99	3705
<b>42.5</b>	31.24	7.20	0.97	3750
<b>43</b>	30.54	7.21	0.98	3792
<b>43.5</b>	31.13	7.41	0.95	3835
<b>44</b>	30.68	7.50	0.95	3879
<b>44.5</b>	29.97	7.16	0.96	3922
<b>45</b>	30.00	6.94	0.98	3969
<b>45.5</b>	31.73	7.29	0.99	4014
<b>46</b>	34.17	7.68	0.98	4058
<b>46.5</b>	33.59	7.39	1.00	4103
<b>47</b>	33.22	7.23	0.94	4146
<b>47.5</b>	33.46	7.16	0.91	4197
<b>48</b>	33.51	7.00	0.91	4239
<b>48.5</b>	33.67	7.23	0.95	4284
<b>49</b>	32.85	7.08	0.95	4327
<b>49.5</b>	34.43	7.56	0.97	4371
<b>50</b>	34.22	7.33	0.97	4411
<b>50.5</b>	34.51	7.35	0.96	4456
<b>51</b>	34.83	7.38	0.92	4503
<b>51.5</b>	35.28	7.14	0.93	4547
<b>52</b>	34.66	6.87	0.91	4588
<b>52.5</b>	36.46	7.30	0.89	4633
<b>53</b>	37.65	7.91	0.92	4678
<b>53.5</b>	37.04	7.69	0.93	4722
<b>54</b>	37.03	7.41	0.92	4765
<b>54.5</b>	37.45	7.10	0.94	4809
<b>55</b>	37.75	7.05	0.97	4852
<b>55.5</b>	36.02	6.83	0.95	4895
<b>56</b>	36.08	6.91	0.99	4938
<b>56.5</b>	35.98	6.77	0.97	4981
<b>57</b>	35.40	6.50	0.97	5023
<b>57.5</b>	34.52	6.20	0.98	5064
<b>58</b>	34.33	6.18	0.94	5110

<b>58.5</b>	33.98	6.11	0.96	5150
<b>59</b>	36.16	6.28	0.95	5192
<b>59.5</b>	36.29	6.32	0.95	5233
<b>60</b>	37.03	6.44	0.94	5277
<b>60.5</b>	36.25	6.19	0.94	5318
<b>61</b>	36.93	6.35	0.92	5362
<b>61.5</b>	35.87	6.13	0.93	5405
<b>62</b>	34.77	5.88	0.94	5451
<b>62.5</b>	35.51	6.09	0.93	5495
<b>63</b>	35.39	5.91	0.92	5537
<b>63.5</b>	35.58	6.06	0.93	5580
<b>64</b>	34.74	5.94	0.91	5622
<b>64.5</b>	34.09	5.77	0.90	5668
<b>65</b>	35.34	5.96	0.95	5713
<b>65.5</b>	34.68	5.96	0.96	5756
<b>66</b>	34.85	5.89	0.93	5799
<b>66.5</b>	34.13	5.71	0.92	5842
<b>67</b>	34.17	5.51	0.92	5885
<b>67.5</b>	33.73	5.40	0.92	5929
<b>68</b>	36.55	5.76	0.94	5973
<b>68.5</b>	35.60	5.84	0.95	6018
<b>69</b>	35.47	5.91	0.91	6061
<b>69.5</b>	34.45	5.70	0.95	6101
<b>70</b>	33.42	5.76	0.92	6146
<b>70.5</b>	33.24	5.63	0.92	6189
<b>71</b>	32.91	5.59	0.94	6232
<b>71.5</b>	32.57	5.49	0.99	6275
<b>72</b>	32.48	5.44	1.01	6311
<b>72.5</b>	31.94	5.40	1.04	6352
<b>73</b>	31.73	5.25	1.03	6391
<b>73.5</b>	31.95	5.12	1.02	6434
<b>74</b>	31.92	5.07	1.05	6478
<b>74.5</b>	32.84	5.39	1.06	6521
<b>75</b>	32.43	5.57	1.05	6563
<b>75.5</b>	31.98	5.53	1.08	6600
<b>76</b>	32.23	5.55	1.08	6638
<b>76.5</b>	33.72	5.59	1.08	6682
<b>77</b>	33.48	5.85	1.07	6726
<b>77.5</b>	33.20	5.69	1.05	6770
<b>78</b>	33.61	5.70	0.99	6813
<b>78.5</b>	32.53	5.46	0.99	6855
<b>79</b>	35.01	5.80	0.99	6898
<b>79.5</b>	34.87	5.83	0.98	6944
<b>80</b>	34.78	6.24	1.00	6988
<b>80.5</b>	36.12	6.35	0.99	7032
<b>81</b>	37.94	7.12	1.03	7072
<b>81.5</b>	38.50	7.21	1.02	7117
<b>82</b>	40.29	7.23	1.00	7162

<b>82.5</b>	39.19	7.00	0.98	7205
<b>83</b>	38.37	6.87	0.95	7248
<b>83.5</b>	37.67	6.81	0.97	7295
<b>84</b>	36.70	6.72	0.95	7337
<b>84.5</b>	36.38	6.46	0.96	7381
<b>85</b>	36.06	6.60	0.95	7427
<b>85.5</b>	36.93	6.50	0.95	7470
<b>86</b>	36.33	6.11	0.95	7515
<b>86.5</b>	37.67	6.01	0.93	7556
<b>87</b>	37.45	5.97	0.95	7601
<b>87.5</b>	37.36	5.99	0.94	7644
<b>88</b>	36.85	5.75	0.94	7688
<b>88.5</b>	37.52	5.76	0.99	7728
<b>89</b>	36.95	5.54	0.96	7770
<b>89.5</b>	36.36	5.60	0.94	7814
<b>90</b>	37.05	5.88	0.93	7859
<b>90.5</b>	36.01	5.92	0.96	7901
<b>91</b>	36.50	5.95	0.94	7946
<b>91.5</b>	36.77	5.85	0.88	7988
<b>92</b>	39.34	6.46	0.87	8030
<b>92.5</b>	39.30	6.21	0.86	8076
<b>93</b>	42.64	6.64	0.88	8119
<b>93.5</b>	42.07	6.58	0.90	8164
<b>94</b>	42.12	6.43	0.88	8211
<b>94.5</b>	40.94	5.99	0.90	8254
<b>95</b>	40.08	5.73	0.89	8300
<b>95.5</b>	39.36	5.57	0.92	8357
<b>96</b>	38.96	5.50	0.95	8442
<b>96.5</b>	38.33	5.24	0.93	8538
<b>97</b>	37.91	5.20	0.91	8628
<b>97.5</b>	39.05	5.12	0.90	8706
<b>98</b>	38.79	5.27	0.90	8779
<b>98.5</b>	39.61	5.25	0.91	8854
<b>99</b>	39.54	5.13	0.90	8930
<b>99.5</b>	40.08	5.18	0.90	9005
<b>100</b>	39.84	5.10	0.93	9083
<b>100.5</b>	39.43	4.98	0.94	9155
<b>101</b>	39.28	5.03	0.97	9232
<b>101.5</b>	39.18	4.83	1.03	9312
<b>102</b>	38.10	4.75	1.04	9391
<b>102.5</b>	37.48	4.67	1.02	9470
<b>103</b>	37.72	4.65	1.01	9548
<b>103.5</b>	36.51	4.66	1.05	9627
<b>104</b>	36.52	4.67	1.04	9708
<b>104.5</b>	37.84	5.06	1.06	9786
<b>105</b>	37.53	5.46	1.07	9867
<b>105.5</b>	36.49	5.42	1.06	9947
<b>106</b>	37.66	5.67	1.07	10026

<b>106.5</b>	37.73	5.37	1.06	10103
<b>107</b>	36.60	5.17	1.07	10183
<b>107.5</b>	37.17	5.09	1.04	10263
<b>108</b>	38.12	5.39	1.01	10343
<b>108.5</b>	37.28	5.11	1.00	10420
<b>109</b>	36.51	5.02	1.06	10500
<b>109.5</b>	36.56	5.08	1.08	10579
<b>110</b>	36.04	4.91	1.09	10657
<b>110.5</b>	35.51	4.81	1.08	10737
<b>111</b>	36.15	4.88	1.06	10819
<b>111.5</b>	36.30	4.87	1.08	10901
<b>114.4</b>	35.19	4.78	1.08	11371
<b>115</b>	33.78	4.57	1.07	11450
<b>115.4</b>	32.73	4.27	1.05	11532
<b>116</b>	31.74	4.10	1.05	11612
<b>116.4</b>	31.61	4.03	1.05	11692
<b>117</b>	30.88	3.79	1.06	11766
<b>117.4</b>	31.48	3.68	1.04	11841
<b>118</b>	31.11	3.59	1.02	11915
<b>118.4</b>	30.91	3.63	1.01	11998
<b>119</b>	30.67	3.61	0.99	12073
<b>119.4</b>	29.72	3.50	0.98	12155
<b>120</b>	28.84	3.46	0.97	12253
<b>120.4</b>	28.48	3.38	0.98	12311
<b>121</b>	28.59	3.46	1.00	12352
<b>121.4</b>	27.87	3.53	0.99	12396
<b>122</b>	27.29	3.59	0.99	12429
<b>122.4</b>	26.99	3.66	1.01	12463
<b>123</b>	26.99	3.76	1.01	12503
<b>123.4</b>	26.61	3.67	1.01	12538
<b>124</b>	26.24	3.57	1.01	12576
<b>124.4</b>	26.27	3.62	1.04	12607
<b>125</b>	26.82	3.70	1.06	12635
<b>125.4</b>	26.67	3.65	1.05	12667
<b>126</b>	26.19	3.65	1.05	12703
<b>126.4</b>	26.19	3.72	1.07	12738
<b>127</b>	25.97	3.73	1.07	12775
<b>127.4</b>	25.76	3.63	1.08	12809
<b>128</b>	26.32	3.88	1.08	12844
<b>128.4</b>	26.44	3.92	1.07	12881
<b>129</b>	25.70	3.77	1.03	12920
<b>129.4</b>	25.59	3.80	1.01	12954
<b>130</b>	25.60	3.80	1.01	12993
<b>130.4</b>	25.02	3.77	1.02	13025
<b>131</b>	24.75	3.65	1.01	13065
<b>131.4</b>	24.34	3.75	1.03	13100
<b>132</b>	24.95	3.94	1.02	13133
<b>132.4</b>	25.13	3.81	1.03	13165

<b>133</b>	25.37	3.70	1.04	13201
<b>133.4</b>	24.85	3.70	1.03	13239
<b>134</b>	24.97	3.57	1.02	13279
<b>134.4</b>	24.72	3.56	1.05	13315
<b>135</b>	24.91	3.66	1.04	13349
<b>135.4</b>	25.18	3.76	1.05	13385
<b>136</b>	25.10	3.79	1.04	13419
<b>136.4</b>	25.49	3.64	1.05	13456
<b>137</b>	25.30	3.53	1.03	13492
<b>137.4</b>	25.04	3.53	1.03	13527
<b>138</b>	24.33	3.40	1.02	13554
<b>138.4</b>	24.72	3.51	1.01	13583
<b>139</b>	25.36	3.67	1.01	13622
<b>139.4</b>	25.51	3.78	1.02	13652
<b>140</b>	26.13	3.96	1.02	13690
<b>140.4</b>	26.76	4.04	1.02	13721
<b>141</b>	27.40	4.07	1.05	13754
<b>141.4</b>	27.97	4.11	1.04	13793
<b>142</b>	27.98	3.98	1.04	13823
<b>142.4</b>	28.20	3.79	1.04	13857
<b>143</b>	28.25	3.75	0.99	13890
<b>143.4</b>	27.89	3.76	1.00	13924
<b>144</b>	28.48	3.76	1.02	13954
<b>144.4</b>	28.12	3.62	0.98	13989
<b>145</b>	28.21	3.45	0.96	14025
<b>145.4</b>	29.05	3.46	0.94	14060
<b>146</b>	30.83	3.42	0.96	14093
<b>146.4</b>	30.89	3.64	0.99	14132
<b>147</b>	30.19	3.77	0.99	14161
<b>147.4</b>	29.38	3.68	0.98	14196
<b>148</b>	28.67	3.65	0.97	14236
<b>148.4</b>	28.69	3.57	0.96	14275
<b>149</b>	28.81	3.65	0.97	14307
<b>149.4</b>	28.08	3.67	0.98	14335
<b>150</b>	28.14	3.82	0.95	14371
<b>150.4</b>	27.97	3.65	0.95	14405
<b>151</b>	27.64	3.57	0.95	14442
<b>151.4</b>	27.19	3.51	0.97	14469
<b>152</b>	27.41	3.39	0.97	14499
<b>152.4</b>	27.16	3.41	0.97	14540
<b>153</b>	26.67	3.41	1.01	14579
<b>153.4</b>	26.50	3.43	1.00	14613
<b>154</b>	27.13	3.47	0.99	14653
<b>154.4</b>	26.76	3.39	0.97	14687
<b>155</b>	26.21	3.25	0.94	14734
<b>155.4</b>	26.81	3.41	0.92	14776
<b>156</b>	26.51	3.38	0.93	14850
<b>156.4</b>	26.05	3.30	0.95	14941

<b>157</b>	25.82	3.35	0.97	15032
<b>157.4</b>	25.58	3.40	0.98	15104
<b>158</b>	25.18	3.37	0.98	15178
<b>158.4</b>	25.18	3.26	1.00	15252
<b>159</b>	24.81	3.26	1.00	15327
<b>159.4</b>	24.15	3.16	0.98	15401
<b>160</b>	23.87	3.08	0.95	15471
<b>160.4</b>	23.07	2.97	0.96	15533
<b>161</b>	22.57	2.95	0.93	15586
<b>161.4</b>	22.33	2.91	0.95	15656
<b>162</b>	22.36	3.09	0.96	15713
<b>162.4</b>	22.13	3.11	0.96	15776
<b>163</b>	22.71	3.14	0.93	15833
<b>163.4</b>	22.29	3.09	0.91	15896
<b>164</b>	22.13	3.11	0.92	15961
<b>164.4</b>	22.23	2.98	0.92	16023
<b>165</b>	21.85	2.93	0.89	16086
<b>165.4</b>	21.33	3.02	0.90	16148
<b>166</b>	21.15	2.98	0.88	16206
<b>166.4</b>	20.53	2.87	0.88	16270
<b>167</b>	20.69	2.94	0.87	16332
<b>167.4</b>	20.42	3.04	0.88	16398
<b>168</b>	20.42	3.02	0.89	16458
<b>168.4</b>	20.41	3.05	0.86	16515
<b>169</b>	20.42	2.93	0.85	16578
<b>169.4</b>	20.22	2.82	0.83	16641
<b>170</b>	19.81	2.78	0.84	16707
<b>170.4</b>	19.49	2.75	0.84	16769
<b>171</b>	19.36	2.77	0.84	16833
<b>171.4</b>	19.69	2.87	0.86	16892
<b>172</b>	19.75	2.87	0.85	16948
<b>172.4</b>	19.98	2.98	0.86	17005
<b>173</b>	19.99	2.96	0.86	17068
<b>173.4</b>	19.81	2.89	0.86	17127
<b>174</b>	19.59	2.85	0.85	17194
<b>174.4</b>	19.19	2.87	0.85	17251
<b>175</b>	19.15	2.94	0.84	17315
<b>175.4</b>	18.92	2.99	0.86	17382
<b>176</b>	18.96	2.97	0.88	17436
<b>176.4</b>	18.88	3.07	0.87	17504
<b>177</b>	18.78	3.08	0.89	17567
<b>177.4</b>	18.39	2.90	0.89	17627
<b>178</b>	18.14	2.95	0.89	17697
<b>178.4</b>	18.46	3.01	0.88	17761
<b>179</b>	18.19	2.97	0.86	17820
<b>179.4</b>	18.15	2.94	0.86	17880
<b>180</b>	17.91	2.85	0.87	17933
<b>180.4</b>	17.80	2.84	0.86	18006

<b>181</b>	17.68	2.73	0.86	18071
<b>181.4</b>	17.66	2.79	0.85	18134
<b>182</b>	17.39	2.74	0.84	18201
<b>182.4</b>	17.29	2.78	0.84	18267
<b>183</b>	17.37	2.63	0.87	18326
<b>183.4</b>	17.00	2.66	0.87	18389
<b>184</b>	16.93	2.59	0.87	18454
<b>184.4</b>	16.73	2.47	0.86	18512
<b>185</b>	16.54	2.40	0.86	18575
<b>185.4</b>	16.49	2.42	0.86	18635
<b>186</b>	16.39	2.33	0.85	18695
<b>186.4</b>	16.22	2.36	0.84	18755
<b>187</b>	16.11	2.28	0.87	18819
<b>187.4</b>	16.30	2.25	0.89	18881
<b>188</b>	16.72	2.13	0.90	18953
<b>188.4</b>	16.64	1.97	0.90	19014
<b>189</b>	16.45	1.86	0.90	19082
<b>189.4</b>	16.37	1.89	0.91	19146
<b>190</b>	16.38	1.94	0.92	19198
<b>190.4</b>	16.14	1.92	0.90	19257
<b>191</b>	16.01	1.93	0.90	19317
<b>191.4</b>	15.80	1.93	0.89	19369
<b>192</b>	15.65	1.93	0.91	19436
<b>192.4</b>	15.68	1.98	0.92	19494
<b>193</b>	15.59	2.02	0.93	19558
<b>193.4</b>	15.38	2.06	0.91	19619
<b>194</b>	15.44	2.21	0.89	19680
<b>194.4</b>	15.68	2.23	0.87	19744
<b>195</b>	16.04	2.32	0.86	19802

**Supplementary Table 2.2.** XRF data for KC14.

**KC04**

<b>Depth (cm)</b>	<b>Si/Al (smoothed)</b>	<b>Ba/Al (smoothed)</b>	<b>Zr/Rb (smoothed)</b>	<b>Age (yrs)</b>
4	12.13	4.09	1.03	2539
4.5	11.99	3.98	1.02	2624
5	12.15	4.33	0.98	2706
5.5	11.66	4.45	1.00	2785
6	11.71	4.51	1.00	2862
6.5	12.07	4.97	1.02	2936
7	12.63	5.35	1.00	3010
7.5	12.82	5.18	1.00	3082
8	14.16	6.10	0.97	3154
8.5	14.25	6.52	0.98	3228
9	13.99	6.69	0.97	3299
9.5	13.44	6.51	0.96	3373
10	13.27	6.57	0.97	3445
10.5	13.27	6.58	0.97	3521
11	13.10	6.76	0.99	3600
11.5	14.59	7.51	0.97	3676
12	16.22	8.42	0.95	3751
12.5	16.63	8.81	0.98	3829
13	16.60	9.21	0.99	3906
13.5	17.11	9.47	0.99	3980
14	17.82	9.84	1.01	4056
14.5	18.03	9.74	0.97	4132
15	18.49	9.78	0.96	4207
15.5	18.57	9.73	1.00	4285
16	18.64	9.97	0.98	4360
16.5	19.88	10.69	0.97	4437
17	20.09	10.62	0.95	4510
17.5	20.41	10.54	0.94	4586
18	20.97	10.54	0.96	4659
18.5	20.90	10.27	0.96	4736
19	20.92	10.14	1.02	4811
19.5	21.08	10.10	1.02	4888
20	21.24	10.04	1.03	4964
20.5	23.61	10.82	1.00	5040
21	23.53	10.66	1.01	5116
21.5	23.07	10.36	1.03	5191
22	23.93	10.57	1.00	5266
22.5	23.54	10.32	1.01	5339
23	23.82	10.12	1.00	5414
23.5	23.09	9.61	1.01	5489
24	23.39	9.57	1.02	5565
24.5	23.21	9.42	1.01	5639
25	23.04	9.42	0.96	5717
25.5	23.21	9.31	0.97	5794
26	23.71	9.32	0.98	5871

<b>26.5</b>	24.00	9.44	0.97	5944
<b>27</b>	23.57	9.15	0.93	6019
<b>27.5</b>	24.12	9.35	0.93	6098
<b>28</b>	25.20	9.35	0.94	6184
<b>28.5</b>	24.98	9.02	0.92	6368
<b>29</b>	25.05	8.76	0.92	6537
<b>29.5</b>	26.23	8.65	0.92	6703
<b>30</b>	26.47	8.63	0.91	6869
<b>30.5</b>	27.33	8.70	0.90	7041
<b>31</b>	27.94	8.52	0.92	7212
<b>31.5</b>	28.06	8.10	0.91	7380
<b>32</b>	28.47	8.04	0.96	7554
<b>32.5</b>	28.12	7.86	0.92	7723
<b>33</b>	28.46	8.19	0.94	7892
<b>33.5</b>	27.91	8.18	0.96	8069
<b>34</b>	28.31	8.23	0.93	8235
<b>34.5</b>	28.37	8.27	0.95	8407
<b>35</b>	27.59	8.02	0.93	8582
<b>35.5</b>	26.57	7.72	0.94	8752
<b>36</b>	25.69	7.54	0.93	8925
<b>36.5</b>	24.58	7.29	0.91	9097
<b>37</b>	24.02	7.08	0.91	9267
<b>37.5</b>	23.36	6.85	0.88	9437
<b>38</b>	22.93	6.59	0.89	9609
<b>38.5</b>	22.35	6.35	0.89	9783
<b>39</b>	21.88	6.17	0.88	9952
<b>39.5</b>	21.64	6.15	0.90	10119
<b>40</b>	22.18	6.37	0.91	10290
<b>40.5</b>	22.23	6.47	0.89	10466
<b>41</b>	21.86	6.40	0.90	10637
<b>41.5</b>	21.23	6.22	0.89	10807
<b>42</b>	20.90	6.04	0.90	10980
<b>42.5</b>	20.32	5.92	0.87	11152
<b>43</b>	20.01	5.74	0.86	11326
<b>43.5</b>	19.49	5.64	0.85	11499
<b>44</b>	19.21	5.54	0.84	11674
<b>44.5</b>	19.17	5.62	0.84	11841
<b>45</b>	18.81	5.48	0.83	12011
<b>45.5</b>	18.49	5.31	0.81	12186
<b>46</b>	18.33	5.20	0.83	12359
<b>46.5</b>	18.03	5.13	0.81	12524
<b>47</b>	17.71	4.94	0.83	12693
<b>47.5</b>	17.69	4.90	0.84	12861
<b>48</b>	17.48	4.70	0.83	13037
<b>48.5</b>	17.26	4.62	0.80	13208
<b>49</b>	17.62	4.69	0.84	13380
<b>49.5</b>	17.14	4.54	0.83	13550
<b>50</b>	16.93	4.33	0.81	13722

50.5	16.81	4.25	0.82	13894
51	16.47	4.09	0.80	14069
51.5	16.23	4.12	0.79	14241
52	15.82	4.06	0.77	14408
52.5	15.86	3.95	0.77	14574
53	15.88	3.86	0.76	14745
53.5	15.81	3.88	0.74	14916
54	15.94	3.71	0.73	15084
54.5	15.62	3.67	0.73	15250
55	15.42	3.52	0.75	15412
55.5	15.27	3.49	0.73	15577
56	15.19	3.43	0.73	15738
56.5	14.90	3.31	0.71	15904
57	14.80	3.23	0.71	16069
57.5	14.51	3.17	0.70	16239
58	14.43	3.12	0.71	16429
58.5	14.39	3.01	0.72	16480
59	14.22	2.96	0.72	16501
59.5	14.30	2.98	0.70	16525
60	14.12	2.97	0.71	16551
60.5	14.10	2.95	0.72	16572
61	13.94	2.93	0.74	16595
61.5	13.79	2.92	0.74	16614
62	13.91	2.92	0.73	16632
62.5	14.00	2.84	0.73	16653
63	13.95	2.81	0.73	16668
63.5	14.37	2.83	0.73	16685
64	14.76	3.03	0.74	16704
64.5	14.87	3.02	0.75	16720
65	14.52	2.90	0.77	16738
65.5	14.41	2.95	0.76	16751
66	14.88	3.08	0.78	16769
66.5	14.74	3.12	0.80	16785
67	14.80	3.17	0.79	16805
67.5	14.91	3.25	0.79	16821
68	14.85	3.25	0.78	16843
68.5	14.81	3.14	0.77	16858
69	15.04	3.22	0.75	16876
69.5	15.07	3.20	0.75	16890
70	15.26	3.23	0.75	16907
70.5	15.35	3.33	0.76	16922
71	15.14	3.29	0.76	16936
71.5	15.34	3.26	0.76	16951
72	15.15	3.37	0.74	16966
72.5	15.79	3.57	0.76	16980
73	15.55	3.48	0.78	16997
73.5	15.58	3.50	0.79	17023
74	15.70	3.55	0.80	17043

74.5	15.49	3.42	0.78	17059
75	15.12	3.33	0.78	17069
75.5	15.09	3.31	0.77	17084
76	15.09	3.18	0.75	17106
76.5	14.92	3.15	0.77	17119
77	14.67	3.06	0.77	17136
77.5	14.75	3.13	0.76	17152
78	14.44	3.00	0.77	17166
78.5	14.31	2.99	0.77	17177
79	14.26	2.98	0.77	17193
79.5	14.15	2.94	0.75	17208
80	14.22	2.91	0.75	17223
80.5	14.16	2.89	0.73	17240
81	14.27	3.01	0.74	17257
81.5	14.12	3.04	0.75	17272
82	14.03	3.04	0.74	17286
82.5	14.30	3.16	0.75	17296
83	14.26	3.07	0.78	17313
83.5	14.46	3.21	0.76	17332
84	14.89	3.27	0.76	17348
84.5	14.73	3.17	0.76	17369
85	14.72	3.17	0.77	17389
85.5	14.66	3.12	0.79	17406
86	14.78	3.23	0.80	17423
86.5	14.55	3.11	0.82	17439
87	14.52	3.06	0.83	17452
87.5	14.32	2.96	0.84	17468
88	14.43	2.95	0.83	17487
88.5	14.29	2.78	0.83	17503
89	14.12	2.93	0.82	17517
89.5	14.00	2.95	0.82	17535
90	14.27	2.97	0.81	17545
90.5	14.15	3.00	0.83	17561
91	13.88	2.91	0.80	17577
91.5	13.58	2.85	0.80	17588
92	13.59	2.87	0.79	17602
92.5	13.35	2.77	0.79	17615
93	13.44	2.91	0.77	17629
93.5	13.26	2.95	0.81	17644
94	13.44	3.21	0.79	17659
94.5	13.54	3.33	0.79	17673
95	13.59	3.34	0.78	17689
95.5	13.46	3.29	0.76	17703
96	13.20	3.18	0.77	17718
96.5	12.96	3.09	0.77	17733
97	12.83	3.09	0.77	17747
97.5	12.76	3.11	0.78	17766
100.5	12.84	3.15	0.77	17859

<b>101</b>	13.13	3.23	0.75	17877
<b>101.5</b>	13.44	3.28	0.74	17894
<b>102</b>	13.37	3.29	0.74	17910
<b>102.5</b>	13.29	3.43	0.72	17926
<b>103</b>	13.53	3.53	0.72	17941
<b>103.5</b>	13.72	3.54	0.73	17955
<b>104</b>	13.80	3.60	0.77	17969
<b>104.5</b>	13.82	3.58	0.78	17985
<b>105</b>	14.11	3.69	0.79	17999
<b>105.5</b>	14.21	3.75	0.79	18015
<b>106</b>	14.18	3.70	0.77	18026
<b>106.5</b>	14.29	3.84	0.78	18040
<b>107</b>	14.25	3.78	0.77	18053
<b>107.5</b>	14.40	3.73	0.76	18068
<b>108</b>	14.24	3.61	0.76	18084
<b>108.5</b>	14.24	3.59	0.78	18102
<b>109</b>	14.17	3.44	0.75	18115
<b>109.5</b>	14.00	3.43	0.75	18131
<b>110</b>	13.89	3.35	0.76	18146
<b>110.5</b>	13.88	3.35	0.77	18161
<b>111</b>	13.91	3.29	0.76	18176
<b>111.5</b>	13.88	3.28	0.76	18189
<b>112</b>	13.87	3.30	0.77	18204
<b>112.5</b>	13.82	3.34	0.77	18219
<b>113</b>	14.00	3.33	0.75	18233
<b>113.5</b>	14.12	3.41	0.76	18247
<b>114</b>	14.20	3.51	0.76	18260
<b>114.5</b>	14.28	3.50	0.77	18274
<b>115</b>	14.43	3.49	0.77	18286
<b>115.5</b>	14.37	3.36	0.76	18302
<b>116</b>	14.39	3.31	0.75	18318
<b>116.5</b>	14.51	3.27	0.75	18337
<b>117</b>	14.66	3.25	0.75	18357
<b>117.5</b>	14.75	3.18	0.77	18373
<b>118</b>	14.66	3.18	0.78	18384
<b>118.5</b>	14.66	3.25	0.78	18402
<b>119</b>	14.90	3.36	0.76	18420
<b>119.5</b>	14.60	3.23	0.78	18438
<b>120</b>	14.61	3.30	0.79	18451
<b>120.5</b>	14.51	3.22	0.78	18468
<b>121</b>	14.44	3.21	0.78	18482
<b>121.5</b>	14.29	3.18	0.79	18498
<b>122</b>	14.30	3.19	0.78	18511
<b>122.5</b>	14.13	3.12	0.76	18524
<b>123</b>	14.20	3.26	0.78	18535
<b>123.5</b>	13.90	3.19	0.76	18550
<b>124</b>	14.12	3.14	0.73	18556
<b>124.5</b>	14.17	3.20	0.72	18573

<b>125</b>	14.12	3.16	0.74	18589
<b>125.5</b>	14.17	3.19	0.75	18604
<b>126</b>	14.24	3.04	0.75	18620
<b>126.5</b>	14.17	2.95	0.77	18639
<b>127</b>	14.31	2.91	0.75	18655
<b>127.5</b>	14.15	2.88	0.73	18669
<b>128</b>	14.08	2.84	0.73	18686
<b>128.5</b>	13.88	2.78	0.71	18701
<b>129</b>	13.89	2.85	0.70	18717
<b>129.5</b>	14.15	2.86	0.71	18731
<b>130</b>	14.08	2.90	0.71	18741
<b>130.5</b>	14.16	2.92	0.71	18753
<b>131</b>	14.27	3.18	0.72	18768
<b>131.5</b>	14.14	3.13	0.70	18787
<b>132</b>	14.16	3.20	0.69	18801
<b>132.5</b>	14.13	3.22	0.73	18815
<b>133</b>	13.96	3.16	0.76	18830
<b>133.5</b>	14.02	3.17	0.78	18842
<b>134</b>	14.07	3.15	0.78	18854
<b>134.5</b>	14.20	3.23	0.75	18868
<b>135</b>	14.24	3.21	0.76	18879
<b>135.5</b>	13.99	3.35	0.77	18894
<b>136</b>	14.24	3.38	0.77	18915
<b>136.5</b>	14.35	3.43	0.76	18933
<b>137</b>	14.54	3.42	0.75	18949
<b>137.5</b>	14.43	3.32	0.74	18962
<b>138</b>	14.35	3.33	0.74	18985
<b>138.5</b>	14.16	3.24	0.77	19007
<b>139</b>	14.27	3.15	0.77	19023
<b>139.5</b>	14.13	3.20	0.76	19035
<b>140</b>	14.22	3.24	0.75	19052
<b>140.5</b>	14.06	3.20	0.73	19070
<b>141</b>	14.53	3.26	0.75	19087
<b>141.5</b>	14.68	3.34	0.76	19104
<b>142</b>	14.56	3.21	0.73	19118
<b>142.5</b>	14.58	3.22	0.74	19131
<b>143</b>	14.60	3.16	0.72	19144
<b>143.5</b>	14.69	3.23	0.74	19157
<b>144</b>	14.50	3.14	0.75	19165
<b>144.5</b>	14.57	3.21	0.73	19177
<b>145</b>	14.54	3.15	0.72	19192
<b>145.5</b>	14.47	3.20	0.71	19205
<b>146</b>	14.57	3.17	0.68	19217
<b>146.5</b>	14.79	3.28	0.67	19234
<b>147</b>	14.78	3.29	0.70	19251
<b>147.5</b>	14.78	3.20	0.71	19268
<b>148</b>	14.56	3.15	0.71	19282
<b>148.5</b>	14.33	3.14	0.71	19297

<b>149</b>	14.16	3.07	0.72	19315
<b>149.5</b>	14.11	3.05	0.72	19329
<b>150</b>	14.13	3.03	0.71	19345
<b>150.5</b>	13.99	3.12	0.72	19362
<b>151</b>	13.94	3.00	0.72	19376
<b>151.5</b>	13.81	2.98	0.72	19392
<b>152</b>	13.95	2.95	0.75	19408
<b>152.5</b>	13.75	2.94	0.74	19421
<b>153</b>	13.73	2.96	0.73	19435
<b>153.5</b>	13.97	3.02	0.73	19449
<b>154</b>	14.02	2.97	0.73	19466
<b>154.5</b>	14.00	2.99	0.72	19480
<b>155</b>	14.02	3.00	0.73	19495
<b>155.5</b>	13.94	2.92	0.72	19510
<b>156</b>	13.94	2.90	0.72	19530
<b>156.5</b>	13.75	2.87	0.72	19543
<b>157</b>	14.09	3.23	0.71	19553
<b>157.5</b>	14.06	3.20	0.71	19571
<b>159</b>	14.44	3.58	0.72	19616
<b>159.5</b>	14.52	3.62	0.71	19633
<b>160</b>	14.70	3.69	0.70	19653
<b>160.5</b>	14.60	3.67	0.72	19666
<b>161</b>	14.43	3.61	0.72	19678
<b>161.5</b>	14.37	3.50	0.72	19688
<b>162</b>	14.35	3.49	0.73	19703
<b>162.5</b>	14.33	3.35	0.72	19718
<b>163</b>	14.32	3.33	0.72	19730
<b>163.5</b>	14.12	3.26	0.71	19743
<b>164</b>	14.11	3.22	0.72	19758
<b>164.5</b>	14.11	3.15	0.70	19770
<b>165</b>	14.04	3.13	0.69	19783
<b>165.5</b>	14.04	3.11	0.68	19798
<b>166</b>	14.22	3.22	0.68	19812
<b>166.5</b>	14.27	3.18	0.71	19825
<b>167</b>	14.12	3.13	0.73	19840
<b>167.5</b>	14.15	3.05	0.73	19851
<b>168</b>	14.18	3.04	0.73	19867
<b>168.5</b>	14.17	3.10	0.75	19883
<b>169</b>	14.11	3.09	0.75	19893
<b>169.5</b>	14.02	3.04	0.75	19909
<b>170</b>	14.25	3.10	0.74	19922
<b>170.5</b>	14.25	3.01	0.74	19935
<b>171</b>	14.09	3.03	0.72	19947
<b>171.5</b>	14.12	2.99	0.71	19956
<b>172</b>	14.03	2.99	0.72	19963
<b>172.5</b>	13.99	2.98	0.73	19977
<b>173</b>	14.06	2.94	0.74	19990
<b>173.5</b>	14.00	2.93	0.74	20003

<b>174</b>	14.09	2.94	0.71	20017
<b>174.5</b>	13.93	2.94	0.71	20033
<b>175</b>	13.93	3.01	0.71	20048
<b>175.5</b>	13.89	3.01	0.73	20064
<b>176</b>	13.81	2.94	0.73	20078
<b>176.5</b>	13.66	2.83	0.73	20092
<b>177</b>	13.68	2.86	0.73	20105
<b>177.5</b>	14.07	2.94	0.72	20122
<b>178</b>	14.23	2.96	0.73	20135
<b>178.5</b>	14.16	3.01	0.73	20144
<b>179</b>	14.04	3.01	0.71	20157
<b>179.5</b>	14.09	3.10	0.70	20182
<b>180</b>	14.18	3.13	0.69	20198
<b>180.5</b>	14.23	3.14	0.69	20214
<b>181</b>	14.13	3.15	0.68	20226
<b>181.5</b>	14.01	3.08	0.69	20237
<b>182</b>	14.19	3.07	0.69	20247
<b>182.5</b>	14.16	3.13	0.69	20266
<b>183</b>	14.11	3.17	0.70	20279
<b>183.5</b>	14.16	3.35	0.69	20295
<b>184</b>	14.35	3.50	0.71	20306
<b>184.5</b>	14.39	3.56	0.70	20318
<b>185</b>	14.52	3.64	0.72	20332
<b>185.5</b>	14.62	3.75	0.71	20346
<b>186</b>	14.60	3.79	0.73	20356
<b>186.5</b>	14.58	3.79	0.72	20371
<b>187</b>	14.67	3.74	0.72	20387
<b>187.5</b>	14.85	3.75	0.73	20397
<b>188</b>	14.65	3.71	0.73	20409

**Supplementary Table 2.3.** XRF data for KC04.

**KC12**

<b>Depth (cm)</b>	<b>Si/Al (smoothed)</b>	<b>Ba/Al (smoothed)</b>	<b>Zr/Rb (smoothed)</b>	<b>Age (yrs)</b>
4	21.50	5.19	0.93	649
4.5	21.53	5.30	0.94	766
5	21.77	5.30	0.95	849
5.5	21.81	5.36	0.93	923
6	21.79	5.56	0.94	995
6.5	21.76	5.65	0.94	1060
7.5	21.80	5.70	0.94	1208
8	22.12	5.87	0.97	1278
8.5	22.51	5.90	0.97	1352
9	22.39	5.89	0.96	1427
9.5	22.69	6.03	0.94	1506
10	22.72	6.04	0.95	1576
10.5	22.58	5.98	0.95	1645
11	23.10	6.10	0.95	1718
11.5	23.22	6.18	0.98	1801
12	23.37	6.15	0.97	1863
12.5	23.28	6.09	0.96	1924
13	23.67	6.34	0.97	1988
13.5	24.54	6.80	0.97	2062
14	24.87	6.85	0.98	2128
14.5	25.19	6.75	1.01	2196
15	24.63	6.58	0.99	2259
15.5	24.74	6.51	0.99	2335
16	24.18	6.38	0.99	2403
16.5	24.53	6.46	0.98	2469
17	24.94	6.64	0.97	2532
17.5	24.60	6.51	0.97	2603
18	24.12	6.32	0.97	2671
18.5	23.99	6.36	0.97	2731
19	24.64	6.58	0.95	2802
19.5	25.06	6.71	0.95	2872
20	25.58	6.79	0.95	2945
20.5	25.24	6.78	0.94	3015
21	25.23	6.72	0.92	3088
21.5	25.49	6.75	0.92	3155
22	25.81	6.88	0.93	3223
22.5	25.84	6.87	0.92	3296
23	25.42	6.80	0.91	3359
23.5	25.32	6.74	0.91	3422
24	25.40	6.89	0.93	3485
24.5	25.20	6.87	0.93	3555
25	25.08	6.83	0.93	3629
25.5	25.06	6.85	0.93	3696
26	25.03	6.78	0.92	3768
26.5	24.65	6.62	0.94	3837

<b>27</b>	24.60	6.53	0.91	3919
<b>27.5</b>	24.49	6.42	0.90	3988
<b>28</b>	24.77	6.64	0.90	4056
<b>28.5</b>	24.81	6.59	0.95	4121
<b>29</b>	24.37	6.46	0.98	4181
<b>29.5</b>	25.06	6.70	0.96	4248
<b>30</b>	25.15	6.61	0.98	4319
<b>30.5</b>	24.75	6.51	0.97	4390
<b>31</b>	24.96	6.52	0.95	4459
<b>31.5</b>	25.36	6.63	0.99	4531
<b>32</b>	25.35	6.64	0.95	4602
<b>32.5</b>	25.39	6.61	0.95	4669
<b>33</b>	25.39	6.56	0.94	4734
<b>33.5</b>	25.20	6.38	0.93	4804
<b>34</b>	25.65	6.54	0.92	4872
<b>34.5</b>	26.42	6.76	0.93	4937
<b>35</b>	26.00	6.56	0.92	5006
<b>35.5</b>	25.43	6.37	0.96	5078
<b>36</b>	26.01	6.66	0.96	5138
<b>36.5</b>	26.70	6.75	0.96	5210
<b>37</b>	27.07	6.72	0.95	5278
<b>37.5</b>	26.66	6.60	0.97	5352
<b>38</b>	26.97	6.56	0.94	5420
<b>38.5</b>	26.37	6.29	0.92	5488
<b>39</b>	26.36	6.40	0.90	5553
<b>39.5</b>	26.78	6.47	0.90	5616
<b>40</b>	26.80	6.57	0.92	5687
<b>40.5</b>	26.51	6.44	0.94	5758
<b>41</b>	26.81	6.46	0.93	5828
<b>41.5</b>	26.91	6.54	0.93	5897
<b>42</b>	27.84	6.88	0.92	5966
<b>42.5</b>	28.53	7.05	0.92	6038
<b>43</b>	28.52	6.97	0.93	6111
<b>43.5</b>	28.32	6.81	0.91	6177
<b>44</b>	28.52	6.71	0.89	6245
<b>44.5</b>	28.83	6.60	0.90	6312
<b>45</b>	29.51	6.72	0.88	6380
<b>45.5</b>	29.68	6.67	0.88	6445
<b>46</b>	30.28	6.55	0.90	6509
<b>46.5</b>	30.05	6.41	0.92	6579
<b>47</b>	30.47	6.54	0.92	6635
<b>47.5</b>	31.03	6.73	0.91	6704
<b>48</b>	31.84	6.93	0.90	6780
<b>48.5</b>	31.92	6.92	0.87	6853
<b>49</b>	31.76	6.63	0.88	6917
<b>49.5</b>	31.89	6.52	0.91	6969
<b>50</b>	31.95	6.48	0.95	7040
<b>50.5</b>	32.33	6.68	0.96	7115

<b>51</b>	32.31	6.69	0.93	7178
<b>51.5</b>	32.02	6.67	0.93	7239
<b>52</b>	31.82	6.52	0.94	7319
<b>52.5</b>	31.59	6.54	0.93	7380
<b>53</b>	31.31	6.06	0.93	7436
<b>53.5</b>	31.21	5.91	0.93	7513
<b>54</b>	32.46	6.04	0.92	7580
<b>54.5</b>	33.61	6.40	0.90	7640
<b>55</b>	33.10	6.31	0.90	7718
<b>55.5</b>	32.70	6.13	0.93	7794
<b>56</b>	34.53	6.64	0.93	7859
<b>56.5</b>	34.68	6.61	0.90	7925
<b>62.5</b>	36.20	6.69	0.88	8707
<b>63</b>	37.76	6.64	0.95	8780
<b>63.5</b>	38.25	6.36	0.96	8855
<b>64</b>	37.81	6.22	0.93	8930
<b>64.5</b>	36.77	5.99	0.91	8999
<b>65</b>	36.61	6.05	0.88	9081
<b>65.5</b>	37.20	6.17	0.89	9163
<b>66</b>	36.43	6.24	0.90	9227
<b>66.5</b>	35.23	6.01	0.87	9315
<b>67</b>	34.74	5.76	0.85	9396
<b>67.5</b>	34.53	5.72	0.82	9480
<b>68</b>	35.07	5.97	0.84	9608
<b>68.5</b>	35.18	6.02	0.88	9798
<b>69</b>	36.28	5.93	0.84	9962
<b>69.5</b>	35.85	5.65	0.84	10120
<b>70</b>	34.72	5.49	0.85	10276
<b>70.5</b>	34.08	5.51	0.86	10439
<b>71</b>	34.57	5.64	0.87	10585
<b>71.5</b>	33.88	5.47	0.90	10737
<b>72</b>	33.58	5.54	0.87	10894
<b>72.5</b>	33.66	5.73	0.87	11049
<b>73</b>	34.48	6.03	0.92	11208
<b>73.5</b>	34.28	5.96	0.91	11366
<b>74</b>	33.58	6.04	0.92	11527
<b>74.5</b>	33.22	6.17	0.95	11698
<b>75</b>	33.51	6.28	0.90	11857
<b>75.5</b>	32.73	6.13	0.88	12017
<b>76</b>	31.96	5.84	0.89	12171
<b>76.5</b>	31.24	5.87	0.87	12327
<b>77</b>	30.57	5.85	0.88	12492
<b>77.5</b>	30.88	6.09	0.88	12655
<b>78</b>	31.31	5.92	0.85	12810
<b>78.5</b>	31.02	5.86	0.88	12969
<b>79</b>	30.94	5.85	0.87	13123
<b>79.5</b>	30.28	5.72	0.86	13288
<b>80</b>	29.42	5.68	0.88	13444

<b>80.5</b>	28.69	5.60	0.90	13607
<b>81</b>	27.79	5.61	0.91	13766
<b>81.5</b>	27.21	5.66	0.90	13921
<b>82</b>	27.22	5.77	0.90	14095
<b>82.5</b>	27.00	5.74	0.90	14250
<b>83</b>	26.29	5.71	0.92	14402
<b>83.5</b>	25.88	5.64	0.91	14557
<b>84</b>	25.72	5.45	0.91	14705
<b>84.5</b>	24.97	5.19	0.90	14858
<b>85</b>	24.54	5.01	0.93	15018
<b>86</b>	24.53	5.12	0.94	15307
<b>86.5</b>	24.76	5.22	0.92	15472
<b>87</b>	25.14	5.35	0.91	15638
<b>87.5</b>	25.37	5.38	0.89	15790
<b>88</b>	24.86	5.21	0.87	15951
<b>88.5</b>	25.02	5.12	0.90	16115
<b>89</b>	24.64	4.86	0.89	16279
<b>90</b>	24.33	4.73	0.89	16603
<b>90.5</b>	23.95	4.66	0.90	16756
<b>91</b>	23.66	4.62	0.90	16919
<b>91.5</b>	22.88	4.40	0.91	17077
<b>92</b>	22.39	4.17	0.94	17247
<b>92.5</b>	21.93	3.99	0.93	17394
<b>93</b>	21.49	3.91	0.94	17569
<b>93.5</b>	21.29	3.73	0.93	17737
<b>94</b>	20.60	3.66	0.92	17891
<b>94.5</b>	20.14	3.64	0.91	18041
<b>95</b>	20.19	3.71	0.89	18198
<b>95.5</b>	19.80	3.67	0.89	18349
<b>96</b>	19.32	3.61	0.91	18497
<b>96.5</b>	19.21	3.52	0.92	18653
<b>97</b>	19.18	3.53	0.91	18823
<b>100.5</b>	18.60	3.42	0.90	20095
<b>101</b>	18.34	3.36	0.92	20237
<b>101.5</b>	18.02	3.28	0.90	20366
<b>102</b>	17.81	3.20	0.93	20467
<b>102.5</b>	17.51	3.16	0.93	20574
<b>103</b>	17.33	3.11	0.93	20667
<b>103.5</b>	17.14	3.02	0.94	20793
<b>104</b>	16.80	2.89	0.92	20880
<b>104.5</b>	16.69	2.90	0.93	20969
<b>105</b>	16.67	2.85	0.93	21056
<b>105.5</b>	16.40	2.81	0.92	21168
<b>106</b>	16.22	2.74	0.91	21245
<b>106.5</b>	15.97	2.72	0.89	21318
<b>107</b>	15.68	2.63	0.88	21407
<b>107.5</b>	15.82	2.67	0.88	21497
<b>108</b>	15.55	2.60	0.85	21600

<b>108.5</b>	15.38	2.57	0.83	21675
<b>109</b>	15.23	2.63	0.84	21770
<b>109.5</b>	15.19	2.57	0.82	21858
<b>110</b>	15.34	2.56	0.84	21941
<b>110.5</b>	15.51	2.57	0.84	22033
<b>111</b>	15.34	2.58	0.85	22114
<b>111.5</b>	15.39	2.56	0.84	22205
<b>112</b>	15.33	2.54	0.85	22315
<b>112.5</b>	15.18	2.52	0.84	22419
<b>113</b>	15.05	2.55	0.83	22512
<b>113.5</b>	15.01	2.66	0.83	22599
<b>114</b>	14.99	2.66	0.82	22667
<b>114.5</b>	14.91	2.61	0.84	22759
<b>115</b>	14.77	2.60	0.84	22843
<b>115.5</b>	14.55	2.52	0.85	22950
<b>116</b>	14.53	2.55	0.86	23039
<b>116.5</b>	14.65	2.67	0.86	23122
<b>117</b>	14.52	2.64	0.85	23198
<b>117.5</b>	14.36	2.61	0.83	23288
<b>118</b>	14.37	2.50	0.86	23385
<b>118.5</b>	14.28	2.51	0.86	23476
<b>119</b>	14.09	2.53	0.86	23581
<b>119.5</b>	13.90	2.54	0.86	23686
<b>120</b>	13.92	2.55	0.85	23773
<b>120.5</b>	13.92	2.47	0.86	23865
<b>121</b>	14.16	2.42	0.85	23956
<b>121.5</b>	14.22	2.36	0.84	24061
<b>122</b>	14.27	2.46	0.85	24140
<b>122.5</b>	14.27	2.50	0.84	24209
<b>123</b>	14.12	2.44	0.82	24300
<b>123.5</b>	14.09	2.52	0.82	24384
<b>124</b>	13.93	2.49	0.83	24469
<b>124.5</b>	14.19	2.50	0.84	24557
<b>125</b>	14.06	2.40	0.84	24628
<b>125.5</b>	13.97	2.31	0.84	24719
<b>126</b>	13.80	2.34	0.84	24790
<b>126.5</b>	13.81	2.38	0.84	24884
<b>127</b>	13.69	2.32	0.87	24978
<b>127.5</b>	13.53	2.35	0.87	25054
<b>128</b>	13.74	2.33	0.86	25134
<b>128.5</b>	13.84	2.37	0.85	25228
<b>129</b>	13.81	2.42	0.86	25315
<b>129.5</b>	13.70	2.32	0.85	25408
<b>130</b>	13.58	2.35	0.84	25471
<b>130.5</b>	13.45	2.31	0.85	25554
<b>131</b>	13.49	2.37	0.85	25643
<b>131.5</b>	13.42	2.36	0.85	25716
<b>132</b>	13.49	2.43	0.84	25796

132.5	13.41	2.35	0.83	25873
133	13.60	2.34	0.83	25957
133.5	13.84	2.41	0.85	26031
134	13.81	2.41	0.84	26126
134.5	13.86	2.46	0.84	26200
135	13.84	2.47	0.81	26251
135.5	13.82	2.58	0.80	26368
136	13.87	2.66	0.81	26454
139	14.13	2.78	0.79	26957
139.5	13.99	2.84	0.78	27059
140	14.01	2.84	0.80	27156
140.5	13.98	2.82	0.78	27211
141	14.10	2.73	0.80	27313
141.5	14.19	2.71	0.82	27404
142	14.15	2.62	0.82	27498
142.5	14.24	2.61	0.83	27577
143	14.17	2.54	0.83	27654
143.5	14.11	2.59	0.84	27756
144	14.20	2.55	0.82	27838
144.5	14.26	2.56	0.82	27906
145	14.40	2.58	0.81	27964
145.5	14.66	2.64	0.81	28046
146	14.72	2.67	0.81	28138
146.5	14.78	2.65	0.81	28217
147	14.74	2.69	0.82	28279
147.5	14.58	2.66	0.81	28379
148	14.49	2.64	0.81	28499
148.5	14.59	2.64	0.81	28600
149	14.63	2.66	0.79	28676
149.5	14.48	2.65	0.80	28790
150	14.38	2.58	0.86	28872
150.5	14.11	2.47	0.85	28947
151	14.07	2.44	0.85	29029
151.5	14.13	2.37	0.87	29090
152	13.99	2.32	0.86	29167
152.5	13.94	2.25	0.85	29230
153	13.98	2.20	0.86	29319
153.5	14.06	2.20	0.87	29401
154	14.13	2.21	0.85	29496
154.5	14.06	2.25	0.83	29612
155	14.19	2.25	0.83	29682
155.5	14.25	2.34	0.83	29800
156	14.31	2.35	0.85	29895
156.5	14.27	2.33	0.84	29957
157	14.13	2.37	0.82	30031
157.5	14.23	2.36	0.81	30154
158	14.22	2.32	0.80	30292
158.5	14.18	2.30	0.80	30380

<b>159</b>	14.40	2.54	0.80	30463
<b>159.5</b>	14.40	2.58	0.79	30546
<b>160</b>	14.14	2.66	0.81	30625
<b>160.5</b>	14.07	2.69	0.82	30686
<b>161</b>	14.16	2.65	0.82	30762
<b>161.5</b>	14.12	2.68	0.80	30848
<b>162</b>	13.95	2.63	0.82	30920
<b>162.5</b>	13.95	2.61	0.84	30993
<b>163</b>	14.04	2.67	0.84	31070
<b>163.5</b>	14.06	2.66	0.84	31158
<b>164</b>	13.99	2.56	0.82	31222
<b>164.5</b>	13.89	2.54	0.83	31321
<b>165</b>	13.99	2.57	0.82	31411
<b>165.5</b>	14.26	2.95	0.82	31493
<b>166</b>	14.14	2.89	0.82	31557
<b>166.5</b>	13.99	2.86	0.80	31616
<b>167</b>	13.81	2.80	0.80	31676
<b>167.5</b>	13.96	2.88	0.80	31766
<b>168</b>	14.10	2.96	0.78	31833
<b>168.5</b>	13.93	2.88	0.77	31920
<b>169</b>	13.87	2.85	0.78	32007
<b>169.5</b>	13.81	2.81	0.80	32101
<b>170</b>	13.71	2.74	0.81	32196
<b>170.5</b>	13.51	2.66	0.81	32279
<b>171</b>	13.74	2.63	0.82	32338
<b>171.5</b>	13.84	2.67	0.83	32407
<b>172</b>	13.81	2.71	0.82	32474
<b>172.5</b>	13.52	2.65	0.81	32542
<b>173</b>	13.35	2.62	0.81	32654
<b>173.5</b>	13.26	2.60	0.82	32715
<b>174</b>	13.19	2.63	0.80	32796
<b>174.5</b>	13.24	2.70	0.78	32876
<b>175</b>	13.21	2.72	0.78	32951
<b>175.5</b>	13.23	2.74	0.79	33047
<b>176</b>	13.09	2.75	0.80	33156
<b>176.5</b>	13.16	2.82	0.80	33226
<b>177</b>	13.05	2.81	0.79	33300
<b>177.5</b>	13.23	2.87	0.78	33383
<b>178</b>	13.16	2.84	0.78	33484
<b>178.5</b>	13.22	2.85	0.79	33563
<b>179</b>	13.42	2.93	0.80	33651
<b>179.5</b>	13.45	2.92	0.78	33738
<b>180</b>	13.44	2.97	0.79	33820
<b>180.5</b>	13.40	3.00	0.78	33890
<b>181</b>	13.65	3.11	0.76	33981
<b>181.5</b>	13.81	3.13	0.75	34054
<b>182</b>	13.65	3.14	0.74	34142
<b>182.5</b>	13.65	3.08	0.74	34251

<b>183</b>	13.74	3.11	0.76	34324
<b>183.5</b>	13.50	3.15	0.76	34411
<b>184</b>	13.35	3.14	0.76	34492
<b>184.5</b>	13.32	3.10	0.78	34569
<b>185</b>	13.30	3.05	0.77	34659
<b>185.5</b>	13.52	3.02	0.76	34733
<b>186</b>	13.56	3.07	0.75	34822
<b>186.5</b>	13.55	3.07	0.77	34905
<b>187</b>	13.56	3.02	0.79	35010
<b>187.5</b>	13.59	3.00	0.77	35085
<b>188</b>	13.58	3.04	0.77	35165
<b>188.5</b>	13.57	3.03	0.77	35292
<b>189</b>	13.41	2.98	0.77	35359
<b>189.5</b>	13.39	3.04	0.77	35465
<b>190</b>	13.36	2.99	0.76	35550
<b>190.5</b>	13.38	3.07	0.75	35633
<b>191</b>	13.34	3.06	0.74	35718
<b>191.5</b>	13.33	3.06	0.74	35809
<b>192</b>	13.36	3.12	0.74	35890
<b>192.5</b>	13.54	3.17	0.76	35999
<b>193</b>	13.62	3.17	0.76	36095
<b>193.5</b>	13.53	3.15	0.77	36176
<b>194</b>	13.38	3.05	0.76	36284
<b>194.5</b>	13.42	3.11	0.76	36388
<b>195</b>	13.45	3.04	0.76	36484
<b>195.5</b>	13.36	3.03	0.76	36590
<b>196</b>	13.32	3.01	0.74	36711
<b>196.5</b>	13.27	2.99	0.76	36818
<b>197</b>	13.18	2.99	0.77	36919
<b>0.77</b>	197.5	2.92	13.17	37075
<b>0.80</b>	198	2.94	13.19	37300
<b>0.79</b>	198.5	3.06	13.28	37503
<b>0.79</b>	199	3.11	13.38	37667
<b>0.83</b>	199.5	3.14	13.25	37779
<b>0.82</b>	200	3.12	13.29	37896
<b>0.83</b>	200.5	3.03	13.33	37991
<b>0.82</b>	201	2.97	13.25	38125
<b>0.83</b>	201.5	2.81	13.27	38250
<b>0.83</b>	202	2.73	13.22	38342
<b>0.83</b>	202.5	2.65	13.02	38432
<b>0.81</b>	203	2.64	13.06	38517
<b>0.82</b>	203.5	2.63	13.03	38620
<b>0.80</b>	204	2.71	13.06	38670
<b>0.80</b>	204.5	2.71	12.99	38761
<b>0.79</b>	205	2.66	13.11	38857
<b>0.82</b>	205.5	2.66	12.99	38935
<b>0.80</b>	206	2.56	12.85	39031
<b>0.80</b>	206.5	2.50	12.71	39120

<b>0.81</b>	207	2.49	12.81	39208
<b>0.80</b>	207.5	2.55	12.89	39282
<b>0.78</b>	208	2.57	12.72	39372
<b>0.76</b>	208.5	2.67	12.77	39452
<b>0.77</b>	209	2.60	12.65	39531
<b>0.76</b>	209.5	2.71	12.63	39619
<b>0.79</b>	210	2.73	12.66	39723
<b>0.78</b>	210.5	2.72	12.81	39809
<b>0.78</b>	211	2.67	12.79	39874
<b>0.77</b>	211.5	2.65	12.79	39968
<b>0.79</b>	212	2.61	12.72	40085
<b>0.80</b>	212.5	2.56	12.66	40167
<b>0.78</b>	213	2.57	12.63	40243
<b>0.77</b>	213.5	2.66	12.87	40375
<b>0.76</b>	214	2.66	12.98	40490
<b>0.75</b>	214.5	2.57	12.85	40558
<b>0.75</b>	215	2.57	12.74	40643
<b>0.78</b>	215.5	2.54	12.54	40721
<b>0.80</b>	216	2.63	12.52	40775
<b>0.81</b>	216.5	2.55	12.61	40827
<b>0.79</b>	217	2.68	12.64	40932
<b>0.77</b>	217.5	2.67	12.62	41021
<b>0.78</b>	218	2.62	12.63	41072
<b>0.78</b>	218.5	2.51	12.50	41168
<b>0.77</b>	219	2.49	12.40	41272
<b>0.78</b>	219.5	2.48	12.40	41335
<b>0.77</b>	220	2.50	12.36	41426
<b>0.75</b>	220.5	2.49	12.32	41488
<b>0.74</b>	221	2.47	12.23	41559
<b>0.75</b>	221.5	2.44	12.18	41640
<b>0.75</b>	222	2.39	12.20	41703
<b>0.76</b>	222.5	2.40	12.11	41776
<b>0.74</b>	223	2.42	12.22	41851
<b>0.74</b>	223.5	2.48	12.24	41961
<b>0.76</b>	224	2.63	12.39	42122
<b>0.75</b>	224.5	2.61	12.65	42210
<b>0.74</b>	225	2.62	12.70	42340
<b>0.74</b>	225.5	2.64	12.68	42416
<b>0.74</b>	226	2.65	12.54	42524
<b>0.78</b>	226.5	2.61	12.52	42632
<b>0.77</b>	227	2.59	12.58	42706
<b>0.77</b>	227.5	2.54	12.31	42834
<b>0.79</b>	228	2.52	12.13	42937
<b>0.79</b>	228.5	2.59	12.22	43005
<b>0.81</b>	229	2.63	12.36	43081
<b>0.83</b>	229.5	2.66	12.27	43136
<b>0.83</b>	230	2.70	12.30	43184
<b>0.83</b>	230.5	2.66	12.20	43247

<b>0.83</b>	231	2.61	12.22	43292
<b>0.83</b>	231.5	2.59	12.25	43367
<b>0.85</b>	232	2.57	12.28	43440
<b>0.82</b>	232.5	2.53	12.33	43546
<b>0.84</b>	233	2.51	12.38	43633
<b>0.82</b>	233.5	2.55	12.29	43770
<b>0.82</b>	234	2.61	12.23	43863
<b>0.81</b>	234.5	2.63	12.37	43936

**Supplementary Table 2.4.** XRF data for KC12.

<b>KC02</b>						
<b>Depth (cm)</b>	<b>CSF</b>	<b>DBD (g/cm3)</b>	<b>IBRD MAR (g/cm2/kyr)</b>	<b>BiSi (%)</b>	<b>BiSi MAR (g/cm2/kyr)</b>	<b>Age (yrs)</b>
1	0.6586	0.47	0.018	17	0.45527896	527
11	0.0027	0.55	0.009	27	0.872509123	2112
21	0.0020	0.61	0.007	32	1.147963111	3761
31	0.0033	0.47	0.009	31	0.865240336	5401
41	0.0022	0.60	0.008	45	1.580160542	7051
51	0.0007	0.60	0.002	42	1.195307928	8718
61	0.0011	0.65	0.003	36	1.101101992	10486
71	0.0021	0.54	0.005	30	0.790692958	12265
81	0.0037	0.76	0.014	21	0.780459923	14023
91	0.0022	0.72	0.008	22	0.761810176	15792
101	0.0023	0.75	0.008	12	0.444174648	17566
111	0.0109	0.48	0.025	4	0.085538899	19335
121	0.0056	0.78	0.728	3	3.315670013	19767
131	0.0038	0.72	0.458	2	2.119253175	19969
141	0.0166	0.78	2.152	1	1.608039393	20152
151	0.0056	0.76	0.703	2	2.428247956	20332
161	0.0105	0.66	1.144	3	3.232894007	20509
171	0.0018	0.69	0.212	2	2.816549604	20683
181	0.0051	1.15	0.972	1	0.969165074	20862
191	0.0046	0.73	0.553	1	1.690482953	21054
201	0.0036	0.78	0.467	1	1.884248732	21236
211	0.0031	0.77	0.395	1	1.672536203	21426
221	0.0030	0.74	0.365	2	2.787970101	21614

**Supplementary Table 2.5.** Measured CSF, DBD, IBRD MAR, BiSi and BiSi MAR in KC02.

KC14						
Depth (cm)	CSF	DBD (g/cm <sup>3</sup> )	IBRD MAR (g/cm <sup>2</sup> /kyr)	BiSi (%)	BiSi MAR (g/cm <sup>2</sup> /kyr)	Age (yrs)
3	0.0027	0.54	0.016	16	0.930	310
13	0.0008	0.76	0.007	24	2.036	1189
25	0.0008	0.74	0.006	25	2.011	2214
37	0.0002	0.65	0.002	34	2.444	3267
49	0.0009	0.52	0.005	35	2.046	4327
61	0.0012	0.52	0.007	38	2.150	5362
73	0.0008	0.47	0.004	48	2.480	6391
85	0.0009	0.49	0.005	52	2.771	7427
97	0.0010	0.46	0.005	53	2.636	8628
109	0.0007	0.52	0.003	39	2.020	10500
121	0.0005	0.62	0.003	23	1.417	12352
133	0.0004	0.67	0.004	22	2.081	13201
145	0.0017	0.68	0.016	26	2.447	14025
157	0.0016	0.65	0.015	27	2.441	15032
169	0.0001	0.82	0.001	11	0.700	16578
181	0.0006	0.81	0.004	7	0.436	18071
193	0.0021	0.73	0.012	8	0.461	19558
205	0.0005	0.79	0.003	4	0.278	21055
217	0.0014	0.91	0.476	4	13.138	21305
229	0.0005	0.86	0.153	3	11.170	21510
241	0.0021	0.79	0.619	3	10.235	21670
253	0.0016	0.77	0.454	3	9.616	21824
265	0.0147	0.86	4.771	2	6.168	21965
277	0.0009	0.86	0.281	3	9.995	22106
289	0.0010	0.88	0.324	3	8.282	22260
301	0.0005	0.83	0.146	4	12.783	22420
313	0.0010	0.86	0.321	3	9.376	22565
325	0.0010	0.87	0.315	2	7.741	22739
337	0.0126	0.84	3.974	2	6.626	23098

**Supplementary Table 2.6.** Measured CSF, DBD, IBRD MAR, BiSi and BiSi MAR in KC14.

<b>KC04</b>						
<b>Depth (cm)</b>	<b>CSF</b>	<b>DBD (g/cm<sup>3</sup>)</b>	<b>IBRD MAR (g/cm<sup>2</sup>/kyr)</b>	<b>BiSi (%)</b>	<b>BiSi MAR (g/cm<sup>2</sup>/kyr)</b>	<b>Age (yrs)</b>
4.5	0.0032	0.77	0.074	10	0.526	2624
14	0.0080	0.67	0.143	15	0.724	4056
34	0.0024	0.66	0.016	11	0.212	8235
44	0.0017	0.87	0.020	4	0.102	11674
54	0.0041	0.81	0.041	2	0.052	15084
64	0.0013	0.85	0.151	1	0.284	16704
74	0.0012	0.81	0.135	1	0.228	17043
94	0.0187	0.85	2.209	1	0.157	17659
106	0.0065	0.75	0.598	1	0.280	18026
115	0.0048	0.79	0.489	1	0.319	18286
126	0.0137	0.87	1.699	1	0.298	18620
139	0.0364	1.09	7.032	1	0.307	19023
149	0.0194	0.80	2.025	1	0.150	19315
159	0.0143	0.82	1.566	1	0.239	19616
179	0.0004	0.82	0.049	1	0.256	20356
186	0.0080	0.74	0.725	1	0.281	20572
194	0.0021	0.78	0.215	1	0.334	20930
206	0.0004	0.86	0.053	1	0.278	21274
217	0.0054	0.88	0.685	1	0.332	21274
227	0.0064	0.78	0.643	1	0.247	21606
239	0.0019	0.54	0.091	3	0.401	22290
245.5	0.0019	0.77	0.184	3	0.690	22992

**Supplementary Table 2.7.** Measured CSF, DBD, IBRD MAR, BiSi and BiSi MAR in KC04.

<b>KC12</b>						
<b>Depth (cm)</b>	<b>CSF</b>	<b>DBD (g/cm<sup>3</sup>)</b>	<b>IBRD MAR (g/cm<sup>2</sup>/kyr)</b>	<b>BiSi (%)</b>	<b>BiSi MAR (g/cm<sup>2</sup>/kyr)</b>	<b>Age (yrs)</b>
1	0.0015	0.65	0.007	8	0.364	369
5	n.d.	n.d.	n.d.	18	n.d.	849
13	0.0006	0.75	0.003	19	0.979	1988
21	n.d.	n.d.	n.d.	27	n.d.	3088
23	0.0013	0.78	0.007	21	1.108	3359
29	n.d.	n.d.	n.d.	26	n.d.	4181
33	0.0009	0.81	0.005	15	0.829	4734
43	0.0015	0.71	0.007	15	0.717	6111
53	0.0011	0.62	0.005	21	0.863	7436
63	0.0012	0.59	0.005	24	0.940	8780
69	n.d.	n.d.	n.d.	43	n.d.	9962
73	0.0016	0.64	0.003	16	0.283	11208
83	0.0010	0.92	0.003	12	0.317	14402
93	0.0002	0.92	0.001	6	0.157	17569
101	n.d.	n.d.	n.d.	3	n.d.	20237
103	0.0009	0.93	0.005	4	0.227	20667
113	0.0006	0.90	0.004	1	0.057	22512
123	0.0036	0.87	0.020	1	0.078	24300
133	0.0018	0.81	0.009	1	0.067	25957
143	0.0024	0.87	0.013	1	0.074	27654
153	0.0010	0.80	0.005	1	0.045	29319
163	0.0031	0.73	0.014	2	0.075	31070
173	0.0005	0.80	0.002	1	0.068	32654
183	0.0002	0.77	0.001	2	0.089	34324
193	0.0005	0.86	0.002	0	0.025	36095
199	n.d.	n.d.	n.d.	1	n.d.	37667
203	0.0025	0.83	0.013	1	0.035	38517
211	n.d.	n.d.	n.d.	1	n.d.	39874
213	0.0176	0.81	0.090	1	0.045	40243
223	0.0001	0.86	0.001	1	0.035	41851
233	0.0006	0.82	0.003	1	0.056	43633

**Supplementary Table 2.8.** Measured CSF, DBD, IBRD MAR, BiSi and BiSi MAR in KC12.

KC02						
Depth (cm)	Total diatom abundance (millions of valves/g of sediment)	Proportion of <i>Fragilariopsis kerguelensis</i> (%)	Proportion of <i>Chaetoceros</i> subg. <i>Hyalochaete</i> (%)	Proportion of extinct species (%)	Proportion of robust species (%)	Age (yrs)
0.5	63	55.9	4.2	1.5	2.5	476
5.5	53	50.1	4.4	1.2	2.2	1208
10.5	53	48.0	5.2	0.9	3.5	2030
20.5	98	46.9	5.9	0.6	2.3	3681
30.5	113	48.2	7.1	0.7	4.3	5321
40.5	102	46.0	5.0	1.4	1.7	6970
50.5	136	47.9	10.0	2.1	0.9	8632
60.5	178	54.1	9.5	1.2	0.2	10394
70.5	74	60.5	4.8	0.7	1.7	12179
80.5	76	54.0	8.7	0.7	1.8	13935
90.5	93	52.9	7.6	0.8	1.7	15703
100.5	60	57.3	10.3	0.9	0.7	17478
110.5	10	52.3	12.6	1.7	3.3	19248
120.5	2	41.4	8.5	7.0	7.3	19762
140.5	3	57.8	6.1	2.8	3.1	20141
160.5	1	46.2	3.0	19.5	12.4	20501
180.5	0	50.4	3.0	17.8	11.9	20853
200.5	1	46.8	4.0	13.9	10.4	21226
210.5	1	44.4	2.4	11.1	20.8	21417
220.5	0	46.0	2.2	18.7	14.4	21604
230.5	0	50.6	2.3	10.6	10.6	21820
236.5	1	53.9	5.2	10.4	6.1	22088

**Supplementary Table 2.9.** Total diatom abundance and the proportion of *Fragilariopsis kerguelensis*, *Chaetoceros* subg. *Hyalochaete*, extinct species and robust species (as a percentage of the total diatom abundance) measured in KC02.

KC14

Depth (cm)	Total diatom abundance (millions of valves/g of sediment)	Proportion of <i>Fragilariopsis kerguelensis</i> (%)	Proportion of <i>Chaetoceros</i> subg. <i>Hyalochaete</i> (%)	Proportion of extinct species (%)	Proportion of robust species (%)	Age (yrs)
0.5	28	57.4	4.8	0.0	1.3	111
5.5	45	60.5	3.0	1.1	2.3	535
10.5	55	50.8	4.8	1.1	1.1	969
15.5	55	53.3	6.1	0.7	0.7	1401
20.5	56	40.6	10.4	0.0	0.0	1831
25.5	79	44.8	5.4	1.1	1.1	2255
30.5	71	47.6	11.1	0.6	2.4	2691
35.5	85	52.5	5.3	0.6	2.0	3132
38.5	91	52.7	9.0	0.2	2.6	3397
45.5	108	54.3	5.5	0.7	2.3	4014
50.5	134	57.1	7.2	0.2	0.7	4456
55.5	134	57.1	6.2	0.4	0.7	4895
59.5	167	44.0	8.4	0.0	0.7	5233
62.5	133	61.5	5.2	0.0	1.8	5495
65.5	148	55.3	7.7	0.4	0.7	5756
70.5	123	48.5	12.1	0.8	1.1	6189
75.5	130	52.9	11.2	0.7	0.2	6600
80.5	121	58.5	5.6	0.9	0.2	7032
85.5	153	61.8	8.9	0.4	0.2	7470
90.5	126	58.9	10.3	0.5	0.2	7901
95.5	179	64.1	6.7	0.5	0.2	8357
100.5	111	40.6	14.5	0.2	0.4	9155
105.5	110	71.7	4.3	1.6	0.0	9947
110.5	98	61.1	9.1	0.4	1.1	10737
115.5	77	69.6	4.1	0.2	1.6	11532
120.5	94	49.6	15.8	0.2	1.4	12311
130.5	70	55.3	8.5	0.9	1.7	13025
140.5	92	59.8	9.6	0.0	0.4	13721
150.5	65	62.0	8.9	0.5	1.6	14405
161	25	57.3	11.4	0.0	1.9	15586
170.5	29	50.0	13.8	0.2	0.9	16769
180.5	13	43.4	29.4	0.2	2.7	18006
190.5	6	41.9	18.6	1.6	7.1	19257
200.5	2	43.3	12.1	3.6	11.7	20498
210.5	1	54.9	6.9	10.3	10.9	21181
220.5	0	38.2	5.9	20.6	22.1	21371
230.5	0	42.0	20.0	10.0	16.0	21527
240.5	0	56.1	3.0	12.1	7.6	21664
250.5	0	50.0	2.9	20.6	14.7	21778
260.5	0	50.0	0.0	35.3	8.8	21913

270.5	1	71.5	2.5	5.9	2.5	22021
280.5	0	40.0	2.5	20.0	10.0	22140
290.5	0	33.3	10.3	33.3	10.3	22276
300.5	0	32.9	10.5	22.4	14.5	22408
310.5	0	33.3	3.6	33.3	17.1	22530
320.5	1	65.5	2.7	4.5	1.7	22668
330.5	1	65.3	3.3	5.3	3.8	22833

**Supplementary Table 2.10.** Total diatom abundance and the proportion of *Fragilariopsis kerguelensis*, *Chaetoceros* subg. *Hyalochaete*, extinct species and robust species (as a percentage of the total diatom abundance) measured in KC14.

KC04						
Depth (cm)	Total diatom abundance (millions of valves/g of sediment)	Proportion of <i>Fragilariopsis kerguelensis</i> (%)	Proportion of <i>Chaetoceros</i> subg. <i>Hyalochaete</i> (%)	Proportion of extinct species (%)	Proportion of robust species (%)	Age (yrs)
0.5	18	64.3	7.2	0.0	1.7	2235
10.5	55	68.8	5.3	0.0	1.0	3521
20.5	79	50.4	8.4	0.2	0.2	5040
28.5	90	61.7	10.5	0.2	1.9	6368
30.5	105	69.5	6.3	0.2	0.5	7041
40.5	25	74.4	5.2	0.5	0.7	10466
50.5	5	62.3	9.0	1.0	2.7	13894
60.5	2	70.6	6.3	3.1	2.5	16572
80.5	1	62.3	0.0	7.2	13.0	17240
100.5	1	73.6	0.0	11.1	4.2	17859
120.5	1	76.6	0.0	15.6	3.1	18468
140.5	1	80.0	0.0	10.0	5.0	19070
160.5	1	75.8	4.5	1.5	4.5	19666
180.5	1	73.5	0.0	2.0	4.1	20214
200.5	2	83.3	0.0	2.9	2.9	20759
220.5	2	81.6	1.4	1.4	4.1	21383
240.5	10	70.7	2.2	0.7	2.4	22514
247.5	5	82.5	1.7	1.1	1.1	23192

**Supplementary Table 2.11.** Total diatom abundance and the proportion of *Fragilariopsis kerguelensis*, *Chaetoceros* subg. *Hyalochaete*, extinct species and robust species (as a percentage of the total diatom abundance) measured in KC04.

KC12

Depth (cm)	Total diatom abundance (millions of valves/g of sediment)	Proportion of <i>Fragilariopsis kerguelensis</i> (%)	Proportion of <i>Chaetoceros</i> subg. <i>Hyalochaete</i> (%)	Proportion of extinct species (%)	Proportion of robust species (%)	Age (yrs)
0.5	26	69.4	2.9	0.2	1.2	330
5.5	38	69.0	4.0	0.0	0.4	923
10.5	61	71.9	2.6	0.2	3.1	1645
15.5	36	65.6	3.2	0.0	1.4	2335
20.5	63	65.2	4.2	0.0	1.2	3015
25.5	50	65.3	4.5	0.0	1.2	3696
30.5	78	72.4	2.9	0.2	1.3	4390
35.5	71	61.6	4.2	0.2	0.9	5078
40.5	46	64.9	3.4	0.5	2.5	5758
45.5	89	65.4	2.6	0.0	1.1	6445
50.5	77	70.9	2.6	0.2	0.8	7115
55.5	122	62.9	2.8	0.0	0.9	7794
60.5	117	70.3	1.1	0.0	0.4	8445
65.5	107	73.6	2.2	0.0	0.0	9163
70.5	74	76.1	1.9	0.0	0.6	10439
75.5	49	65.8	4.5	0.2	1.3	12017
80.5	35	69.3	1.8	0.2	1.1	13607
85.5	29	72.1	3.1	0.9	2.2	15169
90.5	40	72.7	1.3	0.2	1.0	16756
95.5	30	62.3	2.6	0.0	3.4	18349
100.5	14	73.8	1.6	0.2	1.6	20095
105.5	3	74.8	2.4	1.2	4.2	21168
110.5	0	60.2	1.6	5.7	8.1	22033
120.5	1	48.6	1.6	4.9	8.6	23865
140.5	0	40.0	2.1	15.8	18.9	27211
160.5	0	53.4	0.0	12.1	22.4	30686
180.5	0	41.8	1.3	20.3	15.2	33890
200.5	0	50.0	0.0	7.7	19.2	37991
220.5	0	33.3	5.1	20.5	15.4	41488

**Supplementary Table 2.12.** Total diatom abundance and the proportion of *Fragilariopsis kerguelensis*, *Chaetoceros* subg. *Hyalochaete*, extinct species and robust species (as a percentage of the total diatom abundance) measured in KC12.

<b>KC02</b>		
<b>Depth (cm)</b>	<b>Mean grain size (<math>\mu\text{m}</math>)</b>	<b>Age (yrs)</b>
0.5	8.2	476
5.5	8.8	1208
10.5	8.9	2030
15.5	9.3	2855
20.5	10.4	3681
25.5	10.3	4502
30.5	11.2	5321
35.5	11.2	6146
40.5	11.7	6970
45.5	11.8	7783
50.5	11.7	8632
55.5	11.9	9509
60.5	11.1	10394
65.5	10.5	11284
70.5	9.3	12179
75.5	11.4	13053
80.5	9.3	13935
85.5	9.4	14823
90.5	9.2	15703
95.5	8.9	16592
100.5	8.2	17478
110.5	4.3	19248
120.5	3.8	19762
130.5	3.0	19960
140.5	4.2	20141
150.5	3.2	20324
160.5	2.6	20501
170.5	2.7	20674
180.5	12.1	20853
190.5	3.1	21044
200.5	2.5	21226
210.5	3.0	21417
220.5	2.7	21604
230.5	2.6	21820
240.5	2.9	22503

**Supplementary Table 2.13.** Bulk mean grain size measured in KC02.

KC14

Depth (cm)	Mean grain size (µm)	Age (yrs)	Depth (cm)	Mean grain size (µm)	Age (yrs)
0.5	7.4	111	<b>170.5</b>	6.5	16769
0.6	7.5	132	<b>175.5</b>	7.6	17382
10.5	8.0	969	<b>180.5</b>	5.2	18006
15.5	7.5	1401	<b>185.5</b>	6.2	18635
20.5	8.1	1831	<b>190.5</b>	4.3	19257
25.5	8.3	2255	<b>195.5</b>	4.0	19865
30.5	9.2	2691	<b>200.5</b>	4.0	20498
35.5	10.2	3132	<b>205.5</b>	3.9	21074
40.5	10.6	3573	<b>210.5</b>	3.6	21181
45.5	11.5	4014	<b>215.5</b>	3.6	21277
50.5	11.7	4456	<b>220.5</b>	3.5	21371
55.5	10.9	4895	<b>225.5</b>	3.3	21447
60.5	11.3	5318	<b>230.5</b>	3.2	21527
65.5	10.9	5756	<b>235.5</b>	2.9	21603
70.5	9.8	6189	<b>240.5</b>	3.4	21664
75.5	9.5	6600	<b>245.5</b>	2.9	21720
80.5	11.6	7032	<b>250.5</b>	2.7	21778
85.5	9.3	7470	<b>255.5</b>	3.6	21855
90.5	9.5	7901	<b>260.5</b>	3.8	21913
95.5	9.5	8357	<b>265.5</b>	2.9	21972
100.5	12.3	9155	<b>270.5</b>	4.0	22021
105.5	11.1	9947	<b>275.5</b>	3.1	22082
110.5	11.6	10737	<b>280.5</b>	4.1	22140
115.5	10.1	11532	<b>285.5</b>	3.9	22211
120.5	9.5	12311	<b>290.5</b>	3.4	22276
125.5	10.0	12667	<b>295.5</b>	4.1	22351
130.5	10.0	13025	<b>300.5</b>	3.4	22408
135.5	7.9	13385	<b>305.5</b>	3.6	22471
140.5	9.1	13721	<b>310.5</b>	3.1	22530
145.5	8.9	14060	<b>315.5</b>	3.8	22593
150.5	10.5	14405	<b>320.5</b>	3.7	22668
155.5	7.2	14776	<b>325.5</b>	3.1	22751
160.5	6.2	15533	<b>330.5</b>	3.7	22833
165.5	5.2	16148	<b>335.5</b>	3.0	22949

**Supplementary Table 2.14.** Bulk mean grain size measured in KC14.

KC04

Depth (cm)	Mean grain size (µm)	Age (yrs)	Depth (cm)	Mean grain size (µm)	Age (yrs)
0.5	5.9	2235	127.5	3.5	18669
5.5	6.2	2785	132.5	3.3	18815
10.5	6.8	3521	137.5	3.1	18962
17.5	7.7	4586	142.5	3.0	19131
22.5	7.0	5339	147.5	3.0	19268
30.5	5.1	7041	152.5	3.0	19421
37.5	9.5	9437	157.5	3.4	19571
42.5	5.0	11152	162.5	3.1	19718
47.5	4.3	12861	167.5	3.5	19851
52.5	3.4	14574	172.5	3.2	19977
57.5	3.5	16239	177.5	3.4	20122
62.0	3.5	16632	182.5	3.2	20266
67.5	3.2	16821	187.5	3.1	20397
72.5	3.1	16980	192.5	3.0	20530
77.5	3.2	17152	197.5	2.6	20669
82.5	3.1	17296	202.5	3.0	20813
87.5	2.9	17468	207.5	3.2	20977
92.5	3.1	17615	212.5	2.7	21140
97.5	3.0	17766	217.5	2.5	21288
102.5	6.3	17926	222.5	2.9	21447
107.5	2.8	18068	227.5	3.4	21630
112.5	3.4	18219	233.0	3.9	21819
117.5	3.5	18373	237.5	4.0	22039
122.5	3.8	18524	242.5	4.3	22734
			247.5	4.0	23192

Supplementary Table 2.15. Bulk mean grain size measured in KC04.

**KC12**

<b>Depth (cm)</b>	<b>Mean grain size (<math>\mu\text{m}</math>)</b>	<b>Age (yrs)</b>	<b>Depth (cm)</b>	<b>Mean grain size (<math>\mu\text{m}</math>)</b>	<b>Age (yrs)</b>
0.5	7.0	330	120.5	4.1	23865
5.5	6.8	923	125.5	4.4	24719
10.5	6.6	1645	130.5	4.3	25554
15.5	7.1	2335	135.5	3.8	26368
20.5	7.3	3015	140.5	3.9	27211
25.5	7.1	3696	145.5	3.7	28046
30.5	7.9	4390	150.5	3.9	28947
35.5	9.2	5078	155.5	3.5	29800
40.5	9.9	5758	160.5	3.3	30686
45.5	10.4	6445	165.5	3.4	31493
50.5	10.0	7115	170.5	3.6	32279
60.5	11.0	8445	175.5	3.5	33047
65.5	11.4	9163	180.5	3.2	33890
70.5	11.5	10439	185.5	3.7	34733
75.5	9.6	12017	190.5	3.5	35633
80.5	7.9	13607	195.5	3.5	36590
85.5	7.2	15169	200.5	3.5	37991
90.5	7.1	16756	205.5	4.1	38935
95.5	6.8	18349	210.5	3.0	39809
100.5	6.1	20095	215.5	3.6	40721
105.5	4.8	21168	220.5	4.5	41488
110.5	4.6	22033	225.5	3.9	42416
115.5	4.0	22950	230.5	3.1	43247

**Supplementary Table 2.16.** Bulk mean grain size measured in KC12.

KC02			
Depth (cm)	BiSi-leached mean grain size ( $\mu\text{m}$ )	Sortable silt (%)	Age (yrs)
1	11.7	52.0	527
11	14.4	52.9	2112
21	7.9	47.4	3761
31	7.8	46.2	5401
41	8.3	48.6	7051
51	9.8	50.4	8718
61	8.0	49.5	10486
71	6.1	39.8	12265
81	6.6	42.5	14023
91	7.8	41.3	15792
101	3.9	23.9	17566
111	3.3	16.0	19335
121	3.4	18.4	19767
131	2.4	8.1	19969
141	4.3	13.5	20152
151	4.0	13.6	20332

**Supplementary Table 2.17.** BiSi-leached mean grain size and sortable silt percent measured in KC02.

**KC14**

<b>Depth (cm)</b>	<b>BiSi- leached mean grain size (<math>\mu\text{m}</math>)</b>	<b>Sortable silt (%)</b>	<b>Age (yrs)</b>
13	8.4	48.7	1189
25	7.2	44.3	2214
37	8.1	46.8	3267
49	6.8	42.5	4327
61	8.0	48.6	5362
73	7.7	46.9	6391
85	6.8	42.5	7427
97	7.7	46.5	8628
109	7.4	45.8	10500
121	7.7	48.0	12352
133	4.3	27.0	13201
145	7.3	43.6	14025
157	6.9	43.0	15032
169	3.7	22.3	16578
181	6.0	37.8	18071
193	4.4	27.8	19558
205	4.0	23.7	21055

**Supplementary Table 2.18.** BiSi-leached mean grain size and sortable silt percent measured in KC14.

**KC04**

<b>Depth (cm)</b>	<b>BiSi- leached mean grain size (<math>\mu\text{m}</math>)</b>	<b>Sortable silt (%)</b>	<b>Age (yrs)</b>
4.5	4.2	27.7	2624
14	4.8	27.5	4056
34	4.3	26.1	8235
44	3.6	20.5	11674
54	3.4	17.3	15084
64	3.3	18.1	16704
74	3.2	16.2	17043
84	3.4	18.7	17348
94	4.7	24.3	17659
106	3.2	14.6	18026
115	3.3	16.4	18286
126	4.6	19.3	18620
139	9.8	18.5	19023
149	3.3	17.1	19315

**Supplementary Table 2.19.** BiSi-leached mean grain size and sortable silt percent measured in KC04.

**KC12**

<b>Depth (cm)</b>	<b>BiSi- leached mean grain size (<math>\mu\text{m}</math>)</b>	<b>Sortable silt (%)</b>	<b>Age (yrs)</b>
1	7.6	45.0	369
13	6.3	39.5	1988
23	6.5	38.9	3359
33	7.0	43.0	4734
43	6.3	39.8	6111
53	7.1	40.9	7436
63	7.9	44.3	8780
73	5.8	36.4	11208
83	7.4	43.7	14402
93	4.9	32.4	17569
103	4.9	33.2	20667
113	4.3	26.6	22512
123	4.4	27.2	24300
133	4.6	29.3	25957
143	3.8	22.8	27654
153	3.8	23.9	29319

**Supplementary Table 2.20.** BiSi-leached mean grain size and sortable silt percent measured in KC12.

## References

- Adamson, D., & Pickard, J. (1983). Late Quaternary ice movement across the Vestfold Hills, East Antarctica. *Antarctic Earth Science. 4th International Symposium*, 465–469.
- Álvarez-Solas, J., Montoya, M., Ritz, C., Ramstein, G., Charbit, S., Dumas, C., ... Ganopolski, A. (2011). Heinrich event 1: An example of dynamical ice-sheet reaction to oceanic changes. *Climate of the Past*, 7(4), 1297–1306. <https://doi.org/10.5194/cp-7-1297-2011>
- Ambblas, D., & Canals, M. (2016). Contourite drifts and canyon-channel systems on the Northern Antarctic Peninsula Pacific margin. *Geological Society Memoir*, 46(1), 393–394. <https://doi.org/10.1144/M46.17>
- Armand, L. K., & Zielinski, U. (2001). Diatom species of the genus *Rhizosolenia* from Southern Ocean sediments: Distribution and taxonomic notes. *Diatom Research*, 16(2), 259–294. <https://doi.org/10.1080/0269249X.2001.9705520>
- Armand, L., O'Brien, P., Armbrecht, L., Barker, H., Caburlotto, A., Connell, T., ... Young, A. (2018). Interactions of the Totten Glacier with the Southern Ocean through multiple glacial cycles (IN2017-V01): Post-survey report, (March). <https://doi.org/10.4225/13/5ACEA64C48693>
- Arndt, J. E., Schenke, H. W., Jakobsson, M., Nitsche, F. O., Buys, G., Goleby, B., ... Wigley, R. (2013). The international bathymetric chart of the Southern Ocean (IBCSO) version 1.0-A new bathymetric compilation covering circum-Antarctic waters. *Geophysical Research Letters*, 40(12), 3111–3117. <https://doi.org/10.1002/grl.50413>
- Arrigo, K. R., van Dijken, G. L., & Bushinsky, S. (2008). Primary production in the Southern Ocean, 1997-2006. *Journal of Geophysical Research: Oceans*, 113(8). <https://doi.org/10.1029/2007JC004551>
- Barker, S., & Diz, P. (2014). Timing of the descent into the last Ice Age determined by the bipolar seesaw. *Paleoceanography*, 29(6), 489–507. <https://doi.org/10.1002/2014PA002623>
- Bentley, M. J., Ocofaigh, C., Anderson, J. B., Conway, H., Davies, B., Graham, A. G. C., ... Zwartz, D. (2014). A community-based geological reconstruction of Antarctic Ice Sheet deglaciation since the Last Glacial Maximum. *Quaternary Science Reviews*, 100, 1–9. <https://doi.org/10.1016/j.quascirev.2014.06.025>
- Berg, S., Wagner, B., Cremer, H., Leng, M. J., & Melles, M. (2010a). Late Quaternary environmental and climate history of Rauer Group, East Antarctica. *Palaeogeography*,

*Palaeoclimatology, Palaeoecology*, 297(1), 201–213.

<https://doi.org/10.1016/j.palaeo.2010.08.002>

Berg, S., Wagner, B., White, D. A., & Melles, M. (2010b). No significant ice-sheet expansion beyond present ice margins during the past 4500yr at Rauer Group, East Antarctica.

*Quaternary Research*, 74(1), 23–25. <https://doi.org/10.1016/j.yqres.2010.04.004>

Bishop, J. K. B. (1988). The barite-opal-organic carbon association in oceanic particulate matter.

*Nature*, 332(6162), 341–343. <https://doi.org/10.1038/332341a0>

Blott, S. J., & Pye, K. (2001). Gradistat: A grain size distribution and statistics package for the analysis of unconsolidated sediments. *Earth Surface Processes and Landforms*, 26(11),

1237–1248. <https://doi.org/10.1002/esp.261>

Blunier, T., Schwander, J., Stauffer, B., Stocker, T., Dällenbach, A., Indermühle, A., ... Barnola, J.

M. (1997). Timing of the Antarctic Cold Reversal and the atmospheric CO<sub>2</sub> increase with respect to the Younger Dryas event. *Geophysical Research Letters*, 24(21), 2683–2686.

<https://doi.org/10.1029/97GL02658>

Bond, G., Heinrich, H., Broecker, W., Labeyrie, L., McManus, J., Andrews, J., ... Ivy, S. (1992).

Evidence for massive discharges of icebergs into the North Atlantic ocean during the last glacial period. *Nature*, 360(6401), 245–249. <https://doi.org/10.1038/360245a0>

Bradley, S. L., Hindmarsh, R. C. A., Whitehouse, P. L., Bentley, M. J., & King, M. A. (2015). Low post-glacial rebound rates in the Weddell Sea due to Late Holocene ice-sheet readvance.

*Earth and Planetary Science Letters*, 413, 79–89. <https://doi.org/10.1016/j.epsl.2014.12.039>

Broecker, W., Bond, G., Klas, M., Clark, E., & McManus, J. (1992). Origin of the northern

Atlantic's Heinrich events. *Climate Dynamics*, 6(3–4), 265–273.

<https://doi.org/10.1007/BF00193540>

Broecker, W. S. (1994). Massive iceberg discharges as triggers for global climate change.

*Nature*, 372(6505), 421–424. <https://doi.org/10.1038/372421a0>

Burke, A., & Robinson, L. F. (2012). The southern ocean's role in carbon exchange during the

last deglaciation. *Science*, 335(6068), 557–561. <https://doi.org/10.1126/science.1208163>

Calov, R., Ganopolski, A., Petoukhov, V., Claussen, M., & Greve, R. (2002). Large-scale instabilities of the Laurentide ice sheet simulated in a fully coupled climate-system model.

*Geophysical Research Letters*, 29(24), 69-1-69–4. <https://doi.org/10.1029/2002GL016078>

Chow, T. J., & Goldberg, E. D. (1960). On the marine geochemistry of barium. *Geochimica et*

*Cosmochimica Acta*, 20(3–4), 192–198. [https://doi.org/10.1016/0016-7037\(60\)90073-9](https://doi.org/10.1016/0016-7037(60)90073-9)

- Clark, P. U., Alley, R. B., Keigwin, L. D., Licciardi, J. M., Johnsen, S. J., & Wang, H. (1996). Origin of the first global meltwater pulse following the last glacial maximum. *Paleoceanography*, 11(5), 563–577. <https://doi.org/10.1029/96PA01419>
- Clark, P. U., Dyke, A. S., Shakun, J. D., Carlson, A. E., Clark, J., Wohlfarth, B., ... McCabe, A. M. (2009). The Last Glacial Maximum. *Science*, 325(5941), 710–714. <https://doi.org/10.1126/science.1172873>
- Clark, P. U., Mitrovica, J. X., Milne, G. A., & Tamisiea, M. E. (2002). Sea-level fingerprinting as a direct test for the source of global meltwater pulse IA. *Science*, 295(5564), 2438–2441. <https://doi.org/10.1126/science.1068797>
- Coolen, M. J. L., Hopmans, E. C., Rijpstra, W. I. C., Muyzer, G., Schouten, S., Volkman, J. K., & Sinninghe Damsté, J. S. (2004). Evolution of the methane cycle in Ace Lake (Antarctica) during the Holocene: Response of methanogens and methanotrophs to environmental change. In *Organic Geochemistry* (Vol. 35, pp. 1151–1167). Pergamon. <https://doi.org/10.1016/j.orggeochem.2004.06.009>
- Crespin, J., Yam, R., Crosta, X., Massé, G., Schmidt, S., Campagne, P., & Shemesh, A. (2014). Holocene glacial discharge fluctuations and recent instability in East Antarctica. *Earth and Planetary Science Letters*, 394, 38–47. <https://doi.org/10.1016/j.epsl.2014.03.009>
- Crosta, X., Debret, M., Denis, D., Courty, M. A., & Ther, O. (2007). Holocene long- and short-term climate changes off Adélie Land, East Antarctica. *Geochemistry, Geophysics, Geosystems*, 8(11), n/a-n/a. <https://doi.org/10.1029/2007GC001718>
- Crosta, X., & Koç, N. (2007, January 1). Chapter Eight Diatoms: From Micropaleontology to Isotope Geochemistry. *Developments in Marine Geology*. Elsevier. [https://doi.org/10.1016/S1572-5480\(07\)01013-5](https://doi.org/10.1016/S1572-5480(07)01013-5)
- Crosta, X., Pichon, J. J., & Labracherie, M. (1997). Distribution of Chaetoceros resting spores in modern peri-Antarctic sediments. *Marine Micropaleontology*, 29(3–4), 283–299. [https://doi.org/10.1016/S0377-8398\(96\)00033-3](https://doi.org/10.1016/S0377-8398(96)00033-3)
- Crosta, X., Romero, O., Armand, L. K., & Pichon, J. J. (2005). The biogeography of major diatom taxa in Southern Ocean sediments: 2. Open ocean related species. *Palaeogeography, Palaeoclimatology, Palaeoecology*, 223(1–2), 66–92. <https://doi.org/10.1016/j.palaeo.2005.03.028>
- Crowley, T. J. (1992). North Atlantic Deep Water cools the southern hemisphere. *Paleoceanography*, 7(4), 489–497. <https://doi.org/10.1029/92PA01058>

- Cunningham, W. L., Leventer, A., Andrews, J. T., Jennings, A. E., & Licht, K. J. (1999). Late Pleistocene-Holocene marine conditions in the Ross Sea, Antarctica: Evidence from the diatom record. *Holocene*, 9(2), 129–139. <https://doi.org/10.1191/095968399675624796>
- Dehairs, F., Stroobants, N., & Goeyens, L. (1991). Suspended barite as a tracer of biological activity in the Southern Ocean. *Marine Chemistry*, 35(1–4), 399–410. [https://doi.org/10.1016/S0304-4203\(09\)90032-9](https://doi.org/10.1016/S0304-4203(09)90032-9)
- DeMaster, D. J. (1981). The supply and accumulation of silica in the marine environment. *Geochimica et Cosmochimica Acta*, 45(10), 1715–1732. [https://doi.org/10.1016/0016-7037\(81\)90006-5](https://doi.org/10.1016/0016-7037(81)90006-5)
- Deschamps, P., Durand, N., Bard, E., Hamelin, B., Camoin, G., Thomas, A. L., ... Yokoyama, Y. (2012). Ice-sheet collapse and sea-level rise at the Bølling warming 14,600 years ago. *Nature*, 483(7391), 559–564. <https://doi.org/10.1038/nature10902>
- Diamond, D. (2002). Determination of silicate in brackish or seawater by flow injection analysis. QuickChem Method 31-114-27-1-D. *Lachat Instruments QuickChem Method Manual*.
- Domack, E., O'Brien, P., Harris, P., Taylor, F., Quilty, P. G., De Santis, L., & Raker, B. (1998). Late quaternary sediment facies in Prydz Bay, East Antarctica and their relationship to glacial advance onto the continental shelf. *Antarctic Science*, 10(3), 236–246. <https://doi.org/10.1017/s0954102098000339>
- Domack, E. W., Jull, A. J. T., & Nakao, S. (1991). Advance of East Antarctic outlet glaciers during the Hypsithermal: implications for the volume state of the Antarctic ice sheet under global warming. *Geology*, 19(11), 1059–1062. [https://doi.org/10.1130/0091-7613\(1991\)019<1059:AOEAOG>2.3.CO;2](https://doi.org/10.1130/0091-7613(1991)019<1059:AOEAOG>2.3.CO;2)
- Dymond, J., & Collier, R. (1996). Particulate barium fluxes and their relationships to biological productivity. *Deep-Sea Research Part II: Topical Studies in Oceanography*, 43(4–6), 1283–1308. [https://doi.org/10.1016/0967-0645\(96\)00011-2](https://doi.org/10.1016/0967-0645(96)00011-2)
- Dypvik, H., & Harris, N. B. (2001). Geochemical facies analysis of fine-grained siliciclastics using Th/U, Zr/Rb and (Zr + Rb)/Sr ratios. *Chemical Geology*, 181(1–4), 131–146. [https://doi.org/10.1016/S0009-2541\(01\)00278-9](https://doi.org/10.1016/S0009-2541(01)00278-9)
- Flückiger, J., Knutti, R., & White, J. W. C. (2006). Oceanic processes as potential trigger and amplifying mechanisms for Heinrich events. *Paleoceanography*, 21(2). <https://doi.org/10.1029/2005PA001204>

- Folk, R. L., & Ward, W. C. (1957). Brazos River bar [Texas]; a study in the significance of grain size parameters. *Journal of Sedimentary Research*, 27(1), 3–26.  
<https://doi.org/10.1306/74d70646-2b21-11d7-8648000102c1865d>
- Fralick, P. W., & Kronberg, B. I. (1997). Geochemical discrimination of clastic sedimentary rock sources. *Sedimentary Geology*, 113(1–2), 111–124. [https://doi.org/10.1016/S0037-0738\(97\)00049-3](https://doi.org/10.1016/S0037-0738(97)00049-3)
- Fretwell, P., Pritchard, H. D., Vaughan, D. G., Bamber, J. L., Barrand, N. E., Bell, R., ... Zirizzotti, A. (2013). Bedmap2: Improved ice bed, surface and thickness datasets for Antarctica. *Cryosphere*, 7(1), 375–393. <https://doi.org/10.5194/tc-7-375-2013>
- Gibson, J. A. E., Paterson, K. S., White, C. A., & Swadling, K. M. (2009). Evidence for the continued existence of abraxas lake, vestfold hills, east Antarctica during the last glacial maximum. *Antarctic Science*, 21(3), 269–278. <https://doi.org/10.1017/S0954102009001801>
- Gingele, F. X., Kuhn, G., Maus, B., Melles, M., & Schöne, T. (1997). Holocene ice retreat from the Lazarev Sea shelf, East Antarctica. *Continental Shelf Research*, 17(2), 137–163.  
[https://doi.org/10.1016/S0278-4343\(96\)00026-X](https://doi.org/10.1016/S0278-4343(96)00026-X)
- Golledge, N. R., Menviel, L., Carter, L., Fogwill, C. J., England, M. H., Cortese, G., & Levy, R. H. (2014). Antarctic contribution to meltwater pulse 1A from reduced Southern Ocean overturning. *Nature Communications*, 5(1), 1–10. <https://doi.org/10.1038/ncomms6107>
- Goodwin, I. D. (1993). Holocene deglaciation, sea-level change, and the emergence of the Windmill Islands, Budd Coast, Antarctica. *Quaternary Research*, 40(1), 55–69.  
<https://doi.org/10.1006/qres.1993.1057>
- Goodwin, I. D. (1996). A mid to late holocene readvance of the law dome ice margin, Budd Coast, East Antarctica. *Antarctic Science*, 8(4), 395–406.  
<https://doi.org/10.1017/s0954102096000570>
- Gore, D. B., Rhodes, E. J., Augustinus, P. C., Leishman, M. R., Colhoun, E. A., & Rees-Jones, J. (2001). Bunge Hills, East Antarctica: Ice free at the Last Glacial Maximum. *Geology*, 29(12), 1103–1106. [https://doi.org/10.1130/0091-7613\(2001\)029<1103:BHEAIF>2.0.CO;2](https://doi.org/10.1130/0091-7613(2001)029<1103:BHEAIF>2.0.CO;2)
- Greenwood, S. L., Simkins, L. M., Halberstadt, A. R. W., Prothro, L. O., & Anderson, J. B. (2018). Holocene reconfiguration and readvance of the East Antarctic Ice Sheet. *Nature Communications*, 9(1). <https://doi.org/10.1038/s41467-018-05625-3>

- Gregoire, L. J., Otto-Bliesner, B., Valdes, P. J., & Ivanovic, R. (2016). Abrupt Bølling warming and ice saddle collapse contributions to the Meltwater Pulse 1a rapid sea level rise. *Geophysical Research Letters*, *43*(17), 9130–9137. <https://doi.org/10.1002/2016GL070356>
- Hall, B. L., Henderson, G. M., Baroni, C., & Kellogg, T. B. (2010). Constant Holocene Southern-Ocean 14 C reservoir ages and ice-shelf flow rates. *Earth and Planetary Science Letters*, *296*(1–2), 115–123. <https://doi.org/10.1016/j.epsl.2010.04.054>
- Hall, I. R., Moran, S. B., Zahn, R., Knutz, P. C., Shen, C. C., & Edwards, R. L. (2006). Accelerated drawdown of meridional overturning in the late-glacial Atlantic triggered by transient pre-H event freshwater perturbation. *Geophysical Research Letters*, *33*(16). <https://doi.org/10.1029/2006GL026239>
- Hanebuth, T., Stattegger, K., & Grootes, P. M. (2000). Rapid flooding of the Sunda Shelf: A late-glacial sea-level record. *Science*, *288*(5468), 1033–1035. <https://doi.org/10.1126/science.288.5468.1033>
- Harris, P. T., Brancolini, G., Armand, L., Busetti, M., Beaman, R. J., Giorgetti, G., ... Trincardi, F. (2001). Continental shelf drift deposit indicates non-steady state Antarctic bottom water production in the Holocene. *Marine Geology*, *179*(1–2), 1–8. [https://doi.org/10.1016/S0025-3227\(01\)00183-9](https://doi.org/10.1016/S0025-3227(01)00183-9)
- Harris, P. T., & O'Brien, P. E. (1998). Bottom currents, sedimentation and ice-sheet retreat facies successions on the Mac Robertson shelf, East Antarctica. *Marine Geology*, *151*(1–4), 47–72. [https://doi.org/10.1016/S0025-3227\(98\)00047-4](https://doi.org/10.1016/S0025-3227(98)00047-4)
- Haslett, J., & Parnell, A. (2008). A simple monotone process with application to radiocarbon-dated depth chronologies. *Journal of the Royal Statistical Society. Series C: Applied Statistics*, *57*(4), 399–418. <https://doi.org/10.1111/j.1467-9876.2008.00623.x>
- Heaton, T. J., Köhler, P., Butzin, M., Bard, E., Reimer, R. W., Austin, W. E. N., ... Skinner, L. C. (2020). Marine20 - The Marine Radiocarbon Age Calibration Curve (0-55,000 cal BP). *Radiocarbon*, *62*(4), 779–820. <https://doi.org/10.1017/RDC.2020.68>
- Heinrich, H. (1988). Origin and consequences of cyclic ice rafting in the Northeast Atlantic Ocean during the past 130,000 years. *Quaternary Research*, *29*(2), 142–152. [https://doi.org/10.1016/0033-5894\(88\)90057-9](https://doi.org/10.1016/0033-5894(88)90057-9)
- Hemer, M. A., & Harris, P. T. (2003). Sediment core from beneath the Amery Ice shelf, East Antarctica, suggests mid-Holocene ice-shelf retreat. *Geology*, *31*(2), 127–130. [https://doi.org/10.1130/0091-7613\(2003\)031<0127:SCFBTA>2.0.CO;2](https://doi.org/10.1130/0091-7613(2003)031<0127:SCFBTA>2.0.CO;2)

- Hillenbrand, C. D., Crowhurst, S. J., Williams, M., Hodell, D. A., McCave, I. N., Ehrmann, W., ... Larter, R. D. (2021). New insights from multi-proxy data from the West Antarctic continental rise: Implications for dating and interpreting Late Quaternary palaeoenvironmental records. *Quaternary Science Reviews*, 257, 106842. <https://doi.org/10.1016/j.quascirev.2021.106842>
- Hillenbrand, C. D., Smith, J. A., Kuhn, G., Esper, O., Gersonde, R., Larter, R. D., ... Korte, M. (2010). Age assignment of a diatomaceous ooze deposited in the Western Amundsen Sea embayment after the last glacial maximum. *Journal of Quaternary Science*, 25(3), 280–295. <https://doi.org/10.1002/jqs.1308>
- Hodgson, D. A., Noon, P. E., Vyverman, W., Bryant, C. L., Gore, D. B., Appleby, P., ... Wood, P. B. (2001). Were the Larsemann Hills ice-free through the Last Glacial Maximum? *Antarctic Science*, 13(4), 440–454. <https://doi.org/10.1017/S0954102001000608>
- Hogg, A. G., Heaton, T. J., Hua, Q., Palmer, J. G., Turney, C. S. M., Southon, J., ... Wacker, L. (2020). SHCal20 Southern Hemisphere Calibration, 0-55,000 Years cal BP. *Radiocarbon*, 62(4), 759–778. <https://doi.org/10.1017/RDC.2020.59>
- Hogg, A. G., Heaton, T. J., Ramsey, C. B., Boswijk, G., Palmer, J. G., Turney, C. S. M., ... Gumbley, W. (2019). The Influence of Calibration Curve Construction and Composition on the Accuracy and Precision of Radiocarbon Wiggle-Matching of Tree Rings, Illustrated by Southern Hemisphere Atmospheric Data Sets from AD 1500–1950. *Radiocarbon*, 61(5), 1265–1291. <https://doi.org/10.1017/rdc.2019.42>
- Holder, L., Duffy, M., Opdyke, B., Leventer, A., Post, A., O'Brien, P., & Armand, L. K. (2020). Controls Since the mid-Pleistocene Transition on Sedimentation and Primary Productivity Downslope of Totten Glacier, East Antarctica. *Paleoceanography and Paleoclimatology*, 35(12). <https://doi.org/10.1029/2020PA003981>
- Huang, T., Sun, L., Wang, Y., Liu, X., & Zhu, R. (2009). Penguin population dynamics for the past 8500 years at Gardner Island, Vestfold Hills. *Antarctic Science*, 21(6), 571–578. <https://doi.org/10.1017/S0954102009990332>
- Hulbe, C. L., MacAyeal, D. R., Denton, G. H., Kleman, J., & Lowell, T. V. (2004). Catastrophic ice shelf breakup as the source of Heinrich event icebergs. *Paleoceanography*, 19(1). <https://doi.org/10.1029/2003pa000890>
- Igarashi, A., Numanami, H., Tsuchiya, Y., & Fukuchi, M. (2001). Bathymetric distribution of fossil foraminifera within marine sediment cores from the eastern part of Lützow-Holm Bay, East Antarctica, and its paleoceanographic implications. *Marine Micropaleontology*, 42(3–4), 125–162. [https://doi.org/10.1016/S0377-8398\(01\)00004-4](https://doi.org/10.1016/S0377-8398(01)00004-4)

- Ivins, E. R., James, T. S., Wahr, J., Ernst, E. J., Landerer, F. W., & Simon, K. M. (2013). Antarctic contribution to sea level rise observed by GRACE with improved GIA correction. *Journal of Geophysical Research: Solid Earth*, *118*(6), 3126–3141. <https://doi.org/10.1002/jgrb.50208>
- Kingslake, J., Scherer, R. P., Albrecht, T., Coenen, J., Powell, R. D., Reese, R., ... Whitehouse, P. L. (2018). Extensive retreat and re-advance of the West Antarctic Ice Sheet during the Holocene. *Nature*, *558*(7710), 430–434. <https://doi.org/10.1038/s41586-018-0208-x>
- Kirkup, H., Melles, M., & Gore, D. B. (2002). Late quaternary environment of southern Windmill Islands, East Antarctica. *Antarctic Science*, *14*(4), 385–394. <https://doi.org/10.1017/S0954102002000202>
- Knorr, G., & Lohmann, G. (2003). Southern ocean origin for the resumption of Atlantic thermohaline circulation during deglaciation. *Nature*, *424*(6948), 532–536. <https://doi.org/10.1038/nature01855>
- Kohfeld, K. E., Graham, R. M., de Boer, A. M., Sime, L. C., Wolff, E. W., le Quéré, C., & Bopp, L. (2013). Southern Hemisphere westerly wind changes during the Last Glacial Maximum: Paleo-data synthesis. *Quaternary Science Reviews*, *68*, 76–95. <https://doi.org/10.1016/j.quascirev.2013.01.017>
- Konrad, H., Shepherd, A., Gilbert, L., Hogg, A. E., McMillan, M., Muir, A., & Slater, T. (2018). Net retreat of Antarctic glacier grounding lines. *Nature Geoscience*, *11*(4), 258–262. <https://doi.org/10.1038/s41561-018-0082-z>
- Krissek, L. A. (1995). *Late Cenozoic Ice-Rafting Records from Leg 145 Sites in the North Pacific: Late Miocene Onset, Late Pliocene Intensification, and Pliocene—Pleistocene Events. Proceedings of the Ocean Drilling Program, 145 Scientific Results* (Vol. 145). <https://doi.org/10.2973/odp.proc.sr.145.118.1995>
- Larter, R. D., Hogan, K. A., & Dowdeswell, J. A. (2016). Large sediment drifts on the upper continental rise west of the Antarctic Peninsula. *Geological Society Memoir*, *46*(1), 401–402. <https://doi.org/10.1144/M46.132>
- Leventer, A., Domack, E., Dunbar, R., Pike, J., Stickley, C., Maddison, E., ... McClennen, C. (2006). Marine sediment record from the East Antarctic margin reveals dynamics of ice sheet recession. *GSA Today*, *16*(12), 4–10. <https://doi.org/10.1130/GSAT01612A.1>
- Li, X., Rignot, E., Mouginot, J., & Scheuchl, B. (2016). Ice flow dynamics and mass loss of Totten Glacier, East Antarctica, from 1989 to 2015. *Geophysical Research Letters*, *43*(12), 6366–6373. <https://doi.org/10.1002/2016GL069173>

- Lougheed, B. C., & Obrochta, S. P. (2016). MatCal: Open Source Bayesian 14C Age Calibration in Matlab. *Journal of Open Research Software*, 4. <https://doi.org/10.5334/jors.130>
- MacAyeal, D. R. (1993). Binge/purge oscillations of the Laurentide Ice Sheet as a cause of the North Atlantic's Heinrich events. *Paleoceanography*, 8(6), 775–784. <https://doi.org/10.1029/93PA02200>
- MacKintosh, A., Golledge, N., Domack, E., Dunbar, R., Leventer, A., White, D., ... Lavoie, C. (2011). Retreat of the East Antarctic ice sheet during the last glacial termination. *Nature Geoscience*, 4(3), 195–202. <https://doi.org/10.1038/ngeo1061>
- Mackintosh, A. N., Verleyen, E., O'Brien, P. E., White, D. A., Jones, R. S., McKay, R., ... Masse, G. (2014). Retreat history of the East Antarctic Ice Sheet since the Last Glacial Maximum. *Quaternary Science Reviews*, 100, 10–30. <https://doi.org/10.1016/j.quascirev.2013.07.024>
- Masson, V., Vimeux, F., Jouzel, J., Morgan, V., Delmotte, M., Ciais, P., ... Vaikmae, R. (2000). Holocene climate variability in Antarctica based on 11 ice-core isotopic records. *Quaternary Research*, 54(3), 348–358. <https://doi.org/10.1006/qres.2000.2172>
- McCave, I. N., & Andrews, J. T. (2019, May 15). Distinguishing current effects in sediments delivered to the ocean by ice. I. Principles, methods and examples. *Quaternary Science Reviews*. Elsevier Ltd. <https://doi.org/10.1016/j.quascirev.2019.03.031>
- McCave, I. N., & Hall, I. R. (2006). Size sorting in marine muds: Processes, pitfalls, and prospects for paleoflow-speed proxies. *Geochemistry, Geophysics, Geosystems*, 7(10), n/a-n/a. <https://doi.org/10.1029/2006GC001284>
- McCave, I. N., Manighetti, B., & Robinson, S. G. (1995). Sortable silt and fine sediment size/composition slicing: Parameters for palaeocurrent speed and palaeoceanography. *Paleoceanography*, 10(3), 593–610. <https://doi.org/10.1029/94PA03039>
- McCave, I. N., Thornalley, D. J. R., & Hall, I. R. (2017). Relation of sortable silt grain-size to deep-sea current speeds: Calibration of the 'Mud Current Meter.' *Deep-Sea Research Part I: Oceanographic Research Papers*, 127, 1–12. <https://doi.org/10.1016/j.dsr.2017.07.003>
- McManus, J. F., Francois, R., Gherardl, J. M., Kelgwin, L., & Drown-Leger, S. (2004). Collapse and rapid resumption of Atlantic meridional circulation linked to deglacial climate changes. *Nature*, 428(6985), 834–837. <https://doi.org/10.1038/nature02494>
- McMinn, A. (2000). Late Holocene increase in sea ice extent in fjords of the Vestfold Hills, eastern Antarctica. *Antarctic Science*, 12(1), 80–88. <https://doi.org/10.1017/s0954102000000110>

- McMullen, K., Domack, E., Leventer, A., Olson, C., Dunbar, R., & Brachfeld, S. (2006). Glacial morphology and sediment formation in the Mertz Trough, East Antarctica. In *Palaeogeography, Palaeoclimatology, Palaeoecology* (Vol. 231, pp. 169–180). Elsevier. <https://doi.org/10.1016/j.palaeo.2005.08.004>
- Miura, H., Moriwaki, K., Maemoku, H., & Hirakawa, K. (1998). Fluctuations of the East Antarctic ice-sheet margin since the last glaciation from the stratigraphy of raised beach deposits along the Soya Coast. *Annals of Glaciology*, 27, 297–301. <https://doi.org/10.3189/1998aog27-1-297-301>
- Morlighem, M., Rignot, E., Binder, T., Blankenship, D., Drews, R., Eagles, G., ... Young, D. A. (2020). Deep glacial troughs and stabilizing ridges unveiled beneath the margins of the Antarctic ice sheet. *Nature Geoscience*, 13(2), 132–137. <https://doi.org/10.1038/s41561-019-0510-8>
- Mortlock, R. A., Charles, C. D., Froelich, P. N., Zibello, M. A., Saltzman, J., Hays, J. D., & Burckle, L. H. (1991). Evidence for lower productivity in the Antarctic Ocean during the last glaciation. *Nature* (Vol. 351). <https://doi.org/10.1038/351220a0>
- Mortlock, R. A., & Froelich, P. N. (1989). A simple method for the rapid determination of biogenic opal in pelagic marine sediments. *Deep Sea Research Part A, Oceanographic Research Papers*, 36(9), 1415–1426. [https://doi.org/10.1016/0198-0149\(89\)90092-7](https://doi.org/10.1016/0198-0149(89)90092-7)
- Noble, T. L., Rohling, E. J., Aitken, A. R. A., Bostock, H. C., Chase, Z., Gomez, N., ... Williams, T. (2020). The Sensitivity of the Antarctic Ice Sheet to a Changing Climate: Past, Present, and Future. *Reviews of Geophysics*, 58(4), e2019RG000663. <https://doi.org/10.1029/2019RG000663>
- O'Brien, P. E., Post, A. L., Edwards, S., Martin, T., Caburlotto, A., Donda, F., ... Armand, L. K. (2020). Continental slope and rise geomorphology seaward of the Totten Glacier, East Antarctica (112°E-122°E). *Marine Geology*, 427, 106221. <https://doi.org/10.1016/j.margeo.2020.106221>
- Orsi, A. H., Whitworth III, T., & Nowlin, W., D. (1995). On the extent and frontal structure of the Antarctic Circumpolar Current. *Deep Sea Res. Pt. I*, 2(43), 96–97.
- Parnell, A. C., Haslett, J., Allen, J. R. M., Buck, C. E., & Huntley, B. (2008). A flexible approach to assessing synchronicity of past events using Bayesian reconstructions of sedimentation history. *Quaternary Science Reviews*, 27(19–20), 1872–1885. <https://doi.org/10.1016/j.quascirev.2008.07.009>

- Paterne, M., Michel, E., & Héros, V. (2019). Variability of marine  $^{14}\text{C}$  reservoir ages in the Southern Ocean highlighting circulation changes between 1910 and 1950. *Earth and Planetary Science Letters*, 511, 99–104. <https://doi.org/10.1016/j.epsl.2019.01.029>
- Patterson, M. O., McKay, R., Naish, T., Escutia, C., Jimenez-Espejo, F. J., Raymo, M. E., ... Yamane, M. (2014). Orbital forcing of the East Antarctic ice sheet during the Pliocene and Early Pleistocene. *Nature Geoscience*, 7(11), 841–847. <https://doi.org/10.1038/ngeo2273>
- Pedro, J. B., Bostock, H. C., Bitz, C. M., He, F., Vandergoes, M. J., Steig, E. J., ... Cortese, G. (2016). The spatial extent and dynamics of the Antarctic Cold Reversal. *Nature Geoscience*, 9(1), 51–55. <https://doi.org/10.1038/ngeo2580>
- Pedro, J. B., van Ommen, T. D., Rasmussen, S. O., Morgan, V. I., Chappellaz, J., Moy, A. D., ... Delmotte, M. (2011). The last deglaciation: Timing the bipolar seesaw. *Climate of the Past*, 7(2), 671–683. <https://doi.org/10.5194/cp-7-671-2011>
- Post, A. L., O'Brien, P. E., Edwards, S., Carroll, A. G., Malakoff, K., & Armand, L. K. (2020). Upper slope processes and seafloor ecosystems on the Sabrina continental slope, East Antarctica. *Marine Geology*, 422, 106091. <https://doi.org/10.1016/j.margeo.2019.106091>
- Prothro, L. O., Majewski, W., Yokoyama, Y., Simkins, L. M., Anderson, J. B., Yamane, M., ... Ohkouchi, N. (2020). Timing and pathways of East Antarctic Ice Sheet retreat. *Quaternary Science Reviews*, 230. <https://doi.org/10.1016/j.quascirev.2020.106166>
- Rebesco, M., Domack, E., Zgur, F., Lavoie, C., Leventer, A., Brachfeld, S., ... Pettit, E. (2014a). Boundary condition of grounding lines prior to collapse, Larsen-B Ice Shelf, Antarctica. *Science*, 345(6202), 1354–1358. <https://doi.org/10.1126/science.1256697>
- Rebesco, M., Hernández-Molina, F. J., van Rooij, D., & Wåhlin, A. (2014b). Contourites and associated sediments controlled by deep-water circulation processes: State-of-the-art and future considerations. *Marine Geology*, 352, 111–154. <https://doi.org/10.1016/j.margeo.2014.03.011>
- Rebesco, M., Pudsey, C. J., Canals, M., Camerlenghi, A., Barker, P. F., Estrada, F., & Giorgetti, A. (2002). Sediment drifts and deep-sea channel systems, Antarctic Peninsula Pacific Margin. *Geological Society Memoir*, 22(1), 353–371. <https://doi.org/10.1144/GSL.MEM.2002.022.01.25>
- Rignot, E., Mouginot, J., Scheuchl, B., van den Broeke, M., van Wessem, M. J., & Morlighem, M. (2019, January 22). Four decades of Antarctic ice sheet mass balance from 1979–2017. *Proceedings of the National Academy of Sciences of the United States of America*. National Academy of Sciences. <https://doi.org/10.1073/pnas.1812883116>

- Roberts, D., Hodgson, D. A., McMinn, A., Verleyen, E., Terry, B., Corbett, C., & Vyverman, W. (2006). Recent rapid salinity rise in three East Antarctic lakes. *Journal of Paleolimnology*, 36(4), 385–406. <https://doi.org/10.1007/s10933-006-9010-0>
- Roberts, D., & McMinn, A. (1999). A diatom-based palaeosalinity history of Ace lake, Vestfold Hills, Antarctica. *Holocene*, 9(4), 401–408. <https://doi.org/10.1191/095968399671725699>
- Shen, Q., Wang, H., Shum, C. K., Jiang, L., Hsu, H. T., & Dong, J. (2018). Recent high-resolution Antarctic ice velocity maps reveal increased mass loss in Wilkes Land, East Antarctica. *Scientific Reports*, 8(1), 1–8. <https://doi.org/10.1038/s41598-018-22765-0>
- Siegert, M. J., Kingslake, J., Ross, N., Whitehouse, P. L., Woodward, J., Jamieson, S. S. R., ... Sugden, D. E. (2019). Major Ice Sheet Change in the Weddell Sea Sector of West Antarctica Over the Last 5,000 Years. *Reviews of Geophysics*, 57(4), 1197–1223. <https://doi.org/10.1029/2019RG000651>
- Skinner, L. C., Fallon, S., Waelbroeck, C., Michel, E., & Barker, S. (2010). Ventilation of the deep southern ocean and deglacial CO<sub>2</sub> rise. *Science*, 328(5982), 1147–1151. <https://doi.org/10.1126/science.1183627>
- Skinner, L. C., Muschitiello, F., & Scrivner, A. E. (2019). Marine Reservoir Age Variability Over the Last Deglaciation: Implications for Marine Carbon Cycling and Prospects for Regional Radiocarbon Calibrations. *Paleoceanography and Paleoclimatology*, 34(11), 1807–1815. <https://doi.org/10.1029/2019PA003667>
- Smith, J. A., Graham, A. G. C., Post, A. L., Hillenbrand, C. D., Bart, P. J., & Powell, R. D. (2019, December 1). The marine geological imprint of Antarctic ice shelves. *Nature Communications*. Nature Research. <https://doi.org/10.1038/s41467-019-13496-5>
- Stewart, A. L., & Thompson, A. F. (2012). Sensitivity of the ocean's deep overturning circulation to easterly Antarctic winds. *Geophysical Research Letters*, 39(17). <https://doi.org/10.1029/2012GL053099>
- Tooze, S., Halpin, J. A., Noble, T. L., Chase, Z., O'Brien, P. E., & Armand, L. (2020). Scratching the Surface: A Marine Sediment Provenance Record From the Continental Slope of Central Wilkes Land, East Antarctica. *Geochemistry, Geophysics, Geosystems*, 21(11). <https://doi.org/10.1029/2020GC009156>
- Venturelli, R. A., Siegfried, M. R., Roush, K. A., Li, W., Burnett, J., Zook, R., ... Rosenheim, B. E. (2020). Mid-Holocene Grounding Line Retreat and Readvance at Whillans Ice Stream, West Antarctica. *Geophysical Research Letters*, 47(15). <https://doi.org/10.1029/2020GL088476>

- Verleyen, E., Hodgson, D. A., Sabbe, K., Cremer, H., Emslie, S. D., Gibson, J., ... Vyverman, W. (2011, February 1). Post-glacial regional climate variability along the East Antarctic coastal margin-Evidence from shallow marine and coastal terrestrial records. *Earth-Science Reviews*. Elsevier. <https://doi.org/10.1016/j.earscirev.2010.10.006>
- Wagner, B., Cremer, H., Hultsch, N., Gore, D. B., & Melles, M. (2004). *Late Pleistocene and Holocene history of Lake Terrasovoje, Amery Oasis, East Antarctica, and its climatic and environmental implications*. *Journal of Paleolimnology* (Vol. 32). <https://doi.org/10.1007/s10933-004-0143-8>
- Warnock, J. P., & Scherer, R. P. (2015). A revised method for determining the absolute abundance of diatoms. *Journal of Paleolimnology*, 53(1), 157–163. <https://doi.org/10.1007/s10933-014-9808-0>
- Weaver, A. J., Saenko, O. A., Clark, P. U., & Mitrovica, J. X. (2003). Meltwater pulse 1A from Antarctica as a trigger of the Bølling-Allerød warm interval. *Science*, 299(5613), 1709–1713. <https://doi.org/10.1126/science.1081002>
- Weber, M. E., Clark, P. U., Kuhn, G., Timmermann, A., Spreng, D., Gladstone, R., ... Ohlwein, C. (2014). Millennial-scale variability in Antarctic ice-sheet discharge during the last deglaciation. *Nature*, 510(7503), 134–138. <https://doi.org/10.1038/nature13397>
- Wu, L., Wilson, D. J., Wang, R., Yin, X., Chen, Z., Xiao, W., & Huang, M. (2020). Evaluating Zr/Rb ratio from XRF scanning as an indicator of grain-size variations of glaciomarine sediments in the Southern Ocean. *Geochemistry, Geophysics, Geosystems*. <https://doi.org/10.1029/2020gc009350>
- Zhang, Q. (1985). Periglacial landforms in the Vestfold Hills, East Antarctica. *Studies of Late Quaternary Geology and Geomorphology in the Vestfold Hills, East Antarctica*, 18–26.
- Zwartz, D., Bird, M., Stone, J., & Lambeck, K. (1998). Holocene sea-level change and ice-sheet history in the Vestfold Hills, East Antarctica. *Earth and Planetary Science Letters*, 155(1–2), 131–145. [https://doi.org/10.1016/s0012-821x\(97\)00204-5](https://doi.org/10.1016/s0012-821x(97)00204-5)

# Chapter 3

## Scratching the surface: a marine sediment provenance record from the continental slope of central Wilkes Land, East Antarctica

### Abstract

The geology of Wilkes Land, East Antarctica, is masked by kilometres of ice and remains largely unexplored. Defining the sediment provenance adjacent to this hidden region is important for distinguishing the proximal subglacial basement terranes and refining the dynamic regional glaciological history. This study presents a detrital sediment provenance record spanning c. 23.5 ka from the continental slope of central Wilkes Land. Sediment provenance was characterised using U-Pb geochronology and trace element geochemistry from detrital zircon, titanite and apatite and Pb-isotopic signatures from detrital feldspar. These data were compared with new feldspar Pb-isotopic signatures and existing U-Pb zircon datasets from rare nearby coastal outcrop. A principally igneous source was revealed with dominant age populations between c. 1360-1100 Ma and c. 1620-1490 Ma, characteristic of rocks of the proximal Wilkes and Banzare provinces, respectively. Minor detritus was additionally sourced from the proximal Nuyina Province (c. 1450-1390 Ma). Temporal variation in the climate and ice sheet configuration are likely responsible for subtle downcore changes observed in detrital sediment provenance. High sedimentation rates during the glacial period suggest reworking of continental shelf sediments and downslope transport in debris flows during ice sheet advance. Glacial meltwater fluxes fed largely by the Totten Glacier were responsible for supplying detritus during deglaciation. During the

Holocene, detritus was derived from a broad coastal region and delivered to the slope via multiple glacial outlets. These results present the first substantial offshore evidence to support recent interpretations that the subglacial crust of central Wilkes Land has a dominantly Mesoproterozoic history.

### **3.1. Introduction**

The subglacial geology of Wilkes Land, East Antarctica, is poorly characterised, due to its concealment beneath 0.4 - 4 km of thick ice (Fretwell et al. 2013) with sparse coastal rock outcrop. Yet a better understanding of the ice-covered continental crust has the potential to provide valuable insights into the dynamic tectonic history of East Antarctica and its role during supercontinent cycles (Aitken et al., 2016a; Mulder et al., 2019). Additionally, deciphering the bedrock composition can help identify sediment erosion and transport pathways and constrain subglacial conditions (e.g., geothermal heat flow, topography, basal erosion) deemed to have impacted Antarctic Ice Sheet evolution (Golledge et al., 2013; Jamieson et al., 2010; Lowry et al., 2020). In this context, the Sabrina Subglacial Basin in Wilkes Land (Aitken et al., 2016b) is of particular interest, forming part of an extensive glacial drainage system that is predominantly situated below sea-level (Fretwell et al., 2013; Young et al., 2011). This region drains into the ocean via the rapidly retreating Totten Glacier (Rignot et al., 2019) and has the capacity to raise global sea-level by 3.5 m (Greenbaum et al., 2015).

Multiple sedimentary features of the continental slope of the Sabrina Coast provide evidence for sediment delivery via meltwater fluxes supplied by major glacier systems throughout the Late Cenozoic (c. 34 Ma to present) (Donda et al., 2020). The Totten Glacier is considered to have played a central role in controlling these sediment-laden meltwater fluxes that have historically shaped the submarine landscape. The slope bathymetry in this region is characterised by two large contourite ridges to the west and a dendritic network of gullies that develop into submarine canyons to the east (O'Brien et al., 2020; Post et al., 2020). These sedimentary features have been observed and interpreted in other regions around

East Antarctica (De Santis et al., 2007; Donda et al., 2020; O'Brien et al., 2016) and West Antarctica (Amblas and Canals, 2016; Dowdeswell et al., 2004, 2006; Gales et al., 2013) and provide records of sediment erosion during the evolution of the ice sheet.

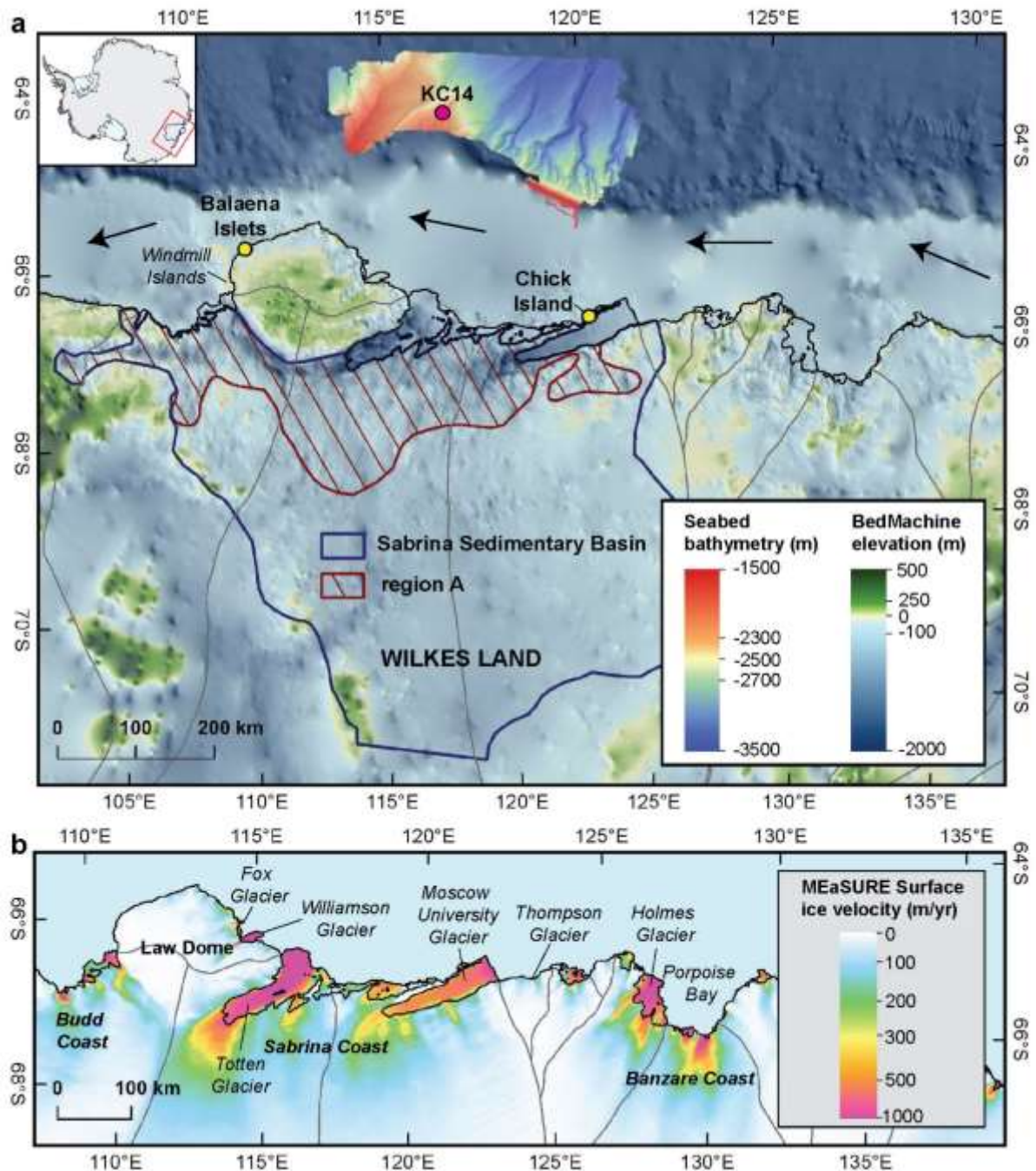


**Figure 3.1.** (a) Simplified outline of the Sabrina Sedimentary Basin (bold dark blue line) is from Maritati et al. (2019) after Aitken et al. (2016b). Region A, an area of thin sedimentary rock cover (<1 km thick) and basement rock exposure is interpreted by Aitken et al. (2016b).

Grey lines mark the boundaries of ice drainage basins (Mouginot et al., 2017). Black arrows represent the westward-flowing Antarctic Coastal Current. Inset shows the study location (red box) on a map of Antarctica. **(b)** MEaSURES surface ice velocity from InSAR data, highlighting major glacier outflows in central Wilkes Land (Mouginot et al., 2012; Rignot et al., 2011).

Studies of marine sediment provenance around Antarctica have been used to investigate the subglacial terrain in the absence of onshore geological data and to complement non-unique geophysical signatures (Licht and Hemming, 2017; Pierce et al., 2014; Roy et al., 2007; Williams et al., 2010). In this study, we aim to test existing interpretations of subglacial bedrock composition and erosion pathways in central Wilkes Land. We do this by characterising the isotopic and geochemical signature of detrital grains in a sediment core recovered from the eastern flank of a large contourite ridge situated on the continental slope of the Sabrina Coast in central Wilkes Land (Fig. 3.1a).

## **3.2. Background: a brief glaciological and geological history of Wilkes Land**

Our interpretation of the composition, provenance, and transport of continentally-derived detritus from Antarctica is informed by current understanding of the temporal changes to the Antarctic Ice Sheet and the regional geological history. Here we provide a brief synopsis of the EAIS configuration from its maximum extent during the Last Glacial Period to present, followed by a summary of the geological evolution of central Wilkes Land, East Antarctica.

### **3.2.1. Evolution of the East Antarctic Ice Sheet from the Late Pleistocene to present**

The expansion and retreat of the ice sheet over glacial to interglacial timescales has left an imprint on the sedimentary basin infill in central Wilkes Land (Aitken et al., 2016b). Region A of the Sabrina Sedimentary Basin (Fig. 3.1a) is characterised by a thin subglacial sedimentary rock veneer (<1 km in thickness), in some places exposing crystalline basement rock at the base of the ice sheet (Aitken et al., 2016b). The scarcity of sedimentary rock between the base of the ice sheet and basement geology is interpreted as indicating repeated erosion during cyclic waxing and waning of the ice sheet in this region (Aitken et al., 2016b). Ancient shelf sedimentary megasequences provide additional evidence of repeated ice sheet advance and retreat from the beginning of the Oligocene to the mid-Miocene (Gulick et al., 2017).

Sedimentary bedforms on the continental shelf and slope of central Wilkes Land also preserve a dynamic history of sediment erosion, transport, and deposition. Throughout the Late Cenozoic (phases 2-4 of Donda et al., 2007), the EAIS was unstable and sediment-laden meltwater fluxes sourced from major outlet glaciers (Fig. 3.1b) had an important influence on the morphology of the seabed on the continental shelf, slope and rise (Donda et al., 2007; Leitchenkov, 2015). In the west of the study region, large sediment contourites formed on the continental slope and are maintained by debris flows and fall out from sediment-rich meltwater plumes (Donda et al., 2020; O'Brien et al., 2020). Donda et al. (2020) suggested that the proximal Totten Glacier likely supplies a significant component of detritus to the slope in sediment-laden meltwater fluxes, maintaining these submarine landforms. Gullies developed in the east of the study region, where turbidite flows and meltwater fed by major glacial systems scoured into the seabed (Donda et al., 2020; O'Brien et al., 2020; Post et al., 2020).

Previous studies on the continental shelf of the Sabrina Coast provide evidence for maximum expansion of the ice sheet to within 2-5 km of the shelf break during past

glaciations (Fernandez et al., 2018; Post et al., 2020), but uncertainty remains around the exact position of the maximum grounding line extent. During the Last Glacial Period, as the ice sheet expanded close to the edge of the present-day continental shelf, the advancing ice remobilised sediments on the continental shelf and redeposited them on the continental slope (Post et al., 2020). As the ice sheet retreated, rising sea-level and sea-surface temperatures in the Southern Ocean promoted iceberg calving and meltwater production (Weber et al., 2014). The supply of detritus to the continental slope during deglaciation was controlled by erosion at the base of the grounded ice sheet, and the release of englacial debris in meltwater plumes and from icebergs as IBRD (Donda et al., 2020; O'Brien et al., 2020).

### **3.2.2. The subglacial geology of central Wilkes Land**

Throughout successive periods of supercontinent assembly (e.g., Nuna, Rodinia and Gondwana), much of the East Antarctic and southern Australian lithosphere accreted and consolidated forming a contiguous Australo-Antarctic component (Aitken et al., 2016a; Boger, 2011; Fitzsimons, 2003). This ancient tectonic relationship has cemented strong geological and structural affinities between the two now conjugate margins (Williams et al., 2019). Hampering our understanding, the basement rock geology is concealed under sedimentary basins and regolith in southern Australia and thick ice in East Antarctica. Existing interpretations in Wilkes Land rely on analysis of rare coastal rock outcrop (Maritati et al., 2019; Morrissey et al., 2017; Mulder et al., 2019; Tucker et al., 2017) combined with borehole analyses from southern Australia (Kirkland et al., 2017; Spaggiari and Smithies, 2015) and airborne geophysical data (Aitken et al., 2014). From west to east, three geologically distinct Mesoproterozoic provinces have been identified using these methods: the Albany-Fraser Orogen (c. 1300-1140 Ma), Madura Province (c. 1475-1390 Ma) and Coompana Province (c. 1610-1490 Ma); their Antarctic equivalents defined as the Wilkes, Nuyina and Banzare provinces, respectively (Aitken et al., 2014; Fitzsimons, 2003; Maritati et al., 2019). The geological relationships between southern Australia and East Antarctica are summarised below (Fig. 3.2) to provide context for our

provenance analysis. A more comprehensive regional geological history can be found in the references herein.

The Albany-Fraser Orogen (Fig. 3.2) is characterised by reworked Archean and Proterozoic crust (Spaggiari et al., 2015). Exposed metasedimentary rocks of the Windmill Islands (Fig. 3.1.) within the Wilkes Province in East Antarctica compare to those of the Mount Ragged Formation (Clark et al., 2000) in the Albany-Fraser Orogen, on the basis of shared detrital U-Pb age signatures (Fitzsimons, 2003; Morrissey et al., 2017). Granite and charnockite intrusions in the Windmill Islands in East Antarctica have crystallization ages between c. 1325-1170 Ma, coeval with the Recherche (c. 1300-1290 Ma, Nelson et al., 1995) and Esperance (c. 1200-1140 Ma, Nelson et al., 1995) supersuites of the Nornalup Zone, the easternmost zone of the Albany-Fraser Orogen (Morrissey et al., 2017). The Rodona Shear Zone in southern Australia (Fig. 3.2a) is interpreted to be equivalent to the Totten Fault (of Aitken et al., 2014; Fig. 3.2a) underlying the Totten Glacier, marking the suture zone between the continental crust of the Albany-Fraser Orogen/Wilkes Province to the west and the oceanic crust of the Madura/Nuyina Province to the east (Maritati et al., 2019; Spaggiari et al., 2018).

The Madura and Coompana provinces have been distinguished geophysically (Aitken et al., 2014). Low magnetic intensities are representative of the c. 1610 Ma Toolgana and c. 1490 Ma Undawidgi supersuites of the Coompana Province and are distinct from the high magnetic intensities of the c. 1190-1140 Ma Moodini Supersuite that intrudes both the Madura and Coompana provinces (Kirkland et al., 2017). Comparable geophysical signatures for these three igneous supersuites are also identified in central Wilkes Land (Aitken et al., 2014; Maritati et al., 2019). Outcrop is very sparse in this region although recent zircon U-Pb-Hf geochronology undertaken on basement igneous samples from Chick Island (Fig. 3.1) reveal c. 1150 Ma granodioritic plutons with affinity to the Moodini Supersuite (Maritati et al., 2019). Furthermore, older c. 1530-1290 Ma xenocrystic zircon grains yield U-Pb-Hf signatures that correlate with older magmatic suites within both the Madura and Coompana provinces, suggesting that Chick Island lies close to the boundary

between the Nuyina and Banzare provinces in East Antarctica (Maritati et al., 2019). The crystalline basement rocks of the Coompana Province in Australia are overlain by two large sedimentary basins: the Neoproterozoic-Devonian Officer Basin and the Cretaceous-Tertiary Eucla Basin, the former of which has been recently correlated with the East Antarctic Sabrina Sedimentary Basin (coincident with the Sabrina Subglacial Basin) based on zircon U-Pb-Hf analyses from Neoproterozoic-aged sandstone erratics discharged from the Vanderford Glacier and found in the vicinity of the Windmill Islands (Maritati et al., 2019).

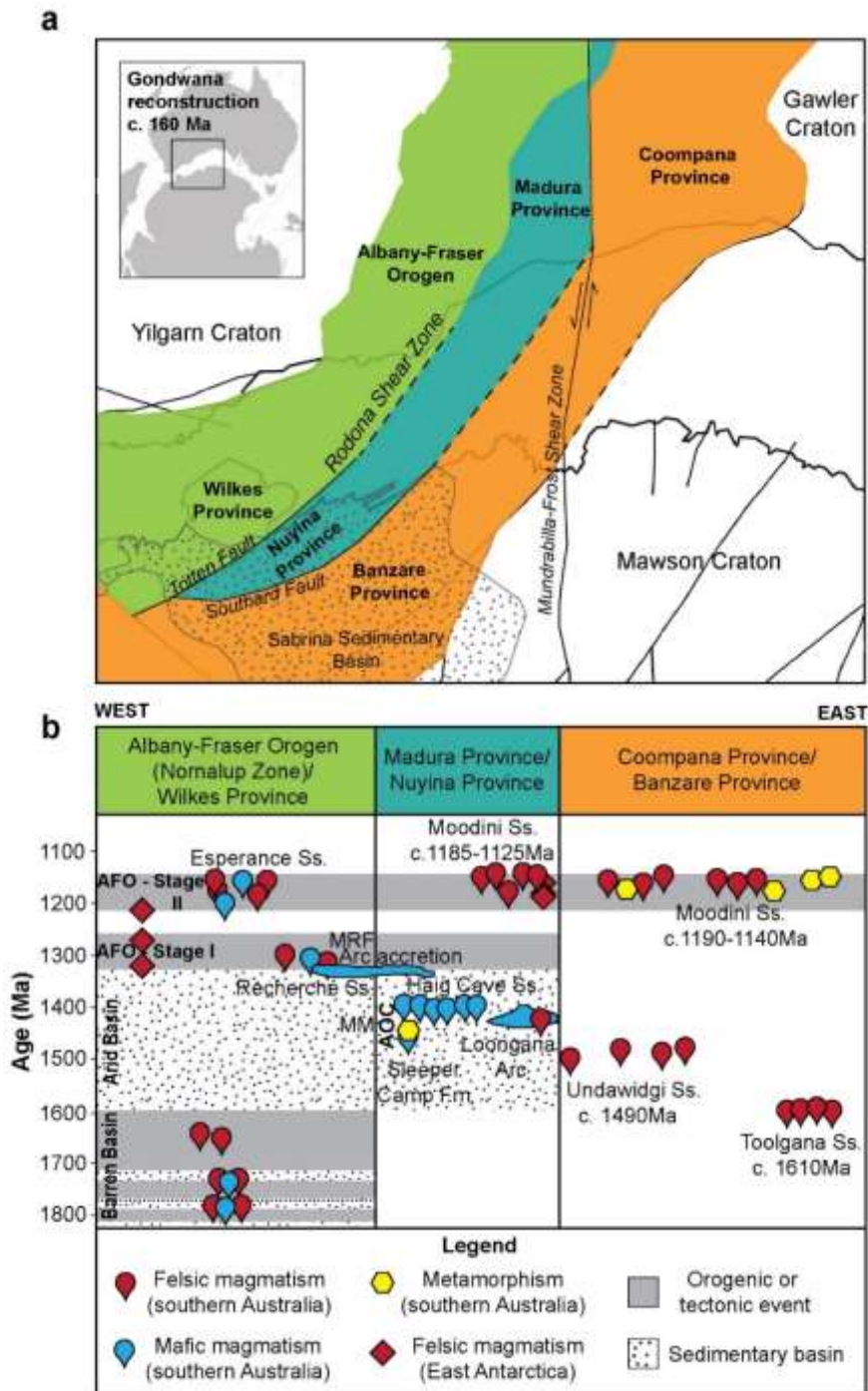


**Figure 3.2.** Geological provinces of southern Australia and East Antarctica. **(a)** Full-fit Gondwana tectonic reconstruction at c. 160 Ma with Antarctica fixed in its present-day reference frame (Matthews et al., 2016). Larger-scale geographic location is shown in the inset. Geological provinces in southern Australia and conjugate regions of East Antarctica shown using most recent interpretation of Maritati et al. (2019). Fault positions are after Aitken et al. (2014) and Maritati et al. (2019). **(b)** Time-space diagram with geological provinces of southern Australia and their Antarctic counterparts shown from west to east.

Key magmatic and metamorphic events associated with the formation of provinces are interpreted from U-Pb analyses of in-situ zircon from basement rocks. Data from southern Australia is from Wingate et al. (2015a, 2015b) and data from East Antarctica is from Maritati et al. (2019) and Morrissey et al. (2017). AOC – Arubiddy Ophiolite Complex, MM – Malcolm Metamorphics, MRF – Mount Ragged Formation, Ss. - Supersuite. Ages and spatial positions are approximate.

## 3.3 Methods

### 3.3.1. Sampling locations and descriptions

We report results from a marine sediment core recovered from the continental slope adjacent to Sabrina Coast of central Wilkes Land, East Antarctica, and nearby basement rocks (Fig. 3.1 and Supplementary Table 3.1). Core IN2017\_V01-A042-KC14 (hereafter referred to as KC14) was recovered in 2017 employing a 15 cm square Kasten corer from aboard the *RV Investigator* (Armand et al., 2018). KC14 was targeted for this study due to its proximity to Totten Glacier and its continuous sequence of sediment deposition. The core is 3.38 m long and was recovered from the eastern flank of a large contourite ridge 2100 m below sea level. The core sedimentology consists predominantly of glacial clay and silty clay overlain by biosiliceous silty clay in the Holocene (Armand et al., 2018). To complement the offshore samples, the nearest onshore basement rocks from Chick Island (Maritati et al., 2019) and Balaena Islets (Cameron et al., 1958) were sampled for feldspar Pb isotope analysis.

### 3.3.2. Radiocarbon dating

The bulk AIOM fraction of six samples from KC14 was radiocarbon-dated. Prior to dating, all samples (weighing approximately 5 g) were dried in an oven at 60°C, ground and submerged in 2M HCl for several hours on a hotblock at 80°C for carbonate removal. Each sample was subsequently rinsed with Milli-Q water to remove any residual acid and dried at 60°C. Radiocarbon analysis by Accelerator Mass Spectrometry was performed by DirectAMS. The raw age data was corrected

for the Marine Reservoir Effect and calibrated using the Marine13 calibration curve in MatCal 2.41 (Lougheed and Obrochta, 2016). A uniform marine reservoir age of  $917.5 \pm 30$  yr was applied as this is the median of the range of reservoir ages currently defined for the Southern Ocean (Paterne et al., 2019). Median calibrated ages are reported with a 95% confidence limit.

### 3.3.3. Quantification of iceberg-rafted debris flux

The IBRD flux was calculated at 10 cm intervals along the core following the protocol of Kriesek (1995) and Patterson et al. (2014):

$$IBRD \text{ flux} = CSF \times DBD \text{ (g/cm}^3\text{)} \times LSR \text{ (cm/kyr)}$$

The coarse sand fraction (CSF) (250  $\mu$ m-2 mm) was isolated by wet-sieving a known weight of each sample. Authigenic grains and microfossils were removed from the samples under a microscope. The remaining material was weighed on a microbalance and calculated as a fraction of the bulk sample. Cuvettes with a precise volume of 5.49 cm<sup>3</sup> were used to calculate the dry bulk density (DBD). The linear sedimentation rate (LSR) was calculated at intervals between the calibrated bulk organic carbon ages.

### 3.3.4. Biogenic silica concentrations

The BiSi concentration was measured at 10 cm intervals along KC14 following a protocol based on DeMaster (1981) and Mortlock and Froelich (1989). Samples (30 +/- 3 mg) were leached in 30 mL 1M NaCaO<sub>3</sub> solution and maintained at 85°C on a hotblock. After one hour, a 1 mL aliquot was centrifuged at 10,000 rpm for 45 seconds to separate the sediment from the leached biogenic silica. A 200  $\mu$ L aliquot of the solution was then diluted in 9 ml of Milli-Q water and the dissolved silica was analysed immediately using a Quickchem 8500 Series 2 FIA (Method 31-114-27-1-A, (Diamond, 2002)). This process was repeated for a total of five hours. The BiSi in

all samples was fully leached after three hours. The percent standard deviation of two replicate analyses of in-house sediment standards, over a two-day period, was 15% and 7%, respectively, for an Antarctic margin (Collaborative East Antarctic Marine Census (CEAMARC)) standard (15.2% BiSi) and a Chile margin sediment standard (6.6% BiSi). The BiSi flux was calculated in the same way as the IBRD flux, replacing the CSF with the BiSi mass fraction from each sample.

### **3.3.5. Trace element, U-Pb and Pb-Pb analysis**

#### **3.3.5.1. Sample preparation**

The fine (<63 µm), intermediate (63-250 µm) and coarse (>250 µm-2 mm) fractions were acquired from two-centimeter-thick sediment samples (weighing approximately 20 g) at 10 cm intervals along KC14 by wet-sieving. For subsequent analysis and interpretation, all the sampled 10 cm intervals were used from the intermediate size fraction, supplemented by four samples at ~1 m intervals from each of the coarse and fine fractions. In the fine fraction, detrital grains were separated from clay minerals and subsequently mounted in resin. In the intermediate fraction, the heavy and light mineral fractions were manually separated by suspending the grains in Milli-Q water and rotating them around a watchglass. Non-magnetic and weakly magnetic grains were then separated from the dried heavy mineral fraction using a Fe-B-Nd hand magnet and mounted in epoxy resin. For the coarse fraction, the CSF samples used to calculate the IBRD flux were mounted in epoxy resin. The one-inch round resin discs were then sanded and polished to expose the interior of the grains. Basement rock samples were similarly prepared with rock chips from each sample mounted in resin before being dried and polished.

#### **3.3.5.2. Sample imaging**

Sample mounts were imaged and analysed on a FEI MLA650 environmental scanning electron microscope (SEM) at the Central Science Laboratory, University of Tasmania. Using Mineral Liberation Analysis (MLA) software, all mineral types in each mount were identified and colour-coded using a pre-defined mineral library. In

this way, detrital zircon, apatite, titanite, K-feldspar and plagioclase feldspar from KC14, and K-feldspar and plagioclase feldspar from the four basement samples, were located in preparation for Laser Ablation-Inductively Coupled Plasma Mass Spectrometry (LA-ICPMS). Where possible, high-resolution backscatter (BSE) and cathodoluminescence (CL) images of zircons from the intermediate (63-250  $\mu\text{m}$ ) fraction were acquired, capturing the external morphology, internal structure and zoning of the grains, and identifying optimal sites for LA-ICPMS analysis. Elongation ratios (length: width) for imaged zircons were quantified using the MLA software. The detrital titanite, apatite and feldspar grain morphologies were examined under a microscope.

### **3.3.5.3. LA-ICPMS analysis**

LA-ICPMS measurements were made using an ASI Resolution S-155 System with a large format cell and a Coherent CompexPro 110 Excimer laser coupled with an Agilent 7900 ICPMS at the Discipline of Earth Sciences/Centre of Ore Deposit and Earth Sciences (CODES), University of Tasmania (UTAS). Specific instrumental parameters and standard reference materials used are listed in Supplementary Table 3.2. Detrital zircon, apatite and titanite were targeted from all size fractions for U-Pb analysis. Detrital plagioclase and K-feldspars were selected from the CSF only for Pb-Pb analysis.

The experimental setup for U-Pb and trace element analysis of zircon, apatite and titanite follows Thompson et al. (2018). A glass primary standard, NIST610, was used to calculate a correction factor for the  $^{207}\text{Pb}/^{206}\text{Pb}$  ratio using values proposed by Baker et al. (2004). Primary standard 91500 (Horstwood et al., 2016) was used for the calibration of all U-Pb ratios in zircon, with Plešovice (Sláma et al., 2008) and Temora (Black et al., 2003) used as secondary reference materials and treated as unknowns. During the analysis of apatite, OD306 (Thompson et al., 2016) was used as a primary standard and Otter Lake (Barfod et al., 2005), Emerald Lake (Coulson et al., 2002), 401 apatite (Thompson et al., 2016), McClure Mountain (Schoene and Bowring, 2006) and Durango (McDowell et al., 2005) as secondary reference materials. An in-house primary standard, 19686-titanite, was

used for titanite analysis with Mt. Dromedary (Miller et al., 1985) and FC-3 (Schmitz and Bowring, 2001) as secondary reference materials.

Initial U-Pb-trace element data reduction follows Thompson et al. (2018) and Halpin et al. (2014) using Microsoft Excel macro spreadsheets created at the University of Tasmania. Following these data reduction steps, we filtered the zircon dataset to exclude: 1) processed signal intervals spanning less than 50% of the overall analysis time, 2) high  $^{204}\text{Pb}$  values exceeding 100 cps, 3) concordance outside the range 80-110%, and 4) grains displaying high Light Rare Earth Element (LREE) and P-contents ( $n=15$ ) symptomatic of mixed ablation of apatite or monazite micro-inclusions. A total of 139 analyses (44% of the dataset) were eliminated using these criteria and were excluded from interpretation. All rare earth element (REE) data were chondrite-normalised using values proposed by Sun and McDonough (1989). A common-Pb correction procedure was applied for the detrital apatite and titanite U-Pb-trace element datasets, which were discordant due to common Pb. We followed the five-stage iterative  $^{207}\text{Pb}$ -correction method of Chew et al. (2011), with estimates of initial Pb-isotopic compositions from the Stacey and Kramers (1975) crustal Pb evolution model. Some analyses recorded significant differences in the calculated  $^{207}\text{Pb}$ -corrected  $^{206}\text{Pb}/^{238}\text{U}$  ages after the fifth iteration. To account for this, the uncertainty for common Pb on all analyses was increased using the absolute difference in the common Pb predicted by the fourth and fifth iterations. Subsequent to this common Pb correction procedure, we further filtered the apatite and titanite dataset to exclude processed signal intervals spanning less than 50% of the total analysis time, which eliminated 22% and 10% of the apatite and titanite datasets, respectively. Probability-density plots were produced using DensityPlotter version 8.4 (Vermeesch, 2018). For zircon,  $^{207}\text{Pb}$ -corrected  $^{206}\text{Pb}/^{238}\text{U}$  ages were used for grains with  $^{207}\text{Pb}/^{206}\text{Pb}$  ages younger than 1000 Ma ( $n=9$ ) and showing no evidence of Pb loss, and  $^{207}\text{Pb}/^{206}\text{Pb}$  ages were used for the remainder ( $> 1000$  Ma; 95% of the dataset). For apatite and titanite, plotted ages are fifth iteration  $^{207}\text{Pb}$ -corrected  $^{206}\text{Pb}/^{238}\text{U}$  ages. Tera-Wasserburg plots (Supplementary Fig. 3.1) were constructed using IsoplotR (Vermeesch, 2018).

A comprehensive description of the method used for Pb-Pb analysis of detrital feldspar using the UTAS LA-ICPMS system is given by Mulder et al. (2019). Lines, rather than spots, were used for feldspar ablation to maintain the signal intensity and smooth, unaltered areas of individual grains were targeted for analysis. Data reduction also followed Mulder et al. (2019); only one analysis with a signal less than 50% of the total analysis time was excluded from interpretation. No correction for the in-growth of radiogenic Pb was applied due to the avoidance of U and Th inclusions. NIST612 was ablated for the calibration of all Pb-Pb ratios, using values proposed by Baker et al. (2004) and glass reference materials GSD-1g (Jochum et al., 2011) and BCR-2g (Jochum et al., 2016) were used as secondary standards and treated as unknowns. No feldspar reference standard was available during this study, however, the UTAS facility uses glass reference materials for Pb-isotopic compositions on a wide range of minerals without a measurable 'matrix effect' on the quadrupole ICPMS system (e.g., monazite: Berry et al., 2016; pyrite: Hawke et al., 2015; zircon: Thompson et al., 2018).

Weighted average values for all LA-ICPMS standards were calculated using the Microsoft Excel add-in Isoplot v. 4.15 (Ludwig, 2012), all of which fall within  $2\sigma$  error of the published reference values (Supplementary Table 3.3).

## **3.4. Results**

### **3.4.1. Bulk organic carbon ages, IBRD flux and biogenic silica concentrations**

The median calibrated calendar ages for KC14 capture a Quaternary record spanning c. 23,500 cal yrs BP. Based on the bulk radiocarbon ages and low BiSi concentrations (representing low productivity characteristic of glacial conditions), the base of the core to 170 cm represents the Last Glacial Period (interval 4, Fig. 3.3). At 170 cm, BiSi concentrations start to increase, indicating increased productivity, which we infer represents the deglaciation and a transition into the Holocene

(interval 3, Fig. 3.3). Estimated LSRs were highest during the glacial (377 cm/kyr) and moderate in the Holocene (10-11 cm/kyr). A sharp decline in the LSR to 8 cm/kyr followed by an increase to 14 cm/kyr marks the deglacial transition between the Last Glacial Period and the Holocene (Fig. 3.3). The CSF ranges between 0.0001-0.0147, with an average of 0.003 in the glacial and 0.001 in the Holocene (Fig. 3.3). The BiSi flux averages 7.6 g/cm<sup>2</sup>/kyr in the glacial and 2.0 g/cm<sup>2</sup>/kyr in the Holocene and positively correlates with the IBRD flux. The IBRD flux ranges between 0.001-3.4 g/cm<sup>2</sup>/kyr with an average of 0.4 g/cm<sup>2</sup>/kyr during the glacial period and 0.004 g/cm<sup>2</sup>/kyr during the Holocene (Fig. 3.3).

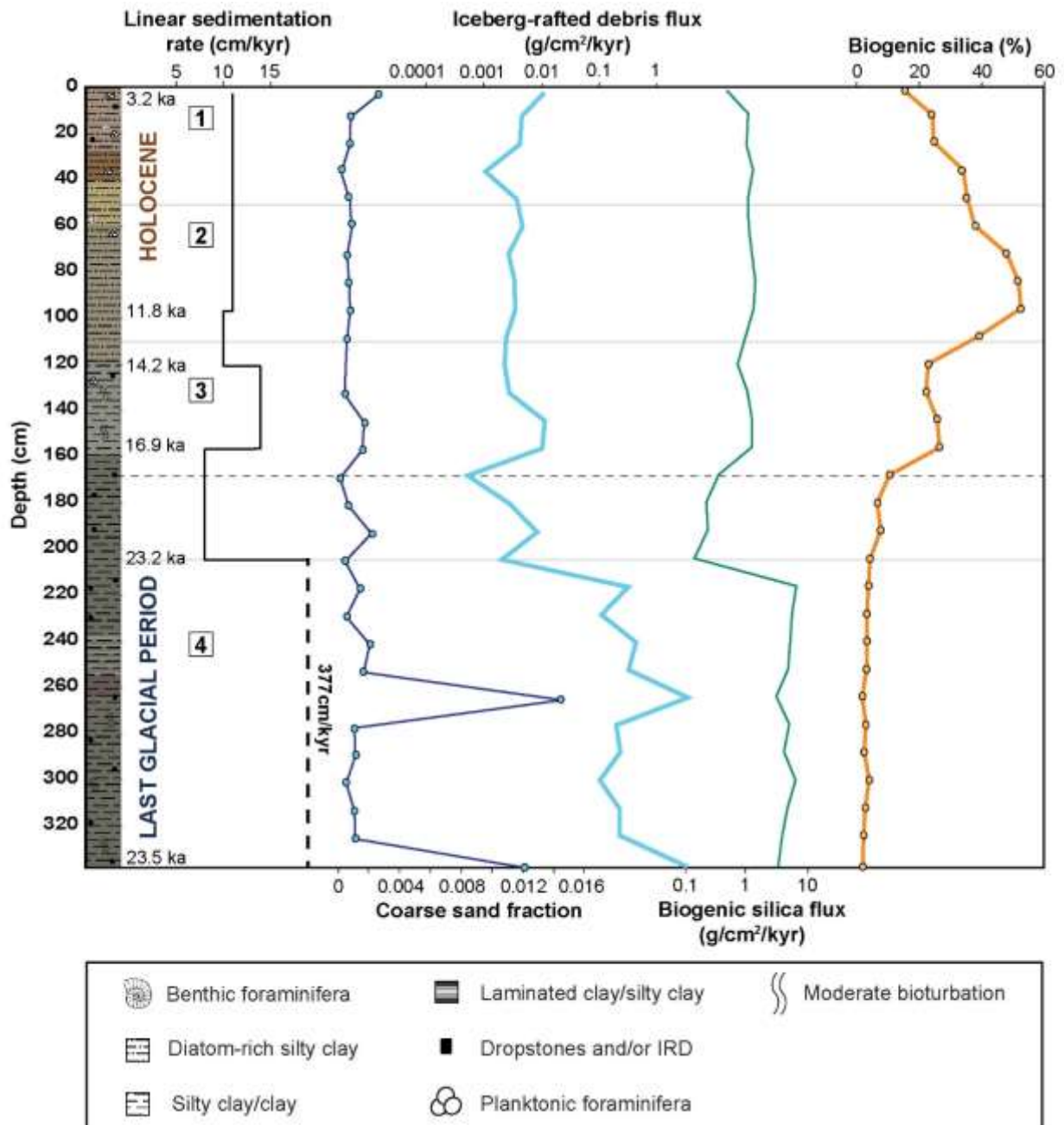


**Figure 3.3.** KC14 downcore calibrated bulk organic radiocarbon ages, LSR, CSF, IBRD flux, BiSi flux and BiSi concentrations. A sedimentary log (Armand et al., 2018) shows downcore variability in sedimentary features and composition. Variation in colour on the sedimentary log represents sediment colour logged onboard *RV Investigator* using the Munsell Color Chart. Four depth intervals, representing distinct changes in BiSi concentrations, are separated by grey lines. The horizontal dashed line corresponds with a marked decrease in the IBRD flux and an increase in BiSi concentrations. These changes are interpreted to represent the beginning of the deglacial transition between the Last Glacial Period and the Holocene.

### 3.4.2. Detrital mineralogy and grain morphology/textures

The detrital mineralogy of KC14 consists of abundant quartz and feldspar with minor biotite and amphibole, and rare pyroxene and olivine. All detrital zircon grains in this study are smaller than 150  $\mu\text{m}$ , with 72% falling within the fine fraction (<63  $\mu\text{m}$ ). Four fine zircon grains are located as inclusions within coarse detrital grains such as quartz, and as such are regarded as the coarse fraction for interpretation of transport processes. Of the zircons imaged under CL, 27% are fragmented predominantly across the prism axis of the grain (e.g., Fig. 3.4: 3, 5, 6, 12, 15, 16 and 19), and 33% display multiple fine cracks (e.g., Fig. 3.4: 5, 8, 9, 14, 15, 17, 18, 24, 25 and 26). All measured zircons ( $n = 64$ ) are short and approximately equidimensional in shape, with aspect ratios between 1:1 and 2.15:1, although the fragmentation observed suggests many grains were originally more elongate prior to transport and deposition at the core site. Most of the grains imaged (80%) are angular to sub-angular with a minority displaying a sub-rounded morphology (Fig. 3.4). Many of the zircons (53% of those imaged) reveal well-defined fine-scale oscillatory growth zoning, definitive of igneous zircon (e.g., Fig. 3.4: 1-3, 5-7, 9, 10, 13, 16-20, 23 and 30) whereas others record a more complex growth history, with broader growth zones (e.g., Fig. 3.4: 11), core-rim textures (e.g., Fig. 3.4: 12, 13, 26 and 29), patchy and sector zoning (e.g., Fig. 3.4: 4, 22, 24, 25 and 28) and localised recrystallisation (e.g., Fig. 3.4: 4, 12 and 23). A range of morphologies and textures are preserved in all age groups, dominated by short, commonly broken and angular grains with oscillatory zoning. Inspection of detrital apatite, titanite and feldspar grains under a microscope similarly revealed dominantly angular and broken morphologies across all size fractions.

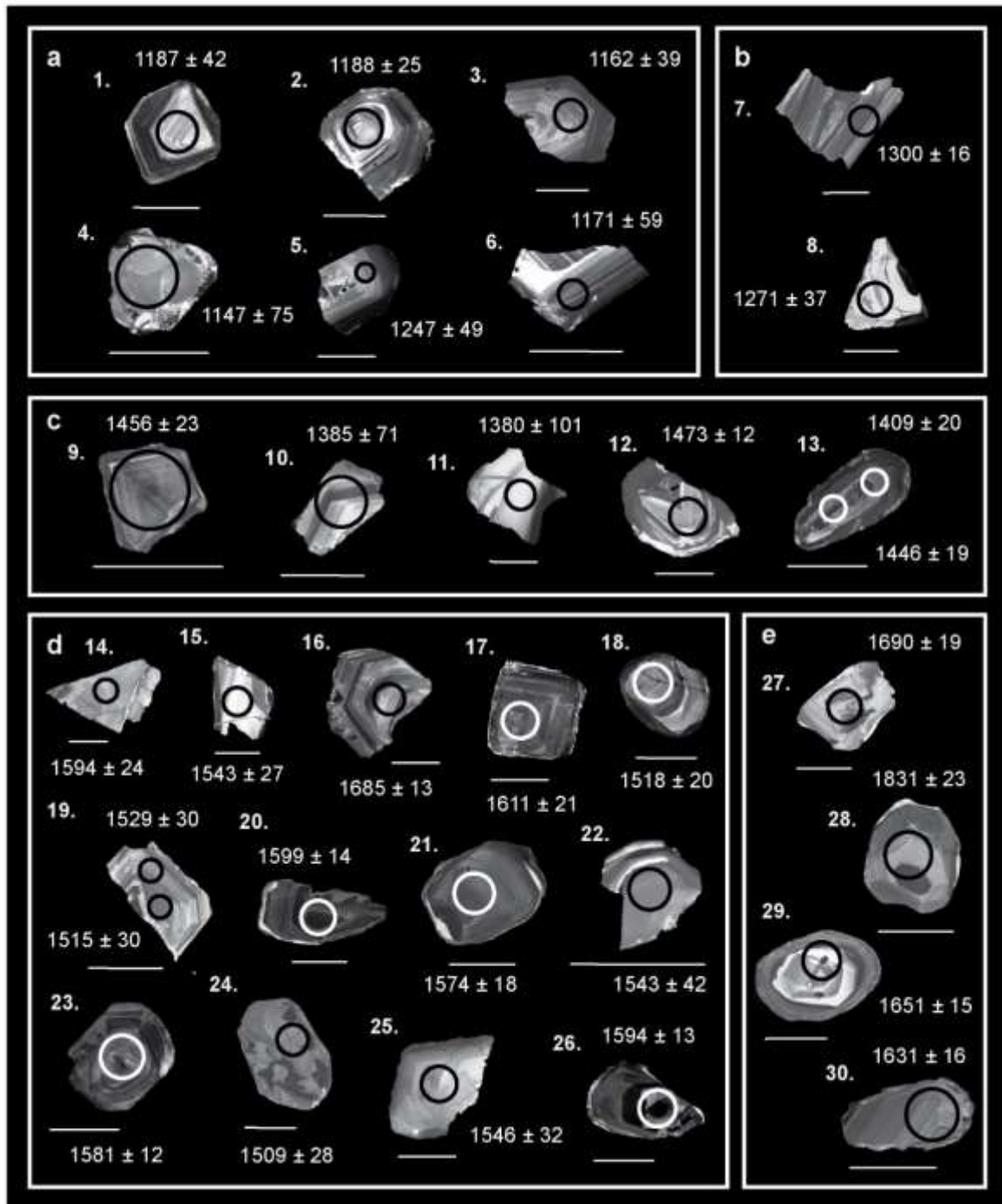


**Figure 3.4.** Representative CL images of detrital zircon grains from the intermediate fraction of KC14. Circles represent LA-ICPMS analysis sites. Scale bars at 50  $\mu\text{m}$  are shown as white lines under each grain. Ages are  $^{207}\text{Pb}/^{206}\text{Pb}$  where  $> 1000$  Ma and  $^{207}\text{Pb}$ -corrected  $^{206}\text{Pb}/^{238}\text{U}$  where  $< 1000$  Ma  $\pm 1\sigma$  error. Grains are divided into the following broad age groups, most of which are associated with major periods of magmatism and metamorphism in southern Australia and East Antarctica (Fig. 3.2): **(a)** c. 1250-1100 Ma (Albany-Fraser/Wilkes Province Stage II, including the Moodini Supersuite) **(b)** c. 1345-1260 Ma

(Albany-Fraser/Wilkes Province Stage I) **(c)** c. 1480-1390 Ma (Madura/Nuyina Province) **(d)** c. 1610-1490 Ma (Toolgana and Undawidgi supersuites of Coompana/Banzare Province) **(e)** > 1610 Ma.

### **3.4.3 Detrital zircon, apatite and titanite geochronology**

Compiled U-Pb ages from all depth intervals of KC14 reveal dominant age populations between c. 1360-1100 Ma for detrital zircon and between c. 1200-1100 Ma for detrital titanite and apatite (Fig. 3.5a). The detrital zircon age distribution exhibits strong multimodality; the dominant c. 1360-1100 Ma peaks representing 51% of the dataset, with secondary peaks between c. 1620-1490 Ma (17%). A very small number of zircon analyses exhibit ages older than 1620 Ma (8%) and between c. 700-500 Ma (5%). In contrast, the detrital titanite and apatite age distributions are largely unimodal, with most ages predominantly falling within the main c. 1200-1100 Ma population (66% and 86% for titanite and apatite respectively; Fig. 3.5a). A minor portion of detrital titanite and apatite analyses are older than c. 1300 Ma and a very small population between c. 750-500 Ma is present in the detrital apatite record (Fig. 3.5a).

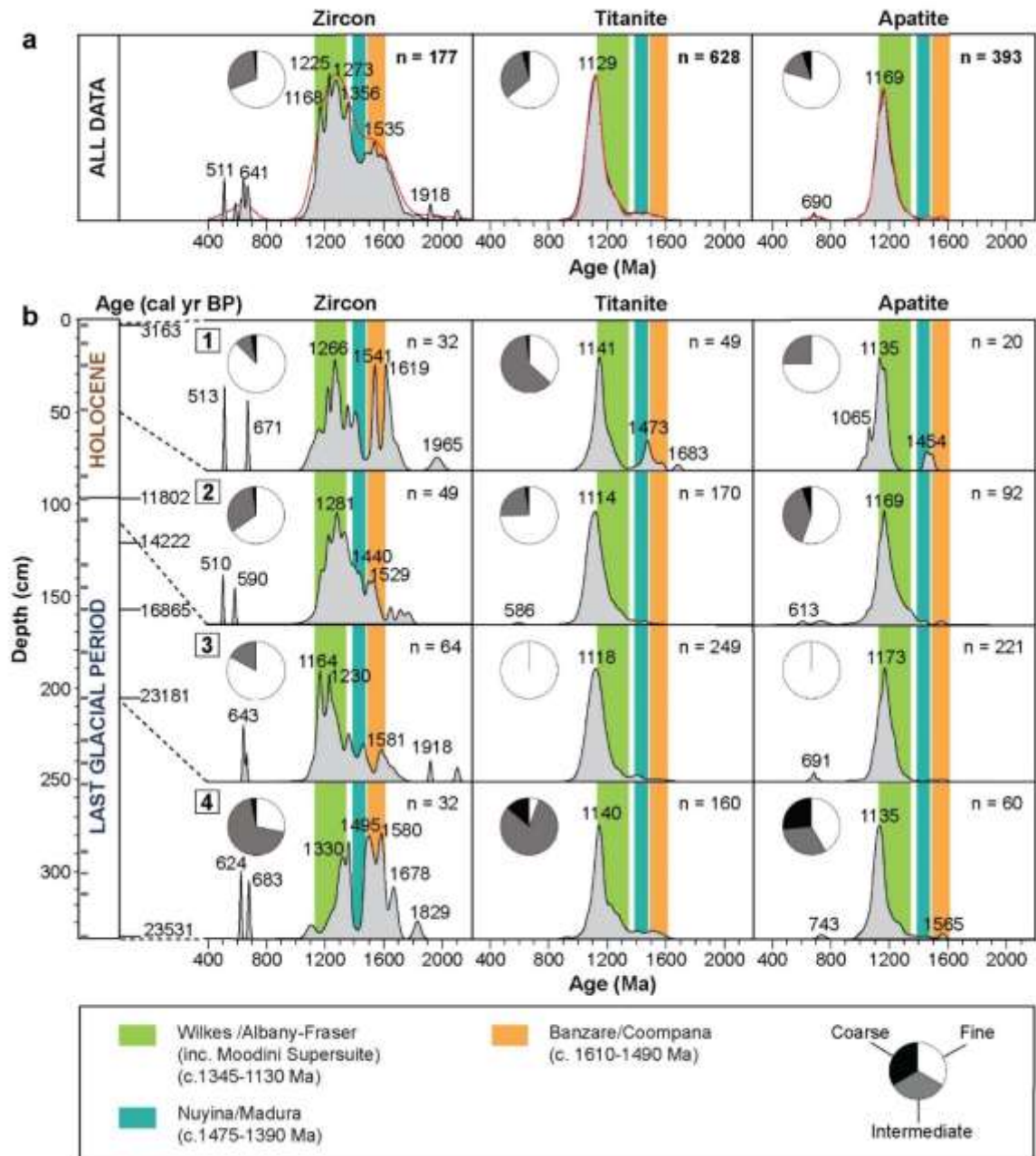


**Figure 3.5.** Detrital age signatures in KC14. **(a)** Age spectra for detrital zircon, titanite and apatite for the entire KC14 core presented as probability-density plots (black curve, grey fill). Kernel density curve is shown in red. **(b)** Probability-density plots showing downcore age variability in detrital zircon, titanite and apatite. Grey rectangles within the stylised core on left hand side show where sediment samples were taken from within each depth interval of KC14 for U-Pb analysis. Major age peaks and total number of analyses (n) are indicated. Age signatures of geological provinces in East Antarctica/southern Australia (as in Figure 3.2) are highlighted as coloured bars for comparison. Although the Moodini Supersuite intrudes the Banzare/Coompana and Nuyina/Madura provinces, it is here grouped with the

Wilkes Province/Albany-Fraser Orogen due to the overlap in age ranges. Pie charts show relative proportion of each mineral size fraction contributing to the age signature for each depth interval. Intervals 1-4 represent changes in BiSi concentration and are the same as those presented in Figure 3.3.

Although the main c. 1360-1100 Ma age population is prevalent throughout the detrital zircon record, subtle changes in the relative proportions of age populations are observed with depth. Detrital zircon ages between c. 1620-1490 Ma are more prominent at the top and bottom of the core (intervals 1 and 4, Fig. 3.5b). Major peaks within this population occur at c. 1620 Ma and c. 1540 Ma within interval 1 and at c. 1580 Ma and c. 1495 Ma within interval 4. In intervals 2 and 3, where BiSi is most abundant, detrital zircon grains within the c. 1620-1490 Ma age range are significantly reduced, and a minor c. 1450-1390 Ma population can be seen (Fig. 3.5b) that is otherwise not discernible in the whole core record (Fig. 3.5a). This population is also present as a small peak in interval 1 (at c. 1400 Ma) but is completely absent from interval 4. The youngest age population (c. 750-500 Ma) exists in all depth intervals for detrital zircon and most of the apatite record (intervals 2-4, Fig. 3.5b), but only exists within interval 2 for titanite (Fig. 3.5b). These rare c. 750-500 Ma detrital zircon (n=9), apatite (n=10) and titanite (n=1) grains were all obtained from the fine fraction. The detrital titanite and apatite age distributions are largely consistent throughout the transition from the Last Glacial Period through to the Holocene, with the addition of very minor peaks at c. 1470 Ma and c. 1450 Ma, respectively, in interval 1 of the core (Fig. 3.5b).

#### **3.4.4. Detrital zircon, apatite and titanite trace element geochemistry**

The detrital zircon grains in KC14 yield chondrite-normalised REE abundances between  $10^{-4}$  and  $10^4$  with steep heavy rare earth element (HREE) enrichment, a positive Ce anomaly and a negative Eu anomaly (Fig. 3.6a), typical of magmatic zircon (Rubatto, 2017). A minority of grains exhibit flatter HREE signatures, more typical of high-temperature metamorphic zircon. The REE patterns in primary

magmatic zircon (c. 1150 Ma) from Chick Island basement rock samples (Maritati et al., 2019) span those of the detrital zircon in KC14 (Fig. 3.6a). Detrital zircon Th/U ratios (Fig. 3.6a inset) are variable but most have Th/U > 0.1, typical of magmatic zircon. Detrital apatite and titanite grains exhibit chondrite-normalised REE abundances between  $10^1$  and  $10^5$  and present a range of REE patterns (Supplementary Fig. 3.2a, b). However, most of these grains are LREE-enriched and present a strong negative Eu anomaly associated with a magmatic source rock composition (Belousova et al., 2002a; O'Sullivan et al., 2020; Olierook et al., 2019). A minor portion of detrital titanite grains reveal a positive Eu anomaly and HREE enrichment, associated with a metamorphic source rock type (Supplementary Fig. 3.2b). The detrital apatite and zircon geochemical data reveal a dominantly granitoid source rock type using discrimination plots from Belousova et al. (2002a, 2002b). Most of the detrital titanite grains have high Fe concentrations ranging between 7500-20000 ppm, characteristic of igneous titanite (Olierook et al., 2019).

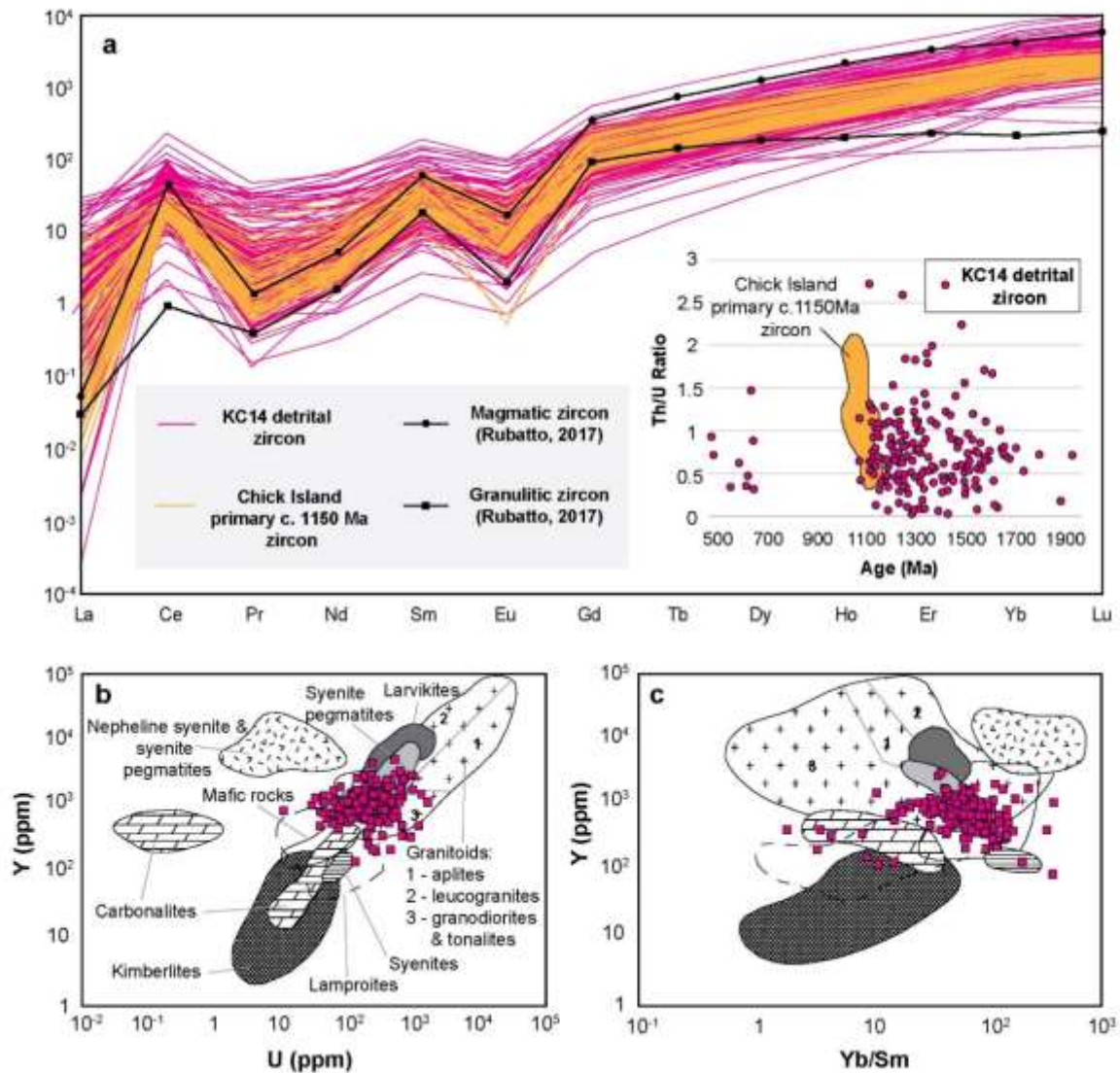


**Figure 3.6.** Detrital zircon trace element geochemistry. **(a)** Chondrite-normalised REE diagrams and Th/U ratios for detrital zircon in KC14 and primary c. 1150 Ma zircon from Chick Island basement rocks (Maritati et al., 2019). Typical REE compositions for magmatic and granulitic (i.e., high temperature metamorphic) zircon from Rubatto (2017) are shown. **(b, c)** KC14 detrital zircon trace element data overlain on source rock discrimination diagrams from Belousova et al. (2002b).

### 3.4.5. Feldspar Pb-isotopic compositions

Feldspar analysed from basement rocks from the Sabrina and Budd coasts (Fig. 3.1) provide new potential source rock datasets to help assess offshore detrital provenance. Feldspar within a granite from Balaena Islets (PRR-21189) yield  $^{206}\text{Pb}/^{204}\text{Pb}$  values of 16.6-16.7 and  $^{207}\text{Pb}/^{204}\text{Pb}$  values of 15.5-15.6, plotting above the average crustal growth curve of Stacey and Kramers (1975) (Fig. 3.7a, b). In contrast, Chick Island basement feldspar grains from c. 1150 Ma granodiorite (CI-814A2) and coeval granite xenoliths (CI-814B and CI-810A) (Moodini Supersuite equivalents; Maritati et al., 2019) show a wider isotopic distribution with  $^{206}\text{Pb}/^{204}\text{Pb}$  of 16.6-16.9 and  $^{207}\text{Pb}/^{204}\text{Pb}$  of 15.4-15.6 (Fig. 3.7a, b). Analysed grains from both locations broadly overlap with Pb-isotopic signatures from other Australo-Antarctic domains (Mulder et al., 2019).

The Pb-isotopic compositions of feldspars in the offshore record are more diverse. Detrital K-feldspar and plagioclase from the coarse fraction in KC14 have  $^{206}\text{Pb}/^{204}\text{Pb}$  of 15.9-17.5 and  $^{207}\text{Pb}/^{204}\text{Pb}$  of 15.1-15.7 (Fig. 3.7). These values predominantly span the mantle to average crust growth curves, with approximately 20% of the detrital feldspar compositions from KC14 overlapping the average-to-upper crustal basement rock compositions analysed from the Balaena Islets (and Windmill Islands, defining the broader Wilkes Province) and Chick Island (near the boundary between the Nuyina and Banzare provinces) (Fig. 3.7).

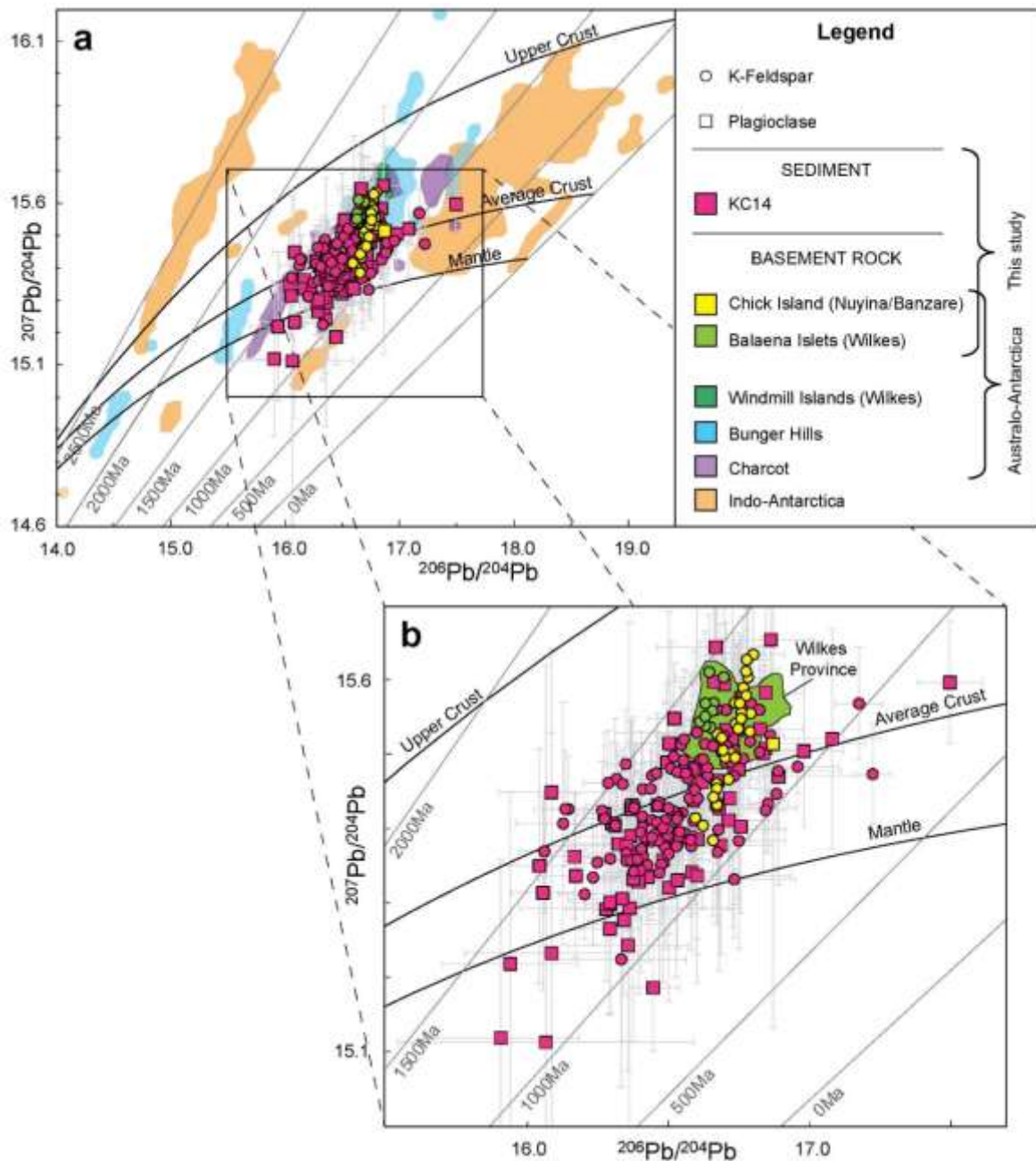


**Figure 3.7.** New detrital and bedrock feldspar Pb-isotopic datasets compared to regional Antarctic feldspar Pb-isotopic compositions. **(a)** Pb-isotopic signatures from detrital feldspar in KC14 (pink symbols) and basement rock feldspar from Balaena Islets (green symbols) and Chick Island (yellow symbols) overlain on Pb-isotopic feldspar domains from various locations in East Antarctica. Error bars ( $2\sigma$ ) are shown for all analyses in this study. Indo-Antarctic basement rock data are from Flowerdew et al. (2013) and Mulder et al. (2019). Australo-Antarctic basement rock data are from Mulder et al. (2019) (Windmill Islands, Bunger Hills, Charcot) and this study (Chick Island and Balaena Islets). Growth curves for the mantle ( $\mu = 9$ ), average crust ( $\mu = 9.74$ ) and upper crust ( $\mu = 12$ ) are plotted using the Pb

isotope evolution model of Stacey and Kramers (1975). **(b)** Inset to **(a)**, highlighting the analyses from this study. Black outline/green fill polygon shows Pb-isotopic compositions of basement rocks from the Wilkes Province (Windmill Islands and Balaena Islets).

## 3.5. Discussion

The rapidly retreating, fast-flowing Totten Glacier (Rignot et al., 2011; Fig. 3.1b) is the closest major outlet glacier to the KC14 core site and is an obvious candidate for detrital delivery from the Totten glacial drainage basin. Indeed, the Totten Glacier is interpreted to have discharged sediment-laden meltwater and plumes throughout the Late Cenozoic, from the early development of the EAIS to the present day (Donda et al., 2020), and is suggested to have contributed to the contourite ridge where KC14 was recovered (O'Brien et al., 2020).

The most recent interpretation of the subglacial geology in central Wilkes Land from Maritati et al. (2019) is based on matching geophysical signatures across the margins of southern Australia and East Antarctica and U-Pb analyses of primary and inherited zircon from rare plutonic outcrop at Chick Island. This tectonic framework suggests that the Wilkes, Nuyina and Banzare provinces underlie the Totten catchment area, with the Totten Glacier exploiting a suture between the Wilkes and Nuyina provinces in the coastal region of the catchment, and the Banzare Province situated in the hinterland.

Based on these recent interpretations, it is anticipated that detritus on the continental slope and specifically sampled at KC14 should have an age and composition that reflects the Totten catchment basement terranes. In this paradigm, given that erosion is largely focused along the ice sheet margins at the coast (Golledge et al., 2013; Jamieson et al., 2010), the source regions for detritus sampled at KC14 should be concentrated in the Wilkes and Nuyina provinces. We now explore this hypothesis in section 3.5.1.

### **3.5.1. Was the Totten Glacier the main conduit for KC14 detritus?**

Previous work has identified that specific regions along the East Antarctic margin are characterised by distinct detrital zircon age signatures (Pierce et al, 2014), consistent with the known onshore geology (Veevers, 2012; Veevers and Saeed, 2011). Three of these regions are defined here as Prydz Bay Sector (60°E – 100°E), Wilkes Sector (100°E – 136°E) and the Eastern Sector (136°E – 180°E), broadly corresponding to those allocated by Pierce et al. (2014) (Fig. 3.8). Rocks of the Prydz Bay sector have peak zircon age populations at c. 990-900 Ma and c. 650-500 Ma (Veevers, 2012; Veevers and Saeed, 2011). The Eastern Sector is dominated by Cambrian granites (c. 600-400 Ma) that intruded during the Ross Orogeny, with secondary older (> 1610 Ma) age peaks representative of Archean-Paleoproterozoic rocks of Adélie Land (Veevers, 2012; Veevers and Saeed, 2011). The Wilkes Sector has a signature dominated by rocks that are predominantly Late Mesoproterozoic in age (c. 1200-1000 Ma). The detritus from KC14 has an age signature that is clearly distinct from the Prydz Bay and Eastern sectors (inset in Fig. 3.8). Broadly, the detrital zircon age signature recorded at KC14 matches well with other detrital sediment records from the Wilkes Sector further to the east (Pierce et al., 2014; Fig. 3.8), but reveals additional prominent c. 1360-1220 Ma age peaks that are diagnostic of the Wilkes Province (Figs 3.5a and 3.8).

A derivation from the Totten Glacier catchment predicts mainly Wilkes and Nuyina age signatures for KC14 detritus. The abundant c. 1200-1000 Ma zircon, apatite and titanite detritus in KC14 (Fig. 3.5) could potentially be derived from voluminous plutonic rocks in any or all three of the proximal Wilkes, Nuyina and Banzare provinces (Fig. 3.2). Therefore, this age group is not particularly useful for identifying unique source regions in Wilkes Land. A minor proportion of c. 1450-1390 Ma zircon, c. 1470 Ma titanite and c. 1450 Ma apatite in KC14 suggests some of the detritus was likely sourced from the Nuyina Province (c. 1475-1390 Ma). However, a significant component of detrital zircon with an age between c. 1620-1490 Ma is also present in KC14 (Fig. 3.5), characteristic of the c. 1610 Ma Toolgana and c. 1490 Ma

Undawidgi supersuites in the Banzare Province. This c. 1620-1490 Ma Banzare signature, coupled with the distinctive c. 1360-1220 Ma Wilkes signature, implicates both these provinces as dominant sources. The Pb-isotopic compositions of KC14 detrital feldspar grains partially overlap feldspar compositions from plutonic rocks in the Balaena Islets (Wilkes Province) and Chick Island (near the boundary of Nuyina and Banzare provinces), supporting this interpretation (Fig. 3.7).

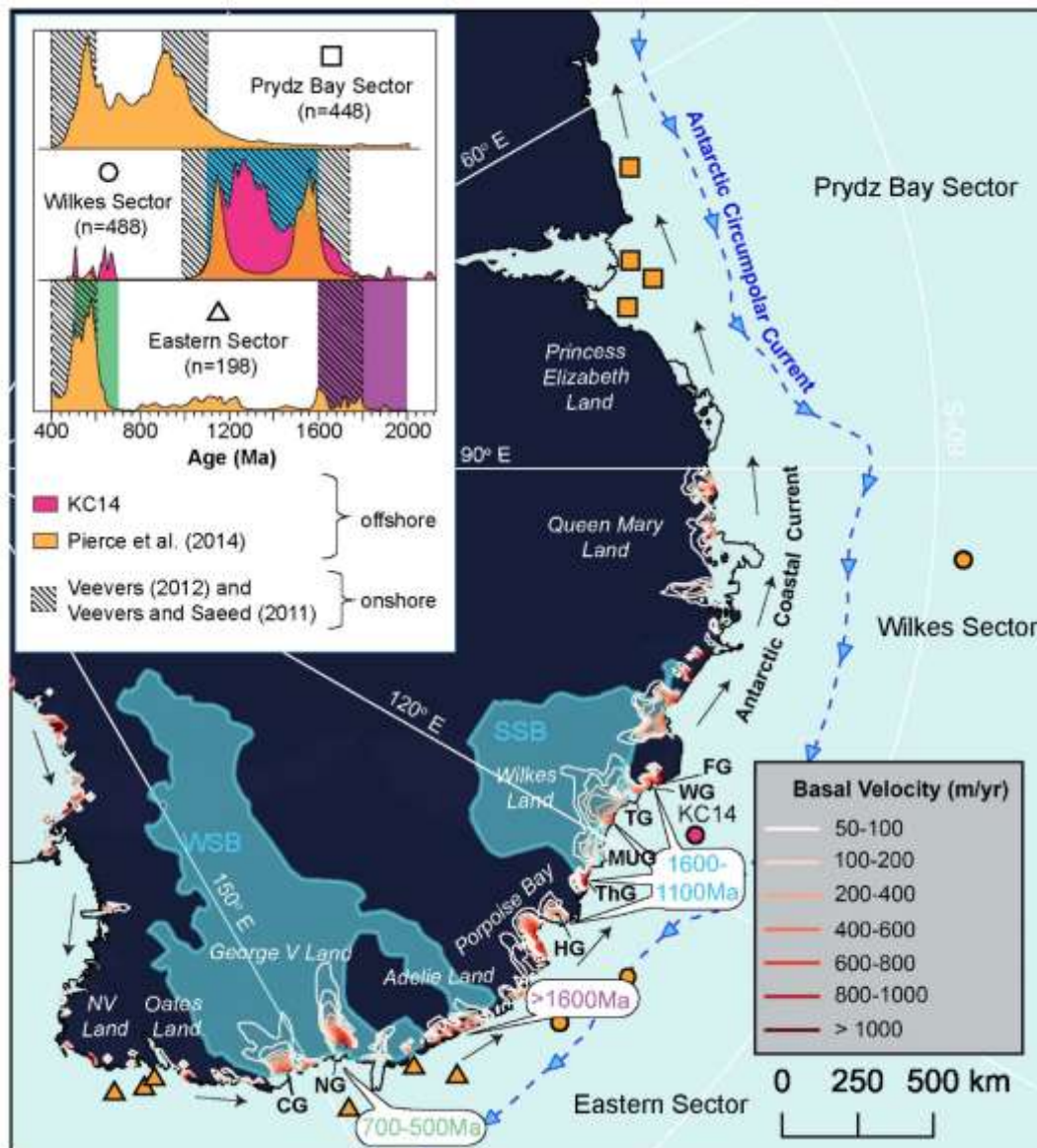


**Figure 3.8.** Comparison of predicted detrital source regions from the East Antarctic coast with onshore and offshore marine core records. Shown are locations of cores from Pierce et al. (2014) (orange symbols) and of KC14 (pink circle). Inset: U-Pb detrital zircon age signatures for each sector including KC14. Offshore data from Pierce et al. (2014). Striped

boxes highlight dominant age populations of compiled onshore data from Veevers (2012) and Veevers and Saeed (2011). Coloured bars represent main detrital age populations in KC14 and correspond with coloured text on the map, indicating inferred provenance regions of each respective age population. WSB – Wilkes Subglacial Basin, SSB – Sabrina Sedimentary Basin (blue polygons). CG – Cook Glacier, FG – Fox Glacier, HG – Holmes Glacier, MUG – Moscow University Glacier, NG – Ninnis Glacier, NV – Northern Victoria, TG – Totten Glacier, ThG – Thompson Glacier, WG – Williamson Glacier. Blue dashed line with arrows shows the position of the southern boundary of the eastward-flowing Antarctic Circumpolar Current (Orsi et al., 1995). Black arrows represent the westward-flowing Antarctic Coastal Current. Modelled basal velocity contours for an ice sheet slightly advanced relative to the present-day grounding line are from Aitken et al. (2016b) for the region between 90°E and 180°E.

There are a number of scenarios that could explain the scarcity of Nuyina-age detritus (which is a signature expected if the Totten Glacier was the main conduit) in addition to the abundance of Banzare-age detritus at the KC14 core site. One scenario is that some erosion was focused in the hinterland of the Totten catchment, encapsulating Banzare crust. However, much of this region is covered by kilometers of Sabrina Basin sedimentary strata (Aitken et al., 2016b) so we do not expect crystalline bedrock exposure. Furthermore, the high angularity and broken morphologies of most detrital grains from all size fractions in KC14 (Fig. 3.4) supports a relatively local provenance and argues against recycling through pre-glacial sedimentary systems. This is further supported by the high abundance of detrital feldspar grains which are typically unable to withstand prolonged weathering and erosion (Johnson et al., 2018).

A second scenario could be envisaged whereby the Nuyina Province may be less extensive than interpreted by Maritati et al. (2019), such that basal erosion in the coastal region of the Totten catchment sources Banzare crust in addition to Wilkes. This interpretation could account for the strong Banzare-age signature and weak Nuyina-age signature in the detrital zircon record (Fig. 3.5a). Testing of this hypothesis is difficult without higher-resolution geophysical data linking the conjugate

margins of southern Australia and East Antarctica and/or geological sampling (e.g., dredging of basement rock ridges or sampling of proximal marine sediment cores).

A third scenario that could explain the scarcity of Nuyina-age detritus is an underrepresentation of mafic rock types in the detrital zircon record (Licht and Hemming, 2017; Shao et al., 2019). The Nuyina Province likely comprises juvenile mafic rocks similar to the Arubiddy Ophiolite Complex of the Madura Province (Fig. 3.2b). Although detailed analysis of zircon grains revealed well-developed oscillatory growth zoning (Fig. 3.4) and trace element signatures typical of a felsic igneous source (Fig. 3.6; Supplementary Figure 3.2), this could be a biased record related to the high abundance of zircon in felsic rocks compared to the typically small amounts of zircon contained in mafic rocks (Licht and Hemming, 2017; Shao et al., 2019). Another bias in favor of felsic rock compositions may also be introduced by the different weathering rates of mafic and felsic rock types. Mafic rocks have a lower resistance to weathering, leading to limited preservation of mafic rock components over time (Licht and Hemming, 2017). Derivation of KC14 detritus from at least some mafic-intermediate crust is supported by the presence of minor amphibole, pyroxene and olivine grains. Evidence for mafic source components is also provided by the spread in detrital feldspar Pb-isotopic compositions (plagioclase in particular) to mantle-like values (Fig. 3.7). This signature suggests the presence of unexposed juvenile rocks in the hinterland, likely within the Nuyina and Banzare provinces, related to reworking of oceanic crust during a series of accretionary tectonic events (Kirkland et al., 2017; Maritati et al., 2019; Spaggiari et al., 2018).

Although the underrepresentation of mafic source rocks in the detrital zircon record potentially explains the paucity of Nuyina-age detritus in KC14, this scenario alone does not explain the abundance of Banzare-age detritus. A fourth scenario, and one that we suggest is most plausible, is that the Totten Glacier was one of a number of outlet glaciers that contributed detritus to KC14, as described in section 3.5.2 below.

## **3.5.2. A case for a distributed Wilkes Land provenance for KC14**

Two main age distribution patterns are observed in the detrital zircon record. In intervals 1 and 4 of KC14 (broadly equivalent to the Holocene and Last Glacial Period, respectively), detrital zircon age peaks associated with the Banzare Province (c. 1620-1490 Ma) are prevalent alongside the c. 1360-1100 Ma Wilkes signature (Fig. 3.5b). In the middle biosiliceous portion of the core (intervals 2 and 3, Fig. 3.5b), Banzare-age peaks are reduced and Nuyina-age peaks (c. 1450-1390 Ma) are more prominent. We suggest these subtle changes in the detrital zircon record over time support the supply of detritus from multiple source regions. Below, we relate downcore changes in sediment provenance to temporal changes in the climate and ice sheet configuration.

### **3.5.2.1. A broad source region during interglacials**

The most recently deposited sediment is captured by KC14 interval 1 (Fig. 3.5b), which should therefore yield an age signature that is most representative of the subglacial rock types being eroded at the base of the ice sheet in the present day. The Banzare-age detrital zircon signature in this interval suggests that some of this more recently-deposited detritus was sourced from where the Banzare Province is exposed to the base of the ice sheet at or close to the coast. The interpreted extension of the Banzare Province beneath multiple subglacial catchments east of the Totten catchment (Maritati et al., 2019) suggests likely detrital contributions from the Moscow University, Thompson and Holmes glaciers (Fig. 3.9). This idea is supported by recent interpretations of the continental slope morphology that suggest that the contourite ridge from which KC14 was recovered is fed not only by detritus from the Totten Glacier, but also by fine sediment plumes transported westward across the slope by the Antarctic Coastal Current (O'Brien et al., 2020). With an ice sheet slightly advanced relative to modern grounding line, the ice sheet model of (Aitken et al., 2016b) predicts high basal erosion (using basal velocity as a proxy) across a broad coastal area of central Wilkes Land (Fig. 3.9a). The dominance of Wilkes and Banzare-age peaks in interval 1 of our marine core record supports the

predictions of this ice sheet model which shows high basal erosion focused in zones mostly underlain by the Wilkes and Banzare provinces (Figs 3.5b and 3.9a).

### **3.5.2.2. Debris flows during the Last Glacial Period**

Curiously, the detrital zircon signature during the glacial (interval 4) resembles that of the Holocene (interval 1) described above (Fig. 3.5b). We interpret the detrital age signal in the glacial section of KC14 (interval 4; Figs 3.3 and 3.5) to represent reworked sediment remobilised off the shelf and deposited downslope during glacial advance, a process recently inferred in this region (O'Brien et al., 2020; Post et al., 2020) and in previous studies around the Antarctic margin (Diekmann et al., 2000; Dowdeswell et al., 2006, 2004; Gales et al., 2013; Pudsey, 2000). This interpretation is supported by the high glacial sedimentation rate (377 cm/kyr) (interval 4, Fig. 3.3), at a time when basal erosion by the ice sheet was minimum (Golledge et al., 2013; Fig. 3.9b), suggesting that reworking of shelf sediments by debris flows was the most likely process contributing to the high sediment accumulation (O'Brien et al., 2020; Post et al., 2020). The relatively small concentrations of BiSi measured in the glacial section of the core (interval 4; 1.9-7.9 %) likely comprise reworked diatoms from earlier warm periods that were redeposited with the sediment from the continental shelf, explaining the high BiSi flux during this same glacial period (interval 4, Fig. 3.3). Coarse debris (250  $\mu\text{m}$  – 2 mm) that matches the criteria of IBRD was likely mobilised by downslope sediment transport. This process explains the higher calculated 'IBRD' flux during the glacial (Fig. 3.3), when iceberg calving would have been infrequent and the quantity of IBRD is expected to be low (Bertram et al., 2018; Wilson et al., 2018). A mixture of this coarse debris and fall-out of finer sediment from suspension in sediment-laden plumes likely contributed to the maintenance of the large contourite ridge where KC14 is located (O'Brien et al., 2020; Post et al., 2020). The similarity in age distribution between intervals 1 and 4 suggests that the sediment reworked in debris flows as the ice sheet advanced was initially deposited during past warmer climate periods, when the position of the retreated ice sheet margin and the provenance of continentally-derived detritus was similar to that of the present day.

### 3.5.2.3. A proximal provenance during deglaciation

A prominent decline in the sedimentation rate from 377 cm/kyr to 8 cm/kyr at c. 23.2 cal yrs BP (Fig. 3.3) indicates the ceasing of abundant sediment supply in debris flows to the slope. We interpret this decrease in sedimentation as the point when the ice sheet reached its maximum extent, and the associated reworking of shelf sediments ceased. The onset of deglaciation (c. 16.9 - 14.2 cal yrs BP) is marked by a rise in BiSi concentrations representing a growth in primary productivity and warmer, ice-free conditions above the core site (intervals 2 and 3, Fig. 3.3). During this time, the sedimentation rate increased to 14 cm/kyr and IBRD became more abundant, reflecting a change in the mode of sediment transport to the continental slope. Whilst sedimentation during the glacial period was dominated by the supply of reworked sediment in mass flows, deglacial sedimentation was likely controlled by the release of englacial IBRD from the base of melting icebergs and in sediment-laden meltwater fluxes associated with climate warming and ice sheet retreat, as interpreted in other studies in East Antarctica (Bertram et al., 2018; Wilson et al., 2018).

The deglacial sediment provenance signature is represented by detrital ages from biosiliceous sediments in intervals 2 and 3 of the core (Figs 3.3 and 3.5b). In comparison to intervals 1 and 4, the more prominent Wilkes and Nuyina-age signatures, coupled with a significantly reduced Banzare-age signal in these deglacial intervals, suggests that detritus was sourced from the coastal region of the Totten catchment area. At the onset of deglaciation, with an ice sheet extended further offshore of its present-day position, the terminus of the Totten Glacier was situated in closer proximity to the KC14 core site and would likely be the principal outlet for detritus during this time. Recently, Prothro et al. (2018) interpreted that most englacial debris that melted out of the base of ice shelves in the Ross Sea region during retreat was deposited proximal to the grounding line. We interpret this to be the case in central Wilkes Land. With a narrower “cone of influence”, the abundant detritus being supplied by the Totten Glacier to the slope would dampen the signal produced from detritus from more distal sources, explaining the relatively

enhanced Nuyina age signature and reduced Banzare age signature in the detrital zircon record (intervals 2 and 3, Fig. 3.5b).

#### **3.5.2.4. Evidence for minor far-field provenance**

Minor detrital c. 750-500 Ma ages are present throughout the detrital zircon record, that are not known to be characteristic of basement rocks of central Wilkes Land nor the conjugate regions in southern Australia. The compiled age spectra from the offshore (Pierce et al., 2014) and onshore (Veevers, 2012; Veevers and Saeed, 2011) records of the Eastern Sector show a dominant age population between c. 740-400 Ma (Fig. 3.8). Westward transport of detritus over long distances from one sector to another by icebergs driven by the Antarctic Coastal Current is supported by evidence from warm climates and transitions of the Early Pliocene (Cook et al., 2014; Williams et al., 2010). Icebergs calved off from the Eastern Sector have been observed tracking westward along the shelf to the Wilkes Sector (Budge and Long, 2018). We propose westward transport of a minor component of detritus from the Eastern Sector via icebergs driven by the Antarctic Coastal Current to the KC14 core site. This hypothesis would account for the rare, but distinct c. 750-500 Ma detrital age population characteristic of the basement rock and intruded granites of George V Land (Lamarque et al., 2018). Provenance from the east could also account for minor older c. 2200-1700 Ma detrital zircon ages that correlate with Archean and Paleoproterozoic rocks of the Adélie Land coast (Ménot et al., 2007).

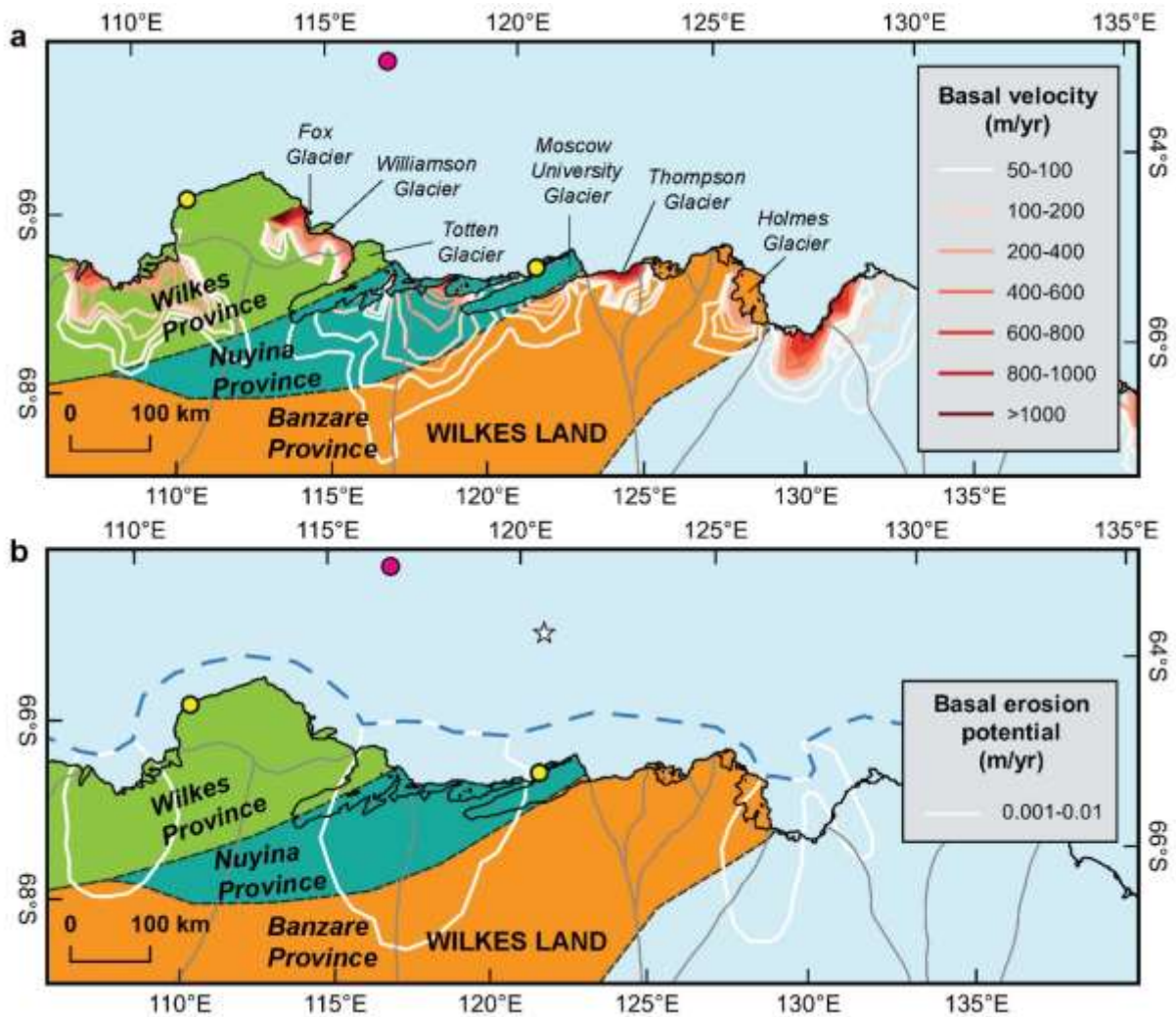


**Figure 3.9.** Basal ice sheet velocity in central Wilkes Land overlain on subglacial geological provinces interpreted from geophysical data and coastal outcrop (Aitken et al., 2014; Maritati et al., 2019). Coastal (yellow) and offshore (pink) sample locations are shown. Grey lines mark the boundaries of ice drainage basins (Mouginot et al., 2017). **(a)** Map showing modelled ice sheet basal velocity contours predicted for an ice sheet slightly advanced relative to the present from Aitken et al. (2016b) and clipped to the modern grounding line (Mouginot et al., 2017). **(b)** Map showing modelled basal erosion potential at 21 ka from Golledge et al. (2013). The modelled maximum extent of the ice sheet is indicated with a blue dashed line (Golledge et al., 2013). The position of a grounding zone wedge (GSW) identified by Post et al. (2020) is shown (white star), as new evidence indicating the former maximum extent of the ice sheet at that location.

## 3.6. Conclusions

This investigation presents the first sediment provenance record from the continental slope of central Wilkes Land, defining the sedimentary environment, transport, and source of detritus to this part of the Wilkes Sector from c. 23.5 ka to present.

Detailed multiproxy analyses allow the following conclusions to be drawn:

- 1) The main Mesoproterozoic (c. 1360-1000 Ma and c. 1620-1490 Ma) age populations in the KC14 detritus indicate sourcing from dominantly felsic granitoid rocks of the proximal Wilkes and Banzare provinces, with smaller contributions from the adjacent Nuyina Province (c. 1450-1390 Ma) in central Wilkes Land. The unexpectedly small contribution from Nuyina Province, and relative importance of material from the Banzare Province, is hypothesised to reflect sourcing of detritus from a broad source region, including the Totten Glacier catchment and subglacial catchments further east.
- 2) Debris flows instigated by the advancing ice sheet remobilised sediments from the continental shelf and redeposited them on the slope during the Last Glacial Period. These sediments, deposited prior to glacial advance, have the same provenance signature as detritus deposited during the current interglacial.
- 3) The deglacial signature is dominated by detritus from the Wilkes and Nuyina provinces that underlie Totten Glacier, suggesting dominant sourcing of detritus from the coastal region of the Totten catchment area when the ice sheet margin was extended further offshore of its present day position. This is likely due to the proximity of Totten Glacier to the core site and the dampening of detrital age signatures from more distal source regions during this time.

- 4) Minor c. 750-500 Ma and 2200-1700 Ma detrital zircon in KC14 was likely derived from rocks in the Eastern Sector and transported to the core site via icebergs driven by the Antarctic Coastal Current.

This new sediment provenance record provides the first offshore evidence from the Sabrina Coast to support existing subglacial bedrock interpretations from available geophysical and rare outcrop geological data in central Wilkes Land. These findings can be used to support plate tectonic reconstructions and to help infer the properties of the Antarctic crust that are relevant to basal ice sheet conditions and associated ice sheet configuration.

### 3.7. Supplementary Information

Sample/ Core ID	Location	Latitude	Longitude	Sample type	Lithology
CI-814A2	Chick Island	- 66.7892	120.9906	Basement rock	Granodiorite
CI-814B	Chick Island	- 66.7892	120.9906	Basement rock	Granite xenolith
CI-810A	Chick Island	- 66.7894	120.9908	Basement rock	Granite xenolith
PRR- 21189	Balaena Islets	- 66.017	111.1	Basement rock	Granite
KC14	Continental slope of Sabrina Coast	- 64.539	116.64	Marine sediment	Silty clay

**Supplementary Table 3.1.** Sample locations and descriptions.

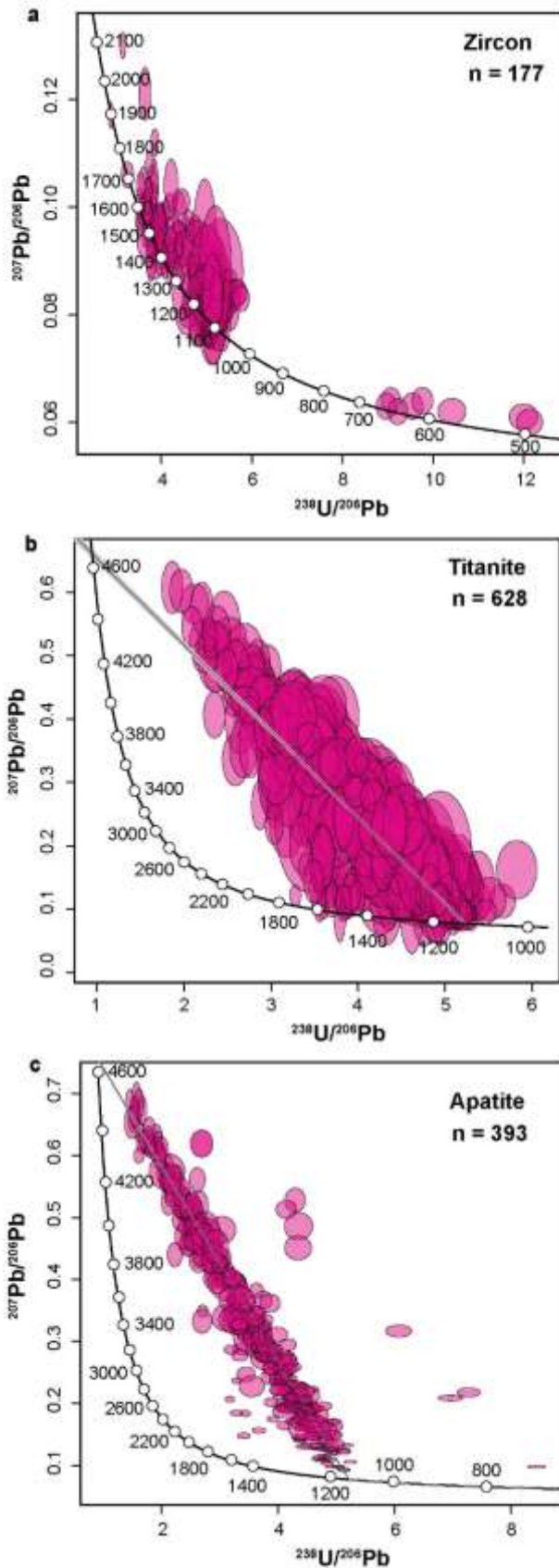
Mineral	Ablation Duration (s)	Analysis Type	Primary Standards	Secondary Standards	Trace elements and isotope measured
Zircon	30	13µm/ 29µm spot	NIST610 91500	Plešovice Temora	<sup>49</sup> Ti, <sup>56</sup> Fe, <sup>90</sup> Zr, <sup>178</sup> Hf, <sup>202</sup> Hg, <sup>204</sup> Pb, <sup>206</sup> Pb, <sup>207</sup> Pb, <sup>208</sup> Pb, <sup>232</sup> Th, <sup>235</sup> U, <sup>238</sup> U and REEs
Apatite	30	13µm/ 29µm spot	NIST610 OD306	401ap Otter Lake Emerald Lake Durango McClure Mt.	<sup>31</sup> P, <sup>43</sup> Ca, <sup>56</sup> Fe, <sup>140</sup> Ce, <sup>232</sup> Th, <sup>204</sup> Pb, <sup>206</sup> Pb, <sup>207</sup> Pb, <sup>208</sup> Pb, <sup>232</sup> Th, <sup>238</sup> U and REEs
Titanite	30	13µm/ 29µm spot	NIST610 19686	FC-3 Mt. Dromedary	<sup>157</sup> Gd, <sup>49</sup> Ti, <sup>56</sup> Fe, <sup>90</sup> Zr, <sup>178</sup> Hf, <sup>232</sup> Th, <sup>204</sup> Pb, <sup>206</sup> Pb, <sup>207</sup> Pb, <sup>208</sup> Pb, <sup>202</sup> Hg, <sup>235</sup> U, <sup>238</sup> U and REEs
Feldspar	64.59	110 µm line	NIST612	BCR-2g GSD-1g	<sup>29</sup> Si, <sup>204</sup> Pb, <sup>206</sup> Pb, <sup>207</sup> Pb, <sup>208</sup> Pb, <sup>39</sup> K, <sup>43</sup> Ca, <sup>232</sup> Th, <sup>56</sup> Fe, <sup>238</sup> U, <sup>202</sup> Hg and REEs

**Supplementary Table 3.2.** List of parameters and Standard Reference Materials used for detrital zircon, apatite, and titanite U-Pb analysis and detrital feldspar Pb-Pb analysis. REEs – Rare Earth Elements.

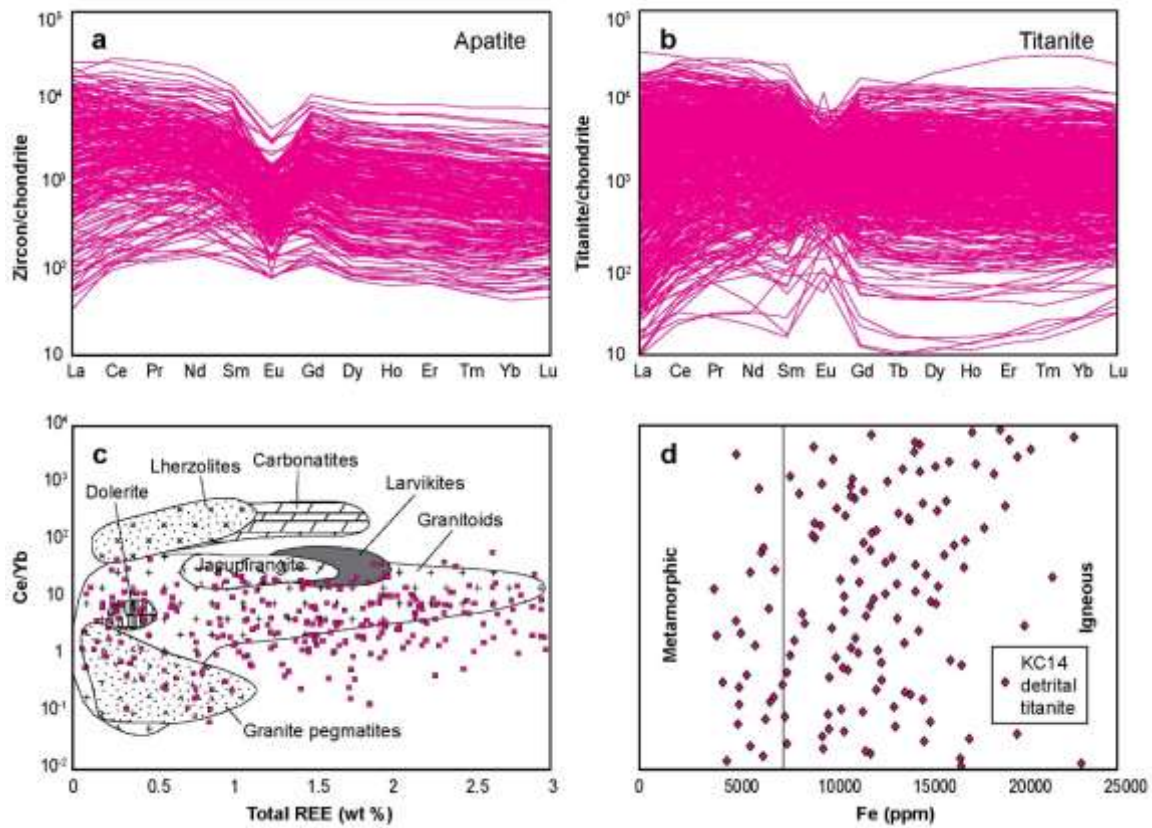
Standard	Mineral	Weighted average	Recommended value	Reference
<b>BCR-2g</b>	Glass	208Pb/204Pb ratio: 38.91 ± 0.32	208Pb/204Pb ratio: 38.908 ± 0.009	Jochum et al. (2016)
		207Pb/204Pb ratio: 15.67 ± 0.14	207Pb/204Pb ratio: 15.626 ± 0.006	GeoReM database
		206Pb/204Pb ratio: 18.84 ± 0.14	206Pb/204Pb ratio: 18.765 ± 0.007	
<b>GSD-1g</b>	Glass	208Pb/204Pb ratio: 39.00 ± 0.21	208Pb/204Pb ratio: 38.908 ± 0.009	Jochum et al. (2011)
		207Pb/204Pb ratio: 15.78 ± 0.09	207Pb/204Pb ratio: 15.745 ± 0.002	GeoReM database
		206Pb/204Pb ratio: 19.62 ± 0.10	206Pb/204Pb ratio: 19.579 ± 0.004	
<b>Plešovice</b>	Zircon	206Pb/238U age: 338.7 ± 2.3 Ma	206Pb/238U age: 337.13 ± 0.37 Ma	Sláma et al. (2008)
<b>Plešovice</b>	Zircon	206Pb/238U age: 339.7 ± 1.7 Ma		
<b>Plešovice</b>	Zircon	206Pb/238U age: 340.1 ± 3.7 Ma		
<b>Temora</b>	Zircon	206Pb/238U age: 413.4 ± 4.2 Ma	206Pb/238U age: 416.8 ± 1.1 Ma	Black et al. (2003)
<b>Temora</b>	Zircon	206Pb/238U age: 415.5 ± 3.1 Ma		
<b>Temora</b>	Zircon	206Pb/238U age: 418.7 ± 7.9 Ma		
<b>FC-3 Titanite</b>	Titanite	206Pb/238U age: 27.8 ± 2.8 Ma	206Pb/238U age: 28.13 ± 0.48 Ma	Schmitz and Bowring (2001)
<b>FC-3 Titanite</b>	Titanite	206Pb/238U age: 27.5 ± 2 Ma		
<b>Mt. Dromedary</b>	Titanite	206Pb/238U age: 98 ± 2.3 Ma	206Pb/238U age: 98.7 ± 0.6 Ma	Miller et al. (1985)
<b>Mt. Dromedary</b>	Titanite	206Pb/238U age: 97.6 ± 3.3 Ma		
<b>401 ap</b>	Apatite	206Pb/238U age: 528.5 ± 8.6 Ma	206Pb/238U age: 530.3 ± 1.4 Ma	Thompson et al. (2016)
<b>401 ap</b>	Apatite	206Pb/238U age: 532 ± 16 Ma		
<b>McClure Mt.</b>	Apatite	206Pb/238U age: 530.1 ± 9.1 Ma	206Pb/238U age: 523.98 ± 0.12 Ma	Schoene and Bowring (2006)
<b>McClure Mt.</b>	Apatite	206Pb/238U age: 525.1 ± 7 Ma		

<b>Otter Lake</b>	Apatite	206Pb/238U age: 928 ± 39 Ma	206Pb/238U age: 913 ± 7.0 Ma	Barfod et al. (2005)
<b>Emerald Lake</b>	Apatite	206Pb/238U age: 93.3 ± 2.4 Ma	206Pb/238U age: 92.2 ± 0.9 Ma	Coulson et al. (2002)
<b>Durango</b>	Apatite	206Pb/238U age: 30.2 ± 2.7 Ma	206Pb/238U age: 31.44 ± 0.18 Ma	McDowell et al. (2005)

**Supplementary Table 3.3.** List of secondary Standard Reference Materials used for U-Pb analysis of detrital zircon, titanite and apatite, and Pb-Pb analysis of detrital feldspar. Weighted average values for each session on the instrument are shown. Published recommended values are given. All errors are  $2\sigma$ .



**Supplementary Fig. 3.1.** Terra-Wasserburg diagrams for detrital zircon, titanite and apatite in KC14. Error ellipses are plotted at  $2\sigma$ . **(a)** Detrital zircon analyses showing high concordance. **(b)** Highly discordant detrital titanite analyses. Discordia line fitted through analyses is shown in black with  $2\sigma$  uncertainty (grey). **(c)** Highly discordant detrital apatite analyses. Discordia line fitted through analyses is shown in black with  $2\sigma$  uncertainty (grey).



**Supplementary Fig. 3.2.** Chondrite-normalised REE and trace element compositions for detrital apatite and titanite in KC14. **(a)** Chondrite-normalised REE composition for detrital apatite analyses. **(b)** Chondrite-normalised REE composition for detrital titanite analyses. **(c)** Detrital apatite analyses overlain on source rock composition discrimination diagram of Belousova et al. (2002b). **(d)** Fe concentrations in detrital titanite with approximate ranges for typical metamorphic and igneous source rock types shown from Olierook et al. (2019).

# References

- Aitken, A. R. A., Betts, P. G., Young, D. A., Blankenship, D. D., Roberts, J. L., & Siegert, M. J. (2016a). The Australo-Antarctic Columbia to Gondwana transition. *Gondwana Research*, 29(1), 136–152. <https://doi.org/10.1016/j.gr.2014.10.019>
- Aitken, A. R. A., Roberts, J. L., Van Ommen, T. D., Young, D. A., Golledge, N. R., Greenbaum, J. S., Blankenship, D. D., & Siegert, M. J. (2016b). Repeated large-scale retreat and advance of Totten Glacier indicated by inland bed erosion. *Nature*, 533, 385–389. <https://doi.org/10.1038/nature17447>
- Aitken, A. R. A., Young, D. A., Ferraccioli, F., Betts, P. G., Greenbaum, J. S., Richter, T. G., Roberts, J. L., Blankenship, D. D., & Siegert, M. J. (2014). The subglacial geology of Wilkes Land, East Antarctica. *Geophysical Research Letters*, 41(7), 2390–2400. <https://doi.org/10.1002/2014GL059405>
- Amblas, D., & Canals, M. (2016). Contourite drifts and canyon-channel systems on the Northern Antarctic Peninsula Pacific margin. *Geological Society Memoir*, 46(1), 393–394. <https://doi.org/10.1144/M46.17>
- Armand, L., O'Brien, P., Armbrecht, L., Barker, H., Caburlotto, A., Connell, T., Cotterle, D., Duffy, M., Edwards, S., Evangelinos, D., Fazey, J., Flint, A., Focardi, A., Gifford, S., Holder, L., Hughes, P., Lawler, K.-A., Lieser, J., Leventer, A., ... Young, A. (2018). *Interactions of the Totten Glacier with the Southern Ocean through multiple glacial cycles (IN2017-V01): Post-survey report. March*. <https://doi.org/10.4225/13/5ACEA64C48693>
- Baker, J., Peate, D., Waight, T., & Meyzen, C. (2004). Pb isotopic analysis of standards and samples using a  $^{207}\text{Pb}$ - $^{204}\text{Pb}$  double spike and thallium to correct for mass bias with a double-focusing MC-ICP-MS. *Chemical Geology*, 211(3–4), 275–303. <https://doi.org/10.1016/j.chemgeo.2004.06.030>
- Barfod, G. H., Krogstad, E. J., Frei, R., & Albarède, F. (2005). Lu-Hf and PbSL geochronology of apatites from Proterozoic terranes: A first look at Lu-Hf isotopic closure in metamorphic apatite. *Geochimica et Cosmochimica Acta*, 69(7), 1847–1859. <https://doi.org/10.1016/j.gca.2004.09.014>
- Belousova, E. A., Griffin, W. L., O'Reilly, S. Y., & Fisher, N. I. (2002a). Igneous zircon: Trace element composition as an indicator of source rock type. *Contributions to Mineralogy and Petrology*, 143(5), 602–622. <https://doi.org/10.1007/s00410-002-0364-7>

- Belousova, E. A., Griffin, W. L., O'Reilly, S. Y., & Fisher, N. I. (2002b). Apatite as an indicator mineral for mineral exploration: Trace-element compositions and their relationship to host rock type. *Journal of Geochemical Exploration*, 76(1), 45–69. [https://doi.org/10.1016/S0375-6742\(02\)00204-2](https://doi.org/10.1016/S0375-6742(02)00204-2)
- Berry, R., Thompson, J., Meffre, S., & Goemann, K. (2016). U–Th–Pb monazite dating and the timing of arc–continent collision in East Timor. *Australian Journal of Earth Sciences*, 63(4), 367–377. <https://doi.org/10.1080/08120099.2016.1217930>
- Bertram, R. A., Wilson, D. J., van de Flierdt, T., McKay, R. M., Patterson, M. O., Jimenez-Espejo, F. J., Escutia, C., Duke, G. C., Taylor-Silva, B. I., & Riesselman, C. R. (2018). Pliocene deglacial event timelines and the biogeochemical response offshore Wilkes Subglacial Basin, East Antarctica. *Earth and Planetary Science Letters*, 494, 109–116. <https://doi.org/10.1016/j.epsl.2018.04.054>
- Black, L. P., Kamo, S. L., Allen, C. M., Aleinikoff, J. N., Davis, D. W., Korsch, R. J., & Foudoulis, C. (2003). TEMORA 1: A new zircon standard for Phanerozoic U-Pb geochronology. *Chemical Geology*, 200(1–2), 155–170. [https://doi.org/10.1016/S0009-2541\(03\)00165-7](https://doi.org/10.1016/S0009-2541(03)00165-7)
- Boger, S. D. (2011). Antarctica - Before and after Gondwana. In *Gondwana Research* (Vol. 19, Issue 2, pp. 335–371). <https://doi.org/10.1016/j.gr.2010.09.003>
- Budge, J. S., & Long, D. G. (2018). A Comprehensive Database for Antarctic Iceberg Tracking Using Scatterometer Data. *IEEE Journal of Selected Topics in Applied Earth Observations and Remote Sensing*, 11(2), 434–442. <https://doi.org/10.1109/JSTARS.2017.2784186>
- Cameron, R. L., Loken, O. H., & Molholm, J. R. T. (1958). USNC-IGY Antarctic glaciological data. Field work 1957 and 1958. Part 1. In *Ohio State University Research Foundation Report*.
- Chew, D. M., Sylvester, P. J., & Tubrett, M. N. (2011). U-Pb and Th-Pb dating of apatite by LA-ICPMS. *Chemical Geology*, 280(1–2), 200–216. <https://doi.org/10.1016/j.chemgeo.2010.11.010>
- Clark, D. J., Hensen, B. J., & Kinny, P. D. (2000). Geochronological constraints for a two-stage history of the Albany-Fraser Orogen, Western Australia. *Precambrian Research*, 102(3–4), 155–183. [https://doi.org/10.1016/S0301-9268\(00\)00063-2](https://doi.org/10.1016/S0301-9268(00)00063-2)
- Cook, C. P., Hill, D. J., van de Flierdt, T., Williams, T., Hemming, S. R., Dolan, A. M., Pierce, E. L., Escutia, C., Harwood, D., Cortese, G., & Gonzales, J. J. (2014). Sea surface temperature control on the distribution of far-traveled Southern Ocean ice-rafted detritus during the Pliocene. *Paleoceanography*, 29(6), 533–548. <https://doi.org/10.1002/2014PA002625>

- Coulson, I. M., Villeneuve, M. E., Dipple, G. M., Duncan, R. A., Russell, J. K., & Mortensen, J. K. (2002). Time-scales of assembly and thermal history of a composite felsic pluton: Constraints from the Emerald Lake area, northern Canadian Cordillera, Yukon. *Journal of Volcanology and Geothermal Research*, 114(3–4), 331–356. [https://doi.org/10.1016/S0377-0273\(01\)00294-3](https://doi.org/10.1016/S0377-0273(01)00294-3)
- De Santis, L., Brancolini, G., Accettella, D., Cova, A., Caburlotto, A., Donda, F., Pelos, C., Zgur, F., & Presti, M. (2007). New insights into submarine geomorphology and depositional processes along the George V Land continental slope and upper rise (East Antarctica). *Online Proceedings of the 10th ISAES X, Edited by A. K. Cooper and C. R. Raymond et al., USGS Open-File Report 2007-1047, Extended Abstract 061*, 1–5.
- DeMaster, D. J. (1981). The supply and accumulation of silica in the marine environment. *Geochimica et Cosmochimica Acta*, 45(10), 1715–1732. [https://doi.org/10.1016/0016-7037\(81\)90006-5](https://doi.org/10.1016/0016-7037(81)90006-5)
- Diamond, D. (2002). Determination of silicate in brackish or seawater by flow injection analysis. QuickChem Method 31-114-27-1-D. *Lachat Instruments QuickChem Method Manual*.
- Diekmann, B., Kuhn, G., Rachold, V., Abelmann, A., Brathauer, U., Fütterer, D. K., Gersonde, R., & Grobe, H. (2000). Terrigenous sediment supply in the Scotia Sea (Southern Ocean): Response to Late Quaternary ice dynamics in Patagonia and on the Antarctic Peninsula. *Palaeogeography, Palaeoclimatology, Palaeoecology*, 162(3–4), 357–387. [https://doi.org/10.1016/S0031-0182\(00\)00138-3](https://doi.org/10.1016/S0031-0182(00)00138-3)
- Donda, F., Brancolini, G., O'Brien, P. E., De Santis, L., & Escutia, C. (2007). Sedimentary processes in the Wilkes Land margin: A record of the Cenozoic East Antarctic Ice Sheet evolution. *Journal of the Geological Society*, 164(1), 243–256. <https://doi.org/10.1144/0016-76492004-159>
- Donda, F., Leitchenkov, G., Brancolini, G., Romeo, R., de Santis, L., Escutia, C., O'brien, P., Armand, L., Caburlotto, A., & Cotterle, D. (2020). The influence of Totten Glacier on the Late Cenozoic sedimentary record. *Antarctic Science*, 1–13. <https://doi.org/10.1017/S0954102020000188>
- Dowdeswell, J. A., Evans, J., O'Cofaigh, C., & Anderson, J. B. (2006). Morphology and sedimentary processes on the continental slope off Pine Island Bay, Amundsen Sea, West Antarctica. *Bulletin of the Geological Society of America*, 118(5–6), 606–619. <https://doi.org/10.1130/B25791.1>

- Dowdeswell, J. A., Ó Cofaigh, C., & Pudsey, C. J. (2004). Continental slope morphology and sedimentary processes at the mouth of an Antarctic palaeo-ice stream. *Marine Geology*, 204(1–2), 203–214. [https://doi.org/10.1016/S0025-3227\(03\)00338-4](https://doi.org/10.1016/S0025-3227(03)00338-4)
- Fernandez, R., Gulick, S., Domack, E., Montelli, A., Leventer, A., Shevenell, A., & Frederick, B. (2018). Past ice stream and ice sheet changes on the continental shelf off the Sabrina Coast, East Antarctica. *Geomorphology*, 317, 10–22. <https://doi.org/10.1016/j.geomorph.2018.05.020>
- Fitzsimons, I. C. W. (2003). Proterozoic basement provinces of southern and southwestern Australia, and their correlation with Antarctica. *Geological Society Special Publication*, 206(1), 93–130. <https://doi.org/10.1144/GSL.SP.2003.206.01.07>
- Flowerdew, M. J., Tyrrell, S., Boger, S. D., Fitzsimons, I. C. W., Harley, S. L., Mikhalsky, E. V., & Vaughan, A. P. M. (2013). Pb isotopic domains from the Indian Ocean sector of Antarctica: Implications for past Antarctica-India connections. *Geological Society Special Publication*, 383(1), 59–72. <https://doi.org/10.1144/SP383.3>
- Fretwell, P., Pritchard, H. D., Vaughan, D. G., Bamber, J. L., Barrand, N. E., Bell, R., Bianchi, C., Bingham, R. G., Blankenship, D. D., Casassa, G., Catania, G., Callens, D., Conway, H., Cook, A. J., Corr, H. F. J., Damaske, D., Damm, V., Ferraccioli, F., Forsberg, R., ... Zirizzotti, A. (2013). Bedmap2: Improved ice bed, surface and thickness datasets for Antarctica. *Cryosphere*, 7(1), 375–393. <https://doi.org/10.5194/tc-7-375-2013>
- Gales, J. A., Larter, R. D., Mitchell, N. C., & Dowdeswell, J. A. (2013). Geomorphic signature of Antarctic submarine gullies: Implications for continental slope processes. *Marine Geology*, 337, 112–124. <https://doi.org/10.1016/j.margeo.2013.02.003>
- Golledge, N. R., Levy, R. H., McKay, R. M., Fogwill, C. J., White, D. A., Graham, A. G. C., Smith, J. A., Hillenbrand, C. D., Licht, K. J., Denton, G. H., Ackert, R. P., Maas, S. M., & Hall, B. L. (2013). Glaciology and geological signature of the Last Glacial Maximum Antarctic ice sheet. *Quaternary Science Reviews*, 78, 225–247. <https://doi.org/10.1016/j.quascirev.2013.08.011>
- Greenbaum, J. S., Blankenship, D. D., Young, D. A., Richter, T. G., Roberts, J. L., Aitken, A. R. A., Legresy, B., Schroeder, D. M., Warner, R. C., van Ommen, T. D., & Siegert, M. J. (2015). Ocean access to a cavity beneath Totten Glacier in East Antarctica. *Nature Geoscience*, 8(4), 294–298. <https://doi.org/10.1038/ngeo2388>
- Gulick, S. P. S., Shevenell, A. E., Montelli, A., Fernandez, R., Smith, C., Warny, S., Bohaty, S. M., Sjunneskog, C., Leventer, A., Frederick, B., & Blankenship, D. D. (2017). Initiation and

long-term instability of the East Antarctic Ice Sheet. *Nature*, 552(7684), 225–229.

<https://doi.org/10.1038/nature25026>

Halpin, J. A., Jensen, T., McGoldrick, P., Meffre, S., Berry, R. F., Everard, J. L., Calver, C. R., Thompson, J., Goemann, K., & Whittaker, J. M. (2014). Authigenic monazite and detrital zircon dating from the Proterozoic Rocky Cape Group, Tasmania: Links to the Belt-Purcell Supergroup, North America. *Precambrian Research*, 250, 50–67.

<https://doi.org/10.1016/j.precamres.2014.05.025>

Hawke, M. L., Meffre, S., Stein, H., Hilliard, P., Large, R., & Gemmell, J. B. (2015).

Geochronology of the DeGrussa volcanic-hosted massive sulphide deposit and associated mineralisation of the Yerrida, Bryah and Padbury Basins, Western Australia. *Precambrian Research*, 267, 250–284. <https://doi.org/10.1016/j.precamres.2015.06.011>

Horstwood, M. S. A., Košler, J., Gehrels, G., Jackson, S. E., McLean, N. M., Paton, C., Pearson, N. J., Sircombe, K., Sylvester, P., Vermeesch, P., Bowring, J. F., Condon, D. J., & Schoene, B. (2016). Community-Derived Standards for LA-ICP-MS U-(Th)-Pb Geochronology – Uncertainty Propagation, Age Interpretation and Data Reporting. *Geostandards and Geoanalytical Research*, 40(3), 311–332. <https://doi.org/10.1111/j.1751-908X.2016.00379.x>

Jamieson, S. S. R., Sugden, D. E., & Hulton, N. R. J. (2010). The evolution of the subglacial landscape of Antarctica. *Earth and Planetary Science Letters*, 293(1–2), 1–27.

<https://doi.org/10.1016/j.epsl.2010.02.012>

Jochum, K. P., Weis, U., Schwager, B., Stoll, B., Wilson, S. A., Haug, G. H., Andreae, M. O., &ENZWEILER, J. (2016). Reference Values Following ISO Guidelines for Frequently Requested Rock Reference Materials. *Geostandards and Geoanalytical Research*, 40(3), 333–350.

<https://doi.org/10.1111/j.1751-908X.2015.00392.x>

Jochum, K. P., Wilson, S. A., Abouchami, W., Amini, M., Chmeleff, J., Eisenhauer, A., Hegner, E., Iaccheri, L. M., Kieffer, B., Krause, J., Mcdonough, W. F., Mertz-Kraus, R., Raczek, I., Rudnick, R. L., Scholz, D., Steinhoefel, G., Stoll, B., Stracke, A., Tonarini, S., ... Woodhead, J. D. (2011). GSD-1G and MPI-DING Reference Glasses for In Situ and Bulk Isotopic Determination. *Geostandards and Geoanalytical Research*, 35(2), 193–226.

<https://doi.org/10.1111/j.1751-908X.2010.00114.x>

Johnson, S. P., Kirkland, C. L., Evans, N. J., McDonald, B. J., & Cutten, H. N. (2018). The complexity of sediment recycling as revealed by common Pb isotopes in K-feldspar.

*Geoscience Frontiers*, 9(5), 1515–1527. <https://doi.org/10.1016/j.gsf.2018.03.009>

- Kirkland, C. L., Smithies, R. H., Spaggiari, C. V., Wingate, M. T. D., Quentin de Gromard, R., Clark, C., Gardiner, N. J., & Belousova, E. A. (2017). Proterozoic crustal evolution of the Eucla basement, Australia: Implications for destruction of oceanic crust during emergence of Nuna. *Lithos*, 278–281, 427–444. <https://doi.org/10.1016/j.lithos.2017.01.029>
- Krissek, L. A. (1995). Late Cenozoic Ice-Rafting Records from Leg 145 Sites in the North Pacific: Late Miocene Onset, Late Pliocene Intensification, and Pliocene—Pleistocene Events. In *Proceedings of the Ocean Drilling Program, 145 Scientific Results* (Vol. 145). <https://doi.org/10.2973/odp.proc.sr.145.118.1995>
- Lamarque, G., Bascou, J., Ménot, R. P., Paquette, J. L., Couzinié, S., Rolland, Y., & Cottin, J. Y. (2018). Ediacaran to lower Cambrian basement in eastern George V Land (Antarctica): Evidence from U–Pb dating of gneiss xenoliths and implications for the South Australia– East Antarctica connection. *Lithos*, 318–319, 219–229. <https://doi.org/10.1016/j.lithos.2018.08.021>
- Leitchenkov, G. L. (2015). Environmental and climate changes in Antarctica in the Geological Past. *Ice and Snow*, 128(4), 107. <https://doi.org/10.15356/2076-6734-2014-4-107-116>
- Licht, K. J., & Hemming, S. R. (2017). Analysis of Antarctic glacial sediment provenance through geochemical and petrologic applications. In *Quaternary Science Reviews* (Vol. 164, pp. 1–24). Elsevier Ltd. <https://doi.org/10.1016/j.quascirev.2017.03.009>
- Lougheed, B. C., & Obrochta, S. P. (2016). MatCal: Open Source Bayesian 14C Age Calibration in Matlab. *Journal of Open Research Software*, 4. <https://doi.org/10.5334/jors.130>
- Lowry, D. P., Golledge, N. R., Bertler, N. A. N., Jones, R. S., McKay, R., & Stutz, J. (2020). Geologic controls on ice sheet sensitivity to deglacial climate forcing in the Ross Embayment, Antarctica. *Quaternary Science Advances*, 1, 100002. <https://doi.org/10.1016/j.qsa.2020.100002>
- Ludwig, K. R. (2012). User's Manual for Isoplot 3.75, a geochronological toolkit for Microsoft Excel. *Berkeley Geochronology Center Special Publication*, 5(5), 1–72.
- Maritati, A., Halpin, J. A., Whittaker, J. M., & Daczko, N. R. (2019). Fingerprinting Proterozoic Bedrock in Interior Wilkes Land, East Antarctica. *Scientific Reports*, 9(1), 1–12. <https://doi.org/10.1038/s41598-019-46612-y>
- Matthews, K. J., Maloney, K. T., Zahirovic, S., Williams, S. E., Seton, M., & Müller, R. D. (2016). Global plate boundary evolution and kinematics since the late Paleozoic. *Global and Planetary Change*, 146, 226–250. <https://doi.org/10.1016/j.gloplacha.2016.10.002>

- McDowell, F. W., McIntosh, W. C., & Farley, K. A. (2005). A precise  $^{40}\text{Ar}$ - $^{39}\text{Ar}$  reference age for the Durango apatite (U-Th)/He and fission-track dating standard. *Chemical Geology*, 214(3–4), 249–263. <https://doi.org/10.1016/j.chemgeo.2004.10.002>
- Ménot, R. P., Duclaux, G., Peucat, J. J., Rolland, Y., Guillot, S., Fanning, M., Bascou, J., Gapais, D., & Pêcher, A. (2007). Geology of the Terre Adélie Craton (135 – 146° E). *10th International Symposium on Antarctic Earth Sciences*, 1047, 5. <https://doi.org/10.3133/of2007-1047.srp059>
- Miller, D. S., Duddy, I. R., Green, P. F., Hurford, A. J., & Naeser, C. W. (1985). Results of interlaboratory comparison of fission-track age standards: Fission-track workshop-1984. *Nuclear Tracks and Radiation Measurements (1982)*, 10(3), 383–391. [https://doi.org/10.1016/0735-245X\(85\)90127-9](https://doi.org/10.1016/0735-245X(85)90127-9)
- Morrissey, L. J., Payne, J. L., Hand, M., Clark, C., Taylor, R., Kirkland, C. L., & Kylander- Clark, A. (2017). Linking the Windmill Islands, east Antarctica and the Albany–Fraser Orogen: Insights from U–Pb zircon geochronology and Hf isotopes. *Precambrian Research*, 293, 131–149. <https://doi.org/10.1016/j.precamres.2017.03.005>
- Mortlock, R. A., & Froelich, P. N. (1989). A simple method for the rapid determination of biogenic opal in pelagic marine sediments. *Deep Sea Research Part A, Oceanographic Research Papers*, 36(9), 1415–1426. [https://doi.org/10.1016/0198-0149\(89\)90092-7](https://doi.org/10.1016/0198-0149(89)90092-7)
- Mouginot, J., Scheuch, B., & Rignot, E. (2012). Mapping of ice motion in antarctica using synthetic-aperture radar data. *Remote Sensing*, 4(9), 2753–2767. <https://doi.org/10.3390/rs4092753>
- Mouginot, J., Scheuchl, B., & Rignot., E. (2017). MEaSURES Antarctic Boundaries for IPY 2007–2009 from Satellite Radar, Version 2. *NASA National Snow and Ice Data Center Distributed Active Archive Center*. <https://doi.org/https://doi.org/10.5067/AXE4121732AD>
- Mulder, J. A., Halpin, J. A., Daczko, N. R., Orth, K., Meffre, S., Thompson, J. M., & Morrissey, L. J. (2019). A Multiproxy provenance approach to uncovering the assembly of East Gondwana in Antarctica. *Geology*, 47(7), 645–649. <https://doi.org/10.1130/G45952.1>
- Nelson, D. R., Myers, J. S., & Nutman, A. P. (1995). Chronology and evolution of the middle proterozoic alban-fraser orogen, western australia. *Australian Journal of Earth Sciences*, 42(5), 481–495. <https://doi.org/10.1080/08120099508728218>
- O'Brien, P. E., Beaman, R., De Santis, L., Domack, E. W., Escutia, C., Harris, P. T., Leventer, A., McMullen, K., Post, A., Quilty, P. G., Shevenell, A. E., & Batchelor, C. L. (2016). Submarine

glacial landforms on the cold East Antarctic margin. *Geological Society Memoir*, 46(1), 501–508. <https://doi.org/10.1144/M46.172>

- O'Brien, P. E., Post, A. L., Edwards, S., Martin, T., Caburlotto, A., Donda, F., Leitchenkov, G., Romeo, R., Duffy, M., Evangelinos, D., Holder, L., Leventer, A., López-Quirós, A., Opdyke, B. N., & Armand, L. K. (2020). Continental slope and rise geomorphology seaward of the Totten Glacier, East Antarctica (112°E-122°E). *Marine Geology*, 427, 106221. <https://doi.org/10.1016/j.margeo.2020.106221>
- Olierook, H. K. H., Taylor, R. J. M., Erickson, T. M., Clark, C., Reddy, S. M., Kirkland, C. L., Jahn, I., & Barham, M. (2019). Unravelling complex geologic histories using U–Pb and trace element systematics of titanite. *Chemical Geology*, 504, 105–122. <https://doi.org/10.1016/j.chemgeo.2018.11.004>
- Orsi, A. H., Whitworth III, T., & Nowlin, W., D. (1995). On the extent and frontal structure of the Antarctic Circumpolar Current. *Deep Sea Res. Pt. I*, 2(43), 96–97.
- O'Sullivan, G., Chew, D., Kenny, G., Henrichs, I., & Mulligan, D. (2020). The trace element composition of apatite and its application to detrital provenance studies. In *Earth-Science Reviews* (Vol. 201, p. 103044). Elsevier B.V. <https://doi.org/10.1016/j.earscirev.2019.103044>
- Paterne, M., Michel, E., & Héros, V. (2019). Variability of marine <sup>14</sup>C reservoir ages in the Southern Ocean highlighting circulation changes between 1910 and 1950. *Earth and Planetary Science Letters*, 511, 99–104. <https://doi.org/10.1016/j.epsl.2019.01.029>
- Patterson, M. O., McKay, R., Naish, T., Escutia, C., Jimenez-Espejo, F. J., Raymo, M. E., Meyers, S. R., Tauxe, L., Brinkhuis, H., Klaus, A., Fehr, A., Bendle, J. A. P., Bijl, P. K., Bohaty, S. M., Carr, S. A., Dunbar, R. B., Flores, J. A., Gonzalez, J. J., Hayden, T. G., ... Yamane, M. (2014). Orbital forcing of the East Antarctic ice sheet during the Pliocene and Early Pleistocene. *Nature Geoscience*, 7(11), 841–847. <https://doi.org/10.1038/ngeo2273>
- Pierce, E. L., Hemming, S. R., Williams, T., van de Fliedert, T., Thomson, S. N., Reiners, P. W., Gehrels, G. E., Brachfeld, S. A., & Goldstein, S. L. (2014). A comparison of detrital U-Pb zircon, <sup>40</sup>Ar/<sup>39</sup>Ar hornblende, <sup>40</sup>Ar/<sup>39</sup>Ar biotite ages in marine sediments off East Antarctica: Implications for the geology of subglacial terrains and provenance studies. In *Earth-Science Reviews* (Vol. 138, pp. 156–178). Elsevier. <https://doi.org/10.1016/j.earscirev.2014.08.010>
- Post, A. L., O'Brien, P. E., Edwards, S., Carroll, A. G., Malakoff, K., & Armand, L. K. (2020). Upper slope processes and seafloor ecosystems on the Sabrina continental slope, East Antarctica. *Marine Geology*, 422, 106091. <https://doi.org/10.1016/j.margeo.2019.106091>

- Prothro, L. O., Simkins, L. M., Majewski, W., & Anderson, J. B. (2018). Glacial retreat patterns and processes determined from integrated sedimentology and geomorphology records. *Marine Geology*, 395, 104–119. <https://doi.org/10.1016/j.margeo.2017.09.012>
- Pudsey, C. J. (2000). Sedimentation on the continental rise west of the Antarctic Peninsula over the last three glacial cycles. *Marine Geology*, 167(3–4), 313–338. [https://doi.org/10.1016/S0025-3227\(00\)00039-6](https://doi.org/10.1016/S0025-3227(00)00039-6)
- Rignot, E., Mouginot, J., & Scheuchl, B. (2011). Ice flow of the antarctic ice sheet. *Science*, 333(6048), 1427–1430. <https://doi.org/10.1126/science.1208336>
- Rignot, E., Mouginot, J., Scheuchl, B., van den Broeke, M., van Wessem, M. J., & Morlighem, M. (2019). Four decades of Antarctic ice sheet mass balance from 1979–2017. In *Proceedings of the National Academy of Sciences of the United States of America* (Vol. 116, Issue 4, pp. 1095–1103). National Academy of Sciences. <https://doi.org/10.1073/pnas.1812883116>
- Roy, M., van de Flierdt, T., Hemming, S. R., & Goldstein, S. L. (2007).  $^{40}\text{Ar}/^{39}\text{Ar}$  ages of hornblende grains and bulk Sm/Nd isotopes of circum-Antarctic glacio-marine sediments: Implications for sediment provenance in the southern ocean. *Chemical Geology*, 244(3–4), 507–519. <https://doi.org/10.1016/j.chemgeo.2007.07.017>
- Rubatto, D. (2017). Zircon: The Metamorphic Mineral. *Reviews in Mineralogy and Geochemistry*, 83(1), 261–295. <https://doi.org/10.2138/rmg.2017.83.9>
- Schmitz, M. D., & Bowring, S. A. (2001). U-Pb zircon and titanite systematics of the Fish Canyon Tuff: An assessment of high-precision U-Pb geochronology and its application to young volcanic rocks. *Geochimica et Cosmochimica Acta*, 65(15), 2571–2587. [https://doi.org/10.1016/S0016-7037\(01\)00616-0](https://doi.org/10.1016/S0016-7037(01)00616-0)
- Schoene, B., & Bowring, S. A. (2006). U-Pb systematics of the McClure Mountain syenite: Thermochronological constraints on the age of the  $^{40}\text{Ar}/^{39}\text{Ar}$  standard MMhb. *Contributions to Mineralogy and Petrology*, 151(5), 615–630. <https://doi.org/10.1007/s00410-006-0077-4>
- Shao, T., Xia, Y., Ding, X., Cai, Y., & Song, M. (2019). Zircon saturation in terrestrial basaltic melts and its geological implications. *Solid Earth Sciences*, 4(1), 27–42. <https://doi.org/10.1016/j.sesci.2018.08.001>
- Sláma, J., Košler, J., Condon, D. J., Crowley, J. L., Gerdes, A., Hanchar, J. M., Horstwood, M. S. A., Morris, G. A., Nasdala, L., Norberg, N., Schaltegger, U., Schoene, B., Tubrett, M. N., & Whitehouse, M. J. (2008). Plešovice zircon - A new natural reference material for U-Pb and Hf isotopic microanalysis. *Chemical Geology*, 249(1–2), 1–35. <https://doi.org/10.1016/j.chemgeo.2007.11.005>

- Spaggiari, C. V., Kirkland, C. L., Smithies, R. H., Wingate, M. T. D., & Belousova, E. A. (2015). Transformation of an Archean craton margin during Proterozoic basin formation and magmatism: The Albany-Fraser Orogen, Western Australia. *Precambrian Research*, 266, 440–466. <https://doi.org/10.1016/j.precamres.2015.05.036>
- Spaggiari, C. V., & Smithies, R. H. (2015). *Eucla Basement Stratigraphic Drilling Results Release Workshop: Extended Abstracts*.
- Spaggiari, C. v., Smithies, R. H., Kirkland, C. L., Wingate, M. T. D., England, R. N., & Lu, Y. J. (2018). Buried but preserved: The Proterozoic Arubiddy Ophiolite, Madura Province, Western Australia. *Precambrian Research*, 317, 137–158. <https://doi.org/10.1016/j.precamres.2018.08.025>
- Stacey, J. S., & Kramers, J. D. (1975). Approximation of terrestrial lead isotope evolution by a two-stage model. *Earth and Planetary Science Letters*, 26(2), 207–221. [https://doi.org/10.1016/0012-821X\(75\)90088-6](https://doi.org/10.1016/0012-821X(75)90088-6)
- Sun, S. S., & McDonough, W. F. (1989). Chemical and isotopic systematics of oceanic basalts: Implications for mantle composition and processes. *Geological Society Special Publication*, 42(1), 313–345. <https://doi.org/10.1144/GSL.SP.1989.042.01.19>
- Thompson, J. M., Meffre, S., & Danyushevsky, L. (2018). Impact of air, laser pulse width and fluence on U-Pb dating of zircons by LA-ICPMS. *Journal of Analytical Atomic Spectrometry*, 33(2), 221–230. <https://doi.org/10.1039/c7ja00357a>
- Thompson, J., Meffre, S., Maas, R., Kamenetsky, V., Kamenetsky, M., Goemann, K., Ehrig, K., & Danyushevsky, L. (2016). Matrix effects in Pb/U measurements during LA-ICP-MS analysis of the mineral apatite. *Journal of Analytical Atomic Spectrometry*, 31(6), 1206–1215. <https://doi.org/10.1039/c6ja00048g>
- Tooze, S., Halpin, J. A., Chase, Z., Armand, L. K., O'Brien, P. E., & Noble, T. L. (2019). *Scratching the surface: a new marine sediment provenance record from the continental slope of central Wilkes Land, East Antarctica*. PANGAEA. <https://doi.org/10.1594/PANGAEA.907799>
- Tucker, N. M., Payne, J. L., Clark, C., Hand, M., Taylor, R. J. M., Kylander-Clark, A. R. C., & Martin, L. (2017). Proterozoic reworking of Archean (Yilgarn) basement in the Bunger Hills, East Antarctica. *Precambrian Research*, 298, 16–38. <https://doi.org/10.1016/j.precamres.2017.05.013>

- Veevers, J. J. (2012). Reconstructions before rifting and drifting reveal the geological connections between Antarctica and its conjugates in Gondwanaland. In *Earth-Science Reviews* (Vol. 111, Issues 3–4, pp. 249–318). <https://doi.org/10.1016/j.earscirev.2011.11.009>
- Veevers, J. J., & Saeed, A. (2011). Age and composition of Antarctic bedrock reflected by detrital zircons, erratics, and recycled microfossils in the Prydz Bay-Wilkes Land-Ross Sea-Marie Byrd Land sector (70°-240°E). *Gondwana Research*, 20(4), 710–738. <https://doi.org/10.1016/j.gr.2011.03.007>
- Vermeesch, P. (2018). IsoplotR: A free and open toolbox for geochronology. *Geoscience Frontiers*, 9(5), 1479–1493. <https://doi.org/10.1016/j.gsf.2018.04.001>
- Weber, M. E., Clark, P. U., Kuhn, G., Timmermann, A., Spreng, D., Gladstone, R., Zhang, X., Lohmann, G., Menviel, L., Chikamoto, M. O., Friedrich, T., & Ohlwein, C. (2014). Millennial-scale variability in Antarctic ice-sheet discharge during the last deglaciation. *Nature*, 510(7503), 134–138. <https://doi.org/10.1038/nature13397>
- Williams, S. E., Whittaker, J. M., Halpin, J. A., & Müller, R. D. (2019). Australian-Antarctic breakup and seafloor spreading: Balancing geological and geophysical constraints. In *Earth-Science Reviews* (Vol. 188, pp. 41–58). Elsevier B.V. <https://doi.org/10.1016/j.earscirev.2018.10.011>
- Williams, T., van de Flierdt, T., Hemming, S. R., Chung, E., Roy, M., & Goldstein, S. L. (2010). Evidence for iceberg armadas from East Antarctica in the Southern Ocean during the late Miocene and early Pliocene. *Earth and Planetary Science Letters*, 290(3–4), 351–361. <https://doi.org/10.1016/j.epsl.2009.12.031>
- Wilson, D. J., Bertram, R. A., Needham, E. F., van de Flierdt, T., Welsh, K. J., McKay, R. M., Mazumder, A., Riesselman, C. R., Jimenez-Espejo, F. J., & Escutia, C. (2018). Ice loss from the East Antarctic Ice Sheet during late Pleistocene interglacials. In *Nature* (Vol. 561, Issue 7723, pp. 383–386). Nature Publishing Group. <https://doi.org/10.1038/s41586-018-0501-8>
- Wingate, M. T. D., Kirkland, C. L., Smithies, R. H. (2015). U-Pb geochronology of the Forrest Zone of the Coompana Province. *Eucla Basement Stratigraphic Drilling Results Release Workshop: Extended Abstracts Compiled by C. V. Spaggiari and R. H. Smithies: Geological Survey of Western Australia Record 2015/10*, 37–40.
- Wingate, M. T. D., Kirkland, C. L., Spaggiari, C. V., Smithies, R. H. (2015). U-Pb geochronology of the Madura Province. *Eucla Basement Stratigraphic Drilling Results Release Workshop: Extended Abstracts Compiled by C. V. Spaggiari and R. H. Smithies: Geological Survey of Western Australia Record 2015/10*, 14–16.

Young, D. A., Wright, A. P., Roberts, J. L., Warner, R. C., Young, N. W., Greenbaum, J. S., Schroeder, D. M., Holt, J. W., Sugden, D. E., Blankenship, D. D., van Ommen, T. D., & Siegert, M. J. (2011). A dynamic early East Antarctic Ice Sheet suggested by ice-covered fjord landscapes. *Nature*, *474*(7349), 72–75.  
<https://doi.org/10.1038/nature10114>

## Chapter 4

# Exhibit A: Nd-Sr isotopic fingerprint of marine sediments offshore central Wilkes Land, East Antarctica

### Abstract

In central Wilkes Land, East Antarctica, multiple records suggest that the ice sheet retreated approximately 150 km since the termination of the Last Glacial Period. Sedimentation on the continental rise adjacent to the major Totten Glacier system records this change. Recent multi-proxy single-grain sediment provenance analysis of sediment from the continental rise (from the study of Tooze et al. (2020)) pointed to distributed sources of terrigenous detritus and suggested that material supplied from the Totten Glacier may have only been dominant during the early stages of deglaciation. In this study, we report detrital Nd and Sr isotopic signatures from the bulk and fine (< 63  $\mu\text{m}$ ) grain size fractions of detrital sediment from four cores collected along the continental rise of central Wilkes Land. These data reveal a spatially consistent Nd-isotopic signature offshore central Wilkes Land with  $\epsilon_{\text{Nd}}$  values ranging between -14.9 and -12.8. Comparison of detrital  $\epsilon_{\text{Nd}}$  signatures with available whole-rock  $\epsilon_{\text{Nd}}$  signatures from southern Australia and at the coast of central Wilkes Land suggests that Mesoproterozoic (c. 1415-1390 Ma) mafic rocks of the Antarctic Nuyina Province must have contributed to the mixed detrital  $\epsilon_{\text{Nd}}$  signature. This new finding suggests that the Totten Glacier had a major control over the supply of detritus to the continental margin from the onset of deglaciation (c. 22-19 ka) to present. The Sr-isotopic composition of fine sediment (with  $^{87}\text{Sr}/^{86}\text{Sr}$  ratios ranging between 0.72800 and 0.74257) may have been affected by grain size sorting, although an influence of changing sediment provenance cannot be ruled out given the paucity of available whole-rock Sr-isotopic end members.

## 4.1. Introduction

The provenance and geochemical fingerprint of detrital marine sediment proximal to the East Antarctic coastline can provide evidence for subglacial basement rock compositions, source-to-sink sediment transport and paleoenvironmental processes, providing insight into the complex history of the East Antarctic Ice Sheet (e.g., Cook et al., 2017; Licht and Hemming, 2017; Pierce et al., 2014). Marine sediment provenance analysis is particularly beneficial where there is poor basement rock exposure and the subglacial rock types are unknown. Such is the case in central Wilkes Land (between 105-128°E; Fig. 4.1), East Antarctica, where the basement rock terranes are concealed beneath thick ice (Fretwell et al., 2013) and coastal outcrop is exceptionally rare.

Several marine sediment core studies from around the East Antarctic margin have employed single-grain provenance techniques (Cook et al., 2014; Pierce et al., 2014; Tooze et al., 2020; Williams et al., 2010), whilst others have applied bulk neodymium (Nd) and strontium (Sr) isotopic analysis (Bertram et al., 2018; Cook et al., 2013; Hemming et al., 2007; van de Flierdt et al., 2007; Wilson et al., 2018). In the last two decades, the benefits of combining multiple provenance tools have become more widely recognised, leading to some East Antarctic studies incorporating both approaches (Cook et al., 2017; Pierce et al., 2017, 2011; Roy et al., 2007). Single-grain techniques provide detailed information on the rock that the grain was derived from, including its age and composition, whereas bulk isotopes provide a combined geochemical signal of erosion in the source region(s). Combining single-grain and bulk isotope techniques in sediment provenance studies can help eliminate bias introduced by using one single technique. For example, U-Pb dating is typically conducted on detrital zircon grains in marine sediments, biasing the record in favour of felsic rock compositions, as zircons are undersaturated in mafic rock types (Licht and Hemming, 2017; Shao et al., 2019). Moreover, one technique may be able to tell us something about the sediment provenance that the other cannot. For example, unique isotopic signatures may reveal the source of abundant detrital grains derived from rocks of the same age. Alternatively, the results from single-grain analysis may help unravel bulk detrital Nd-Sr isotopic signatures.

In Chapter 3, multi-proxy single-grain sediment provenance analysis from a Kasten core (KC14) recovered from the continental rise of central Wilkes Land supported previous interpretations of the subglacial geology based on airborne geophysical data (Aitken et al., 2014; Maritati et al., 2019) and limited studies of rare coastal outcrop (Maritati et al., 2019; Morrissey et al., 2017; Tucker et al., 2017; Zhang et al., 2012). The study presented a case for a broad sediment provenance with detritus derived from multiple sources along the Budd, Sabrina and Banzare coasts of central Wilkes Land (Fig. 4.1). Subtle temporal variation in the contributions from each province was linked to variation in climate and ice sheet configuration over the Last Glacial Period-Holocene transition. Though the study provided valuable insights into the basement rock compositions and the source-to-sink sediment transport history, there are two main outstanding questions pertaining to the regional ice sheet history:

### **1. Does the Totten Glacier play an important role in the supply of detritus to the margin?**

Based on airborne geophysical data and the geochemical composition and U-Pb age of rare rock outcrop at Chick Island (Aitken et al., 2014; Maritati et al., 2019), the Nuyina Province is interpreted to lie beneath the Totten and Moscow University glaciers, the two largest glaciers in central Wilkes Land (Fig. 4.1). Previous studies propose that the Totten Glacier has a strong influence over sedimentation on the continental slope and rise (Donda et al., 2020; Holder et al., 2020; O'Brien et al., 2020; Post et al., 2020), implying that Nuyina Province should undergo significant erosion in the coastal region of the Totten catchment. However, as shown in Chapter 3, only a minor proportion of detrital zircon from KC14 had a U-Pb age corresponding to rocks of the Haig Cave Supersuite (c. 1415-1390 Ma) that have an age signature uniquely associated with the Nuyina Province. Several scenarios to explain the lack of Nuyina detritus at KC14 were considered in Chapter 3. These are:

- 1) Nuyina Province does not exist or is not as extensive as interpreted from the geophysical data.

- 2) Mafic source rocks that dominate the Haig Cave Supersuite (c. 1415-1390 Ma) were underrepresented in the U-Pb geochronology from KC14 due to the primary analysis of zircons, which are rare in mafic rocks.
- 3) Detrital sediment in KC14 was sourced from a broad region of the central Wilkes Land coast, with differing contributions from each of the Wilkes, Nuyina and Banzare provinces over the Last Glacial Period-Holocene transition.

The last scenario was deemed the most probable and was supported by subtle temporal variation in the U-Pb record in KC14 (Tooze et al., 2020). More prominent c. 1415-1390 Ma detrital zircon ages in the middle (deglacial) section of the core indicated erosion of rocks predominantly from the Nuyina Province that underlies much of the Totten Glacier catchment at the coast. This observation was suggested to reflect an expanded ice sheet with the proximal Totten Glacier dominating the supply of detritus. Ongoing glacial retreat then saw a broader provenance signal from other sources along the coastline.

## **2. Is there variability in the sediment provenance signature across the slope?**

Only one core (KC14) was studied in Chapter 3. Sediment provenance analysis of multiple cores from the continental rise will reveal any spatial variation in the sediment provenance and source-to-sink sediment transport associated with basement rock erosion at the coast.

In this study, we report downcore Nd and Sr-isotopic signatures from four cores transecting the upper continental rise of the Sabrina Coast, central Wilkes Land (Fig. 4.1). Combining this sediment provenance information with data from single-grain provenance analysis of KC14, we aim to resolve outstanding questions from Chapter 3 and uncover more about the history of the ice sheet in this important region of East

Antarctica. Using our data and existing whole-rock Nd-isotopic signatures from southern Australia and East Antarctica, we will test the following hypotheses:

- 1) The Totten Glacier played a major role in supplying detritus to the continental margin from the onset of deglaciation (c. 22-19 ka) to present.
- 2) Source-to-sink sediment transport is spatially consistent across the continental rise.

To test these hypotheses, we specifically seek evidence for: the erosion of rocks of the Nuyina Province in the Totten catchment, and any spatial and temporal variation in sediment provenance associated with the response of the ice sheet to a warming climate over the Last Glacial Period-Holocene transition.

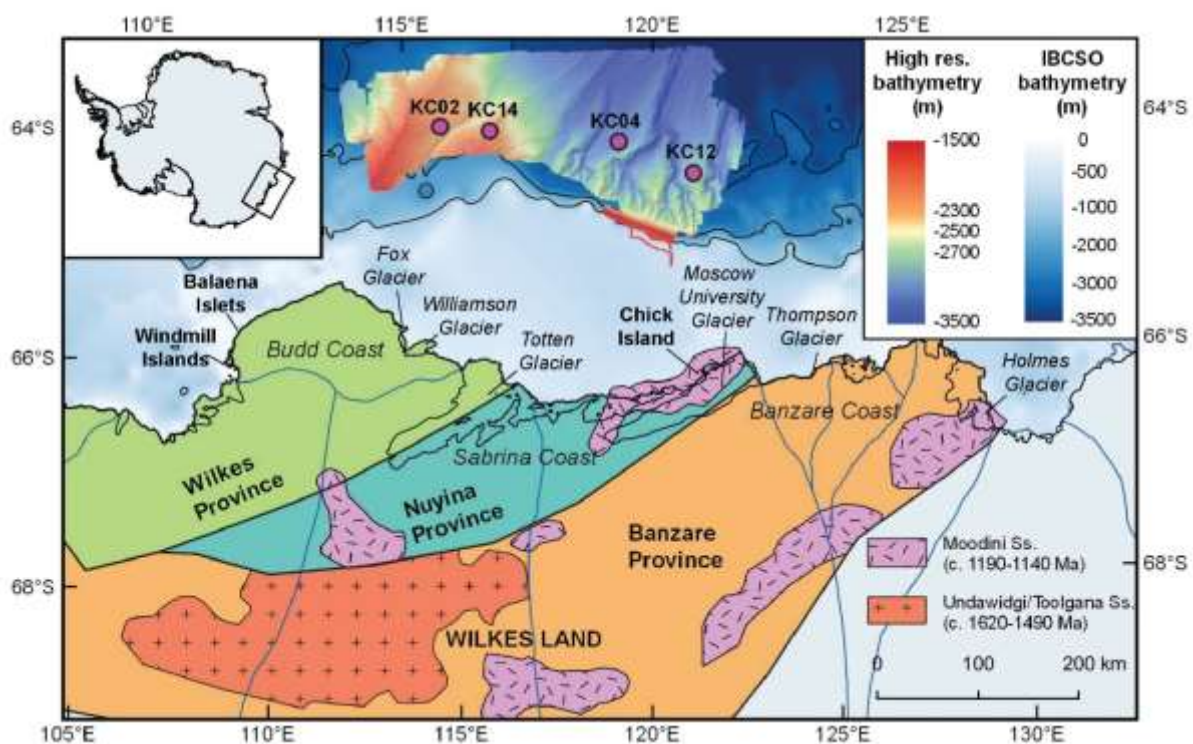


**Figure 4.1. Central Wilkes Land.** Map of central Wilkes Land, East Antarctica with core locations for this study (pink). Basement rock provinces (the Wilkes, Nuyina and Banzare provinces) and igneous plutons (Moodini, Undawidgi and Toolgana supersuites) are interpreted from airborne geophysical data (Aitken et al., 2014; Maritati et al., 2019) and rare

rock outcrop sampled at Chick Island (Maritati et al., 2019). Ice drainage divides (Mouginot et al., 2017) are shown as blue lines. Bathymetry and 1000 m contours are shown using the International Bathymetric Chart of the Southern Ocean (IBCSO), version 1.0 (Arndt et al., 2013). High resolution bathymetry of the continental slope was acquired from *RV Investigator* (voyage IN2017\_V01) (Armand et al., 2018). Inset shows study location (black box) on a map of Antarctica.

## **4.2. Background: existing Nd-isotopic signatures in southern Australia and central Wilkes Land**

At the southern Australian margin that was adjoined to central Wilkes Land during past supercontinents (~116-130°E), analysis of boreholes (white circles, Fig. 4.2a) and rare outcrop (black stars, Fig. 4.2a) from the Albany-Fraser Orogen, Madura Province and Coompana Province have allowed geological and geochemical characterisation of the rocks that are otherwise shrouded by regolith. Equivalents of the Albany-Fraser Orogen, Madura Province and Coompana Province are interpreted to exist beneath the ice in central Wilkes Land, as the Wilkes, Nuyina and Banzare provinces, respectively, based on the following evidence:

- 1) Complementing geophysical signatures across both margins (Aitken et al., 2014; Maritati et al., 2019).
- 2) Rare rock outcrop from Balaena Islets, Bunger Hills and the Windmill Islands in central Wilkes Land with U-Pb zircon geochronology, feldspar Pb-Pb compositions and geochemical compositions matching rocks of the Albany-Fraser Orogen in southern Australia (Black et al., 1992b; Clark et al., 2000; Fitzsimons, 2003; Möller et al., 2002; Morrissey et al., 2017; Mulder et al., 2019; Sheraton et al., 1990, 1992, 1995; Tooze et al., 2020; Tucker et al., 2017; Zhang et al., 2012).

- 3) Rare rock outcrop from Chick Island in central Wilkes Land with U-Pb zircon ages, feldspar Pb-Pb compositions and geochemical properties corresponding to rocks of the Moodini Supersuite that intrude the Madura and Coompana provinces in southern Australia (Maritati et al., 2019; Tooze et al., 2020).
- 4) Detrital zircon, apatite and titanite grains from KC14 with Mesoproterozoic U-Pb ages representative of rocks from all three of the basement rock provinces in southern Australia (Tooze et al., 2020).

Whole-rock Nd and Sr-isotopic analyses from the Albany-Fraser Orogen, the Madura Province and the Coompana Province in southern Australia should therefore be representative of those from the respective Wilkes, Nuyina and Banzare provinces in central Wilkes Land. Due to the lack of whole-rock Sr-isotopic analyses from both continental margins, available Nd-isotopic analyses (expressed as  $\epsilon_{Nd}$ , which is the deviation between the measured  $^{143}Nd/^{144}Nd$  in a sample and the  $^{143}Nd/^{144}Nd$  composition of bulk Earth, (Jacobsen and Wasserburg, 1980)) will be used to establish source rock end members for the Wilkes, Nuyina and Banzare provinces in central Wilkes Land.

### **4.2.1. Whole-rock $\epsilon_{Nd}$ signatures**

Based on previous work on the Mesoproterozoic basement provinces of Southern Australia and the shared Proterozoic evolution with their Antarctic counterparts (Maritati et al., 2019), a broad compositional range of igneous-metamorphic basement complexes can be expected in central Wilkes Land. Here we describe the rocks in each province and their Nd-isotopic character.

The Albany-Fraser Orogen largely comprises of reworked Archean and Paleoproterozoic crust of the Yilgarn Craton and therefore likely contains remnants of older crustal components (Kirkland et al., 2017, 2011). The geology of the Albany-Fraser Orogen is progressively more juvenile with distance from the craton margin

(in an eastward direction) and is divided into complexes (Myers, 1993). The two largest complexes are the Biranup Complex and the Nornalup Complex. The Biranup Complex is adjacent to the Yilgarn Craton and consists predominantly of Archean (c. 2700-2600 Ma) and Proterozoic (c. 1700-1600 Ma and c. 1300 Ma) orthogneisses and regionally-metamorphosed granitoid rocks (Myers, 1993; Nelson et al., 1995). Rare rocky outcrops at the Bunger Hills (Fig. 4.3) in western Wilkes Land consist largely of orthogneisses with Archean and Paleoproterozoic U-Pb crystallisation ages (Tucker et al., 2017). These rocks are interpreted to be equivalent to those of the Biranup Complex in the Albany-Fraser Orogen (Tucker et al., 2017). The Nornalup Complex is the easternmost part of the Albany-Fraser Orogen and is broadly characterised by regionally metamorphosed rocks intruded by juvenile felsic magmas of the Recherche (c. 1300-1290 Ma, Nelson et al., 1995) and Esperance (c. 1200-1140 Ma, Nelson et al., 1995) supersuites. The mixture of older Archean-Paleoproterozoic inclusions with the younger felsic intrusions explains the broad spread of  $\epsilon_{Nd}$  values (-29 to -14; Fig. 4.2b) measured in the Nornalup Complex (Black et al., 1992a; Kirkland et al., 2015; Nelson et al., 1995) and the conjugate Wilkes Province at the Windmill Islands in central Wilkes Land, East Antarctica (Möller et al., 2002; Zhang et al., 2012).

The Madura Province is dominated by juvenile rocks associated with the formation of oceanic crust (Spaggiari et al., 2018). The mafic rocks of the Haig Cave Supersuite (c. 1415-1390 Ma, Kirkland et al., 2015, 2017; Spaggiari et al., 2018) of the Madura Province have a primitive isotopic character, with most  $\epsilon_{Nd}$  values considerably more radiogenic (range: -7.9 to +8.9; Kirkland et al., 2015; Spaggiari et al., 2018) than those of the Albany-Fraser/Wilkes (range: -29.9 to -13.6; Black et al., 1992a; Kirkland et al., 2015; Nelson et al., 1995; Zhang et al., 2012) and Coompana (range: -20.6 to -12.4; Kirkland et al., 2017) provinces (Fig. 4.2b). Widespread felsic intrusions of the Moodini Supersuite (c. 1190-1125 Ma; Kirkland et al., 2017) within the Madura Province have a less radiogenic  $\epsilon_{Nd}$  range (-14 to -11; Fig. 4.2b; Kirkland et al., 2015) than the rocks they intrude. The Coompana Province comprises of felsic plutonic rocks of the Toolgana (c. 1610 Ma; Kirkland et al., 2017) and Undawidgi (c. 1490 Ma; Kirkland et al., 2017) supersuites and abundant intermediate-felsic intrusive rocks of the Moodini Supersuite, all of which have similar  $\epsilon_{Nd}$  ranges (Fig.

4.2b; Toolgana Supersuite: -19.3 to -12.4, Undawidgi Supersuite: -19.4 to -13.2, Moodini Supersuite: -20.6 to -12.4; Kirkland et al., 2017).

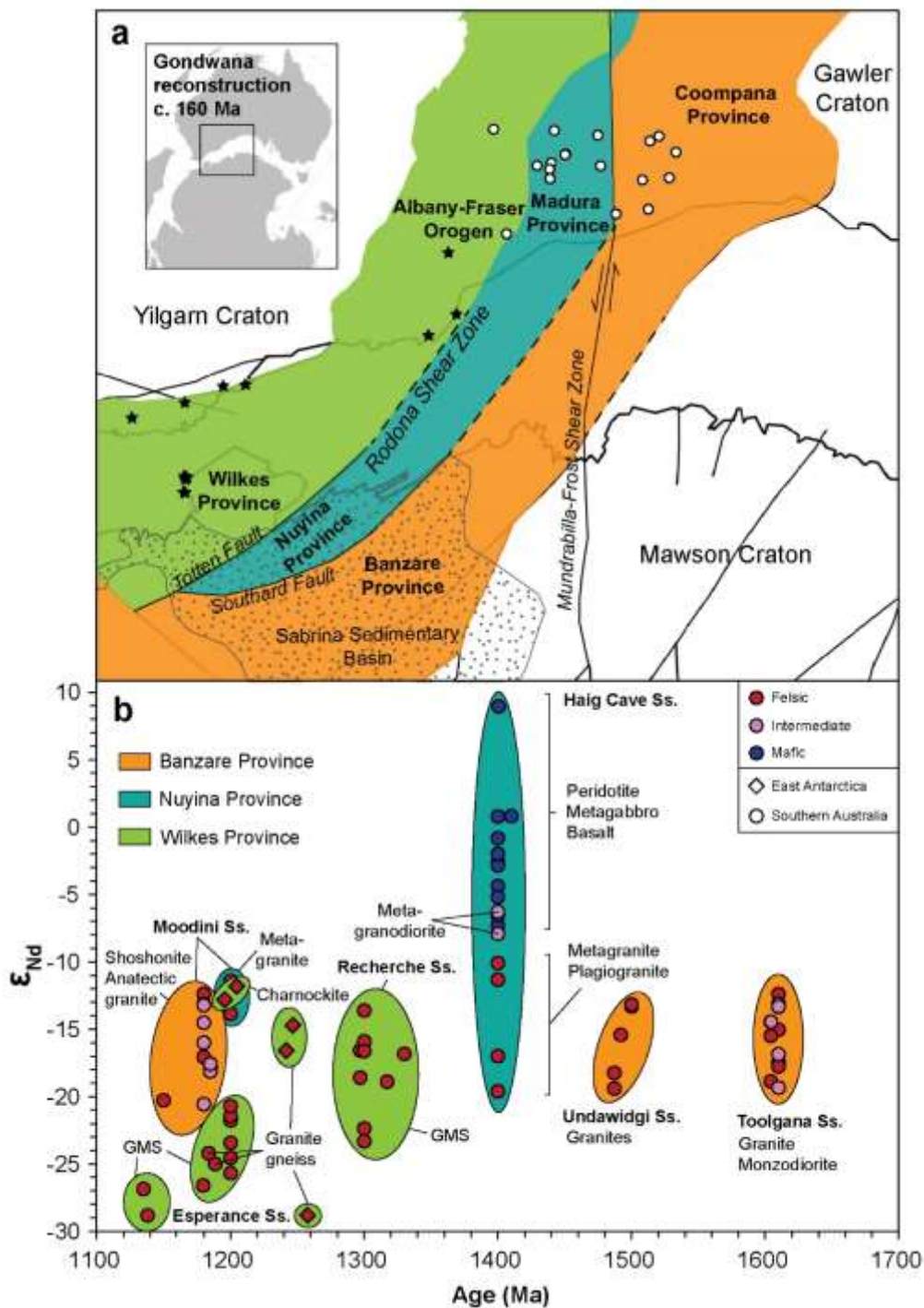


**Figure 4.2. Whole-rock  $\epsilon_{Nd}$  signatures from southern Australia and East Antarctica. (a)** Map showing the margins of southern Australia and central Wilkes Land, East Antarctica in a full-fit Gondwana reconstruction (c. 160 Ma) with Antarctica fixed in its present-day reference frame (Matthews et al., 2016). Geological provinces in southern Australia and conjugate

regions of East Antarctica are shown using the most recent interpretation of Maritati et al. (2019). Fault positions are after Aitken et al. (2014) and Maritati et al. (2019). The locations of boreholes in southern Australia and rare rock outcrop from both margins from which whole-rock  $\epsilon_{Nd}$  signatures were obtained (Kirkland et al., 2015, 2017; Spaggiari et al., 2018) are shown as white circles and black stars, respectively. **(b)** Whole-rock  $\epsilon_{Nd}$  signatures plotted against U-Pb primary zircon ages from rocks recovered from boreholes (Kirkland et al., 2015, 2017; Spaggiari et al., 2018) and rare outcrop from the Albany-Fraser Orogen/Wilkes Province (Black et al., 1992a, 1992b; Nelson et al., 1995; Zhang et al., 2012). Although most of the  $\epsilon_{Nd}$  values were obtained from rocks samples from southern Australia, basement rock provinces are referred to in the figure by their Antarctic equivalent names for simplicity.

## 4.2.2. Detrital $\epsilon_{Nd}$ signatures offshore central Wilkes Land

Detritus eroded from the Antarctic continent is transported to the ocean via gravity flows, glacial meltwater fluxes and by ice-rafting (Cook et al., 2017; Huang et al., 2021; Licht and Hemming, 2017, and references therein). Once deposited in the ocean, finer (<63  $\mu\text{m}$ ) detritus can be redistributed by currents. Contributions of detritus from multiple different source rock terranes eroded from within the same glacial catchment result in an integrated offshore Nd-isotopic signal. Sparse analyses from fine detrital core-top sediments offshore central Wilkes Land reveal an integrated  $\epsilon_{Nd}$  signature between -14.9 and -12.3 (Pierce et al., 2011; Roy et al., 2007; van de Flierdt et al., 2007; Fig. 4.3). However, only three out of five analyses are from south of the east-flowing Antarctic Circumpolar Current, and only one (with a  $\epsilon_{Nd}$  value of -12.3, Roy et al., 2007) from the continental rise proximal to the coastline where the Wilkes, Nuyina and Banzare provinces are interpreted (Fig. 4.3). Moreover, all the available detrital  $\epsilon_{Nd}$  signatures are from core top (Holocene) sediment and do not record temporal change in sediment provenance.

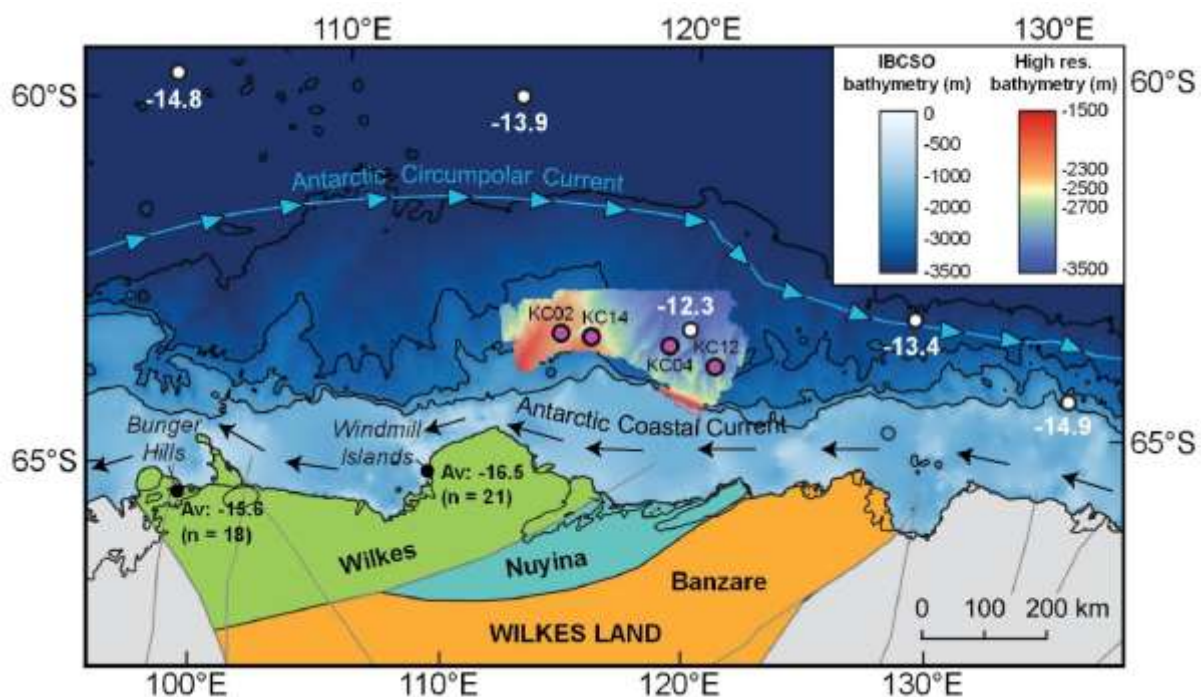


**Figure 4.3. Whole-rock and detrital  $\epsilon_{Nd}$  signatures from central Wilkes Land.** Map showing sparse detrital  $\epsilon_{Nd}$  signatures from core top sediments offshore central Wilkes Land (Pierce et al., 2011; Roy et al., 2007; van de Flierdt et al., 2007) and whole rock  $\epsilon_{Nd}$  signatures from rare outcrop at Bunge Hills (Black et al., 1992b; Sheraton et al., 1990) and the Windmill Islands (Möller et al., 2002; Zhang et al., 2012). Data sources for basement rock provinces, bathymetry and oceanography are as per Figure 4.1.

## 4.3. Methods

### 4.3.1. Core locations

The following four Kasten cores from the upper continental rise adjacent to central Wilkes Land, East Antarctica were studied: KC02, KC14, KC04 and KC12 (Fig. 4.1).

### 4.3.2. Sediment sampling

Marine sediment was sampled for Nd and Sr isotopic analysis in 2 cm slices along each core at intervals corresponding to major peaks and lows in BiSi concentration (see Chapter 2). Approximately 2 g of each sample was wet-sieved to isolate the fine (< 63  $\mu\text{m}$ ) fraction. Additionally, bulk sediment (~ 2 g) from KC02 (n= 4) and KC04 (n

= 4) was sampled for comparison of the Nd and Sr isotopic ratios between the two grain size fractions. To assess reproducibility and sample uniformity, two procedural replicates from KC14 (at 108-110 cm depth) and two samples of the rock Standard Reference Material BCR-2g were prepared for Nd and Sr isotopic analysis.

### **4.3.3. Reductive leaching and sediment digestion**

Separation of the detrital and authigenic fractions was achieved by leaching the sediment in a reductive solution comprising 0.02 M hydroxylamine hydrochloride and 25% acetic acid (Chester and Hughes, 1967). Each bulk sediment sample (~ 2 g) was first leached for one hour on a rotisserie wheel and then for a second time overnight (~16hr), before being washed in Milli-Q water three times. Samples were dried and ground to a fine powder, and  $100 \pm 5$  mg was weighed for subsequent analysis. A multi-stage acid digestion process was carried out to fully dissolve the sediment matrix of each sample. The sediment was first oxidised by adding 2 mL 30% hydrogen peroxide and 2 mL distilled nitric acid ( $\text{HNO}_3$ ) to each of the samples. The first sediment digestion was carried out using 4 mL distilled hydrochloric acid (HCl), 10 mL distilled  $\text{HNO}_3$  and 2 mL Seastar™ hydrofluoric acid. A second digestion used 2 mL distilled  $\text{HNO}_3$  and 2 mL Baseline® Seastar™ perchloric acid.

### **4.3.4. Extraction chromatography for REE isolation**

The REE fraction was separated from the main-group elements (e.g., Sr, Rb, Ba, Al) and transition metals (e.g., Fe), using cation-exchange column chromatography. Biorad™ AG50W-X8 resin was first homogenised and then cleaned by rinsing with several rounds of 6M HCl. Twelve BioRad™ Polyprep® columns were prepared with 1.6 mL of the pre-cleaned Biorad™ AG50W-X8 resin. To condition the resin, 2.5 mL 1M HCl was added. The samples were dried, converted to hydrochloric form and then loaded into individual columns. To remove the matrix (e.g., Fe, Ba) and collect the Sr fraction, two rounds of 0.5 mL 1M HCl were added, followed by three rounds of 2.5 mL 3M HCl and one round of 0.2 mL 6M HCl. After the matrix was removed, the REEs in each sample were eluted with two rounds of 3.5 mL 6M HCl. The resin was reused between samples and cleaned

with two rounds of 5 mL 6M HCl, followed by two rounds of 2 mL Milli-Q Water (MQ), two rounds of 5 mL 3 M HNO<sub>3</sub>, and two final rounds of 2 mL MQ.

### **4.3.5. Lanthanide extraction chromatography for Nd isolation**

The samples were dried down to a small droplet, converted to hydrochloric form and loaded into individual columns containing 0.8 mL of Eichrom® Lnspec™ resin. To remove the light REEs (in particular, Ce and Pr), 9 mL of 0.231 M HCl was first added to each of the columns. Once the acid had completely dripped through each column, specific quantities of 0.231 M HCl were added to each individual column, based on its unique elution profile, to isolate the Nd and remove signal-interfering REEs. The entire Nd extraction process was performed on a total of 51 samples ( $n_{\text{bulk}} = 8$ ,  $n_{\text{fine}} = 43$ ), two procedural replicates, and two samples of the rock Standard Reference Material (BCR-2), with ten samples processed during each column run. Three blanks processed alongside detrital sediment digestion and Nd-isotope column chemistry in the laboratory produced Nd concentrations of 0.045 ppb, 0.024 ppb and 0.008 ppb, respectively.

### **4.3.6. Extraction chromatography for Sr isolation**

The Sr in each sample was isolated following a method modified from Charlier et al. (2006). Eichrom® Sr-spec resin was first cleaned with several rounds of 1M sulphuric acid (H<sub>2</sub>SO<sub>4</sub>), 6M HCl, and 0.05 M HNO<sub>3</sub>. The Sr fraction from the REE extraction method was then dried down and converted to nitrate form by adding 0.1 mL of 9M HNO<sub>3</sub>. Eleven micro-columns were prepared using 0.315 mL of the pre-cleaned resin, which was subsequently conditioned with two rounds of 1 mL 9M HNO<sub>3</sub>. To remove the matrix from each sample, 0.05 mL, 0.1 mL, 0.2 mL and two rounds of 1 mL of 9M HNO<sub>3</sub> was added successively to each column. To begin Sr elution, 0.2 mL 0.05 M HNO<sub>3</sub> was added to each of the columns. The Sr was then eluted from each sample with three successive rounds of 1 mL 0.05M HNO<sub>3</sub>. The samples were then dried and redissolved in 1mL 2% HNO<sub>3</sub>. A volume-specific aliquot of each sample was taken, containing 300 ng of Sr (calculated from the Sr

concentration measured during a test analysis at the Central Science Laboratory, University of Tasmania) and dried down for Sr-isotopic analysis.

Three procedural/column blanks (Blanks 1, 2 and 3) were run alongside the sediment samples during sediment digestion, and all the chromatographic techniques described above. Three more column blanks were processed during extraction chromatography for Sr isolation only (Blanks 4, 5 and 6). Blanks 3 and 6 were measured for their Sr-isotopic composition and blanks 1, 2, 4 and 5 were spiked with  $^{84}\text{Sr}$ . All blank levels measured less than 0.4 % of the 300 ng sample amount (Table 4.1).

Blank ID	$^{87}\text{Sr}/^{86}\text{Sr}$	2SD	n	Sr (pg)
Blank 1	n.d	n.d	n.d	566
Blank 2	n.d	n.d	n.d	1010
Blank 3	0.710449	0.000083	230	n.d
Blank 4	n.d	n.d	n.d	362
Blank 5	n.d	n.d	n.d	250
Blank 6	0.726857	0.000155	64	n.d

**Table 4.1. Blank levels for sample preparation and Sr extraction.** Blanks 1-3 represent contamination introduced during sediment digestion and two sets of chromatographic columns for REE and Sr extraction, respectively. Blanks 4-6 represent contamination introduced during Sr extraction chromatography only. The number of ratios measured (n) for the isotopic composition of Blanks 3 and 5 is shown. n.d – not determined.

### 4.3.7. Instrumental analysis and data processing

The Nd-isotopic composition of each sample was measured at the Australian National University in Canberra, on a ThermoFisher Neptune Multi Collector ICP-MS. Processing of the Nd dataset followed the same procedure as Noble et al. (2013). Every set of four samples was standard-bracketed by the JNdi-1 Standard Reference Material and corrected to  $0.512115 \pm 0.000007$  (2SD), as reported by Tanaka et al. (2000). The average  $^{143}\text{Nd}/^{144}\text{Nd}$  ratio for JNdi-1 (100 ppb) for the full

analytical session was 0.512072, with an external reproducibility of 0.000009 (n = 76). The chondrite-normalised  $^{143}\text{Nd}/^{144}\text{Nd}$  composition of each sediment sample is given as  $\epsilon_{\text{Nd}}$ :

$$\epsilon_{\text{Nd}} = \left[ \left( \frac{^{143}\text{Nd}/^{144}\text{Nd}_{(\text{measured})}}{^{143}\text{Nd}/^{144}\text{Nd}_{(\text{CHUR})}} \right) - 1 \right] \times 10^{-4}$$

where the Nd-isotopic composition of the Chondritic Uniform Reservoir ( $^{143}\text{Nd}/^{144}\text{Nd}_{(\text{CHUR})} = 0.512638$  (Jacobsen and Wasserburg, 1980). All  $\epsilon_{\text{Nd}}$  values are reported with a 2SD error (in  $\epsilon_{\text{Nd}}$  units) that incorporates the internal and external errors of the measurement (n = 50 ratios). Triplicate analysis of KC14: 108-110 cm depth gave an average  $\epsilon_{\text{Nd}}$  value of  $-12.9 \pm 0.4$  (SD). The  $\epsilon_{\text{Nd}}$  value for each individual replicate sample fell within error of the others. The average  $^{143}\text{Nd}/^{144}\text{Nd}$  ratio for Standard Reference Material BCR-2 was  $0.512660 \pm 0.000007$ , which falls within error of the published United States Geological Survey (USGS) value ( $0.512633 \pm 0.000038$ ; Raczek et al., 2003).

The Sr-isotopic composition was measured on a Thermo-Finnigan Triton Thermal Ionisation Mass Spectrometer at the Victoria University of Wellington, New Zealand, using a similar instrumental setup as Charlier et al. (2006). For each sample, standard and procedural/column blank, approximately 240 ratios were measured with eight-second integrations and the peak centre measured every sixty ratios. To correct for instrumental mass fractionation, all  $^{87}\text{Sr}/^{86}\text{Sr}$  ratios were internally normalised to  $^{87}\text{Sr}/^{86}\text{Sr} = 0.1194$  and were corrected for Rb on  $^{87}\text{Sr}$  using the measured  $^{85}\text{Rb}$  on the axial multiplier. Nine measurements of the strontium carbonate Standard Reference Material NBS987 (300 ng) were taken during analysis. The average  $^{87}\text{Sr}/^{86}\text{Sr}$  for NBS987 for the full analytical session was 0.710262 with an external reproducibility of 0.000009 (2SD, n = 9). Standard-corrected  $^{87}\text{Sr}/^{86}\text{Sr}$  ratios were corrected for blank concentrations using the average of the Sr amounts in Blanks 1 and 2 and the isotopic composition for Blank 3. The blank-corrected  $^{87}\text{Sr}/^{86}\text{Sr}$  for BCR-2 was  $0.705004 \pm 0.000083$  (n = 1), which falls within error of the published USGS value ( $0.74958 \pm 0.000034$ ; Raczek et al., 2003). Triplicate analysis of KC14: 108-110 cm depth yielded an average  $^{87}\text{Sr}/^{86}\text{Sr}$  ratio of  $0.738812 \pm 0.000421$  (SD). The spread in the triplicate Sr-isotopic signature is

comparable to other studies from the East Antarctic margin (e.g., Bertram et al., 2018; Cook et al., 2013) and can be attributed to within-sample heterogeneity.

## 4.4. Results

### 4.4.1. Neodymium isotope composition

The  $\epsilon_{Nd}$  of the  $<63 \mu m$  detrital fraction at all core sites ranges between  $-14.9 \pm 0.17$  and  $-12.8 \pm 0.18$  (Fig. 4.4a; Supplementary Table 4.1). The Nd-isotopic signature is very similar between each core, indicating a spatially consistent signature across the continental rise (Fig. 4.4a). In the western cores, KC02 and KC14, some temporal variability in the detrital  $\epsilon_{Nd}$  signature is observed, with  $\epsilon_{Nd}$  values varying by a maximum of 2.1 and 1.5  $\epsilon_{Nd}$  units, respectively (Fig. 4.4b). In KC02, the lowest and highest  $\epsilon_{Nd}$  signatures are both recorded in the glacial section of the core (c. 21-19 ka, Fig. 4.4b). After c. 19 ka, the  $\epsilon_{Nd}$  values in KC02 were less variable. In KC14, less radiogenic  $\epsilon_{Nd}$  values (between -14.6 and -13.8) are observed during the glacial period (before c. 20 ka) than during the deglacial-Holocene period (between -14.1 and -13.1). No significant temporal variability is observed in the eastern cores, KC04 and KC12, where values vary by a maximum of 0.6 and 0.8  $\epsilon_{Nd}$  units, respectively (Fig. 4.4b).

The  $\epsilon_{Nd}$  of bulk sediment samples from KC02 and KC04 ranges between  $-13.0 \pm 0.08$  and  $-13.5 \pm 0.16$ , with averages of  $-13.2$  ( $n = 4$ ,  $SD = 0.17$ ) and  $-13.4$  ( $n = 4$ ,  $SD = 0.15$ ), respectively (Table 4.2, Fig. 4.4a). Where bulk samples were analysed from the same interval as the  $<63 \mu m$  fraction, the  $\epsilon_{Nd}$  value between the two fractions differed by 0.1 – 0.4  $\epsilon_{Nd}$  units, with only one bulk fraction analysis falling slightly out of the  $2\sigma$  error margin of the fine fraction sample from the same depth (KC02, 40-42 cm, Fig. 4.4a).

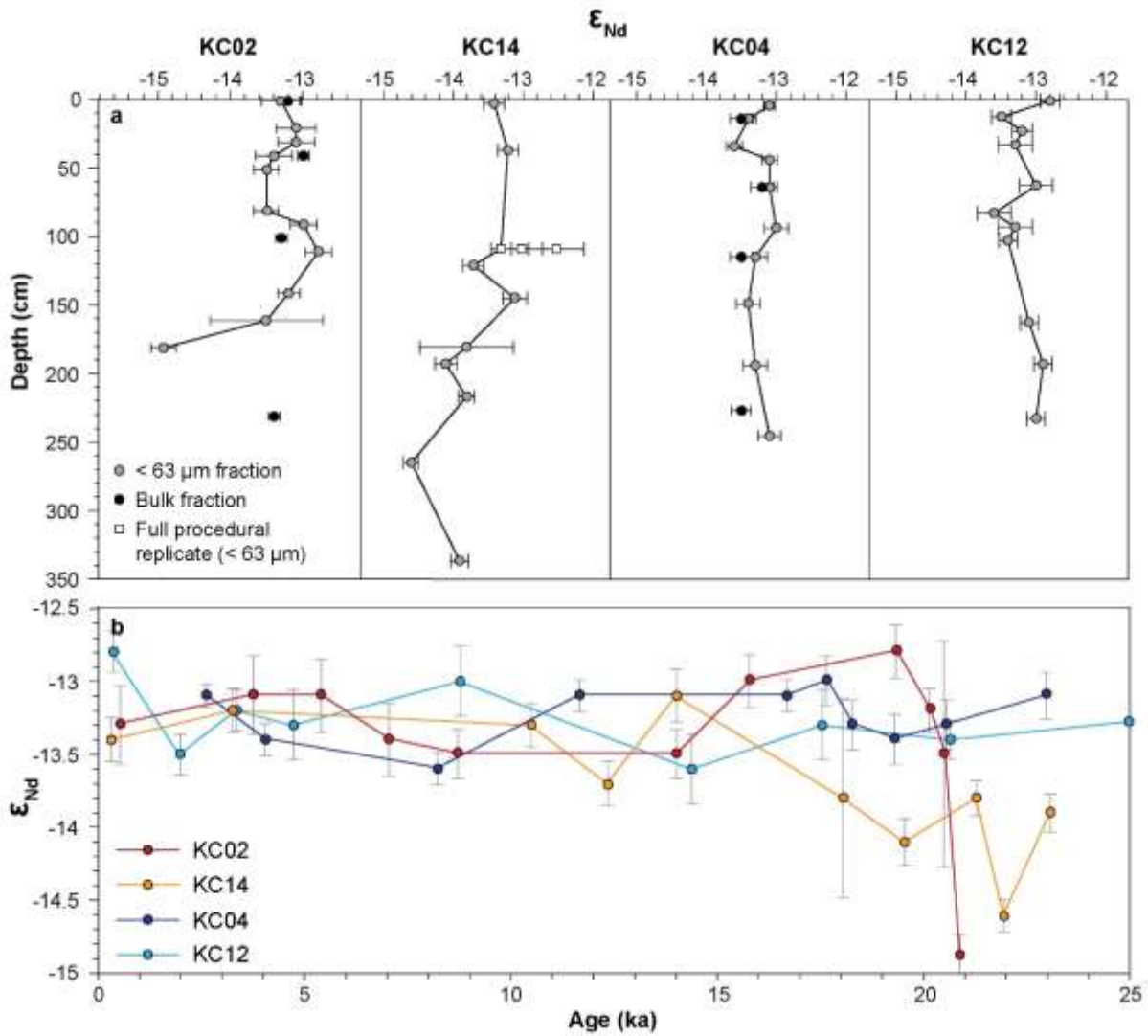


**Figure 4.4. Neodymium isotopic compositions.** Graph showing measured  $\epsilon_{Nd}$  values for the bulk and fine ( $< 63 \mu\text{m}$ ) sediment fractions in each core with (a) depth and (b) age (fine fraction only).  $2\sigma$  error bars for  $\epsilon_{Nd}$  values are shown. Age model construction in (b) is described in Chapter 2. Data for KC12 is cut off at 25 ka.

		Fine fraction ( $< 63 \mu\text{m}$ )				Bulk fraction			
Core ID	Depth interval (cm)	$\epsilon_{\text{Nd}}$	$\pm 2\text{SE}$	$^{87}\text{Sr}/^{86}\text{Sr}$	$\pm 2\text{SE}$	$\epsilon_{\text{Nd}}$	$\pm 2\text{SE}$	$^{87}\text{Sr}/^{86}\text{Sr}$	$\pm 2\text{SE}$
KC02	0-2	-13.3	0.27	0.73580	0.00008	-13.2	0.15	0.73393	0.00008
	40-42	-13.4	0.25	n.d.	n.d.	-13.0	0.08	n.d.	n.d.
	100-102	n.d.	n.d.	0.73924	0.00008	n.d.	n.d.	0.74028	0.00008
KC04	13-15	-13.4	0.11	0.73004	0.00008	-13.5	0.16	0.73028	0.00008
	63-65	-13.1	0.11	0.74016	0.00008	-13.2	0.16	0.73929	0.00008
	114-116	-13.3	0.17	0.73600	0.00008	-13.5	0.16	0.73629	0.00008

**Table 4.2.** Comparison of  $\epsilon_{\text{Nd}}$  and  $^{87}\text{Sr}/^{86}\text{Sr}$  values between the bulk and fine grain size fractions at KC02 and KC04. All values are standard-corrected and  $^{87}\text{Sr}/^{86}\text{Sr}$  ratios are blank-corrected. The total error (2SE) for each  $\epsilon_{\text{Nd}}$  value incorporates the internal and external errors on the Nd-isotopic measurement and is reported in  $\epsilon_{\text{Nd}}$  units.

#### 4.4.2. Strontium isotope composition

The  $^{87}\text{Sr}/^{86}\text{Sr}$  ratio of the fine sediment fraction ranges between 0.73544 and 0.74257 in the western cores (KC02 and KC14), and between 0.72800 and 0.74103 in the eastern cores (KC04 and KC12) (Fig. 4.5a; Supplementary Table 4.1). A broad temporal trend of decreasing  $^{87}\text{Sr}/^{86}\text{Sr}$  ratio values from the glacial to Holocene is observed in KC02, KC14 and KC12. In the western cores, the  $^{87}\text{Sr}/^{86}\text{Sr}$  ratio decreases over time from an average of 0.74048 ( $n = 4$ ,  $\text{SD} = 0.00243$ ) in the glacial period to 0.73876 ( $n = 14$ ,  $\text{SD} = 0.00208$ ) in the deglacial-Holocene period (from  $\sim 20$  ka; Fig. 4.5b). In the east, the  $^{87}\text{Sr}/^{86}\text{Sr}$  ratio at KC12 also decreases over time but to a greater extent than the western cores (glacial average: 0.74027 ( $n = 2$ ,  $\text{SD} = 0.00068$ ), deglacial-Holocene average: 0.73406 ( $n = 8$ ,  $\text{SD} = 0.00457$ ; Fig. 4.5b)). In KC04, the  $^{87}\text{Sr}/^{86}\text{Sr}$  ratios are lower during the earliest part of the record (average: 0.73397 ( $n = 2$ ,  $\text{SD} = 0.00175$ )), and then increase between  $\sim 20$ -17 ka (Fig. 4.5b). At  $\sim 17$  ka, the  $^{87}\text{Sr}/^{86}\text{Sr}$  values in KC04 start to decrease, showing a temporal trend in Sr composition similar to the other core sites. In the eastern cores, the  $^{87}\text{Sr}/^{86}\text{Sr}$  ratios begin to increase again from  $\sim 4$  ka (Fig. 4.5b).

The  $^{87}\text{Sr}/^{86}\text{Sr}$  ratio displays a moderate negative correlation with the  $\epsilon_{\text{Nd}}$  value in the fine fraction samples from the western cores but shows no significant correlation with the  $\epsilon_{\text{Nd}}$  signature in the fine fraction samples from the eastern cores (Fig. 4.6). The  $^{87}\text{Sr}/^{86}\text{Sr}$  ratios of three (KC02: 0-2 cm, KC02: 100-102 cm, and KC04: 63-65 cm) out of five bulk sediment samples were analytically different from the  $^{87}\text{Sr}/^{86}\text{Sr}$  ratios of the corresponding fine fraction samples. However, the difference between the two fractions (0.001-0.002) for those three samples is minor relative to the temporal change in Sr-isotopic composition (maximum temporal variation: 0.006) at each core site (Fig. 4.5).

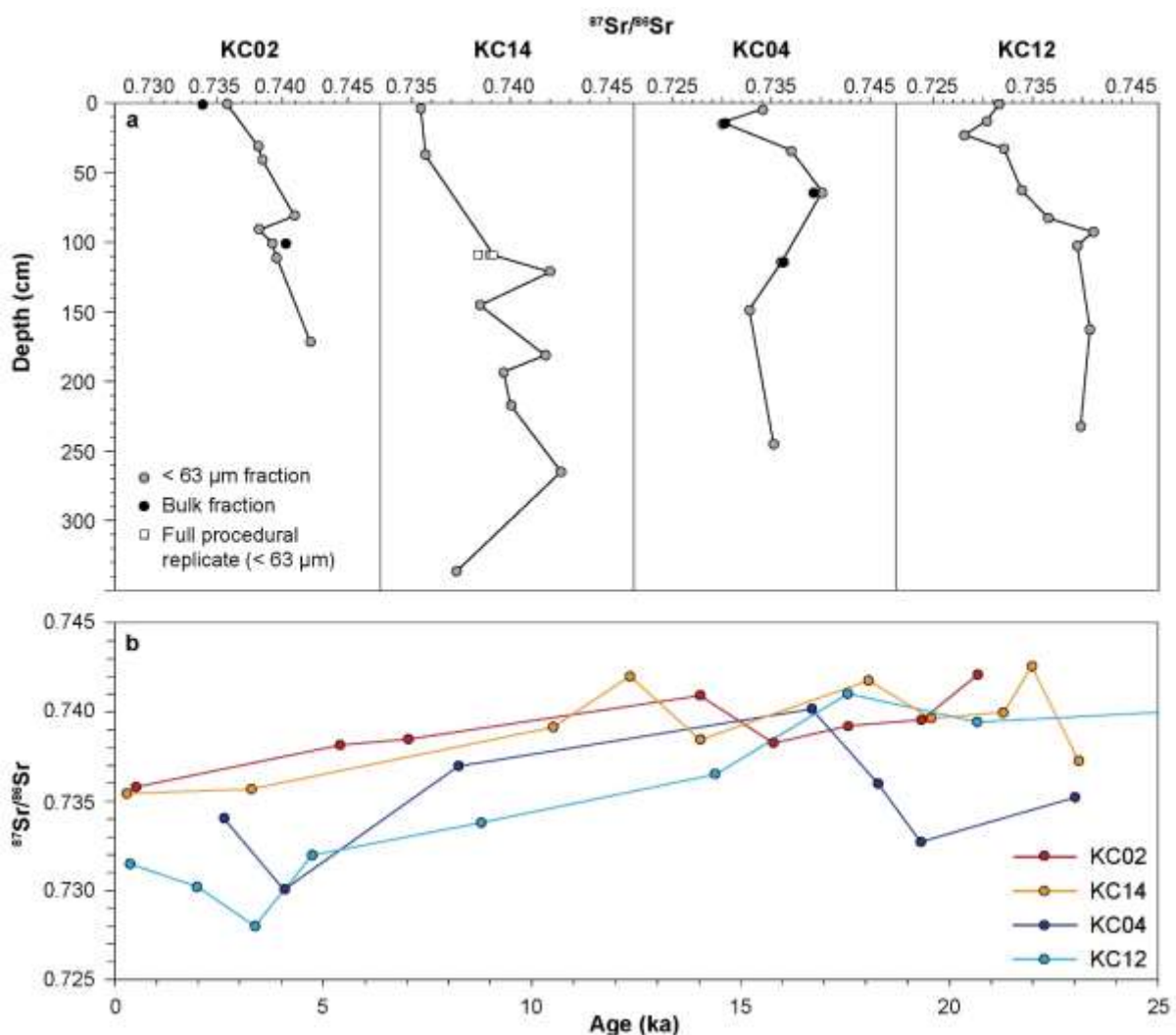


**Figure 4.5. Strontium isotopic compositions.** Graph showing measured  $^{87}\text{Sr}/^{86}\text{Sr}$  ratios of the bulk and fine ( $< 63 \mu\text{m}$ ) sediment fractions in each core with (a) depth at (b) age (fine fraction only).  $2\sigma$  error bars for  $^{87}\text{Sr}/^{86}\text{Sr}$  ratios are smaller than the markers. Age model construction in (b) is described in Chapter 2. Data for KC12 is cut off at 25 ka.

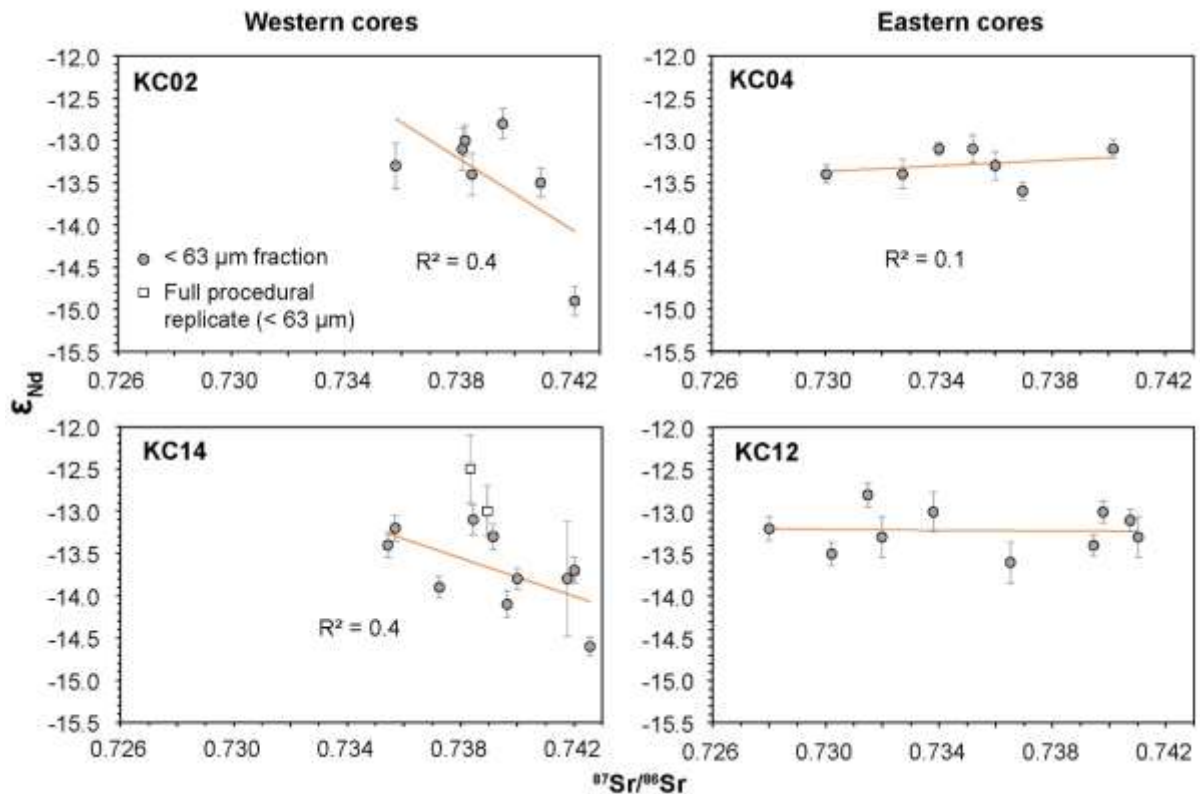


**Figure 4.6. Nd and Sr isotopic compositions.** Crossplots comparing the  $\epsilon_{Nd}$  and  $^{87}Sr/^{86}Sr$  signatures for fine detrital sediment samples at each core site. Error bars for  $^{87}Sr/^{86}Sr$  are smaller than the markers.

## 4.5. Discussion

The detrital sediment from all cores exhibits a consistent Nd-Sr isotopic signature, suggesting a uniform sediment provenance across the continental rise. Moreover, the Nd and Sr isotopic signatures from bulk and fine sediment samples of the same depth interval are typically within error of one another (Figs. 4.4 and 4.5), indicating that the Nd-Sr isotopic signal at the continental rise is unaffected by sediment transport processes that influence grain size. The detrital  $\epsilon_{Nd}$  range from this study closely overlaps signatures from core top sediments within the Wilkes Sector (100°E – 136°E) of the Southern Ocean (Pierce et al., 2011; Roy et al., 2007; van de Flierdt et al., 2007) (Fig. 4.3). The  $\epsilon_{Nd}$  value of surface sediment at KC12 ( $-12.8 \pm 0.14$ ) is close to the measured  $\epsilon_{Nd}$  signature from proximal surface sediment ( $\epsilon_{Nd} = -12.3$ , Roy

et al., 2007) providing more evidence for the integrated offshore Nd-Sr isotopic signal in Holocene sediments to the east of the study region (Fig. 4.3). Minor temporal variability in Nd-isotopic signatures from the western cores suggests varying contributions from different source basement rocks over time in the western part of the study region.

Here we use existing  $\epsilon_{Nd}$  signatures from rocks of the conjugate provinces in southern Australia and rare outcrop at the Windmill Islands to unravel the composite  $\epsilon_{Nd}$  signature of sediments from the continental rise of central Wilkes Land. In particular, we look for evidence for erosion of rocks of the Nuyina Province in the Totten catchment in the studied cores. We then assess subtle temporal variation in the Nd and Sr-isotope records to establish changes in the sediment depositional regime on the continental rise in association with the response of the ice sheet to climate warming over the Last Glacial Period-Holocene transition.

#### **4.5.1. Broad versus narrow sediment provenance**

The detrital  $\epsilon_{Nd}$  range from bulk and fine (<63  $\mu\text{m}$ ) sediment at all four core sites in this study convenes approximately in the middle of the available range of whole-rock  $\epsilon_{Nd}$  signatures from rocks of the Wilkes (Albany-Fraser), Nuyina (Madura) and Banzare (Coompana) provinces (Fig. 4.7). There is significant overlap in the  $\epsilon_{Nd}$  range between all three basement rock provinces (i.e.,  $\epsilon_{Nd}$ : -20 to -12) and with the detrital  $\epsilon_{Nd}$  signatures ( $\epsilon_{Nd}$ : -15 to -13). Consequently, it is difficult to decipher which of the different rock suites are contributing to the mixed  $\epsilon_{Nd}$  signature at the continental rise and which is the most dominant source. In Chapter 3, only a minor component of detritus (~ 5%) exhibited U-Pb age signatures (c. 500 Ma) atypical of those expected in central Wilkes Land on the basis of geophysical interpretations (Tooze et al., 2020). It is therefore anticipated that the detrital  $\epsilon_{Nd}$  signatures in this study represent a regional signature, with most of the detritus derived from the proximal Budd, Sabrina and Banzare coasts, and little to no detritus derived from further east of central Wilkes Land being carried to the core sites via the Antarctic Coastal Current.

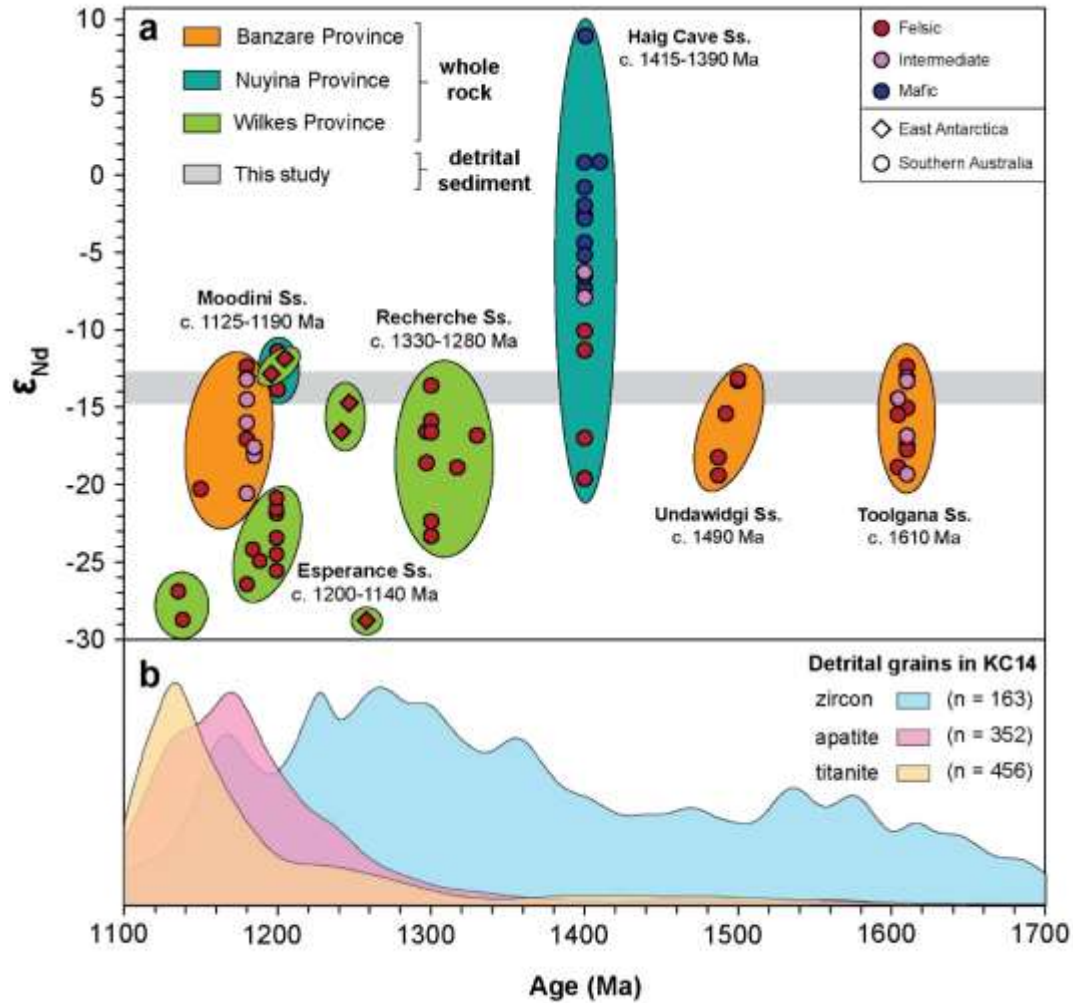


**Figure 4.7. Whole-rock and detrital  $\epsilon_{Nd}$  signatures.** (a) Whole-rock  $\epsilon_{Nd}$  signatures are from the southern Australian (Black et al., 1992a; Kirkland et al., 2015, 2017; Nelson et al., 1995; Spaggiari et al., 2018) and East Antarctic (Zhang et al., 2012) margins and are plotted against the primary zircon  $^{207}Pb/^{206}Pb$  crystallisation age. The dominant magmatic composition of the rocks sampled are shown, though many of the rocks from the Wilkes Province have been regionally metamorphosed (Clark et al., 2000). The total range of detrital  $\epsilon_{Nd}$  signatures from glacial-interglacial bulk and fine sediments from this study are shown as a grey bar. (b) Composite probability density plots showing detrital zircon  $^{207}Pb/^{206}Pb$  ages and detrital apatite and titanite  $^{206}Pb/^{238}U$  ages from KC14 (Chapter 3; Tooze et al., 2020). Age scale is cut off at 1700 Ma and 1100 Ma.

There is a close overlap between our detrital  $\epsilon_{Nd}$  signatures (range: -14.9 to -12.8) and whole-rock  $\epsilon_{Nd}$  signatures from Moodini Supersuite rocks (c. 1190-1125 Ma; Kirkland et al., 2017), particularly the Moodini Supersuite rocks within the Nuyina

Province (range: -13.9 to -11.4; Kirkland et al., 2015; Fig. 4.7a). Moodini plutons are interpreted to dominate the basement geology of the Madura Province and extensively intrude the neighbouring Coompana Province in southern Australia (Kirkland et al., 2017). It is likely that igneous complexes of this age also intrude the conjugate Nuyina and Banzare Provinces (Maritati et al., 2019), which together extend beneath a broad region of the coast of central Wilkes Land across multiple glacial catchments (Fig. 4.8; Aitken et al., 2014; Maritati et al., 2019).

In a simple 'Moodini' sediment provenance scenario, the offshore  $\epsilon_{Nd}$  signatures could entirely reflect a narrow provenance dominated by detritus from intrusive rocks of the Nuyina Moodini Supersuite supplied to the continental rise by the Totten and Moscow University glaciers (Fig. 4.8a). This scenario is supported by single grain U-Pb age spectra from KC14 including a main peak at c. 1170 Ma from detrital zircon ( $n=26$ ) and largely unimodal U-Pb age spectra from detrital titanite (peak: 1130 Ma,  $n=327$ ) and apatite (peak: c. 1170 Ma,  $n=245$ ), matching rocks of the Moodini Supersuite (Tooze et al., 2020; Fig. 4.7b). However, there are also detrital zircon grains in KC14 with U-Pb age peaks corresponding to the Toolgana (c. 1610 Ma) and Undawidgi (c. 1490 Ma) supersuites of Banzare Province, the Haig Cave Supersuite (c. 1450-1390 Ma) of the Nuyina Province, and the Recherche Supersuite (c. 1330-1280 Ma) of the Wilkes Province (Fig. 4.7b), which provide strong evidence for multiple basement rock sources along the proximal Budd, Sabrina and Banzare coasts of central Wilkes Land (Tooze et al., 2020), suggesting a broader provenance is most likely (Fig. 4.8b).

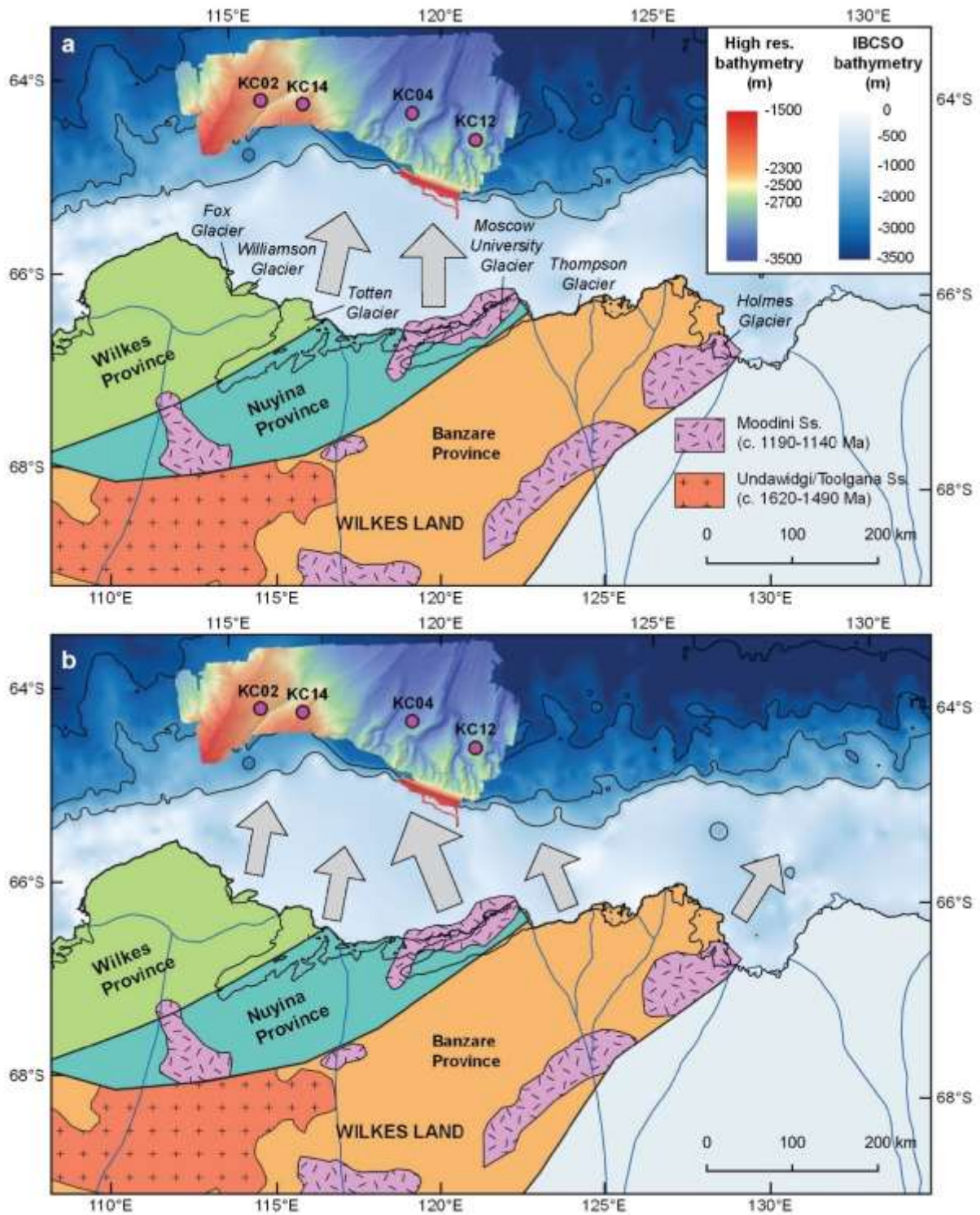


**Figure 4.8. Sediment provenance.** Maps showing two scenarios outlining possible sediment provenance pathways to the continental rise in central Wilkes Land. All map features are as given in Figure 4.1. **(a)** detrital sediment is sourced only from rocks of the Moodini Supersuite that intrudes the Nuyina Province in the coastal region of the Totten and

Moscow University glacier catchments. **(b)** Detrital sediment is derived from multiple source rocks in all three basement provinces via multiple outlet glaciers.

## **4.5.2. The role of Totten Glacier in supplying detritus to the continental margin**

In Chapter 3, we interpreted from the U-Pb geochronology from KC14 that the Totten Glacier, which overlies the boundary between the Wilkes and Nuyina provinces, was a major outlet for detritus only during early deglaciation when the extended ice sheet would have placed the glacier terminus closer to the core site, boosting the signal from proximal basement rock terranes and dampening the signal from detritus derived from more distal sources. This interpretation was based on proportionately higher (although still rare) c. 1415-1390 Ma detrital zircon age peaks (unique to the Haig Cave Supersuite of the Nuyina Province) in deglacial sediments comprising the middle section of the core. However, our newly derived Nd-isotopic results presented here indicate that radiogenic mafic detritus from the Haig Cave Supersuite of the Nuyina Province must be reaching each of the core sites to balance the less radiogenic signal from the Wilkes and Banzare provinces (Fig. 4.7a). The contribution of mafic detritus to the continental margin is also supported by: 1) the presence of sparse detrital mafic mineral grains (e.g., amphibole, pyroxene and olivine) in KC14, 2) minor detrital zircon U-Pb age peaks matching rocks from the Haig Cave Supersuite (c. 1415-1390 Ma) of the Nuyina Province in KC14 (Fig. 4.7b), and 3) a small portion of detrital feldspar grains in KC14 with an approximate age of c. 1400 Ma exhibiting a juvenile (mantle-like) Pb-isotopic character, typical of mafic rocks (Chapter 3; Tooze et al., 2020).

Evidence from this study for the constant supply of mafic detritus with Nuyina affinity to KC14 over time suggests that: 1) the Nuyina Province exists beneath the ice in central Wilkes Land as per geophysical interpretations (Maritati et al., 2019), 2) the rarity of detrital zircon grains with ages between c. 1415-1390 Ma characteristic of the Nuyina Haig Cave Supersuite in KC14 is likely due to zircon undersaturation in mafic rock types (Licht and Hemming, 2017; Shao et al., 2019), and 3) the Totten

Glacier played an important role in the supply of detritus to the continental rise not only during the initial stages of deglaciation, but throughout the Last Glacial Period - Holocene transition.

### **4.5.3. Temporal variation in sediment provenance**

The  $\epsilon_{Nd}$  signatures at the western core sites exhibit some minor temporal variation (Fig. 4.9). In Chapter 3, subtle temporal changes in sediment provenance (inferred from the U-Pb detrital zircon geochronology) and variation in the sediment depositional regime on the continental rise (inferred from the paleoenvironmental proxy record) in KC14 suggested that:

- 1) At the end of the Last Glacial Period, abundant detritus was sourced from continental shelf sediments that were redeposited downslope in gravity flows as the ice sheet advanced.
- 2) Sediment-laden meltwater fluxes fed by the Totten Glacier were responsible for the supply of detritus to KC14 during deglaciation.
- 3) Detritus was sourced from a broad region of the coast during the current interglacial.

Lower  $\epsilon_{Nd}$  values ( $< -14$ ) during the glacial at KC02 and KC14 may indicate a greater supply of Wilkes detritus scoured from the continental shelf and redistributed downslope during ice sheet advance. At the onset of deglaciation, the  $\epsilon_{Nd}$  signature at the western core sites increases to more radiogenic values (Fig. 4.9) characteristic of rocks with a more juvenile isotopic character, such as mafic rocks of the Nuyina Province and rocks of the Moodini Supersuite. The  $\epsilon_{Nd}$  signatures at the eastern core sites yield a very consistent signature that does not fall below  $-13.6$ , suggesting little to no contribution of Wilkes detritus to the eastern core sites (Fig. 4.9). It is likely that most of the detritus from the Wilkes Province would be carried westward by the

Antarctic Coastal Current, resulting in very little or no detritus reaching the eastern core sites.

Temporal variation in sediment provenance along the margin of George V Land, East Antarctica has been assessed in studies of Pliocene and Pleistocene-aged cores. The geochemical fingerprint of sediments in these cores implies erosion of basement rock terranes situated in the hinterlands, some 500 km inland, during the warm interglacials (Bertram et al., 2018; Cook et al., 2017, 2013; Wilson et al., 2018). Here, we observe comparatively very small changes in sediment provenance over the Last Glacial Period-Holocene transition, when the ice sheet retreated approximately 100-200 km from its maximum extent close to the modern-day continental shelf edge (Post et al., 2020). Rather than recording inland erosion of different basement rock sources, which would have a larger temporal effect on the Nd-isotopic fingerprint of offshore sediments, very subtle temporal variation in the Nd-isotopic composition of detrital sediment on the continental rise of central Wilkes Land can be attributed to differing contributions of detritus from the Wilkes, Nuyina and Banzare provinces to the combined offshore Nd-isotopic signal over the Last Glacial Period-Holocene transition. These observations suggest that bedrock erosion at the base of the ice sheet was concentrated along the coast, and not occurring within the hinterlands, implying ocean-forced retreat of the ice sheet over the Last Glacial Period-Holocene transition in central Wilkes Land.

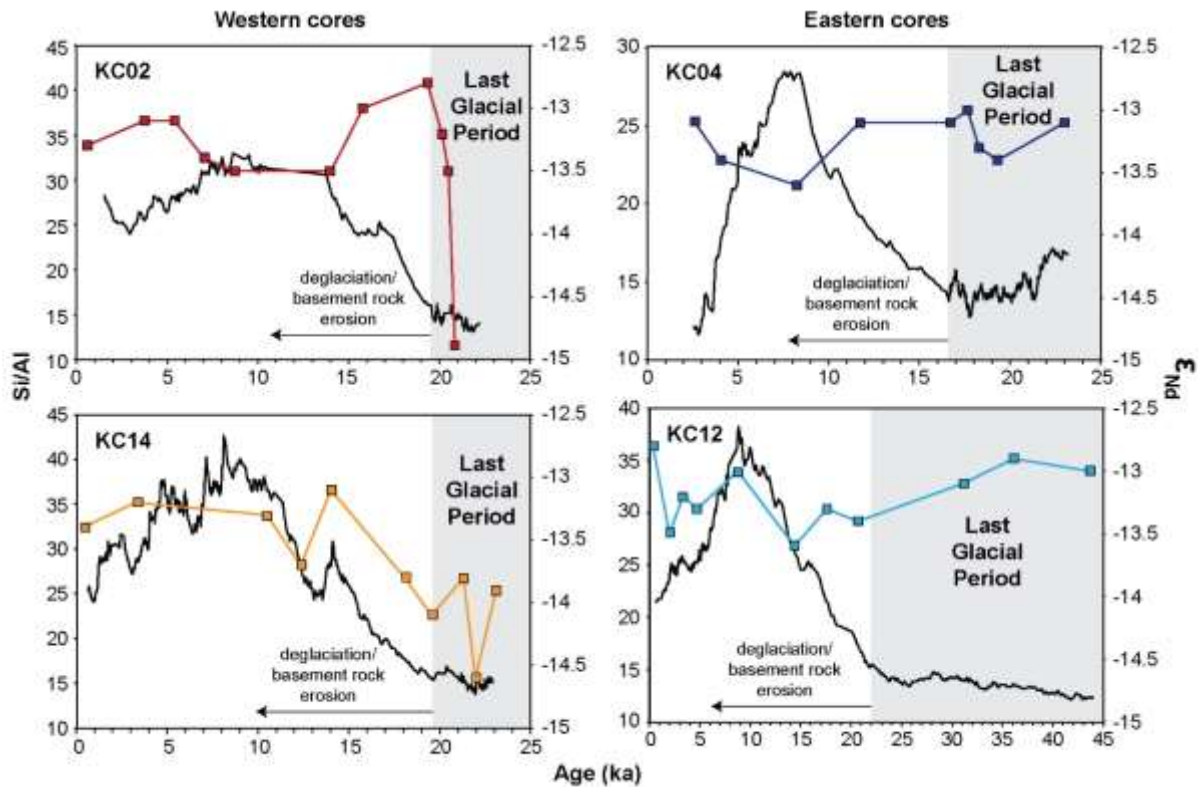


**Figure 4.9.** Temporal variation in  $\epsilon_{Nd}$  signatures at each core site compared with Si/Al ratios (black curve) representing changes in primary biological productivity during the last deglaciation.

#### 4.5.4. Current-driven changes to the Sr-isotopic compositions

Grain size effects on the Sr-isotopic composition of detrital sediment is caused by the naturally higher Rb (parent) content in clays and lower Rb content and therefore lower  $^{87}\text{Sr}/^{86}\text{Sr}$  ratios in coarser sediments (Biscaye and Dasch, 1971; Diekmann and Kuhn, 1999; Goldstein and Hemming, 2003). Temporal changes in the Sr-isotopic composition at each core site therefore may reflect physical changes to the sediment depositional regime on the continental rise (in response to a varying climate), in addition to sediment provenance (Fig. 4.10). West-flowing bottom-intensified currents have been observed in several regions of Antarctic between the continental slope and the southern boundary of the Antarctic Circumpolar Current

(e.g., Bindoff et al., 2000). These currents are diverted westward by the Coriolis Force and are responsible for most of the current-driven sedimentation on the continental rise. As the climate warmed over the Last Glacial Period-Holocene transition, stronger west-flowing bottom-intensified currents would have resulted in the selective deposition of coarser grains and sediment enriched with Zr (Figure 4.11). At the onset of deglaciation, an increase in the current speed and surface biological productivity (see Chapter 2) coincides with a decrease in the  $^{87}\text{Sr}/^{86}\text{Sr}$  in the western cores and more sharply. The following observations collectively indicate that the  $^{87}\text{Sr}/^{86}\text{Sr}$  composition of the fine ( $< 63\mu\text{m}$ ) sediment within each core may, to some extent, be influenced by the grain size effect: 1) The Sr-isotopic composition of the fine detrital sediment in all four cores displays a negative correlation with the mean grain size (Fig. 4.12). In KC02, KC04 and KC12, the correlation is moderate ( $R^2 = 0.30 - 0.57$ ), whereas at KC14, it is relatively poor ( $R^2 = 0.14$ ), 2) there is a negative correlation between the Sr-isotopic signature and the Zr/Rb ratio in each core (although this is very weak in KC02) (Fig. 4.11), 3) at the eastern cores, KC04 and KC12, there is poor correlation between the  $^{87}\text{Sr}/^{86}\text{Sr}$  ratio and the  $\epsilon_{\text{Nd}}$  signature (which is typically unaffected by grain size sorting) (Fig. 4.6).

The analysed bulk sediment samples closely plot with the corresponding fine fraction samples in KC02 and KC04. Since currents are only able to transport fine grains, this observation presents two possible scenarios: 1) the bulk samples are dominated by grains larger than  $63\mu\text{m}$ , and are therefore producing a more provenance-related Sr-isotopic signal, or 2) the bulk samples are dominated by fine material which is affected by current-sorting. Since the bulk and fine fraction samples correlate, the first scenario would suggest that the Sr-isotopic composition of the fine fraction samples is also linked more closely to provenance than current-sorting. Grain size analysis showed that the sediment is dominated by fine material, indicating that the second scenario is more likely, but more bulk fraction analysis is needed to verify this.

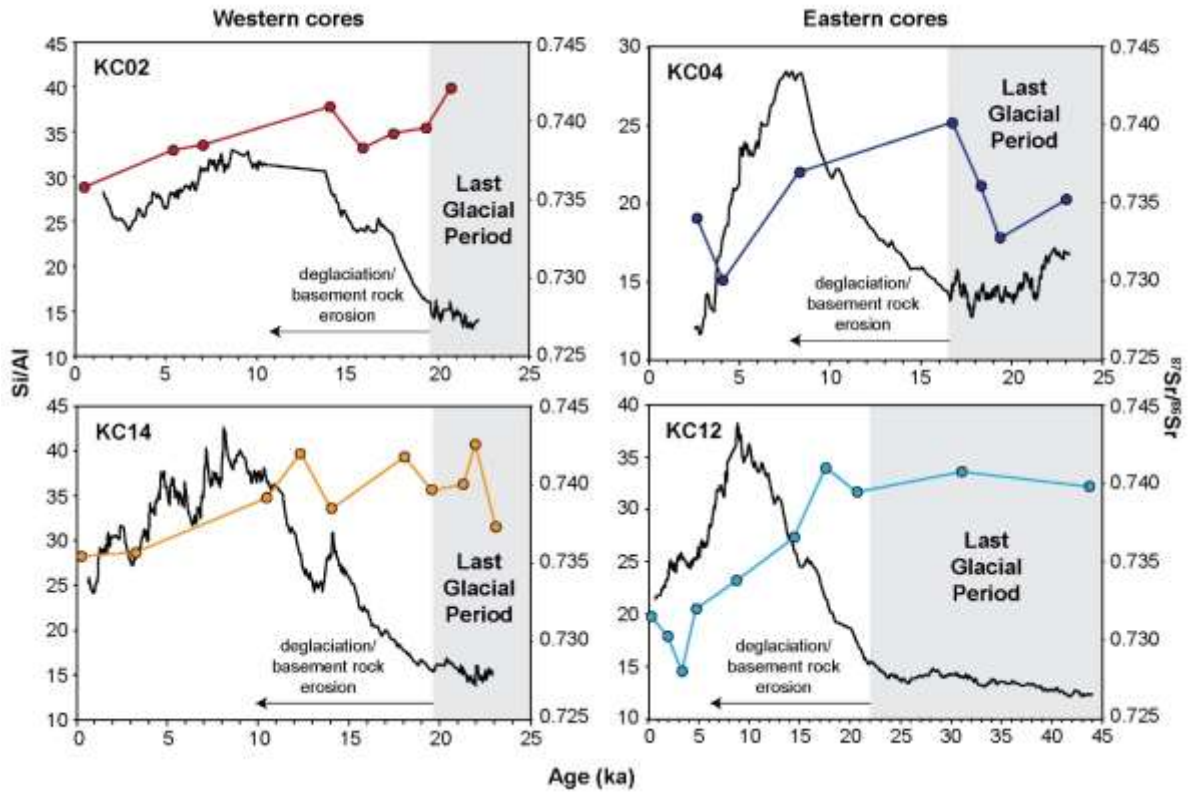


**Figure 4.10.** Temporal variation in  $^{87}\text{Sr}/^{86}\text{Sr}$  signatures (coloured curves) at each core site compared with biological productivity (black curve) as an indicator for warming conditions and ice sheet retreat over the Last Glacial Period-Holocene transition. Increase in current-driven sediment redistribution during the deglaciation may have contributed to the decrease to less radiogenic  $^{87}\text{Sr}/^{86}\text{Sr}$  values through time.

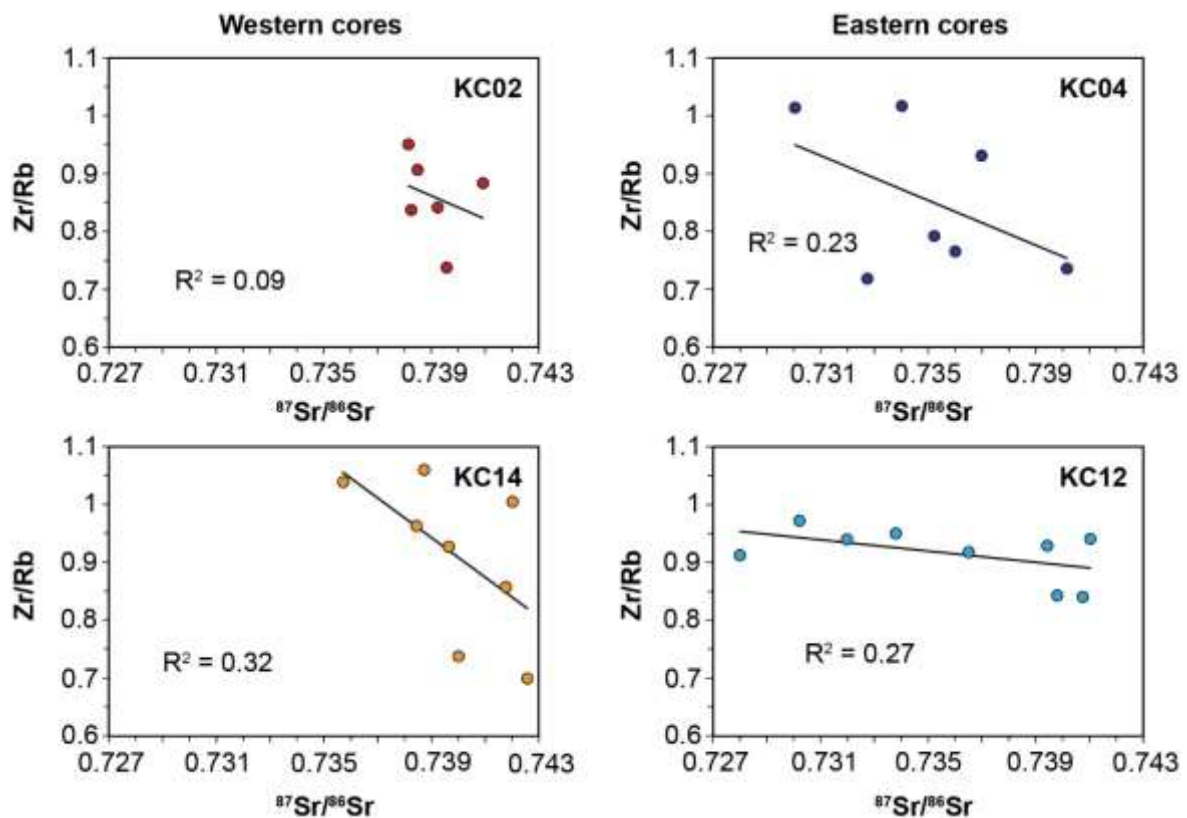


**Figure 4.11. Comparison between Zr/Rb and Sr-isotopic compositions.** Graphs showing the correlation ( $R^2$ ) between the  $^{87}\text{Sr}/^{86}\text{Sr}$  ratio and the Zr/Rb ratio (representing both grain size and paleocurrent speed) in each core.

An increase in the  $^{87}\text{Sr}/^{86}\text{Sr}$  ratio after  $\sim 4$  ka in KC04 and KC12 (Fig. 4.10) may possibly represent the deposition of more glacial clays associated with a small readvance of the ice sheet to the east of the study region during the Late Holocene. In the eastern cores, KC04 and KC12, the stronger negative correlation between  $^{87}\text{Sr}/^{86}\text{Sr}$  and grain size, and the lack of correlation with the  $\epsilon_{\text{Nd}}$  signature suggests that these cores may be more greatly influenced by the grain size effect than the cores recovered from the contourite ridges in the western part of the study region. This interpretation may explain why there is a greater temporal variation in the  $^{87}\text{Sr}/^{86}\text{Sr}$  ratios from the eastern cores than the western cores, which may be showing more of a provenance-related signal similar to the  $\epsilon_{\text{Nd}}$  signature (Fig. 4.10).

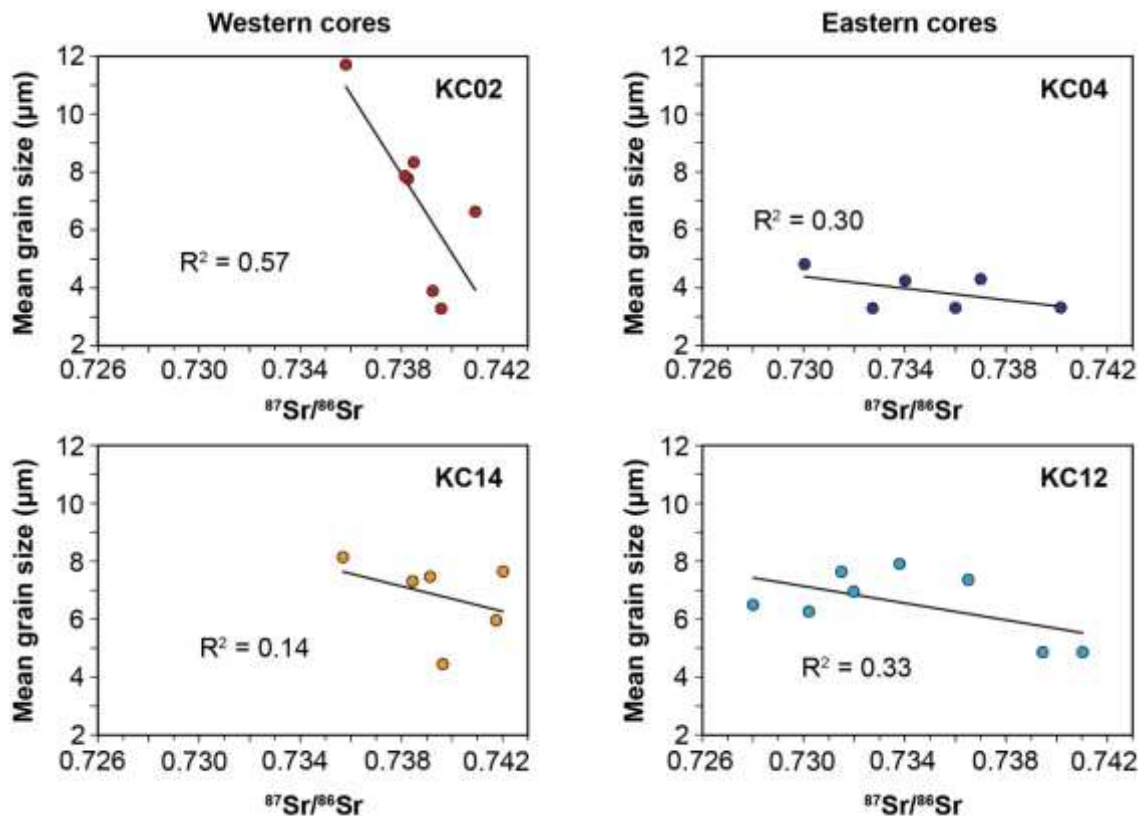


**Figure 4.12. Comparison between mean grain size and Sr-isotopic compositions.**

Graphs showing the correlation ( $R^2$ ) between the  $^{87}\text{Sr}/^{86}\text{Sr}$  ratio and the mean (BiSi-leached) grain size in each core.

## 4.6. Conclusions

We report Nd and Sr isotopic signatures from the bulk and fine detrital sediment in four cores from the continental rise of central Wilkes Land, East Antarctica.

Comparing our bulk isotope data with single-grain provenance analysis of one of the cores (KC14) and source rock  $\epsilon_{\text{Nd}}$  signatures representative of the proximal Wilkes, Nuyina and Banzare provinces, we make the following conclusions:

1. **The Totten Glacier was responsible for the abundant supply of detritus to the continental slope and rise from the end of the Last Glacial Period to present.** With most whole-rock  $\epsilon_{\text{Nd}}$  signatures from the Wilkes and Banzare

provinces below -15, more radiogenic mafic detritus of the Nuyina Province must be contributing to the combined offshore signal to produce detrital  $\epsilon_{Nd}$  signatures between -14.9 and -12.8. Furthermore, the significant overlap between  $\epsilon_{Nd}$  signatures from c. 1180-1125 Ma intrusive rocks of the Moodini Supersuite of the Nuyina Province and the detrital  $\epsilon_{Nd}$  signature range from the studied cores may indicate that rocks of the Moodini Supersuite of the Nuyina Province are the dominant source of c. 1200-1100 Ma detritus in KC14. Evidence of sustained sediment provenance from within the Nuyina Province, coupled with abundant detritus of the Wilkes Province as observed in KC14, suggests that the Totten Glacier supplied abundant detritus to the continental margin over the Last Glacial Period-Holocene transition.

- 2. The  $\epsilon_{Nd}$  signature is consistent across the continental rise.** The measured  $\epsilon_{Nd}$  range within all cores was very similar, suggesting a spatially consistent sediment provenance across the continental rise. Slightly less radiogenic  $\epsilon_{Nd}$  values at the western core sites during the glacial period suggest an enhanced supply of Wilkes detritus to the west of the study region during ice sheet advance.

In the absence of our bulk detrital Nd and Sr-isotopic data and Nd-Sr isotopic source rock end members from whole-rock analysis, spatial variability in sediment provenance and evidence for mafic detritus of the Nuyina Province could not previously be assessed. Similarly, without the single-grain provenance data from KC14 (Tooze et al., 2020), it would be impossible to conclude whether the detritus had a narrow and unique origin or was derived from multiple basement rock terranes at the coast. These findings demonstrate the importance of combining multiple sediment provenance tools to unravel the history of the ice sheet in Antarctica.

## 4.7. Supplementary Information

Core ID	Depth interval (cm)	Fraction	$^{87}\text{Sr}/^{86}\text{Sr}$	$\pm 2\text{SE}$	Blank corrected $^{87}\text{Sr}/^{86}\text{Sr}$	$\pm 2\text{SE}$	$^{143}\text{Nd}/^{144}\text{Nd}$	$\pm 2\text{SE}$	$\epsilon_{\text{Nd}}$	$\pm 2\text{SE}$
KC02	0-2	Bulk	0.733864	0.000006	0.733926	0.00008326	0.51196	0.000002	-13.2	0.15
KC02	40-42	Bulk	n.d	n.d	n.d	n.d	0.51197	0.000002	-13.0	0.08
KC02	100-102	Bulk	0.740197	0.000006	0.740275	0.00008326	0.51196	0.000004	-13.3	0.08
KC02	230-232	Bulk	n.d	n.d	n.d	n.d	0.51195	0.000007	-13.4	0.08
KC02	0-2	< 63 $\mu\text{m}$	0.735735	0.000005	0.735801	0.00008321	0.51196	0.000004	-13.3	0.27
KC02	20-22	< 63 $\mu\text{m}$	n.d	n.d	n.d	n.d	0.51197	0.000004	-13.1	0.27
KC02	30-32	< 63 $\mu\text{m}$	0.738079	0.000006	0.738152	0.00008324	0.51197	0.000003	-13.1	0.25
KC02	40-42	< 63 $\mu\text{m}$	0.738412	0.000006	0.738486	0.00008324	0.51195	0.000003	-13.4	0.25
KC02	50-52	< 63 $\mu\text{m}$	n.d	n.d	n.d	n.d	0.51194	0.000003	-13.5	0.17
KC02	80-82	< 63 $\mu\text{m}$	0.740841	0.000006	0.740921	0.00008325	0.51195	0.000002	-13.5	0.17
KC02	90-92	< 63 $\mu\text{m}$	0.738181	0.000006	0.738254	0.00008327	0.51197	0.000003	-13	0.18
KC02	100-102	< 63 $\mu\text{m}$	0.739161	0.000006	0.739236	0.00008325	n.d	n.d	n.d	n.d
KC02	110-112	< 63 $\mu\text{m}$	0.739495	0.000006	0.739571	0.00008327	0.51198	0.000003	-12.8	0.18
KC02	140-142	< 63 $\mu\text{m}$	n.d	n.d	n.d	n.d	0.51196	0.000003	-13.2	0.15
KC02	160-162	< 63 $\mu\text{m}$	n.d	n.d	n.d	n.d	0.51194	0.000020	-13.5	0.77
KC02	170-172	< 63 $\mu\text{m}$	0.742033	0.000005	0.742116	0.00008323	0.51187	0.000003	-14.9	0.17
KC04	13-15	Bulk	0.730229	0.000006	0.730281	0.00008327	0.51195	0.000003	-13.5	0.16
KC04	63-65	Bulk	0.739212	0.000006	0.739288	0.00008327	0.51196	0.000003	-13.2	0.16
KC04	114-116	Bulk	0.736225	0.000005	0.736293	0.00008323	0.51195	0.000018	-13.5	0.16
KC04	226-228	Bulk	n.d	n.d	n.d	n.d	0.51195	0.000004	-13.5	0.14
KC04	4-5	< 63 $\mu\text{m}$	0.733954	0.000007	0.734016	0.00008332	0.51196	0.000003	-13.1	0.08
KC04	13-15	< 63 $\mu\text{m}$	0.729992	0.000005	0.730043	0.00008322	0.51195	0.000003	-13.4	0.11
KC04	33-35	< 63 $\mu\text{m}$	0.736896	0.000005	0.736966	0.00008323	0.51194	0.000003	-13.6	0.11
KC04	43-45	< 63 $\mu\text{m}$	n.d	n.d	n.d	n.d	0.51197	0.000003	-13.1	0.11
KC04	63-65	< 63 $\mu\text{m}$	0.740084	0.000006	0.740162	0.00008325	0.51196	0.000002	-13.1	0.11
KC04	93-5	< 63 $\mu\text{m}$	n.d	n.d	n.d	n.d	0.51197	0.000003	-13	0.17
KC04	114-116	< 63 $\mu\text{m}$	0.735933	0.000006	0.736000	0.00008325	0.51196	0.000003	-13.3	0.17
KC04	148-150	< 63 $\mu\text{m}$	0.732672	0.000006	0.732731	0.00008326	0.51195	0.000007	-13.4	0.17
KC04	193-195	< 63 $\mu\text{m}$	n.d	n.d	n.d	n.d	0.51196	0.000003	-13.3	0.17
KC04	245-246	< 63 $\mu\text{m}$	0.735141	0.000006	0.735206	0.00008326	0.51197	0.000019	-13.1	0.16
KC12	0-2	< 63 $\mu\text{m}$	0.731430	0.000006	0.731486	0.00008324	0.51198	0.000003	-12.8	0.14
KC12	12-14	< 63 $\mu\text{m}$	0.730160	0.000006	0.730212	0.00008328	0.51195	0.000003	-13.5	0.14
KC12	22-24	< 63 $\mu\text{m}$	0.727958	0.000008	0.728005	0.00008342	0.51196	0.000003	-13.2	0.14
KC12	32-34	< 63 $\mu\text{m}$	0.731928	0.000006	0.731985	0.00008328	0.51196	0.000003	-13.3	0.24
KC12	62-64	< 63 $\mu\text{m}$	0.733738	0.000006	0.733799	0.00008327	0.51197	0.000003	-13	0.24
KC12	82-84	< 63 $\mu\text{m}$	0.736446	0.000006	0.736515	0.00008327	0.51194	0.000016	-13.6	0.24
KC12	92-94	< 63 $\mu\text{m}$	0.740949	0.000006	0.741029	0.00008327	0.51196	0.000003	-13.3	0.24
KC12	102-104	< 63 $\mu\text{m}$	0.739376	0.000006	0.739453	0.00008327	0.51195	0.000007	-13.4	0.13
KC12	162-164	< 63 $\mu\text{m}$	0.740667	0.000006	0.740746	0.00008326	0.51197	0.000004	-13.1	0.13
KC12	192-194	< 63 $\mu\text{m}$	n.d	n.d	n.d	n.d	0.51197	0.000003	-12.9	0.13
KC12	232-234	< 63 $\mu\text{m}$	0.739714	0.000006	0.739792	0.00008324	0.51197	0.000003	-13.0	0.13
KC14	2-4	< 63 $\mu\text{m}$	0.735373	0.000006	0.735439	0.00008325	0.51195	0.000003	-13.4	0.15
KC14	36-38	< 63 $\mu\text{m}$	0.735625	0.000006	0.735691	0.00008326	0.51196	0.000002	-13.2	0.15
KC14	108-110	< 63 $\mu\text{m}$	0.739075	0.000006	0.739151	0.00008325	0.51195	0.000003	-13.3	0.15
KC14	120-122	< 63 $\mu\text{m}$	0.741935	0.000007	0.742018	0.00008331	0.51194	0.000003	-13.7	0.15
KC14	144-146	< 63 $\mu\text{m}$	0.738371	0.000006	0.738444	0.00008329	0.511967	0.000005	-13.1	0.18
KC14	180-182	< 63 $\mu\text{m}$	0.741682	0.000006	0.741765	0.00008325	0.511932	0.000017	-13.8	0.68
KC14	192-194	< 63 $\mu\text{m}$	0.739565	0.000005	0.739642	0.00008323	0.511913	0.000004	-14.1	0.16
KC14	216-218	< 63 $\mu\text{m}$	0.739927	0.000006	0.740005	0.00008327	0.511928	0.000003	-13.8	0.12
KC14	264-266	< 63 $\mu\text{m}$	0.742483	0.000005	0.742567	0.00008323	0.511889	0.000003	-14.6	0.11
KC14	336-338	< 63 $\mu\text{m}$	0.737181	0.000006	0.737252	0.00008327	0.511923	0.000003	-13.9	0.13
KC14	108-110 (repeat 1)	< 63 $\mu\text{m}$	0.738870	0.000006	0.738945	0.00008324	0.51197	0.000008	-13.0	0.30
KC14	108-110 (repeat 2)	< 63 $\mu\text{m}$	0.738268	0.000006	0.738342	0.00008328	0.511996	0.000010	-12.5	0.40
BCR-2g	NA	Bulk rock	0.705019	0.000006	0.705004	0.00008331	0.512670	0.000060	0.6	0.14

Supplementary Table 4.1. Nd and Sr isotopic compositions of all analysed samples.

## References

- Aitken, A. R. A., Young, D. A., Ferraccioli, F., Betts, P. G., Greenbaum, J. S., Richter, T. G., ... Siegert, M. J. (2014). The subglacial geology of Wilkes Land, East Antarctica. *Geophysical Research Letters*, *41*(7), 2390–2400. <https://doi.org/10.1002/2014GL059405>
- Armand, L., O'Brien, P., Armbrecht, L., Barker, H., Caburlotto, A., Connell, T., ... Young, A. (2018). Interactions of the Totten Glacier with the Southern Ocean through multiple glacial cycles (IN2017-V01): Post-survey report, (March). <https://doi.org/10.4225/13/5ACEA64C48693>
- Arndt, J. E., Schenke, H. W., Jakobsson, M., Nitsche, F. O., Buys, G., Goleby, B., ... Wigley, R. (2013). The international bathymetric chart of the Southern Ocean (IBCSO) version 1.0-A new bathymetric compilation covering circum-Antarctic waters. *Geophysical Research Letters*, *40*(12), 3111–3117. <https://doi.org/10.1002/grl.50413>
- Bertram, R. A., Wilson, D. J., van de Fliedrt, T., McKay, R. M., Patterson, M. O., Jimenez-Espejo, F. J., ... Riesselman, C. R. (2018). Pliocene deglacial event timelines and the biogeochemical response offshore Wilkes Subglacial Basin, East Antarctica. *Earth and Planetary Science Letters*, *494*, 109–116. <https://doi.org/10.1016/j.epsl.2018.04.054>
- Bindoff, N. L., Rosenberg, M. A., & Warner, M. J. (2000). On the circulation and water masses over the Antarctic continental slope and rise between 80 and 150°E. *Deep Sea Research Part II: Topical Studies in Oceanography*, *47*(12–13), 2299–2326. [https://doi.org/10.1016/S0967-0645\(00\)00038-2](https://doi.org/10.1016/S0967-0645(00)00038-2)
- Biscaye, P. E., & Dasch, E. J. (1971). The rubidium, strontium, strontium-isotope system in deep-sea sediments: Argentine Basin. *Journal of Geophysical Research*, *76*(21), 5087–5096. <https://doi.org/10.1029/JC076I021P05087>
- Black, L. P., Harris, L. B., & Delor, C. P. (1992a). Reworking of Archaean and Early Proterozoic components during a progressive, Middle Proterozoic tectonothermal event in the Albany Mobile Belt, Western Australia. *Precambrian Research*, *59*(1–2), 95–123. [https://doi.org/10.1016/0301-9268\(92\)90053-Q](https://doi.org/10.1016/0301-9268(92)90053-Q)
- Black, L. P., Sheraton, J. W., Tingey, R. J., & McCulloch, M. T. (1992b). New U-Pb zircon ages from the Denman Glacier area, East Antarctica, and their significance for Gondwana reconstruction. *Antarctic Science*, *4*(4), 447–460. <https://doi.org/10.1017/S095410209200066X>
- Charlier, B. L. A., Ginibre, C., Morgan, D., Nowell, G. M., Pearson, D. G., Davidson, J. P., & Ottley, C. J. (2006). Methods for the microsampling and high-precision analysis of strontium

and rubidium isotopes at single crystal scale for petrological and geochronological applications. *Chemical Geology*, 232(3–4), 114–133.  
<https://doi.org/10.1016/j.chemgeo.2006.02.015>

Chester, R., & Hughes, M. J. (1967). A chemical technique for the separation of ferro-manganese minerals, carbonate minerals and adsorbed trace elements from pelagic sediments. *Chemical Geology*, 2(C), 249–262. [https://doi.org/10.1016/0009-2541\(67\)90025-3](https://doi.org/10.1016/0009-2541(67)90025-3)

Clark, D. J., Hensen, B. J., & Kinny, P. D. (2000). Geochronological constraints for a two-stage history of the Albany-Fraser Orogen, Western Australia. *Precambrian Research*, 102(3–4), 155–183. [https://doi.org/10.1016/S0301-9268\(00\)00063-2](https://doi.org/10.1016/S0301-9268(00)00063-2)

Cook, C. P., Hemming, S. R., van de Flierdt, T., Pierce Davis, E. L., Williams, T., Galindo, A. L., ... Escutia, C. (2017). Glacial erosion of East Antarctica in the Pliocene: A comparative study of multiple marine sediment provenance tracers. *Chemical Geology*, 466, 199–218. <https://doi.org/10.1016/j.chemgeo.2017.06.011>

Cook, C. P., Hill, D. J., van de Flierdt, T., Williams, T., Hemming, S. R., Dolan, A. M., ... Gonzales, J. J. (2014). Sea surface temperature control on the distribution of far-traveled Southern Ocean ice-rafted detritus during the Pliocene. *Paleoceanography*, 29(6), 533–548. <https://doi.org/10.1002/2014PA002625>

Cook, C. P., van de Flierdt, T., Williams, T., Hemming, S. R., Iwai, M., Kobayashi, M., ... Yamane, M. (2013). Dynamic behaviour of the East Antarctic ice sheet during Pliocene warmth. *Nature Geoscience*, 6(9), 765–769. <https://doi.org/10.1038/ngeo1889>

Diekmann, B., & Kuhn, G. (1999). Provenance and dispersal of glacial–marine surface sediments in the Weddell Sea and adjoining areas, Antarctica: ice-rafting versus current transport. *Marine Geology*, 158(1–4), 209–231. [https://doi.org/10.1016/S0025-3227\(98\)00165-0](https://doi.org/10.1016/S0025-3227(98)00165-0)

Donda, F., Leitchenkov, G., Brancolini, G., Romeo, R., de Santis, L., Escutia, C., ... Cotterle, D. (2020). The influence of Totten Glacier on the Late Cenozoic sedimentary record. *Antarctic Science*, 1–13. <https://doi.org/10.1017/S0954102020000188>

Fitzsimons, I. C. W. (2003). Proterozoic basement provinces of southern and southwestern Australia, and their correlation with Antarctica. *Geological Society Special Publication*, 206(1), 93–130. <https://doi.org/10.1144/GSL.SP.2003.206.01.07>

Fretwell, P., Pritchard, H. D., Vaughan, D. G., Bamber, J. L., Barrand, N. E., Bell, R., ... Zirizzotti, A. (2013). Bedmap2: Improved ice bed, surface and thickness datasets for Antarctica. *Cryosphere*, 7(1), 375–393. <https://doi.org/10.5194/tc-7-375-2013>

- Gill, A. E. (1973). Circulation and bottom water production in the Weddell Sea. *Deep-Sea Research and Oceanographic Abstracts*, 20(2), 111–140. [https://doi.org/10.1016/0011-7471\(73\)90048-X](https://doi.org/10.1016/0011-7471(73)90048-X)
- Goldstein, S. L., & Hemming, S. R. (2003). Long-lived Isotopic Tracers in Oceanography, Paleoceanography, and Ice-sheet Dynamics. *Treatise on Geochemistry*, 6–9, 1–37. <https://doi.org/10.1016/B0-08-043751-6/06179-X>
- Hemming, S. R., van de Flierdt, T., Goldstein, S. L., Franzese, A. M., Roy, M., Gastineau, G., & Landrot, G. (2007). Strontium isotope tracing of terrigenous sediment dispersal in the Antarctic circumpolar current: Implications for constraining frontal positions. *Geochemistry, Geophysics, Geosystems*, 8(6), n/a-n/a. <https://doi.org/10.1029/2006GC001441>
- Holder, L., Duffy, M., Opdyke, B., Leventer, A., Post, A., O'Brien, P., & Armand, L. K. (2020). Controls Since the mid-Pleistocene Transition on Sedimentation and Primary Productivity Downslope of Totten Glacier, East Antarctica. *Paleoceanography and Paleoclimatology*, 35(12). <https://doi.org/10.1029/2020PA003981>
- Huang, H., Gutjahr, M., Kuhn, G., Hathorne, E. C., & Eisenhauer, A. (2021). Efficient Extraction of Past Seawater Pb and Nd Isotope Signatures From Southern Ocean Sediments. *Geochemistry, Geophysics, Geosystems*, 22(3), e2020GC009287. <https://doi.org/10.1029/2020GC009287>
- Jacobsen, S. B., & Wasserburg, G. J. (1980). Sm-Nd isotopic evolution of chondrites. *Earth and Planetary Science Letters*, 50(1), 139–155. [https://doi.org/10.1016/0012-821X\(80\)90125-9](https://doi.org/10.1016/0012-821X(80)90125-9)
- Kirkland, C. L., Smithies, R. H., & Spaggiari, C. v. (2015). Foreign contemporaries - Unravelling disparate isotopic signatures from Mesoproterozoic Central and Western Australia. *Precambrian Research*, 265, 218–231. <https://doi.org/10.1016/j.precamres.2014.12.001>
- Kirkland, C. L., Smithies, R. H., Spaggiari, C. v., Wingate, M. T. D., Quentin de Gromard, R., Clark, C., ... Belousova, E. A. (2017). Proterozoic crustal evolution of the Eucla basement, Australia: Implications for destruction of oceanic crust during emergence of Nuna. *Lithos*, 278–281, 427–444. <https://doi.org/10.1016/j.lithos.2017.01.029>
- Kirkland, C. L., Spaggiari, C. v., Pawley, M. J., Wingate, M. T. D., Smithies, R. H., Howard, H. M., ... Poujol, M. (2011). On the edge: U-Pb, Lu-Hf, and Sm-Nd data suggests reworking of the Yilgarn craton margin during formation of the Albany-Fraser Orogen. *Precambrian Research*, 187(3–4), 223–247. <https://doi.org/10.1016/j.precamres.2011.03.002>
- Licht, K. J., & Hemming, S. R. (2017, May 15). Analysis of Antarctic glacigenic sediment provenance through geochemical and petrologic applications. *Quaternary Science Reviews*. Elsevier Ltd. <https://doi.org/10.1016/j.quascirev.2017.03.009>

- Maritati, A., Halpin, J. A., Whittaker, J. M., & Daczko, N. R. (2019). Fingerprinting Proterozoic Bedrock in Interior Wilkes Land, East Antarctica. *Scientific Reports*, 9(1), 1–12. <https://doi.org/10.1038/s41598-019-46612-y>
- Matthews, K. J., Maloney, K. T., Zahirovic, S., Williams, S. E., Seton, M., & Müller, R. D. (2016). Global plate boundary evolution and kinematics since the late Paleozoic. *Global and Planetary Change*, 146, 226–250. <https://doi.org/10.1016/j.gloplacha.2016.10.002>
- Möller, A., Post, N. J., & Hensen, B. J. (2002). Crustal residence history and garnet Sm-Nd ages of high-grade metamorphic rocks from the Windmill Islands area, East Antarctica. *International Journal of Earth Sciences*, 91(6), 993–1004. <https://doi.org/10.1007/s00531-002-0291-x>
- Morrissey, L. J., Payne, J. L., Hand, M., Clark, C., Taylor, R., Kirkland, C. L., & Kylander-Clark, A. (2017). Linking the Windmill Islands, east Antarctica and the Albany–Fraser Orogen: Insights from U–Pb zircon geochronology and Hf isotopes. *Precambrian Research*, 293, 131–149. <https://doi.org/10.1016/j.precamres.2017.03.005>
- Mouginot, J., Scheuchl, B., & Rignot, E. (2017). MEaSURES Antarctic Boundaries for IPY 2007–2009 from Satellite Radar, Version 2. *NASA National Snow and Ice Data Center Distributed Active Archive Center*. <https://doi.org/https://doi.org/10.5067/AXE4121732AD>
- Mulder, J. A., Halpin, J. A., Daczko, N. R., Orth, K., Meffre, S., Thompson, J. M., & Morrissey, L. J. (2019). A Multiproxy provenance approach to uncovering the assembly of East Gondwana in Antarctica. *Geology*, 47(7), 645–649. <https://doi.org/10.1130/G45952.1>
- Myers, J. S. (1993). Precambrian history of the West Australian Craton and adjacent orogens. *Annual Review of Earth & Planetary Sciences*, 21, 453–485. <https://doi.org/10.1146/annurev.ea.21.050193.002321>
- Nelson, D. R., Myers, J. S., & Nutman, A. P. (1995). Chronology and evolution of the middle proterozoic alban-fraser orogen, western australia. *Australian Journal of Earth Sciences*, 42(5), 481–495. <https://doi.org/10.1080/08120099508728218>
- Noble, T. L., Piotrowski, A. M., & McCave, I. N. (2013). Neodymium isotopic composition of intermediate and deep waters in the glacial southwest Pacific. *Earth and Planetary Science Letters*, 384, 27–36. <https://doi.org/10.1016/j.epsl.2013.10.010>
- O'Brien, P. E., Post, A. L., Edwards, S., Martin, T., Caburlotto, A., Donda, F., ... Armand, L. K. (2020). Continental slope and rise geomorphology seaward of the Totten Glacier, East Antarctica (112°E–122°E). *Marine Geology*, 427, 106221. <https://doi.org/10.1016/j.margeo.2020.106221>

- Pierce, E. L., Hemming, S. R., Williams, T., van de Flierdt, T., Thomson, S. N., Reiners, P. W., ... Goldstein, S. L. (2014, August 28). A comparison of detrital U-Pb zircon,  $^{40}\text{Ar}/^{39}\text{Ar}$  hornblende,  $^{40}\text{Ar}/^{39}\text{Ar}$  biotite ages in marine sediments off East Antarctica: Implications for the geology of subglacial terrains and provenance studies. *Earth-Science Reviews*. Elsevier. <https://doi.org/10.1016/j.earscirev.2014.08.010>
- Pierce, E. L., van de Flierdt, T., Williams, T., Hemming, S. R., Cook, C. P., & Passchier, S. (2017). Evidence for a dynamic East Antarctic ice sheet during the mid-Miocene climate transition. *Earth and Planetary Science Letters*, *478*, 1–13. <https://doi.org/10.1016/j.epsl.2017.08.011>
- Pierce, E. L., Williams, T., van de Flierdt, T., Hemming, S. R., Goldstein, S. L., & Brachfeld, S. A. (2011). Characterizing the sediment provenance of East Antarctica's weak underbelly: The Aurora and Wilkes sub-glacial. Pierce, E. L., Williams, T., Van De Flierdt, T., Hemming, S. R., Goldstein, S. L., & Brachfeld, S. A. (2011). *Paleoceanography*, *26*(4). <https://doi.org/10.1029/2011PA002127>
- Post, A. L., O'Brien, P. E., Edwards, S., Carroll, A. G., Malakoff, K., & Armand, L. K. (2020). Upper slope processes and seafloor ecosystems on the Sabrina continental slope, East Antarctica. *Marine Geology*, *422*, 106091. <https://doi.org/10.1016/j.margeo.2019.106091>
- Raczek, I., Jochum, K. P., & Hofmann, A. W. (2003). Neodymium and strontium isotope data for USGS reference materials BCR-1, BCR -2, BHV O-1, BHVO-2, AGV-1, AGV-2, GSP-1, GSP-2 and Eight MPI-DING refer ence glasses. *Geostandards Newsletter*, *27*(2), 173–179. <https://doi.org/10.1111/j.1751-908X.2003.tb00644.x>
- Roy, M., van de Flierdt, T., Hemming, S. R., & Goldstein, S. L. (2007).  $^{40}\text{Ar}/^{39}\text{Ar}$  ages of hornblende grains and bulk Sm/Nd isotopes of circum-Antarctic glacio-marine sediments: Implications for sediment provenance in the southern ocean. *Chemical Geology*, *244*(3–4), 507–519. <https://doi.org/10.1016/j.chemgeo.2007.07.017>
- Shao, T., Xia, Y., Ding, X., Cai, Y., & Song, M. (2019). Zircon saturation in terrestrial basaltic melts and its geological implications. *Solid Earth Sciences*, *4*(1), 27–42. <https://doi.org/10.1016/j.sesci.2018.08.001>
- Sheraton, J. W., Black, L. P., McCulloch, M. T., & Oliver, R. L. (1990). Age and origin of a compositionally varied mafic dyke swarm in the Bunger Hills, East Antarctica. *Chemical Geology*, *85*(3–4), 215–246. [https://doi.org/10.1016/0009-2541\(90\)90002-O](https://doi.org/10.1016/0009-2541(90)90002-O)

- Sheraton, J. W., Black, L. P., & Tindle, A. G. (1992). Petrogenesis of plutonic rocks in a Proterozoic granulite-facies terrane - the Bunger Hills, East Antarctica. *Chemical Geology*, 97(3–4), 163–198. [https://doi.org/10.1016/0009-2541\(92\)90075-G](https://doi.org/10.1016/0009-2541(92)90075-G)
- Sheraton, J. W., Tingey, R. J., Oliver, R. L., & Black, L. P. (1995). Geology of the Bunger Hills-Denman Glacier region, East Antarctica. Retrieved August 22, 2021, from [https://scholar.google.com.au/scholar?hl=en&as\\_sdt=0%2C5&q=Geology+o+f+the+Bunger+Hills-Denma+n+++Glacier+region%2C+Eas+t+Antarctic&btnG=](https://scholar.google.com.au/scholar?hl=en&as_sdt=0%2C5&q=Geology+o+f+the+Bunger+Hills-Denma+n+++Glacier+region%2C+Eas+t+Antarctic&btnG=)
- Spaggiari, C. v., Smithies, R. H., Kirkland, C. L., Wingate, M. T. D., England, R. N., & Lu, Y. J. (2018). Buried but preserved: The Proterozoic Arubiddy Ophiolite, Madura Province, Western Australia. *Precambrian Research*, 317, 137–158. <https://doi.org/10.1016/j.precamres.2018.08.025>
- Tanaka, T., Togashi, S., Kamioka, H., Amakawa, H., Kagami, H., Hamamoto, T., ... Dragusanu, C. (2000). JNdi-1: A neodymium isotopic reference in consistency with LaJolla neodymium. *Chemical Geology*, 168(3–4), 279–281. [https://doi.org/10.1016/S0009-2541\(00\)00198-4](https://doi.org/10.1016/S0009-2541(00)00198-4)
- Tooze, S., Halpin, J. A., Noble, T. L., Chase, Z., O'Brien, P. E., & Armand, L. (2020). Scratching the Surface: A Marine Sediment Provenance Record From the Continental Slope of Central Wilkes Land, East Antarctica. *Geochemistry, Geophysics, Geosystems*, 21(11). <https://doi.org/10.1029/2020GC009156>
- Tucker, N. M., Payne, J. L., Clark, C., Hand, M., Taylor, R. J. M., Kylander-Clark, A. R. C., & Martin, L. (2017). Proterozoic reworking of Archean (Yilgarn) basement in the Bunger Hills, East Antarctica. *Precambrian Research*, 298, 16–38. <https://doi.org/10.1016/j.precamres.2017.05.013>
- van de Fliertdt, T., Goldstein, S. L., Hemming, S. R., Roy, M., Frank, M., & Halliday, A. N. (2007). Global neodymium-hafnium isotope systematics - revisited. *Earth and Planetary Science Letters*, 259(3–4), 432–441. <https://doi.org/10.1016/j.epsl.2007.05.003>
- Williams, T., van de Fliertdt, T., Hemming, S. R., Chung, E., Roy, M., & Goldstein, S. L. (2010). Evidence for iceberg armadas from East Antarctica in the Southern Ocean during the late Miocene and early Pliocene. *Earth and Planetary Science Letters*, 290(3–4), 351–361. <https://doi.org/10.1016/j.epsl.2009.12.031>
- Wilson, D. J., Bertram, R. A., Needham, E. F., van de Fliertdt, T., Welsh, K. J., McKay, R. M., ... Escutia, C. (2018, September 20). Ice loss from the East Antarctic Ice Sheet during late Pleistocene interglacials. *Nature*. Nature Publishing Group. <https://doi.org/10.1038/s41586-018-0501-8>

Zhang, S. H., Zhao, Y., Liu, X. C., Liu, Y. S., Hou, K. J., Li, C. F., & Ye, H. (2012). U-Pb geochronology and geochemistry of the bedrocks and moraine sediments from the Windmill Islands: Implications for Proterozoic evolution of East Antarctica. *Precambrian Research*, 206–207, 52–71. <https://doi.org/10.1016/j.precamres.2012.02.019>

# Chapter 5

## Main conclusions and future work

The research in this thesis captures the first detailed picture of the response of the East Antarctic Ice Sheet to climate variation over the Last Glacial Period-Holocene transition in central Wilkes Land. Providing evidence for changes to the marine sediment depositional regime on the adjacent continental rise, the multi-proxy data from this study sheds light on temporal variation in the oceanography, sea-ice conditions, biological productivity, glaciological processes, sediment provenance and sediment transport mechanisms associated with ice sheet evolution and climate change in the central Wilkes Land region. The results from sediment provenance analysis ground truth geophysical interpretations of the regional subglacial geology and erosion of basement rock at the coast of central Wilkes Land. Since central Wilkes Land encompasses a broad region of the East Antarctic Ice Sheet largely grounded below sea level and sensitive to ocean-forced melting, these findings provide a better understanding of the history of the ice sheet which will ultimately facilitate paleoclimate reconstructions and ice sheet models that predict future ice sheet behaviour. Integrating the main findings and conclusions from this thesis, this chapter provides a summary of the recent history of the ice sheet in central Wilkes Land from the perspective of the ocean, followed by considerations for future work.

### 5.1. Conclusions

During the Last Glacial Period in central Wilkes Land the ice sheet scoured sediments from the continental shelf, redistributing them downslope and onto the continental rise in a series of high energy gravity flows (Fig. 5.1a). The existence of gravity flows and high supply of fine-grained muds during glacial advance is evidenced by one or more of the following in each of the cores: high sedimentation rates (33-331 cm/kyr), higher abundances of coarse debris within a matrix of fine

mud (<4  $\mu\text{m}$ ), and a higher proportion (30-70% of total diatom abundance) of extinct diatoms (Chapter 2). Ceasing of ice sheet advance (and high sedimentation rates) is interpreted to represent the timing of the LLGM in central Wilkes Land, which occurred between c. 22-20 ka (Chapter 2). Terrigenous detritus within the glacial sediments of KC14 exhibited a broader sediment provenance signal, similar to modern day sediments, suggesting that the detrital sediment source and provenance did not change significantly over time (Chapter 3).

Low primary productivity during the Last Glacial Period, associated with the northward extension of the ice sheet and sea ice over the continental rise (Fig. 5.1a) was inferred by low diatom abundances, BiSi concentrations, Ba/Al and Si/Al ratios (Chapter 2). A stratified unit in KC14, KC04 and KC12, proximal to the Totten and Moscow University glaciers, suggests coverage by glacier ice shelves for a period as the ice sheet expanded, resulting in layered, hemipelagic sedimentation (Smith et al., 2019). Similarly, a unique glacial lithological unit with a clotted texture and dropstones in KC02 suggests greater proximity to the calving front of the Totten Glacier and/or sea ice edge, in association with ice sheet expansion during the Last Glacial Period. Slower west-flowing bottom currents during the Last Glacial Period are represented by a lower sortable silt percent, Zr/Rb ratio and mean grain size in each of the cores – demonstrating the selective deposition of finer material as lower energy currents are unable to transport coarser material (McCave et al., 1995, 2017; McCave and Andrews, 2019; McCave and Hall, 2006). These slower currents may have been a result of weaker easterly winds than at present (Stewart and Thompson, 2012).

The onset of deglaciation in central Wilkes Land is marked by a sudden increase in meltwater production (diatom species: *Chaetoceros* subg. *Hyalochaete*), paleocurrent speed (mean grain size, Zr/Rb ratio and sortable silt percent) and biological productivity (Si/Al, Ba/Al, diatom abundance and BiSi concentration), from low glacial values (Chapter 2). As the climate warmed, retreat of the grounding line and sea ice extent led to an enhanced meltwater input to the ocean, and open surface waters ideal for surface biological productivity (Fig. 5.1b). The west-flowing

bottom currents intensified, leading to the focussing of coarser, silty sediments. This change is seen not only in the paleocurrent speed proxies, but also in the Sr-isotopic analyses, which were influenced to some extent by the grain size effect (Chapter 4). A clear increase to more radiogenic  $^{87}\text{Sr}/^{86}\text{Sr}$  ratios is seen in each core, which is approximately concurrent with the interpreted onset of deglaciation at each individual site. This change likely reflects the transition from Rb-rich glacial clays to Zr-rich silty sediments as the current speed increased and the climate warmed (Chapter 4). The shift in the sediment depositional regime on the continental rise of the central Wilkes Land coast, as represented by the paleoenvironmental proxies and Sr-isotopic compositions in each core, reveals that deglaciation initiated at some time between  $22.0 \pm 3.2$  ka and  $19.2 \pm 0.6$  ka. The timing of the onset of deglaciation in central Wilkes Land is one of the earliest constrained in East Antarctica, demonstrating that this is a region highly sensitive to changes in the Earth's climate.

The bulk detrital  $\epsilon_{\text{Nd}}$  signal on the continental rise was consistently above -15 across the last deglaciation (Chapter 4). Source rock end members (acquired from whole-rock analyses of rocks from rare outcrop in East Antarctica and from boreholes and outcrop in southern Australia) all exhibited  $\epsilon_{\text{Nd}}$  values less than -15, except for mafic rocks of the Nuyina Province, providing evidence for the constant supply of mafic detritus to the continental rise over time. Mafic rocks are unique to the Nuyina Province that underlies the Totten Glacier in central Wilkes Land, suggesting that the Totten Glacier was the main conduit for the supply of detritus throughout the time from the termination of the Last Glacial Period to present (Chapter 4). However, it was initially interpreted from the detrital zircon U-Pb geochronology at KC14 that the Totten Glacier only played a major role in the supply of detritus to the continental margin during the initial stages of deglaciation (Chapter 3). This interpretation was based on the prominent c. 1414-1390 Ma age peaks unique to (dominantly mafic) rocks of the Haig Cave Supersuite of the Nuyina Province in deglacial sediments (Chapter 3). The absence of detritus of this age during the glacial period (Fig. 5.1.c), when the ice margin and the Totten Glacier were closer to the core site at the onset of deglaciation, was interpreted to represent a dampened sediment provenance signal from more distal sources (Chapter 3).

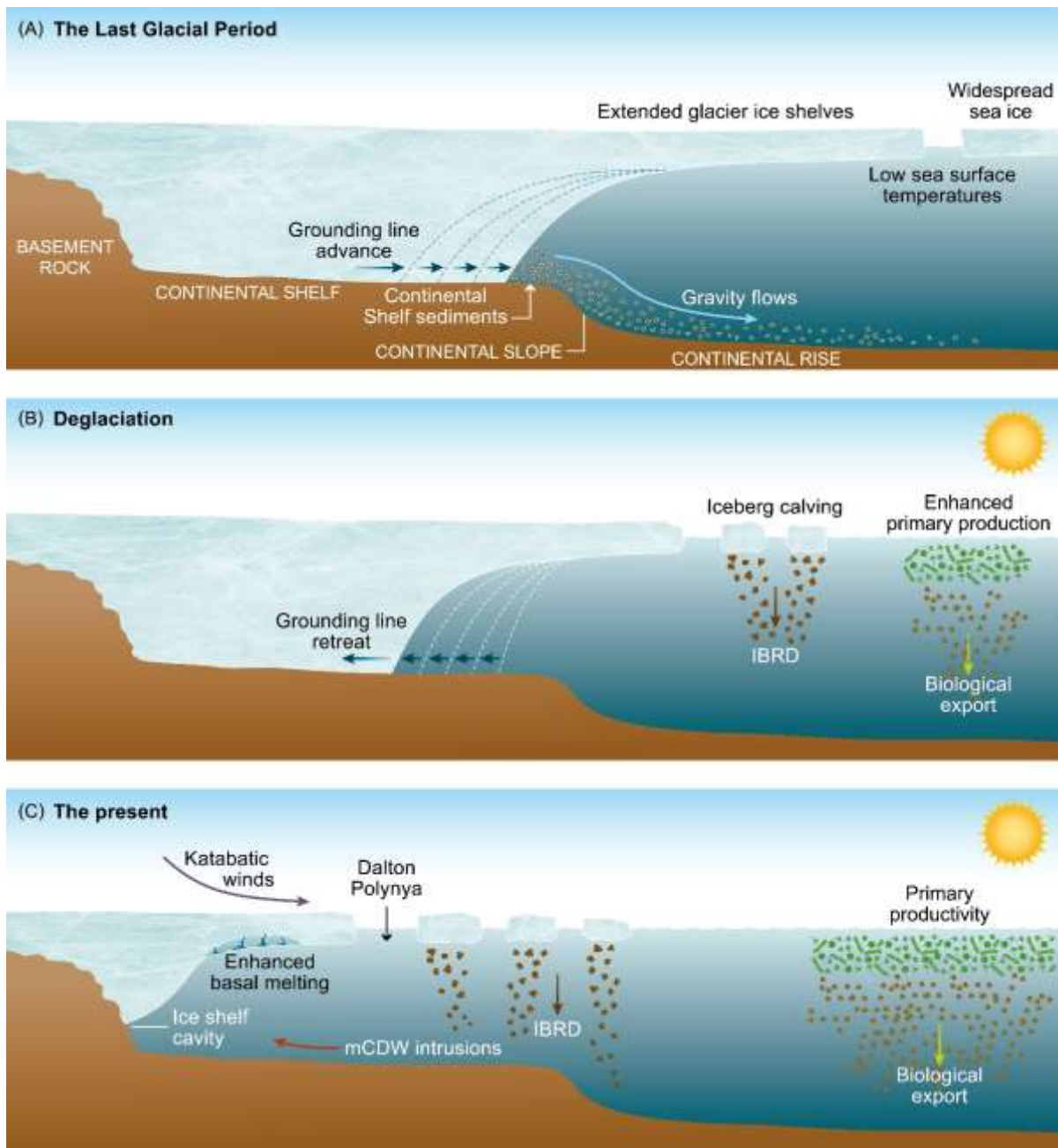


**Figure 5.1.** Different phases of ice sheet configuration and the marine sediment depositional regime on the adjacent continental margin. **(a)** the Last Glacial Period, **(b)** deglaciation, **(c)** the modern day ice sheet.

Despite the reinterpretation of the role of the Totten Glacier, the detrital zircon, apatite and titanite U-Pb age record at KC14 revealed important information on the subglacial geology at the central Wilkes Land coast and the sedimentological history

of the adjacent continental rise. The results from single-grain analysis indicated that 95% of detritus was sourced from the proximal coast with most U-Pb ages matching the interpreted Mesoproterozoic terranes in central Wilkes Land (Chapter 3). This sediment provenance record therefore supports geophysical interpretations of the basement rock terranes concealed beneath the ice. Combining single-grain U-Pb dating with bulk Nd-Sr isotopic analysis helped reduce bias and uncertainties introduced by employing one single technique. The integrated results from these sediment provenance techniques ultimately provided important insight into the glaciological processes and basement rock erosion at the coast of central Wilkes Land over the Last Glacial Period-Holocene transition.

An Antarctic contribution to the significant GMSL rise at ~14.7 ka is supported by a peak in the IBRD MAR in KC14 (~14.6 ka) approximately concurrent with Meltwater Pulse 1A (Hanebuth et al., 2000; Weaver et al., 2003) and with Antarctic Ice Sheet Discharge (AID) event 6 (c. 14.8–14.4 kyr) of Weber et al. (2014), indicating enhanced meltwater production and supply of IBRD to the core site (Fig. 5.1b; Chapter 2). Continued deglaciation was interrupted by the Antarctic Cold Reversal which was indicated by a temporary dip in primary productivity at KC02, KC14 and KC12. Deglaciation throughout the Holocene period (from c. 11 ka) in central Wilkes Land was predominantly characterised by a peak in biological productivity, likely associated with an elevated rate of grounding line and sea ice retreat, followed by a period of cooling marked by a decrease in primary productivity. These phases of Holocene deglaciation are observed in each core and are known as the Holocene Optimum and the Neoglacial Period, respectively. It is possible that there was a modest readvance of the ice sheet during the Neoglacial Period in central Wilkes Land. A readvance is supported by lower productivity associated with cooler conditions and by an increase in the  $^{87}\text{Sr}/^{86}\text{Sr}$  ratios at the eastern core sites, KC04 and KC12 after c. 4 ka, which, if predominantly influenced by the grain size effect, would suggest the deposition of finer clays associated with glacial sedimentation (Chapter 4). However, more evidence is needed for a Neoglacial readvance of the ice sheet in the central Wilkes Land region.

## 5.2. Future work

The research in this thesis provides some of the first physical evidence for the recent history of the ice sheet in central Wilkes Land, and as such there remains a broad range of opportunities for future work. Here I will outline some considerations for future research specifically related to the findings and new questions that have arisen from the work in this thesis.

One of the greatest challenges faced by the Antarctic paleoclimate research community is the construction of reliable age models for marine sediment cores. To assess and/or improve the reliability of the age model used in this study, more dating techniques could be employed for each core, and at a higher resolution. The following dating techniques could be applied to each of the cores studied in this thesis: ramped pyrolysis (e.g., Rosenheim et al., 2008, 2013), paleomagnetic intensity (e.g., Hillenbrand et al., 2021), dating of foraminifera and other carbonates such as bivalves and fish teeth (if and where possible) (e.g., Holder et al., 2020; Majewski et al., 2020), cosmogenic nuclide (e.g.,  $^{10}\text{Be}$ , and  $^{26}\text{Al}$ ) dating (e.g., Johnson et al., 2017; Sjunneskog et al., 2007), luminescence dating (e.g., Berger et al., 2010; Fuchs and Owen, 2008), and the use of stratigraphic markers (e.g., diatom and foraminiferal species, comparison of paleoenvironmental proxies to oxygen isotope records in proximal ice cores, etc) (Li et al., 2021). A more resolute and reliable age model will help to: 1. support/negate interpreted constraints on the timing of the last deglaciation and other climate events in central Wilkes Land, 2. understand/explain the anomalous ages at the bottom of KC12 and at the top of KC04, and 3. estimate the extent to which the age signature from the acid-insoluble organic matter fraction from sediment on the continental rise is affected by contamination by old, recycled carbon (the Local Carbon Offset). Finally, the application of multiple dating techniques to other cores recovered on the 2017 voyage (IN2017\_V01) to the margin of the Sabrina Coast of central Wilkes Land will offer more insight into any local spatial variability in the response of the ice sheet to climate variation.

The database of regional MRAs for the Southern Ocean is expanding (Skinner et al., 2019), however there is still a lack of constraints on MRAs from regions at polar latitudes of the Southern Ocean (poleward of 60°S). Since the MRA varies spatially and temporally (especially at high latitudes and during glacial periods), more constraints on this variability will facilitate the improvement of age models from the Antarctic margin. The recent calculation of a modern regional MRA for the central Wilkes Land region (Holder et al., 2020) highlights the potential for the use of carbonates to obtain more surface sediment ages.

The research conducted in this thesis assessed the millennial-scale variability of conditions on the continental rise associated with variation in ice sheet configuration and climate in central Wilkes Land. The investigation of marine sediment cores capturing longer time scales would provide insight into the orbital-scale variability in the response of the ice sheet to periods of climate warmer than at present. Piston cores recovered from voyage IN2017\_V01 could be used to investigate the deglacial history in central Wilkes Land following warm interglacials of the Late Pleistocene and the Pliocene, when the ice sheet retreated further inland of the modern day grounding line. Sediment provenance techniques conducted on these cores would provide information on basement rock erosion in interior Wilkes Land, and the glaciological/sedimentological processes of these older periods.

Most of the basement rocks interpreted in central Wilkes Land, if comparable to their southern Australian counterparts, have a similar  $\epsilon_{Nd}$  signature range, making it difficult to establish unique source rock end members and predict the proportion of detritus derived from the Wilkes, Nuyina and Banzare provinces. In particular, there is significant overlap in the measured  $\epsilon_{Nd}$  signature ranges of juvenile felsic igneous rocks of the Recherche supersuite of the Wilkes Province with the Moodini Supersuite of the Nuyina and Banzare provinces, and the Toolgana and Undawidgi supersuites of the Banzare Province. A sophisticated Nd-isotope mixing model, capable of distinguishing end members that are not significantly different from one another, would help to pull apart the integrated detrital  $\epsilon_{Nd}$  signature and provide more information on basement rock erosion and glaciological processes at the coast

of central Wilkes Land. There is a lack of Nd and Sr isotope data from rocks at the coast of central Wilkes Land and source rock end member identification so far relies mostly on analyses from boreholes and rare outcrop in southern Australia. Nd-Sr isotopic analyses from rare outcrop at the Windmill Islands, Chick Island and Balaena Islets would build a more comprehensive and reliable source rock end member dataset that can be used in isotopic mixing models and general interpretations of sediment provenance and the history of the ice sheet. Moreover, grain size specific Sr-isotopic analyses would allow for the determination of the extent to which the detrital Sr-isotopic signatures are affected by current transport and grain size in the study region and the measurement of the detrital  $\epsilon_{Nd}$  signature on different size fractions will more sensitively track source rock contributions.

The proposed future research will ultimately contribute to a more detailed understanding of the dynamic history of the ice sheet in central Wilkes Land and facilitate the development of well-constrained models that predict the future of the ice sheet and the implications for sea level rise.

## References

- Berger, G. W., Doran, P. T., & Thomsen, K. J. (2010). Single-grain and multigrain luminescence dating of on-ice and lake-bottom deposits at Lake Hoare, Taylor Valley, Antarctica. *Quaternary Geochronology*, 5(6), 679–690. <https://doi.org/10.1016/j.quageo.2010.05.003>
- Fuchs, M., & Owen, L. A. (2008). Luminescence dating of glacial and associated sediments: review, recommendations and future directions. *Boreas*, 37(4), 636–659. <https://doi.org/10.1111/j.1502-3885.2008.00052.x>
- Hanebuth, T., Stategger, K., & Grootes, P. M. (2000). Rapid flooding of the Sunda Shelf: A late-glacial sea-level record. *Science*, 288(5468), 1033–1035. <https://doi.org/10.1126/science.288.5468.1033>
- Hillenbrand, C. D., Crowhurst, S. J., Williams, M., Hodell, D. A., McCave, I. N., Ehrmann, W., Xuan, C., Piotrowski, A. M., Hernández-Molina, F. J., Graham, A. G. C., Grobe, H., Williams, T. J., Horrocks, J. R., Allen, C. S., & Larter, R. D. (2021). New insights from multi-proxy data from the West Antarctic continental rise: Implications for dating and interpreting Late

Quaternary palaeoenvironmental records. *Quaternary Science Reviews*, 257, 106842.  
<https://doi.org/10.1016/j.quascirev.2021.106842>

Holder, L., Duffy, M., Opdyke, B., Leventer, A., Post, A., O'Brien, P., & Armand, L. K. (2020). Controls Since the mid-Pleistocene Transition on Sedimentation and Primary Productivity Downslope of Totten Glacier, East Antarctica. *Paleoceanography and Paleoclimatology*, 35(12). <https://doi.org/10.1029/2020PA003981>

Johnson, J. S., Smith, J. A., Schaefer, J. M., Young, N. E., Goehring, B. M., Hillenbrand, C. D., Lamp, J. L., Finkel, R. C., & Gohl, K. (2017). The last glaciation of Bear Peninsula, central Amundsen Sea Embayment of Antarctica: Constraints on timing and duration revealed by in situ cosmogenic <sup>14</sup>C and <sup>10</sup>Be dating. *Quaternary Science Reviews*, 178, 77–88.  
<https://doi.org/10.1016/j.quascirev.2017.11.003>

Li, W., Li, X., Mei, X., Zhang, F., Xu, J., Liu, C., Wei, C., & Liu, Q. (2021). A review of current and emerging approaches for Quaternary marine sediment dating. *Science of the Total Environment*, 780, 146522. <https://doi.org/10.1016/j.scitotenv.2021.146522>

Majewski, W., Prothro, L. O., Simkins, L. M., Demianiuk, E. J., & Anderson, J. B. (2020). Foraminiferal Patterns in Deglacial Sediment in the Western Ross Sea, Antarctica: Life Near Grounding Lines. *Paleoceanography and Paleoclimatology*, 35(5), e2019PA003716.  
<https://doi.org/10.1029/2019PA003716>

McCave, I. N., & Andrews, J. T. (2019). Distinguishing current effects in sediments delivered to the ocean by ice. I. Principles, methods and examples. In *Quaternary Science Reviews* (Vol. 212, pp. 92–107). Elsevier Ltd. <https://doi.org/10.1016/j.quascirev.2019.03.031>

McCave, I. N., & Hall, I. R. (2006). Size sorting in marine muds: Processes, pitfalls, and prospects for paleoflow-speed proxies. *Geochemistry, Geophysics, Geosystems*, 7(10), n/a-n/a.  
<https://doi.org/10.1029/2006GC001284>

McCave, I. N., Manighetti, B., & Robinson, S. G. (1995). Sortable silt and fine sediment size/composition slicing: Parameters for palaeocurrent speed and palaeoceanography. *Paleoceanography*, 10(3), 593–610. <https://doi.org/10.1029/94PA03039>

McCave, I. N., Thornalley, D. J. R., & Hall, I. R. (2017). Relation of sortable silt grain-size to deep-sea current speeds: Calibration of the 'Mud Current Meter.' *Deep-Sea Research Part I: Oceanographic Research Papers*, 127, 1–12. <https://doi.org/10.1016/j.dsr.2017.07.003>

Rosenheim, B. E., Day, M. B., Domack, E., Schrum, H., Benthien, A., & Hayes, J. M. (2008). Antarctic sediment chronology by programmed-temperature pyrolysis: Methodology and data

treatment. *Geochemistry, Geophysics, Geosystems*, 9(4).

<https://doi.org/10.1029/2007GC001816>

Rosenheim, B. E., Santoro, J. A., Gunter, M., & Domack, E. W. (2013). Improving Antarctic Sediment <sup>14</sup>C Dating Using Ramped Pyrolysis: An Example from the Hugo Island Trough.

*Radiocarbon*, 55(1), 115–126. [https://doi.org/10.2458/AZU\\_JS\\_RC.V55I1.16234](https://doi.org/10.2458/AZU_JS_RC.V55I1.16234)

Sjunneskog, C., Scherer, R., Aldahan, A., & Possnert, G. (2007). <sup>10</sup>Be in glacial marine sediment of the Ross Sea, Antarctica, a potential tracer of depositional environment and sediment chronology. *Nuclear Instruments and Methods in Physics Research, Section B: Beam Interactions with Materials and Atoms*, 259(1), 576–583.

<https://doi.org/10.1016/j.nimb.2007.01.203>

Skinner, L. C., Muschitiello, F., & Scrivner, A. E. (2019). Marine Reservoir Age Variability Over the Last Deglaciation: Implications for Marine Carbon Cycling and Prospects for Regional Radiocarbon Calibrations. *Paleoceanography and Paleoclimatology*, 34(11), 1807–1815.

<https://doi.org/10.1029/2019PA003667>

Smith, J. A., Graham, A. G. C., Post, A. L., Hillenbrand, C. D., Bart, P. J., & Powell, R. D. (2019). The marine geological imprint of Antarctic ice shelves. In *Nature Communications* (Vol. 10, Issue 1, pp. 1–16). Nature Research.

<https://doi.org/10.1038/s41467-019-13496-5>

Stewart, A. L., & Thompson, A. F. (2012). Sensitivity of the ocean's deep overturning circulation to easterly Antarctic winds. *Geophysical Research Letters*, 39(17).

<https://doi.org/10.1029/2012GL053099>

Weaver, A. J., Saenko, O. A., Clark, P. U., & Mitrovica, J. X. (2003). Meltwater pulse 1A from Antarctica as a trigger of the Bølling-Allerød warm interval. *Science*, 299(5613), 1709–1713.

<https://doi.org/10.1126/science.1081002>

Weber, M. E., Clark, P. U., Kuhn, G., Timmermann, A., Spreng, D., Gladstone, R., Zhang, X., Lohmann, G., Menviel, L., Chikamoto, M. O., Friedrich, T., & Ohlwein, C. (2014). Millennial-scale variability in Antarctic ice-sheet discharge during the last deglaciation. *Nature*,

510(7503), 134–138. <https://doi.org/10.1038/nature13397>